ANALYSER BASED IMAGING APPLIED TO VISUALISING CARTILAGE AND THE DEVELOPMENT OF TECHNIQUE SPECIFIC PHANTOMS

Thesis submitted in accordance with the requirements of the
University of Liverpool for the degree of Doctor in Philosophy

by

Suzanne Teresa Crittell

28th March 2008

“ Copyright © and Moral Rights for this thesis and any accompanying data (where applicable) are retained by the author and/or other copyright owners. A copy can be downloaded for personal non-commercial research or study, without prior permission or charge. This thesis and the accompanying data cannot be reproduced or quoted extensively from without first obtaining permission in writing from the copyright holder/s. The content of the thesis and accompanying research data (where applicable) must not be changed in any way or sold commercially in any format or medium without the formal permission of the copyright holder/s. When referring to this thesis and any accompanying data, full bibliographic details must be given, e.g. Thesis: Author (Year of Submission) "Full thesis title", University of Liverpool, name of the University Faculty or School or Department, PhD Thesis, pagination.”

ABSTRACT

This thesis investigates the application and quantification of the Analyser Based Imaging (ABI) techniques Diffraction Enhanced imaging (DEI) and Multiple Image Radiography (MIR). There were two aims for this work; first, to develop phantoms capable of characterising the images produced by the different sources of contrast inherent to the ABI methods; and second, to study the application of these techniques to imaging cartilage.

Phantoms for the refraction and absorption contrast were developed and imaged using DEI and MIR. Analysis of the absorption images of the absorption phantom showed that the results for both techniques were in line with those predicted by theory. The refraction images of the refraction phantom were as expected. However, further analysis demonstrated the necessity for accuracy in both positioning the phantom in the beam and in positioning the analyser crystal on the rocking curve. Preliminary investigations into the use of colloidal solution in an Ultra-Small Angle X ray Scattering (USAXS) phantom showed that it is plausible that range of colloidal solution concentrations could be used to create a range of contrast. Signal-to-Noise Ratio area (SNR_{AREA}) analysis was carried out for all of the phantom experiments. The results for the absorption phantom showed that the MIR images consistently gave better results than the DEI images, showing the strength of this technique for the absorption contrast, whilst the refraction phantom results highlighted discrepancies between the two ABI methods at large magnitudes of $\tan\alpha$.

Several cartilage experiments were carried out, imaging a range of samples. Cartilage could be seen in the refraction images. However, this was dependent on the size of the sample and the amount of superposition of the surrounding tissue when imaging whole joints. Signal-to-Noise Ratio line (SNR_{LINE}) analysis was carried out for two of the samples and demonstrated a possible link between high SNR_{LINE} values and high contrast in the Magnetic Resonance Image comparisons. Line profiles were also taken of the cartilage regions of a disarticulated sample showing the potential for detecting different cartilage layers.

CONTENTS

LIST OF FIGURES

ACKNOWLEDGMENTS

I would like to thank my supervisors: Prof. Robert Page; Prof. Paul Nolan and Dr. Chris Hall for all their help and guidance throughout my Ph.D. I would also like to thank: Mark Ibison and the rest of the Daresbury imaging group for all their help, particularly on whilst on experiment; Dr. Richard Hodgson and Dr. Robert Campbell for their involvement in the project; and Sarah Rigby for her help and advice whilst I have been writing up.

On a more personal note I would like to say thank you to: my Mum and Dad, and the rest of my family for their ongoing love and support; and Matthew Wong for putting up with me. I would also like to take this opportunity to thank my secondary school science teacher Mr. Harvey, who believed in my potential.

Finally I would like to say thank you to the other students in the group for all the tea breaks (especially the long summer ones!), they made the whole Ph.D. experience much more enjoyable.

GLOSSARY

ABI	Analyser Based Imaging
BM	Bending Magnet
CT	Computed Tomography
CCD	Charge-Coupled Device
DEI	Diffraction Enhanced Imaging
ESRF	European Synchrotron Radiation Facility
Frelon	Fast Readout Low Noise
IC	Ion Chamber
MIR	Multiple Image Radiography
MRI	Magnetic Resonance Imaging
SNR	Signal-to-Noise Ratio
SRS	Synchrotron Radiation Source
USAXS	Ultra-Small Angle X-ray Scattering

CHAPTER 1

1 INTRODUCTION

The work presented in this thesis was carried out as part of a collaboration between the University of Liverpool and STFC Daresbury. The overall project aims were to develop the Analyser Based Imaging (ABI) system in use at the Daresbury Synchrotron Radiation Source (SRS) and investigate the applications of this technique. My role was to concentrate on the potential area of interest for ABI in biological imaging and to develop phantoms which could be used to quantify the quality of the images produced.

ABI is an x-ray imaging modality which uses a crystal, the analyser crystal, placed downstream of the sample to retrieve phase information from the sample. The first recorded use of ABI was at the beginning of the 1980s. Since then several different ABI techniques have been developed, most notably Diffraction Enhanced Imaging (DEI) which was developed by D. Chapman et al., described in the paper "Diffraction enhanced imaging" and was the first ABI method with the ability to create separate refraction and apparent absorption images [1]. DEI paved the way for other ABI techniques such as Multiple Image Radiography (MIR) which is capable of deriving an additional image with contrast based on the Ultra-Small-Angle X-ray Scattering (USAXS) properties of the sample.

ABI techniques such as DEI and MIR are of great importance due to their ability to obtain phase information from the sample in the form of a refraction image. The advantage of using the sample's refraction properties over its absorption properties are two fold. Firstly, the refraction properties are several orders of magnitude more sensitive to changes than the absorption properties. Secondly, as the x-ray energy increases the refraction sensitivity decreases less steeply than the absorption sensitivity, hence offering advantages in dose reduction.

DEI and MIR therefore have the potential for imaging structures that are not visible in conventional x-ray imaging techniques, such as soft tissue structures. The two main areas of soft tissue imaging that research into ABI methods concentrated on have been mammography and cartilage imaging. For this project it was felt that cartilage imaging would be a promising area of research with particular use in the imaging of arthritic joints which show cartilage damage.

In addition to biological samples it was felt that the development of phantoms suitable for each of the sources of contrast would be beneficial. The main purpose of these phantoms was to enable a good comparison to be carried out between the different ABI algorithms and to provide a means of quantifying the images produced.

In summary there were two main aims of this work. Firstly to image a variety of biological samples to asses the ability of this technique to image the structure of cartilage. Secondly to develop phantoms designed specifically for the different sources of contrast in order to compare the different algorithms used to produce the different images.

CHAPTER 2

2 X RAYS

X rays were discovered in November 1895 by Wilhelm Röntgen while investigating the fluorescence produced on the walls of a discharge tube. X rays are part of the Electromagnetic spectrum with wavelengths in the range of Ångströms [2].

2.1 Conventional sources

In conventional x-ray imaging, x-ray tubes are used as sources. They consist of a negative cathode, containing a filament, and a positive anode target, all of which is contained in a vacuum, shown below in Figure 2-1 [3], [4].

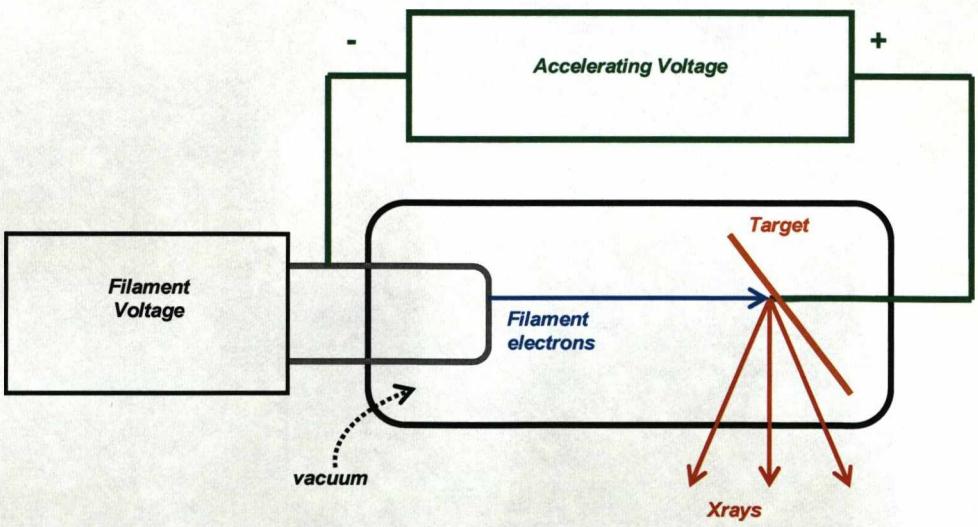

Figure 2-1: Diagram showing the basic components of an x-ray tube [4].

The tube's filament is heated by an applied voltage, providing some of the filament's free electrons with enough energy to overcome the work function of the

material. The newly freed electrons are then attracted to the anode. Upon striking the anode, the electrons lose their kinetic energy. The majority of this energy is lost as heat due to this filament electrons interacting with the outer shell electrons, the rest is converted into x rays [4].

There are two processes by which x rays are created, each producing x rays with different characteristics. If the incoming electron interacts with the electric field of a nucleus in the target and is deflected, as shown in Figure 2-2, it can lose some or all of its kinetic energy in the form of an x-ray photon. This is known as Bremsstrahlung and results in the continuous spectrum shown in Figure 2-3 by the blue line. The maximum kinetic energy possessed by the free electrons is proportional to the voltage applied between the cathode and the anode. This is, therefore, the maximum energy that can be emitted as Bremsstrahlung and occurs when the electron is stopped by the target in a single interaction converting all its energy to a single x-ray photon. From this point, as the energy decreases the relative number of photons will increase steadily until at low energies, the photons begin to be attenuate by the glass walls of the tube and other materials, including filters which are added to the x-ray tube specifically to attenuate low energy photons. This therefore results in a low energy cut-off for the x rays. Filtration of the beam is important because the low energy x rays would be absorbed by the patient, therefore increasing the dose they receive without contributing to the imaging process [4].

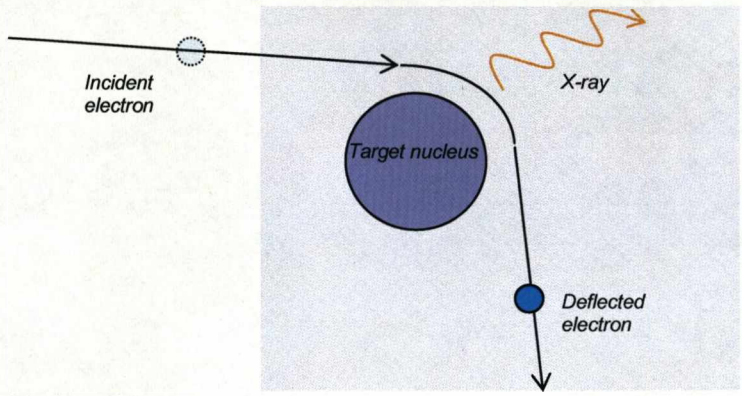

Figure 2-2: Diagram showing an electron being deflected by the field of a nucleus and emitting Bremsstrahlung radiation [4].

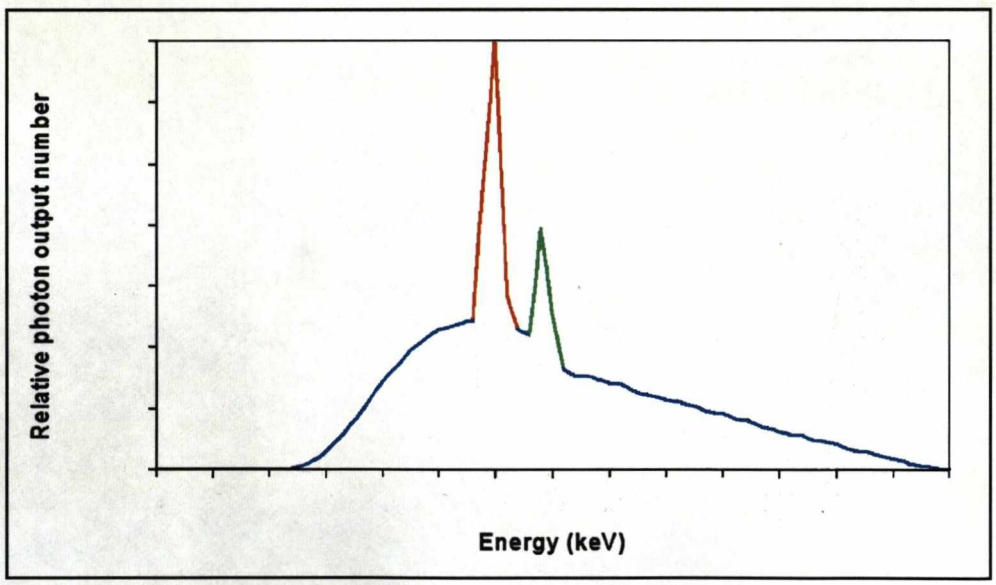

Figure 2-3: An Example x-ray spectra, the continuous Bremsstrahlung spectra is shown in blue, the K_α line is shown in red and the K_β line is shown in green [4].

The second x ray producing process occurs when the incident filament electrons interact with the inner shell electrons of the target atoms. If a filament electron collides with a K shell electron of one of the target's atoms, the atomic electron will be ejected provided that the filament electron's kinetic energy is greater than

the binding energy of the atomic electron. A hole is then left in the K shell. If this hole is filled by an electron from the L shell, an x ray is emitted giving a sharp line in the emission spectra at energy equal to the difference in binding energies between the K and L shells; this is the K_α line and is shown in Figure 2-3 by the red line. Although it is less likely, the hole could instead be filled by an electron from the M shell: again a single x-ray photon is emitted, with energy equal to the difference in the binding energies of the K and M shells; this is the K_β line, shown in Figure 2-3 by the green line. Since the K_α and K_β lines are dependent only on the binding energies of the different shells, they are characteristic of the target material and totally independent of the tube voltage, unlike Bremsstrahlung [4], [5].

Wilhelm Röntgen's experiments in 1895 used a Crooke's tube, also known as a cold cathode tube, which consisted of an evacuated glass tube with a high voltage applied between the cathode and anode contained within the tube. It was not until 1912 that improvements were made to this tube by William Coolidge who introduced the heated filament in the cathode and water cooling a tungsten anode, see Figure 2-4 a). Further improvements were made in the 1960s with the introduction of the rotating anode for improved heat dissipation, shown in Figure 2-4 b) [6].

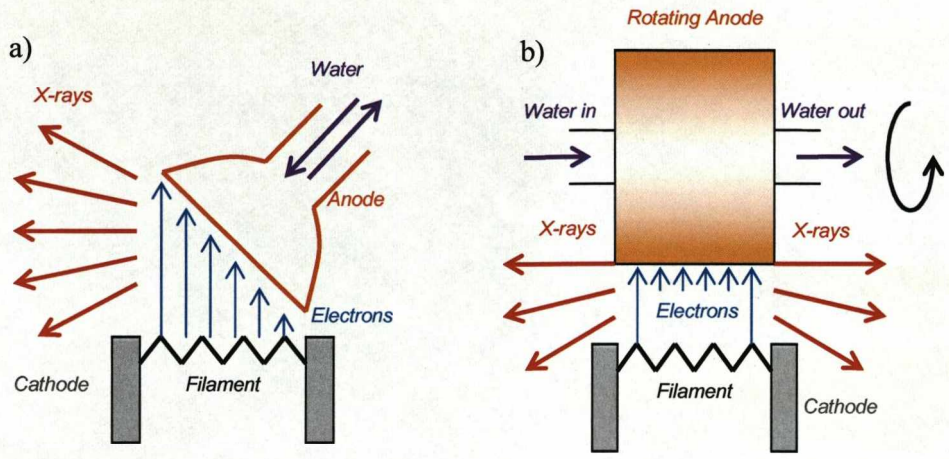

Figure 2-4: a) A diagram of a Coolidge x-ray tube. b) A rotating anode x-ray tube [6].

2.2 **Synchrotron sources**

Synchrotrons have been used in science since the 1940s. The original use was for High Energy Physics experiments, in which particles were accelerated in a circle of constant radius. This was done with the use of magnetic and electric fields that were synchronized with the particle beam. As the particles in these experiments were accelerated they emitted what is now know as synchrotron radiation. It was not long before this radiation was being used 'parasitically' for other experiments. In the 1960s, synchrotrons were developed with the implementation of storage rings, which are large evacuated rings in which the particles are kept circulating. This type of synchrotron radiation source has become known as a first generation source, where the synchrotrons were used for both the production of synchrotron radiation and other types of experiments [6], [7].

Second and third generation synchrotrons are both dedicated to the production of synchrotron radiation and are very similar in design. Electrons are emitted from a heated filament and accelerated by a LINear ACcelerator (LINAC). They are then injected into a booster storage ring which increases their energy further. Finally,

they are injected into the storage ring where they circulate for hours, at some facilities a whole day [6], [7].

Within the storage ring there are two types of devices: bending magnets (BMs) and insertion devices. In second generation synchrotrons, there are very few insertion devices whereas in third generation synchrotrons there are many more. Insertion devices come in two forms, Wigglers and Undulators. The purpose of all three devices is to accelerate the electrons and in doing so stimulating the emission of photons. It is these devices that are the source of the synchrotron radiation. This radiation is then funnelled through beam lines to the experimental hutch [6], [7].

2.2.2 Synchrotron properties

Synchrotrons were a massive departure from previous x-ray sources, i.e. x-ray tubes. The beam emitted by a synchrotron is very high powered and is emitted over a very small range of angles giving a very directional, approximately parallel beam. X rays from conventional sources, however, are emitted at a much lower power over a much larger range of angles. The power of the light source and the range of angles that it emits are used to calculate the source's brilliance, shown in Equation 2-1 [6];

$$Brilliance = \frac{Photons/s}{(mrad)^2 (mm^2 sourcearea)(0.1\%bandwidth)}$$

Equation 2-1

The high intensity twinned with the small angular spread means that synchrotron sources are several orders of magnitude greater in brilliance than conventional sources, shown in Figure 2-5 [6].

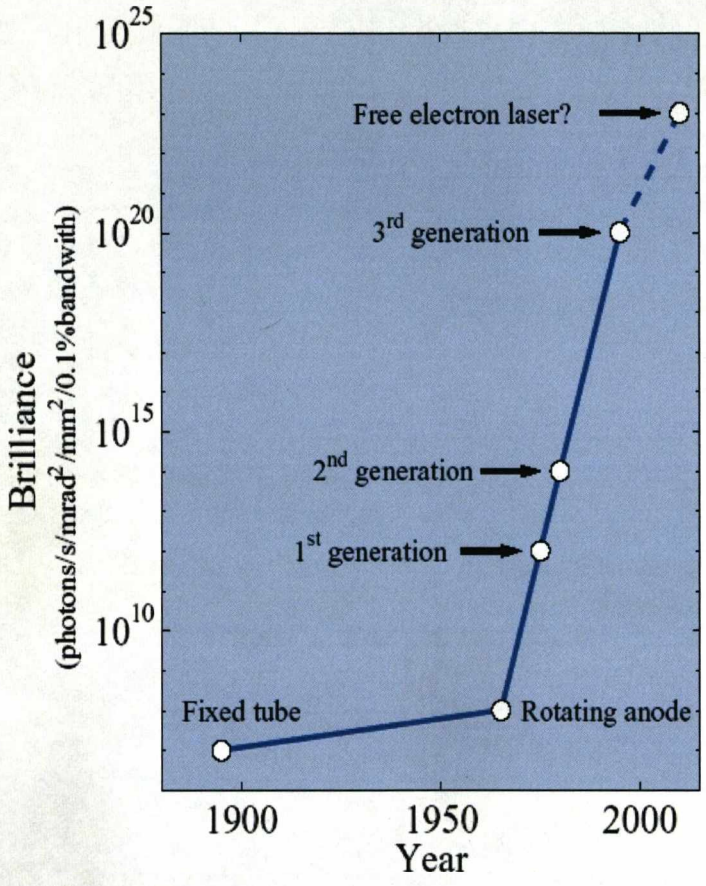

Figure 2-5: Plot showing the increase of the Brilliance of x-ray sources over their history [6].

As mentioned previously, the components in the synchrotron that act as x-ray sources are the devices that are used to accelerate the beam. Since the BMs, Wigglers and Undulators do this in slightly different ways, the x-ray beams that they emit have characteristic differences between them.

2.2.2 *Bending magnets*

The BM's original use was to keep the electrons circling the storage ring and they were the only sources in the first generation synchrotrons. Now the majority of beam lines at synchrotrons are stationed on BMs. They consist of two dipole magnet units, between which the electron beam is accelerated [3], [7].

In the storage ring of a synchrotron the electrons are circulating at a speed u, which is approaching the speed of light. In the frame of reference of the electron the force it feels from the BM is an electrostatic force given by γeuB, where γ is a relativistic constant, e is the charge on an electron, u is the electrons velocity and B is the magnetic field strength. The electrostatic force is equal to the centripetal force on the electron. In the reference frame this is given by the mass of the electron (m_0) multiplied by the centripetal acceleration which is given by the angular velocity (ω_e) multiplied by the tangential speed (u), giving;

$$m_0 \omega_e u = \gamma euB \qquad \text{Equation 2-2}$$

The angular speed of the electron is important because it is linked to the wavelength of light emitted by the bending magnet. The oscillation frequency of the electrons traveling round the arc of the bending magnet is found using the electron's angular speed,

$$\upsilon_e = \frac{\omega_e}{2\pi} = \frac{\gamma eB}{2\pi m_0}. \qquad \text{Equation 2-3}$$

The wavelength in the electron reference frame is, therefore,

$$\lambda_e = \frac{c}{\upsilon_e} = \frac{2\pi m_0 c}{\gamma eB}. \qquad \text{Equation 2-4}$$

where c is the speed of light. In the laboratory frame, due to Doppler shift, the wavelength becomes:

$$\lambda_L = \frac{\lambda_e}{2\gamma} = \frac{\pi m_0 c}{\gamma^2 eB}$$ Equation 2-5

However, the light from a BM is emitted at a range of wavelengths, with λ_L being the central wavelength of a bandwidth $\Delta\lambda$. There is not a single wavelength of light because it is only detected when the electron is directly in front of the beam line. This results in the light emitted by each electron being seen as a short light pulse with time length Δt. From Fourier theorem, $\Delta t \Delta \nu = (1/2\pi)$, where $\Delta \nu$ is the frequency bandwidth. Since Δt is small, $\Delta \nu$ is large and there is therefore a large wavelength bandwidth [7].

2.2.2 Wigglers

Wigglers consist of a series of magnets with alternating polarity, which causes the electron's trajectory to oscillate, see Figure 2-6. In the case of the wiggler the oscillations have a large amplitude and it can be viewed as a series of BMs. The spectrum emitted by the wiggler is the same shape as the spectrum from a bending magnet, however, it is amplified by a factor of 2N, where N is the number of periods along the length L of the wiggler [3], [4].

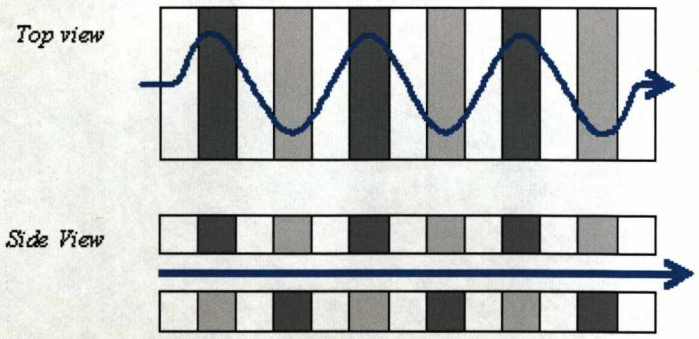

Figure 2-6: Diagram showing the trajectory of electrons through the wiggler [7].

2.2.2 Undulators

Undulators also consist of a periodic array of magnets. However, the field strength of the magnets is lower than that in the wiggler, resulting in the electrons traveling through smaller oscillations. In the undulator, the radiation emitted at each oscillation is in phase with the radiation emitted from the following oscillation. This means that the overall emitted intensity is equal to the square of the sum of the amplitudes of the emitted waves. This coherent addition only holds true for one wavelength of light and its harmonics [3], [4].

2.3 **X-ray interactions**

X rays can be viewed as both particles and waves. When x rays are incident on a material there are many ways by which they can interact; the x ray can undergo Compton scattering, Rayleigh scattering, photoelectric absorption or pair production. With the exception of pair production, which only occurs at energies a lot greater than those used in the experiments, all of these effects contribute to the attenuation of the x-ray beam [1]-[7].

Compton Scattering was discovered in 1927 by Arthur Compton. It occurs when the x-ray photon collides with an outer shell electron (semi-bound electron). This means that the photon's energy, $h\nu$, is much greater than the electrons binding energy. The photon and electron scatter, the scattered electron gains kinetic energy T and the scattered photon has energy $h\nu'$, as shown in Figure 2-7 [3], [4].

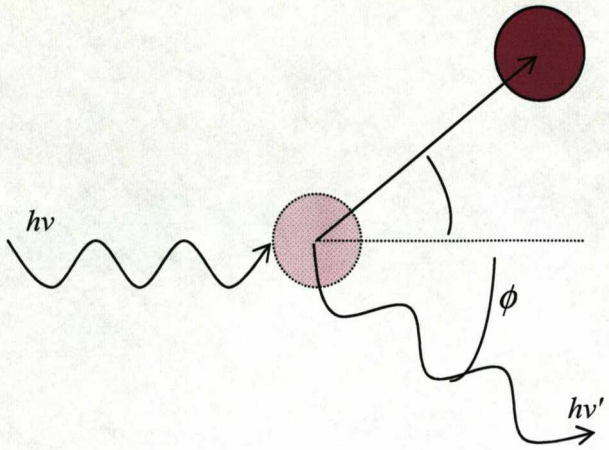

Figure 2-7: Diagram showing the Compton scattering of an electron and an x ray [6].

The kinetic energy of the scattered electron is given by $T=h\nu-h\nu'$, and the energy of the scattered photon is equal to $h\nu'$, which is given by,

$$h\nu' = \frac{h\nu}{\left[1+\left(\frac{h\nu}{m_0 c^2}\right)(1-\cos\phi)\right]} \qquad \text{Equation 2-6}$$

where m_0 is the rest mass of the electron and ϕ is the angle through which the photon scatters.

Photoelectric absorption is the dominant process below 100 keV, the lower end of the diagnostic range and the energy range that our ABI experiments were carried out. In this case the incident x-ray photon, with energy E, interacts with electrons from the inner shells of the atom. If the photon energy is greater than the binding energy of the electron, BE, the electron is ejected with kinetic energy T, given by $T = E - BE$ leaving a hole in the inner shell. The hole is filled by an electron from a higher shell, emitting a characteristic x-ray photon [4], [8].

Rayleigh scattering is only significant at low x-ray energies and therefore mainly occurs in mammography. When the x-ray photon undergoes Rayleigh scattering it is scattered by the all the bound electrons and loses only a very small amount of energy [3]-[5].

All these x-ray interaction processes viewed the x rays as photons. However, their interactions can also be described with the x rays being thought of as waves. They can therefore undergo scattering in the form of refraction, which, as mentioned in the introduction, is a source of contrast in ABI.

In the x-ray region the refractive index has a value less than one with its difference from unity given by the phase difference, δ. The refractive index also takes account of the absorption processes that occur in the medium, given by β. The full equation of the refractive index, n, is given by,

$$n = 1 - \delta + i\beta, \qquad \text{Equation 2-7}$$

The absorption term, β, is

$$\beta = \frac{\mu}{2k}, \qquad \text{Equation 2-8}$$

where μ is the absorption coefficient and k is the wavevector. The phase term, δ, can also be expanded in a similar way,

$$\delta = \frac{2\pi\rho_a f^0(0) r_0}{k^2}, \qquad \text{Equation 2-9}$$

where ρ_a is the atomic number density, r_0 is the Thomson scattering length and $f(Q)$ is the atomic scattering factor, which is a function of Q, the wavevector

transfer. $f^{\circ}(Q)$ is the forward scattering factor for all the electrons in the atom. As $Q \rightarrow 0$, $f^{\circ}(Q) = Z$, the number of electrons in the atom. The atomic scattering factor in full is complex and given by;

$$f(Q) = f^{\circ}(Q) + f' + if'', \qquad \text{Equation 2-10}$$

where f' and f'' are the dispersion corrections. Using this, the refractive index becomes

$$n \equiv 1 - \frac{2\pi\rho_a r_0}{k^2}\{f^{\circ}(0) + f' + if''\} \qquad \text{Equation 2-11}$$

δ, is therefore given by,

$$\delta = \frac{2\pi\rho_a r_0}{k^2}\{f_0(0) + f'\} = \frac{\rho_a r_0 (hc)^2}{2\pi E^2}\{f_0(0) + f'\} \qquad \text{Equation 2-12}$$

so,

$$\delta \propto E^{-2} \qquad \text{Equation 2-13}$$

where E is the x-ray beam energy. The absorption term becomes

$$\beta = -\left(\frac{2\pi\rho_a r_0}{k^2}\right) f'' = \frac{\mu}{2k} \qquad \text{Equation 2-14}$$

$$= -\frac{hc}{4\pi E}\mu$$

$$= -\frac{hc}{4\pi E}\rho\sigma,$$

where ρ is the density of the medium and σ is the absorption cross section, which is $\propto E^{-3}$. Therefore,

$$\beta \propto E^{-4} \qquad \text{Equation 2-15}$$

Thus, δ can be several orders of magnitude greater than β, for example the values for nylon at 25keV are $\delta = 3.5\times10^{-7}$ and $\beta = 8.12\times10^{-11}$. The relationships of δ and β with E, shown in Equation 2-13 and Equation 2-15, respectively are important because they mean that as the x-ray energy increases the absorption effects of the medium decrease more rapidly than the phase difference effects, as shown in Figure 2-8.

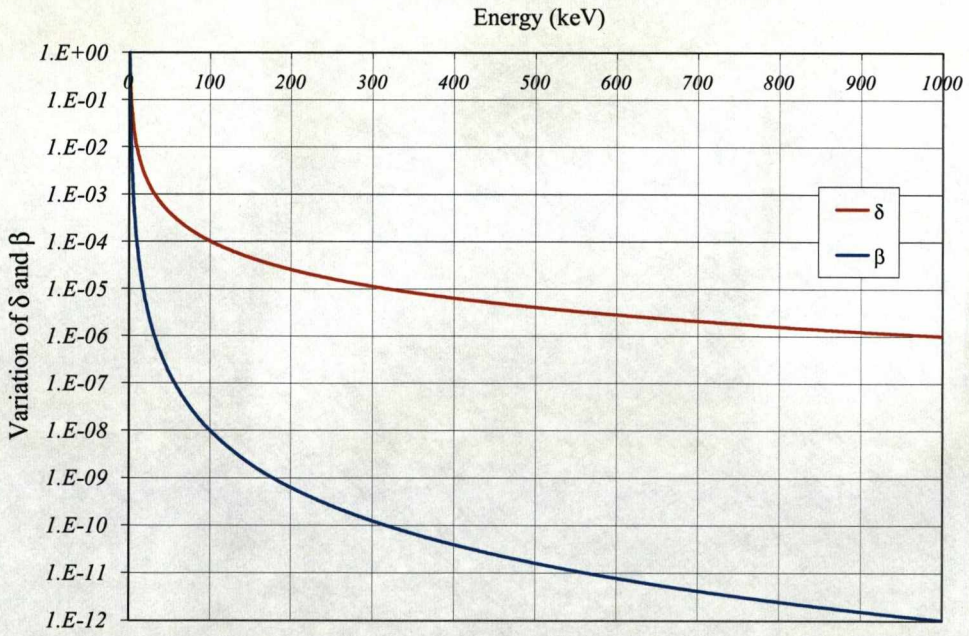

Figure 2-8: Plot showing the variation of δ and β with increasing energy

From Snell's law, the angular deviation of the x-ray beam, $\Delta\theta$, is given by,

$$\Delta\theta \approx (n_1 - n_2)\tan\alpha = (\delta_1 - \delta_2)\tan\alpha \qquad \text{Equation 2-16}$$

where n_1 and n_2 are the refractive indices of two homogeneous media, δ_1 and δ_2 are the phase terms of the two media and α is the angle between the incident beam and the normal of the interface between the two homogeneous media. Therefore although the contrast in the refraction images will decrease with increasing energy, it will decrease less than that in the absorption images, offering greater potential for refraction images at higher energies which has the advantage of giving a lower dose to the sample.

2.4 Monochromator and Analyser Crystals

As described in Section 2.2.2, the x-ray beams emitted by synchrotron sources are polychromatic. However, the high intensity and good collimation of the beam mean it is possible for monochromators to be used at synchrotron sources. Two types of monochromators can be employed; gratings for soft x rays or crystals for hard x rays. For the energy range used for ABI, crystal monochromators are used.

Crystal monochromators work by diffracting the incident x-ray beam, as described by Bragg's law given by Equation 2-17 [6], [9];

$$2d\sin\theta_d = n\lambda, \qquad \text{Equation 2-17}$$

where d is the crystal plane spacing, θ_d is the angle of the incident beam to give the maximum intensity Bragg reflection, n is an integer and λ is the wavelength of light, as shown in Figure 2-9 [9]. The incident beam is composed of several wavelengths each of which has their own characteristic Bragg reflection; unwanted reflections are blocked by shielding.

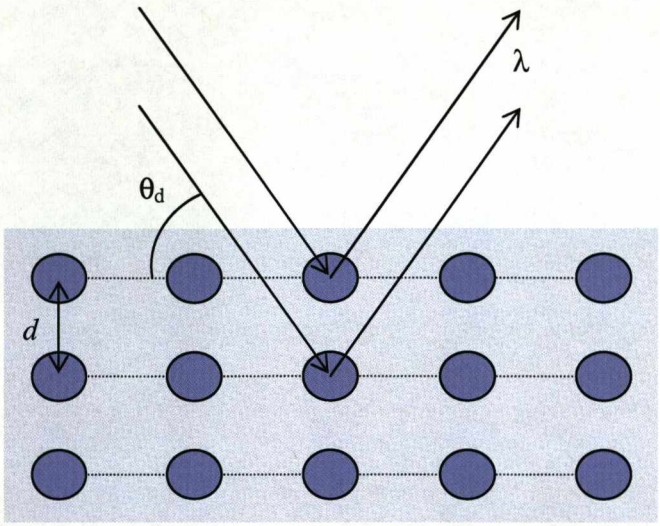

Figure 2-9: Diagram showing the different parameters used in Bragg's Law [9].

The ability of a crystal to diffract the incident beam relies of several different factors. As can be seen from Figure 2-9, the Bragg reflections are dependent on the *d*, the crystal plane spacing, which is in turn dependent on both the type of crystal used and the plane in which the crystal is cut. From Bragg's Law it can be seen that λ must be smaller than $2d$, however, if λ is a lot smaller than $2d$ the value of θ_d is impractically small; this is taken into account when considering the types of crystals to be used as monochromators. The most common types of crystals used are germanium and silicon since large high quality crystals can be produced [7].

In addition to having the required crystal spacing the crystals also need to be of a high enough quality. If the crystal is composed of grains with different orientations, there is a spread in θ_d, giving a spread in λ and therefore meaning the monochromator would give limited resolution. In addition, the crystals must suffer limited radiation damage on exposure to the beam and be thermally stable. To improve thermal stability, the monochromator crystals can be water cooled [7].

In order to improve the resolving power of a monochromator more than one crystal can be used, for example in a double crystal monochromator. However there can be problems with the crystal alignment. To overcome this, two parts of the same crystal can be used instead of two independent crystals. This is a channel-cut crystal and guarantees crystal alignment; it does, however, limit the flexibility of the monochromator [7].

2.5 **X-ray Detection**

There are many different types of x-ray detectors. Some are used to measure properties of the beam, such as energy, and others are used for imaging. The detectors that were used in the experiments are described in this section.

2.5.2 Ion Chambers

The Ion Chamber (IC) is a gas filled detector, shown in Figure 2-10. It consists of a gas container which is negatively charged (the cathode) and a wire which is positively charged (the anode). When an x ray is incident on the chamber ion pairs, consisting of a positive ion and an electron, are created along the x-rays path. A voltage is applied between the cathode and the anode which drives the ion pairs apart, creating a signal when they reach the electrodes. The size of the signal produced is dependent on the number of ion pairs produced. This signal is very small and therefore requires amplification by an external circuit [8].

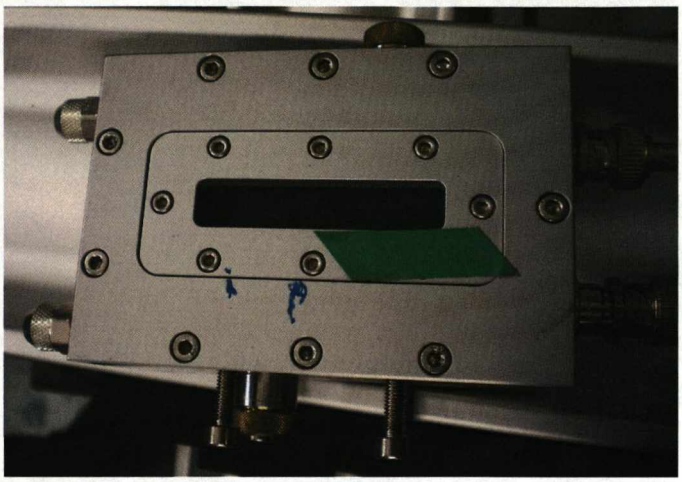

Figure 2-10: A picture of the Ionisation chamber used.

ICs were used in all the experiments to track the path of the beam in the alignment stages and monitor the beam intensities. In some cases it was also used to measure the rocking curve of the analyser crystal (see Section 3.2).

2.5.2 Sodium Iodide Detector

Sodium iodide detectors are inorganic scintillation detectors. The detector consists of a sodium iodide crystal, doped with thallium, coupled to a photomultiplier tube. When the x rays are incident on the crystal, they stimulate the promotion of electrons from the valance band of the crystal into the conduction band. The impurities in the crystal are called activator sites. When the electrons de-excite from the conduction band to the valence band through these sites, they emit photons with wavelengths in the visible region. These photons pass through the crystal to the photomultiplier tube, which consists of a photocathode, which converts the photons into electrons and an electron multiplier, which amplifies the number of electrons, creating a signal. This signal is proportional to the amount of radiation incident on the detector [8].

2.5.2 CCD detector

Charge-Coupled Devices (CCDs) and Frelon cameras, described in Section 2.5.2.1, were used to record the images in the experiments which are described in Chapter 4. These detectors were used because they are 2-dimensional detectors that record the x-ray intensity incident on them.

The CCD was pioneered at the beginning of the 1970s, with scientific CCDs introduced twenty years later. They are integrating detectors that implement a serial readout technique.

Normally made on silicon wafer, CCDs have a depleted region below the surface. The area of the CCD is divided into pixels consisting of metal-oxide-silicon (MOS) electrode structures which create a potential minimum below the surface. When x rays are incident on the detector electrons are promoted to the conduction band via the photoelectric effect, these electrons are then collected in the pixel's potential well. At the end of the exposure time the amount of charge collected in each pixel's potential well is dependent on the number of x rays incident on it. In a process known as clocking, drive pulses are applied to the control electrodes which move the rows of stored charge in the preferred direction. This is done by adjusting the phase of voltage between the three drive lines that are attached to each pixel. When a row of charge reaches the readout section drive pulses are applied to it, driving each pixel individually to the amplifier that is integrated in the chip [8].

As well as electrons being excited into the conduction band by the incident x rays, they can also be thermally excited resulting in a dark current. In order to minimise this CCDs are cooled. In addition, a dark image is taken which can then be subtracted from the object image to correct for this dark current. As well as dark images, flat field images can also be taken which, when subtracted from the object

image, correct for any discontinuities in the image collection over the area of the detector [8].

2.5.2.1 Frelon camera

The Frelon camera is a **F**ast **Re**ad out **Lo**w **N**oise CCD which is coupled to a fibre optical taper. The taper optics have a larger active area than the CCD, giving the detector a larger field of view. The x rays are incident on this active area and converted to visible light by a standard mammographic phosphor screen. These visible photons are then incident on the CCD and the image is recorded [10].

CHAPTER 3

3 IMAGING

Since their discovery in November 1895 x rays have been used in imaging. The first ever x-ray images were taken of Wilhelm Röntgen's wife's hand (see Figure 3-1). Three months later x-ray images were being used in a hospital in Vienna [4].

Figure 3-1: X-ray image taken of Wilhelm Röntgens' wife's hand [11].

3.1 Conventional Imaging

Projection Radiography utilises the different absorption properties of the tissues to produce the image contrast and are used in imaging today. Several other diagnostic imaging techniques have been developed since the first radiographs were taken. Some, for example Computed Tomography, use x rays to produce the image contrast, while others, such as Magnetic Resonance Imaging, do not. These techniques will be discussed in the following sections.

3.1.2 Projection Radiography

In projection radiography, an x-ray beam is incident on the patient. The x-ray beam is then absorbed by the different tissues of the subject. The amount of absorption is dependent on the atomic number (Z) of the tissue (see Section 2.3). Since bone has a higher Z value than the surrounding soft tissue, the x-ray beam is preferentially absorbed by the bone, the resulting radiograph is composed of the absorption profiles of the different tissues superimposed on one another. In addition, the radiograph also has a pattern of scattered x rays on top of the image obscuring it [4].

X-ray imaging is a compromise between the quality of the image and the radiation dose given to the patient. In projection radiography, when imaging bone, a balance between limited image quality and dose is easily found due to the good contrast between the bone and the surrounding soft tissue [4].

It is more difficult, however, to distinguish between different soft tissues. One option is to use a low x-ray energy; this is done in mammography, where a beam energy that is less than 30 keV is used. However, this reduced beam energy leads to a higher dose. In other instances contrast agents, which contain high Z elements, such as iodine, are used to enhance the contrast between different soft tissues [3], [4].

3.1.2 X-ray Computed Tomography

The idea for x-ray Computed Tomography (x-ray CT) was first conceived of in the late 1960s. It is now widely used in diagnostic medical imaging. The advantage of x-ray CT over projection imaging is that projection images consist of a superposition of the surrounding structures which adds to noise in the image, whereas x-ray CT makes it possible to image a patient or sample in 3dimensions, getting rid of the blurring from the surrounding tissues [4].

X-ray CT systems comprise an integrated gantry, which holds a rotating anode x-ray tube, and a detector arrangement. The system rotates at a rate of ~0.4 s per rotation, with the source and detector fixed relative to one another. As the x-ray source rotates it is pulsed. Each pulse lasts for ~2-3ms, which leads to a scan time of ~1s [3].

3.1.2 Magnetic Resonance Imaging (MRI)

Magnetic Resonance Imaging (MRI) has been in commercial use since the start of the 1980s and is used for diagnosis in all parts of the body. It provides sectional images which are characterised by the biochemical differences between different tissues [3].

Unlike CT and projection radiography, MRI uses nuclear magnetic resonance to create its images with the use of a strong magnetic field and radio-frequency pulses [3], [4].

3.2 **Synchrotron Imaging**

As mentioned previously in Section 2.2, synchrotrons have several advantages over x-ray tubes as an x-ray source. These include a higher intensity, lower angular deviation of the beam and the ability to select a single x-ray energy. These factors have led to both improvements in conventional techniques, such as projection imaging and x-ray CT, and to the development of new techniques. In terms of improvements; the collimation of the synchrotron beam leads to a reduction in the diffuse scattering background that is present in conventional images; and the ability to select a single x-ray energy means that the beam can be optimised for imaging a specific part of the body.

The improved beam properties of synchrotrons have made it possible to derive image contrast from the change in phase as the x-ray beam passes through the

sample, instead of the absorption of the beam as it traverses the sample. These techniques will be discussed in the following sections.

3.2.2 Phase Imaging

For the majority of its existence, x-ray imaging has produced images with contrast derived from the attenuation of the x-ray beam that is incident on the sample. However, more recently experimental research has shifted to concentrate on producing images with contrast based on the phase changes of the x-ray beam as it traverses the sample.

As seen in Section 2.3 the refractive index is given by

$$n = 1 + \delta + i\beta, \qquad \text{Equation 3-1}$$

where δ is the phase term and β is the absorption term. The main reason of interest in phase imaging techniques is that δ is several orders of magnitude greater than β, meaning there is potential for increased image contrast [6], [12].

There are three different types of phase imaging modalities; interferometry, in-line holography and diffractometry. Analyser Based Imaging (ABI) is a form of diffractometry and as it forms the basis of the work it is described in the next section [12], [13].

3.2.2 Analyser Based Imaging (ABI)

The first reported use of an ABI method was a Förster et al. in 1980. Since then, many different groups have carried out work in this area with slightly different variations in the method. Most notable is the research published by D. Chapman et al. on their version of ABI, called Diffraction Enhanced Imaging (DEI), which was the first technique to create separate refraction and absorption images. This has then been extended by different groups to produce an additional image with

contrast based in the scattering properties of the sample, this method is commonly referred to as Multiple Image Radiography (MIR) [1], [12], [14]-[18].

No matter what the analysis method, the basic ABI system remains the same, as shown below in Figure 3-2. The synchrotron beam is incident on the monochromator crystal, which is tuned to select a specific beam energy. The monochromated beam then traverses the sample and is incident on the analyser crystal which has been tuned to a specific position. The resulting image is then recorded on the CCD detector [1], [13].

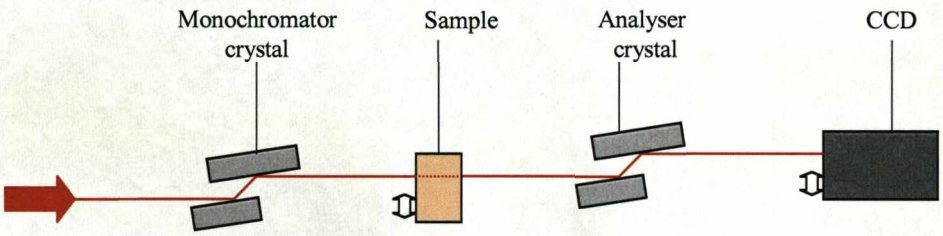

Figure 3-2: Diagram showing the basic ABI system.

The key component of the ABI system is the analyser crystal. The reason it is so important is because it has a finite angular acceptance, characterised by a rocking curve, a plot of relative intensity against the angle of incidence of the x-ray beam on the sample, an example of an experimental rocking curve is shown in Figure 3-3. The DEI and MIR methods use the rocking curve to facilitate the creation of images with different sources of contrast. DEI is capable of creating two separate images, a refraction image and an apparent absorption image [1], [19].

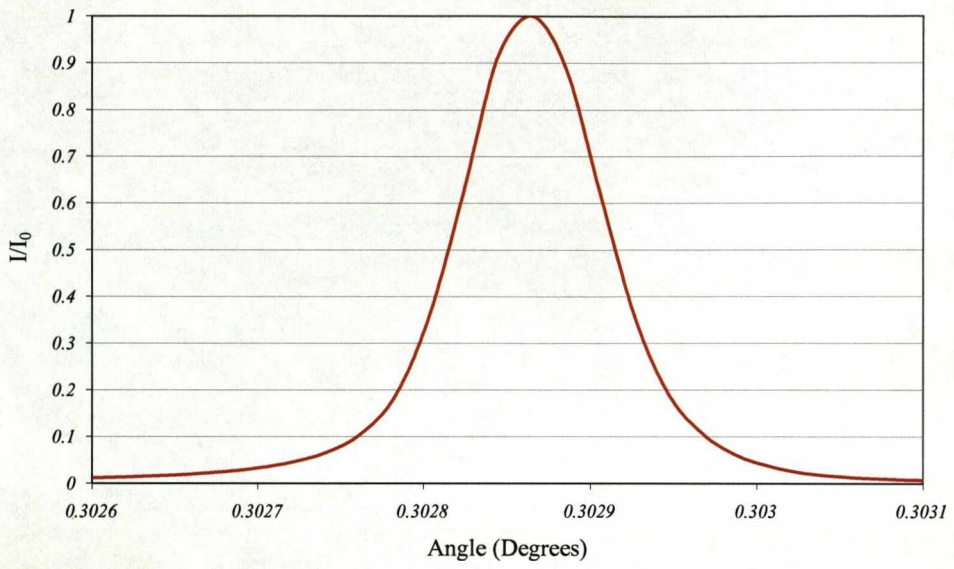

Figure 3-3: An example Rocking curve taken on Station 9.4 at Daresbury SRS using [111] channel cut crystals.

As the x-ray beam traverses the sample and is incident on a boundary between media with different refractive indices, it is deflected by a small amount $\Delta\theta_z$. Using Snell's Law this can be related to the phase term of the refractive index,

$$\Delta\theta_z = (\delta_2 - \delta_1)\tan\alpha, \qquad \text{Equation 3-2}$$

where δ_1 and δ_2 are the phase terms of the two homogeneous media and α is the angle between the incident beam and the normal of the interface between the two homogeneous media [20].

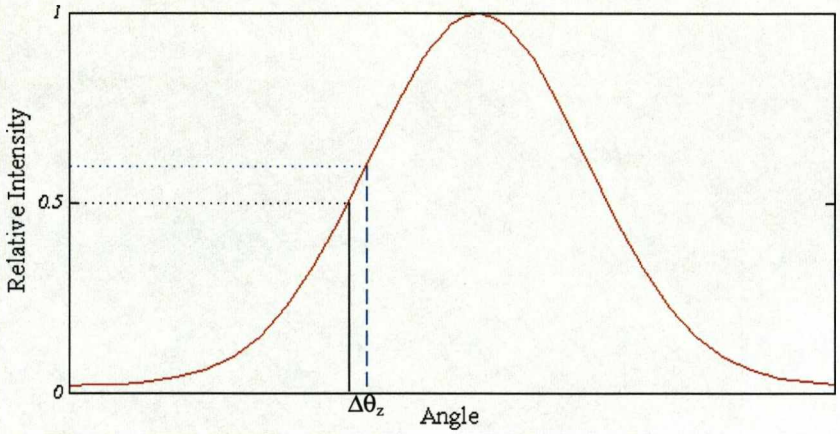

Figure 3-4: Diagram of a rocking curve showing the variation of intensity given by a small change in angle $\Delta\theta_z$.

When the analyser crystal is positioned on the side of the rocking curve this small change in angle ($\Delta\theta_z$) creates a change in the intensity that is diffracted by the analyser crystal. In this way the analyser crystal acts as an intensity amplifier, as demonstrated in Figure 3-4. It is this that creates the contrast in the refraction image [19], [21].

In conventional images, x rays scattered at the μradian level, which is below the level of anti-scatter grids, reach the detector and add to the blurring of the image. However, the small angular acceptance of the analyser crystal prevents most of the scattered radiation from contributing to the images. The absence of these x rays appears as attenuation and is called extinction, which is the loss in intensity due to the diffraction of the beam as it travels through the sample [1], [12], [19].

When the analyser crystal is tuned to the peak of the rocking curve, all the x-rays scattered at this μradian level are rejected. When the analyser crystal is positioned on the shoulder of the rocking curve, some of the x rays scattered at this level are diffracted by the crystal and reach the detector to form part of the image. The

presence of both absorption and extinction contrast leads to the absorption image being known as the apparent absorption image [1], [12], [19].

When the x-ray beam traverses the sample, as previously stated, it undergoes many different interactions. Using the ABI system, only the component of the beam which has been attenuated by both absorption and extinction, and has also been refracted reaches the detector. This has an intensity I_R. Any other components, for example those which have been scattered on a scale greater than μradians or, do not fall within the angular acceptance of the system, therefore contribute nothing to the resulting images [1].

Two images are taken using the DEI method. The analyser crystal is tuned to either side of the rocking curve, at values of $\pm\theta$ from the rocking curve's peak, θ_B. The intensity that the analyser crystal diffracts to at these positions is given by;

$$I_B = I_R R(\theta_B \pm \theta) \qquad \text{Equation 3-3}$$

where $R(\theta)$ is the reflectivity of the analyser crystal[1].

When the analyser crystal is set to the ±50% relative intensity, which is the full width half maximum or the Darwin width ($\Delta\theta_D$) of the rocking curve, Equation 3-3 becomes [1];

$$I_B = I_R R\left(\theta_B \pm \frac{\Delta\theta_D}{2}\right). \qquad \text{Equation 3-4}$$

Any parts of the x-ray beam that are not refracted by the sample will strike the analyser crystal at the angle $\theta_B \pm \Delta\theta_D$ and they will therefore have a reflectivity of

0.5. If however a component of the beam has been refracted by the sample it will have been deviated by some small amount $\Delta\theta_Z$. This deviation means this part of the beam will be incident on the analyser crystal at the angle $\theta_B \pm \Delta\theta_D + \Delta\theta_z$, as demonstrated in Figure 3-4. This will be diffracted by the analyser crystal at a different intensity, given by [1];

$$I_B = I_R R\left(\theta_B \pm \frac{\Delta\theta_D}{2} + \Delta\theta_Z\right). \qquad \text{Equation 3-5}$$

For small values of $\Delta\theta_Z$ and assuming that the slope of the rocking curve is constant at that point, the refractivity term can be expanded using the Taylor series approximation giving;

$$R(\theta_0 + \Delta\theta_Z) = R(\theta_0) + \frac{dR(\theta_0)}{d\theta}\Delta\theta_Z \qquad \text{Equation 3-6}$$

When the analyser is tuned to the low and high angle sides of the rocking curve, respectively, Equation 3-5 becomes [1];

$$I_L = I_R\left(R(\theta_L) + \frac{dR(\theta_L)}{d\theta}\Delta\theta_Z\right) \qquad \text{Equation 3-7}$$

$$I_H = I_R\left(R(\theta_H) + \frac{dR(\theta_H)}{d\theta}\Delta\theta_Z\right) \qquad \text{Equation 3-8}$$

where I_L and I_H are the intensities on the low and high sides of the rocking curve respectively. Equation 3-7 and Equation 3-8 can then be solved for the angle of refraction $\Delta\theta_Z$ and the intensity I_R [1],

$$\Delta\theta_Z = \frac{I_H R(\theta_L) - I_L R(\theta_H)}{I_L\left(\frac{dR(\theta_H)}{d\theta}\right) - I_H\left(\frac{dR(\theta_L)}{d\theta}\right)}$$

Equation 3-9

$$I_R = \frac{I_L\left(\frac{dR(\theta_H)}{d\theta}\right) - I_H\left(\frac{dR(\theta_L)}{d\theta}\right)}{R(\theta_L)\left(\frac{dR(\theta_H)}{d\theta}\right) - R(\theta_H)\left(\frac{dR(\theta_L)}{d\theta}\right)}$$

Equation 3-10

When carried out experimentally, flat field images are also taken at both of the imaging positions, where flat field images are effectively images of the beam and the system optics. Dark field images are also taken, which show the dark current of the CCD. These additional images are taken so as to correct the sample images for artefacts on the detector.

The main drawback of DEI is the way it interprets extinction. As noted previously, extinction is due to the scattering of the x rays at a μradian level. Scattering through these angles is known as Ultra Small Angle X-ray Scattering (USAXS) and is caused by x rays scattering off unresolved structures.

DEI interprets extinction as an added source of attenuation in the apparent absorption image. However, the presence of USAXS increases the width of the rocking curve, therefore decreasing the slope on either side. This, in turn, decreases the intensity seen for the refraction that occurred in the object, which is reflected in the refraction image. The presence of USAXS therefore affects the refraction image, not just the apparent absorption image and inaccuracies are present due to DEI not considering USAXS separately from refraction and absorption [22].

Several groups have set out to overcome this problem by developing different ABI methods. With the exception of one group, who created a method which produced an apparent absorption image and a refraction enhanced scattering image (L. Rigon et al.), work has gone towards creating separate absorption, refraction and USAXS images [16].

For simplicity, all of these techniques will be referred to as Multiple Image Radiography (MIR). All the techniques view the intensity in each pixel of the detector as a convolution of the intrinsic rocking curve with the angular intensity distribution of the x rays emerging from the sample. A series of images is taken with the analyser crystal tuned to N different positions with and without the sample in the beam. This enables two rocking curves to be mapped for each pixel, one with the sample in the beam and the other without. The MIR algorithm calculates the shift between these rocking curves for each pixel. This is shown in Figure 3-4 [17], [18], [23].

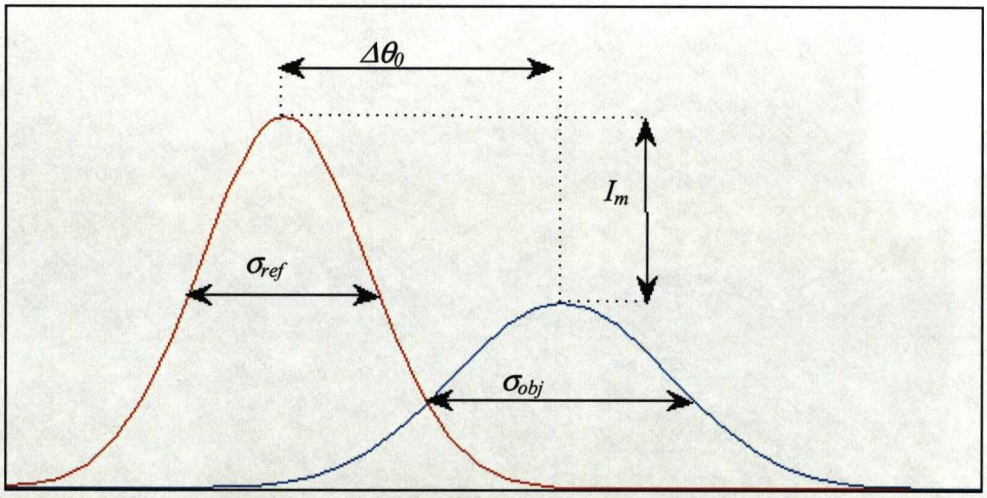

Figure 3-5: A diagram showing how the rocking curve varies for a single pixel. The red curve is the rocking curve plotted from the flat field images and the blue curve is the rocking curve plotted from the sample images. $\Delta\theta_0$ is the change in centre of mass of the rocking curve, I_m is the maximum absorption σ_{ref} is the standard deviation of the reference rocking curve and σ_{obj} is the standard deviation of the sample rocking curve [18].

The calculation of the shift between the rocking curves is possible because the MIR algorithm calculates the zeroth-, first- and second order moments (M_0, M_1, and M_2 respectively) for both data series, for every pixel in the image,

$$M_i = \sum_{j=1..N} (\theta_j)^i \cdot R(\theta) \quad (where\ i=0,1,2), \qquad \text{Equation 3-11}$$

where θ_j is the angle that the analyser was tuned to at the j^{th} position and $R(\theta_j)$ is the intensity at θ_j [18].

Using the calculated moments, it is possible to calculate the different parameters of the rocking curves. The zeroth-moment M_0 gives the integrated intensity. The centre of mass of the rocking curve is given by $\theta_0 = M_1/M_0$ and the standard deviation is given by $\sigma_u = (M_2/M_0 - \theta_0^2)^{1/2}$. These parameters can then be used to find the final the absorption, refraction and USAXS values for each pixel. The integrated absorption is given by;

$$I_{abs} = M_{0,obj} \Big/ M_{0,ref}, \qquad \text{Equation 3-12}$$

where $M_{0,obj}$ is the zeroth-moment for the sample rocking curve and $M_{0,ref}$ is the zeroth-moment for the rocking curve without a sample. The integrated refraction is given by;

$$\Delta\theta_0 = \left(\theta_{0,obj}^2 - \theta_{0,ref}^2\right), \qquad \text{Equation 3-13}$$

where $\theta_{0,obj}$ is the centre of mass for the sample rocking curve and $\theta_{0,ref}$ is the centre of mass for the rocking curve without a sample. The USAXS value is given by:

$$\sigma_u = \left(\sigma_{obj}^2 - \sigma_{ref}^2\right)^{1/2}. \qquad \text{Equation 3-14}$$

Work carried out by B. Marquet et. al, suggests that for such techniques the optimum number of imaging positions is ten, after which the performance saturates [24].

Unlike the DEI method, when the MIR method is applied experimentally only additional dark field images are required, as the flat field images are effectively already accounted for in the method, and the dark field images are subtracted from both the sample images and the reference images.

DEI and MIR both produce 2D-images of 3D objects. As with conventional projection radiography the final images therefore show the structures in the object superimposed on one another. This can be overcome by using Computed Tomography (CT).

3.2.2.1 ABI-CT

CT reconstruction was originally designed for images showing the attenuation of x rays through the sample. It is based on the fact that the intensity at a certain pixel is given by,

$$I = I_0 \exp\left(-\int \mu(x,y)ds\right), \qquad \text{Equation 3-15}$$

where I_0 is the initial beam intensity, I recorded beam intensity and μ(x,y) is the attenuation coefficient at position (x,y) along the x-ray path between A and B, as shown in Figure 3-6, where the ray path can be written as $x\cos\theta + y\sin\theta = t$ [25].

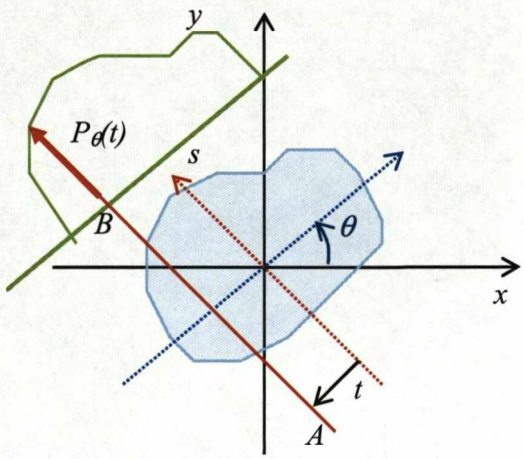

Figure 3-6: Diagram showing the different parameters used to describe the CT reconstruction [25].

From Figure 3-6 the total attenuation at angle θ and ray position (t), is given by recorded intensity profile P_θ[25];

$$P_\theta(t) = \ln\left(\frac{I}{I_0}\right) = \int_{(\theta,t)line} \mu(x,y)ds = \int_{-\infty}^{\infty} f(x,y)ds \qquad \text{Equation 3-16}$$

Using the delta function and the expression for the ray path, the equation for the total attenuation becomes [25];

$$P_\theta(t) = \int_{-\infty}^{\infty}\int_{-\infty}^{\infty} f(x,y)\delta(x\cos\theta + y\sin\theta - t)dxdy \qquad \text{Equation 3-17}$$

This is known as the Radon transform of the function *f(x,y)*. The aim of CT reconstruction is to find *f(x,y)* from the function $P_\theta(t)$ which can be done using the Filtered Back Projection algorithm [3], [25].

As with attenuation, the refraction angle through the sample, $\Delta\theta_z$, is also described in terms of a line integral;

$$\Delta\theta_z = \int \frac{\partial n}{\partial z}(l)dl \qquad \text{Equation 3-18}$$

This means that the Filtered Back Projection algorithm can also be used to reconstruct CT refraction data, therefore making DEI-CT possible. In addition it has been shown that there is a linear relationship between the USAXS image and the sample's scattering properties, therefore making MIR-CT possible [23], [26]-[28].

3.2.2.2 Applications of ABI techniques

The phase sensitivity of the different ABI methods enables materials with low attenuation properties to be visualised. This therefore makes ABI a potentially good method for imaging soft tissue structures [29]. Research into this has fallen into two main areas, mammography and cartilage imaging.

In mammography low energy x-rays are used to differentiate between tumor lesions and normal tissue, a process which utilises the differences in the x-ray absorption of the tissues. In addition to tumors, microcalcifications and speculations can also be a sign of breast cancer and need to be identified in mammograms. ABI techniques, unlike conventional mammography, can draw contrast from very small variations in refractive indices and from the USAXS properties of the sample, as well as the elimination of scattered x rays from the images mean that ABI techniques are well suited to mammography [12],[30].

Work carried out to investigate the application of ABI to mammography has been undertaken by several different groups and seen both mammography phantoms and samples being imaged. The results showed that ABI methods had improved contrast and gave a large increase in the visualization of microcalcifications in samples when compared with conventional techniques.They were also shown to deliver a similar x-ray exposure to the patient [12], [30]-[32].

The work presented in this thesis concentrates on the application of ABI to cartilage imaging since this has been less extensively studied compared with the application to mammography. In addition, diseases such as osteoarthritis mean there is a potential need for a technique that can image articular cartilage [33].

Cartilage is a type of connective tissue; articular cartilage covers the moving surface of synovial joints, such as the knee, to cushion its movement. In diseases such as osteoarthritis, this cartilage becomes damaged. Conventionally x rays are used to diagnose joints affected with osteoarthritis. Since x rays can not visualize joint cartilage this is diagnosis is done indirectly by measuring the space between adjacent bones. If osteoarthritis is present this joint spacing is narrowed due to a loss of joint cartilage. The obvious drawback to this technique is that diagnosis of the disease cannot be made at an early stage because the carilage damage is not visualized. Other conventional modalities such as MRI are not used despite being able to visualize cartilage, as they are considered too costly. Therefore a technique with the ability to image articular cartilage would be useful, particularly if it could show the damage at an early stage [34], [35].

Several groups have carried out work into imaging cartilage using ABI. In the paper 'Diffraction-enhanced X-ray imaging of articular cartilage', J. Mollebhauer et. al, described the first use of DEI to image cartilage from both disarticulate and intact human knee and ankle joints at 18 and 30 keV. The resulting images clearly showed the articular cartilage in both types of sample and an x-ray dose similar to that of conventional radiography was delivered to the sample [35]. A similar experiment was carried out by C. Muehleman et al. who imaged rabbit samples, which showed it was possible to image the articular cartilage in both disarticulated and whole joints. They were also able to visualise a lesion in one of the samples through the surrounding soft tissue [36].

Further work in this area has demonstrated that not only is it possible to visualise the articular cartilage but the structure can be seen in the DEI images, particularly the refraction image, as was demonstrated in the paper "X-ray detection of structural orientation in human articular cartilage" by C. Muehleman et al, in which a 17 keV x-ray beam to image femoral head samples, and produced refraction and apparent absorption images which showed the vertical striations present in the cartilage [33],[37].

Comparisons of DEI with conventional cartilage imaging methods have also been carried out, such as the work carried out by A. Wagner et. al for their paper 'Options and limitation of joint cartilage imaging: DEI in comparison to MRI and sonography' who compared DEI with both MRI and Ultrasound, finding DEI to be a promising technology [34].

DEI has also been applied to imaging many other biological samples, including brain tumours in animal models, liver and lung samples and bone imaging. It has also found non-biological applications including imaging historic artefacts [21], [38]-[41].

3.3 **Image Quality Measures and Phantoms**

As shown in the previous section, there are several different ABI techniques. In order to perform a quantitative assessment of the images they produce, it is necessary to apply image quality measures. These measures involve calculating the contrast and signal to noise ratios for the images where appropriate and make it possible to determine the imaging capabilities of the different methods.

Image phantoms were developed as test objects, so that they could be imaged using the different ABI techniques to aid the comparison of their advantages and disadvantages.

3.3.1 Image Quality Measures

Image quality refers to the degree of visibility of relevant information in an image. In order to measure the image quality it is necessary to measure the Signal-to-Noise Ratio (SNR) and contrast of the image.

Image contrast is the ratio between the darkest and brightest spots in an image. For conventional radiography the contrast is given by:

$$C_{RAD} = \frac{I_{AVE} - I_{MIN}}{I_{AVE}} \qquad \text{Equation 3-19}$$

where I_{AVE} is the average intensity in the background of the image and I_{MIN} is the minimum intensity in the sample. This definition can also be applied to the absorption images created by the ABI techniques and give the contrast of the image as a whole [42].

The contrast for the refraction image ranges from that given by the largest angle (positive), through zero to the largest angle in the opposite direction (negative). Since the average background value is zero, the image contrast calculation, shown in Equation 3-19 can therefore not be used. The same is true of the USAXS images which also have an average value of zero in the background. As an alternative, the SNR can be found for the different images [42].

The SNR compares the signal range to the background noise. The higher the ratio, the less prominent the background noise. The equation for SNR for the absorption images is given by:

$$SNR_{ABS} = \frac{I_{AVE} - I_{MIN}}{\sigma_{BG}}, \qquad \text{Equation 3-20}$$

where σ_{BG} is the standard deviation of the noise measured in the background [42].

The SNR for the refraction image is given by:

$$SNR_{REF} = \frac{\theta_{R,MAX} - \theta_{R,MIN}}{\sigma_{BG}}, \qquad \text{Equation 3-21}$$

where, σ_{BG} is the standard deviation of the noise measured in the background, $\theta_{R,MAX}$ is the maximum refraction value and $\theta_{R,MIN}$ is the minimum refraction value in the image [42].

The SNR for the USAXS image is given by;

$$SNR_{USAXS} = \frac{S_{MAX}}{\sigma_{BG}}, \qquad \text{Equation 3-22}$$

where, σ_{BG} is the standard deviation of the noise in the background and S_{MAX} is the maximum scatter value in the image.

In addition to calculating the SNR for the whole image, the SNR can be calculated for a specific area and for the visibility of the edge of an object, as with the previous the SNR for the whole image, these equations are specific to the different sources of contrast.

For the absorption image the SNR for a specific area of the image is given by:

$$SNR_{ABS,AREA} = \frac{I_{AVE} - I_{AREA}}{\sqrt{\left(\sigma_{AREA}^2 + \sigma_{BG}^2\right)}} \qquad \text{Equation 3-23}$$

where I_{AVE} is the average value for an area in the background, I_{AREA} is the average intensity value for the area of interest, σ_{AREA} is the standard deviation in the area of interest and σ_{BG} is the standard deviation of an area in the background [18].

The SNR value for a specific area in the refraction image is given by:

$$SNR_{REF,AREA} = \frac{\theta_{AREA}}{\sqrt{\left(\sigma_{BG}^2 + \sigma_{AREA}^2\right)}} \qquad \text{Equation 3-24}$$

where, θ_{AREA} is the average refraction value for the area of interest.

Similarly the SNR value for an area in the USAXS image is given by:

$$SNR_{USAXS,AREA} = \frac{S_{AREA}}{\sqrt{\left(\sigma_{BG}^2 + \sigma_{AREA}^2\right)}}, \qquad \text{Equation 3-25}$$

where S_{AREA} is the average USAXS value for the area of interest.

As was described in the previous section ABI methods have been shown to be capable of visualising cartilage. In order to establish how visible the cartilage is the background surrounding it needs to be taken into account. The two image quality measures described earlier however, do not do this. It is therefore necessary to define another image quality measure (SNR_{LINE}), which measures the edge visibility of a structure and is defined as:

$$SNR_{LINE} = \frac{V_{MAX} - V_{MIN}}{\left(\sqrt{2} \cdot \sigma_{BG}\right)} \qquad \text{Equation 3-26}$$

where, σ_{BG} is the standard deviation of the background, and V_{MAX} and V_{MIN} are the maximum and minimum values of a profile through the structures edge, V can be intensity, I in the absorption images, $\Delta\theta_z$ in the refraction images or S in the USAXS images.

3.3.2 Phantoms

Phantoms are used for testing different imaging modalities. Some mimic the anatomy or pathology of the body. Others test the physical properties of the imaging system in order to characterise the image quality. It is for this purpose that phantoms have been imaged using ABI techniques [5].

Several different phantoms have been imaged using both the DEI and MIR techniques in order to demonstrate the imaging capabilities of the different sources of contrast. The simplest example was presented by M. Z. Kiss et al. in their paper "Measurement of image contrast using Diffraction Enhanced Imaging" in which a perspex rod and two different thicknesses of nylon thread were imaged to assess the ability of DEI to resolve the fine structure of the thread and investigate the noise present in the DEI images, compared with conventional radiography [42]. Perspex rods were also imaged by M. Hasnah et al. in several of their papers [43],[44].

In the paper, "Implementation of diffraction-enhanced imaging: experiments at the NSLS and APS" Z. Zhong et al. described the use of a wedge phantom designed to characterise the refraction image. This was constructed of perspex and consisted of wedges with different slopes. The results demonstrated that the measured refraction angle was dependent only on the angle of the wedge [19].

Phantoms have also been imaged to study their scatter properties. For example, M. N. Wernick et al, used a perspex rod partially covered with a stepped region of paper. The results showed that the rod could be clearly seen in the refraction image and that the layers of paper were clearly visible in the USAXS image [17]. Similar phantoms have also been imaged by several other groups [22], [23], [45].

Colloids have also been imaged for their scattering properties. The paper by F. Arfelli et al., "Contrast improvements with diffraction enhanced imaging for scattering materials" described the use of different thicknesses of hollow silica

microsphere powder [46]. L. Rigon et al used a phantom filled with PMMA microspheres 30μm in diameter in their paper "A new DEI algorithm capable of investigating sub-pixel structures [16]. Their results showed that the microspheres showed a different contrast to the air

Phantoms have also been developed for use with DEI-CT and MIR-CT. For example F. Dilmanian et al, used a perspex cylinder with four holes drilled into it at different angles, and J. G. Brankov imaged a perspex jar with a perspex rod and a roll of paper [26], [28].

ABI techniques have also been used to image mammography phantoms in order to compare their ability to resolve specific features with conventional mammographic techniques, with the aim of proving the ABI methods as a potential alternative [1], [12], [18], [47].

In addition phantoms have also been used to test the ABI system itself. An example of this was presented by H. Zhang et al. in the paper 'Crystal tilt error and its correction in diffraction enhanced imaging system', where, a phantom together with a mammography sample were imaged using an ABI system which had the analyser crystal positioned at an angle to study the effects of this introduced tilt error on the images. It was found that this error introduced a change in the Bragg angle across the beam, which led to a variation in intensity in the imaging field. A method of correcting for this was also suggested, which involved employing reference rocking curves for each of the columns of the images [48].

Since there are no phantoms designed specifically for ABI techniques, it was felt that phantoms should be developed to enable the characterisation of the different sources of contrast. These phantoms should therefore be easily reproducible, work over a range of energies and be able to provide a range of contrast values.

3.3.2.1 Test Phantom

The first phantom developed was a small test phantom, shown in Figure 3-7. It was constructed in a sample box and consisted of layers of aluminium for their absorption properties, layers of paper and a piece of elastic, for their scattering properties, and nylon wires for their refraction properties. The motivation behind the construction of this phantom was so that it could be imaged in a preliminary experiment in order to see the effect that would be produced in the different images first hand, and to provide a starting point for further phantom designs.

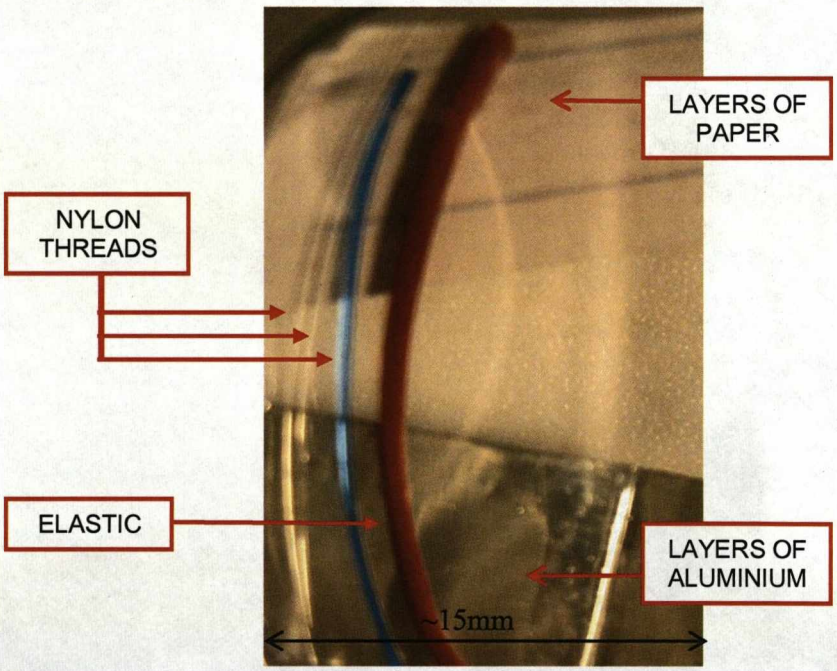

Figure 3-7: A photograph of the test phantom.

Phantoms were then developed for each of the sources of contrast; a wedge phantom for refraction, a step phantom for absorption and colloids were tested for use as a USAXS phantom. In addition to being suitable for the different sources of contrast, there were several other constraints. The phantoms had to be suitable for the range of energies, 20-80 keV on the ABI system on Station 9.4 at Daresbury

SRS. They also had to be the correct size to fit in both the field of view of the CCD and the width of the beam.

3.3.2.2 Absorption Phantom

The absorption phantom was constructed of perspex and consisted of three layers with steps cut to different thicknesses as shown in Figure 3-8, this design was chosen as it would be easily reproducible.

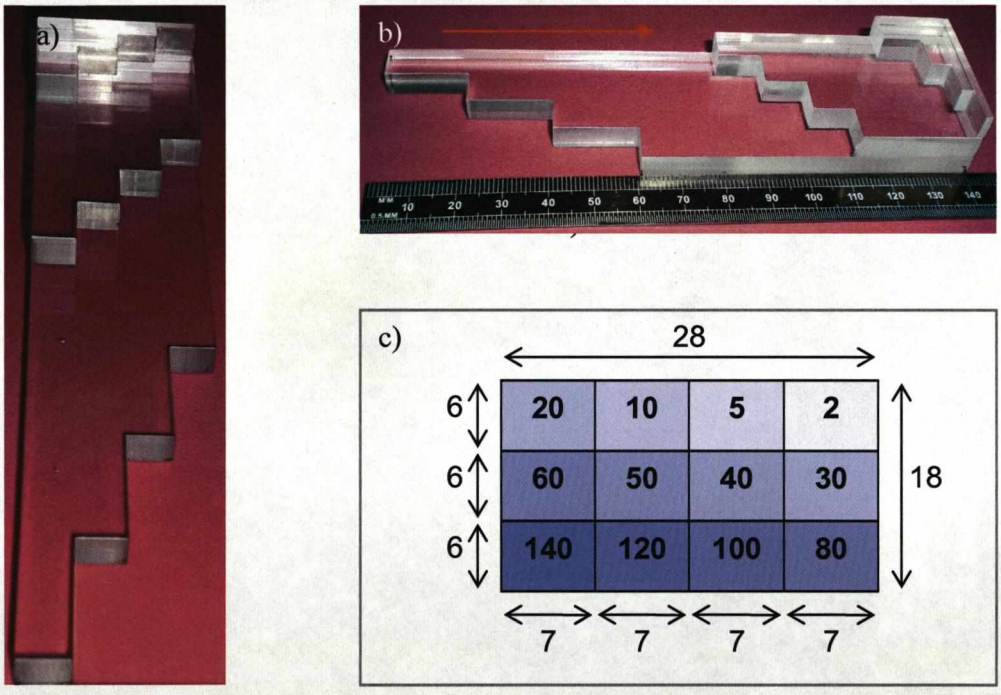

Figure 3-8: Pictures of the absorption phantom. a) A photograph of the phantom from the front. b) A photograph of the phantom from the side, the direction of the beam is shown by the red arrow. c) A diagram (viewed from the front) showing the dimensions and thicknesses of the steps in the absorption phantom. All measurements are in mm.

The different thicknesses were chosen so that for the entire energy range there would be several steps that would show a range in attenuation, therefore providing a range in contrast in the final image. This is demonstrated in Figure 3-9, a plot of I/I_0 against step thickness for different energies, which shows that for the 15 keV beam, the thinnest steps give a range of attenuation and the others almost

completely attenuate the beam. For higher energies there are more steps that do not totally attenuate the beam. The overall size of the phantom was mainly limited by the field of view of the detector which was 40mm × 40mm.

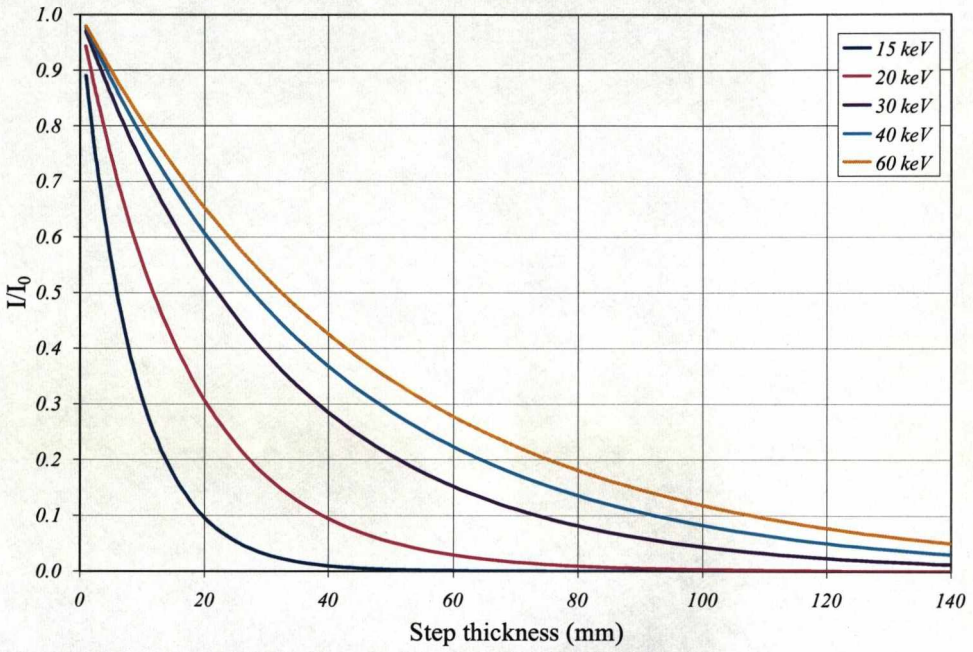

Figure 3-9: A plot showing the variation of the relative intensity (I/I_0) with step thickness for a range of energies.

The absorption phantom was intended to be used to compare the DEI and MIR techniques together with theory. Previous ABI phantom experiments have not concentrated on absorption as a source of contrast, the experiment presented in this thesis is therefore the first to do so. It was felt necessary to look at all of the sources of contrast individually because the ability of the technique to separate out the different effects seen in the sample is what gives the ABI techniques their potential.

3.3.2.3 *Refraction Phantom*

As with the absorption phantom, the refraction phantom was also constructed of perspex and was limited in size by the field of view of the CCD. The phantom consisted of four layers held in place with two posts. The purpose of this phantom was to characterise the refraction contrast over a range of energies. It was constructed of a series of wedges, whose slopes ranged from $tan\alpha = -10$ to $tan\alpha = 10$, shown in Figure 3-10.

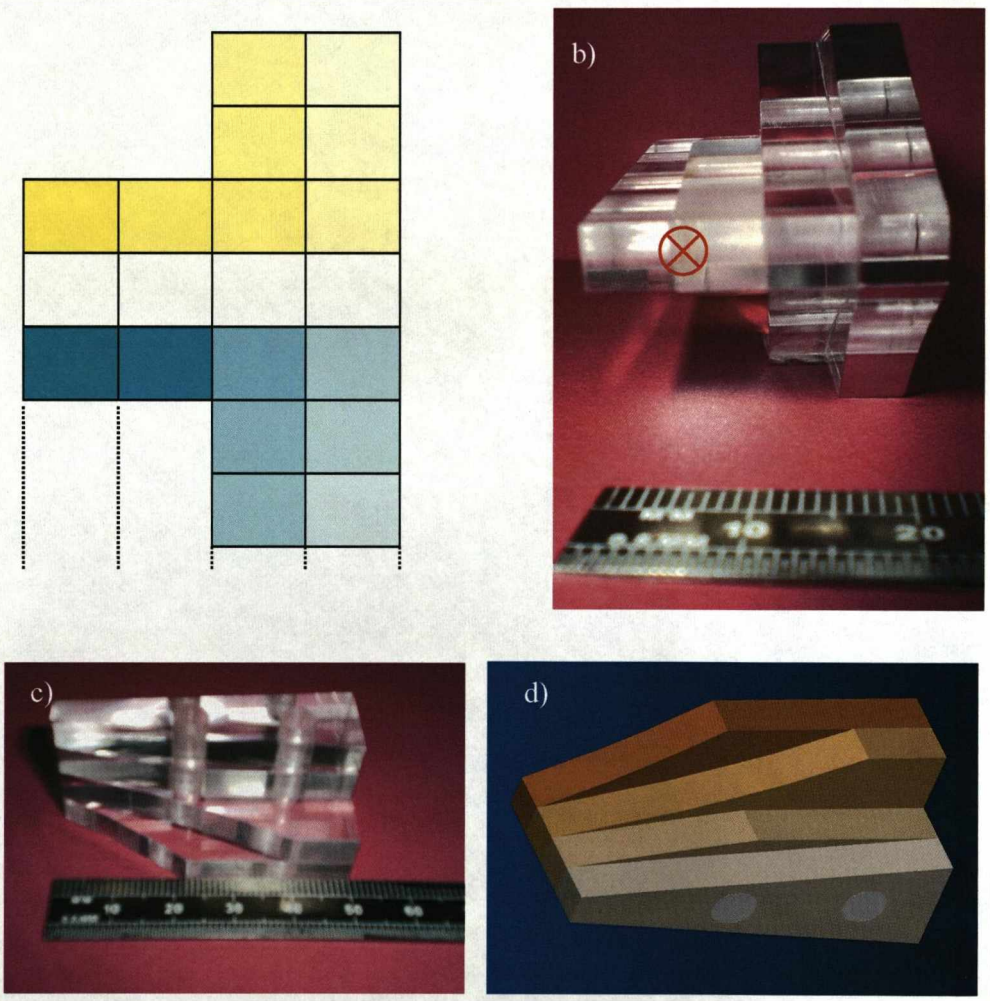

Figure 3-10: a) A diagram showing the values of $tan\alpha$ for each slope. b) A photograph of the refraction phantom shown from the front view, the direction of the beam is shown in red. c) A photograph of the refraction phantom shown from the side view. d) A diagram of the refraction phantom.

Equation 2-16 shows the relationship between $\Delta\theta_z$, the angle the beam is refracted through and α, the angle between the incident beam and the normal of the interface between the two media. This equation can also be written as [19]:

$$\Delta\theta_z = \frac{1}{2\pi} r_e N \lambda^2 \tan\alpha, \qquad \text{Equation 3-27}$$

where N is the number of electrons per unit volume of the phantom material, r_e is the classical electron radius and λ is the wavelength. Equation 3-27 can then be approximated to [19];

$$\Delta\theta_z \cong 1.3\times10^{-6} \rho \lambda^2 \tan\alpha \qquad \text{Equation 3-28}$$

where ρ is the density of the material (g/cm^3). Equation 3-28 was used to calculate the refraction angle at each slope for a range of different energies, the results of which are shown in Figure 3-11.

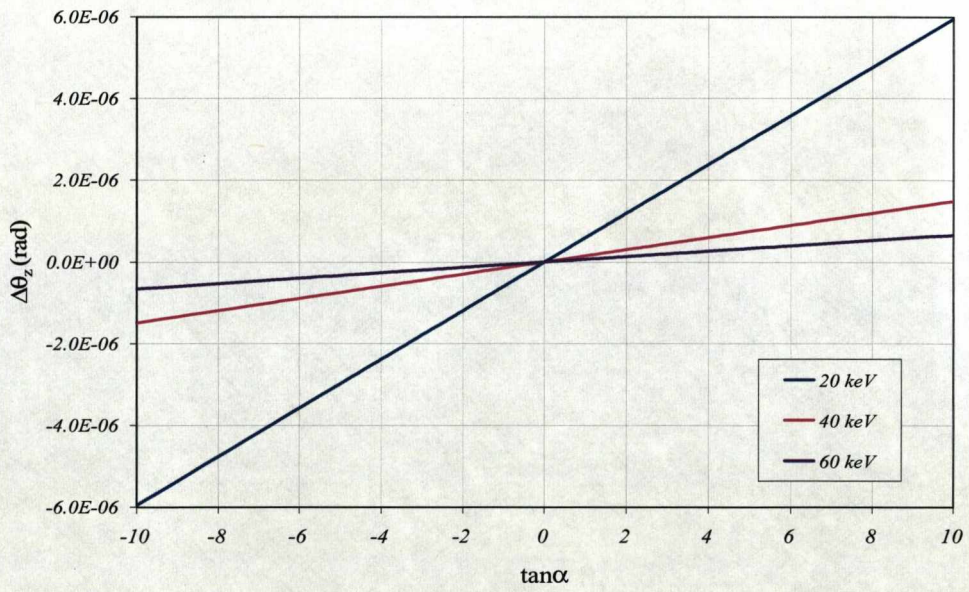

Figure 3-11: A plot of $\Delta\theta_z$ against tanα, to show the variation with energy.

As described in Section 3.2.2.2. Zhong et al. used a wedge phantom in one of their experiments [19]. The phantom used in their experiment did not cover as large a range of tanα as the refraction phantom created for this project. The range of tanα values (tanα =-10 to tanα=10) was chosen as at the extremes it would still give a high response even at high energies and because, although for this thesis biological samples were studied, ABI techniques also have the potential to be used when imaging non-biological samples, in which there is the possibility of there being such large angles, it was therefore deemed important that the phantom should accommodate this.

The phantom used by Z. Zhong et al. was also only imaged using DEI. For this project it was intended that the refraction phantom would be imaged using both DEI and MIR to provide a comparison of the two techniques over a range of tanα. This had not been done before; previous comparisons had used phantoms such as those constructed from Lucite rods as described by M. Wernick et al in the paper "Multiple-image Radiography".

When constructed, the refraction phantom was measured using a Coordinate Measurement Machine in order to provide a more accurate knowledge of the phantom. The results of these measurements are presented in Table 3-1 and show that both sides of Layer 2 have a larger discrepancy in angles than the other layers. The results also show that Layer 1 had the largest percentage difference between the sides. However, the overall construction of the phantom was good with all the angles show a difference of ≤1% from those specified in the design.

Layer	Design		Side 1			Side 2			% Diff between sides
			Measured		% Diff	Measured		% Diff	
	tanα	α (rad)	tanα	α (rad)		tanα	α (rad)		
1	*10*	*1.4711*	*9.8585*	*1.4697*	*0.0966*	*9.5272*	*1.4662*	*0.3339*	*0.2375*
2	*5*	*1.3734*	*4.8322*	*1.3667*	*0.4855*	*4.8242*	*1.3664*	*0.5097*	*0.0243*
3	*3.33*	*1.2791*	*3.3349*	*1.2795*	*0.0314*	*3.3421*	*1.2801*	*0.0778*	*0.0464*
	2.5	*1.1903*	*2.4951*	*1.1896*	*0.0566*	*2.5003*	*1.1903*	*0.0035*	*0.0602*
	2	*1.1071*	*1.9886*	*1.1049*	*0.2064*	*1.9958*	*1.1063*	*0.0756*	*0.1311*
4	*1.67*	*1.0313*	*1.6741*	*1.0323*	*0.1054*	*1.6714*	*1.0316*	*0.0360*	*0.0693*
	1.43	*0.9605*	*1.4309*	*0.9608*	*0.0311*	*1.4308*	*0.9608*	*0.0275*	*0.0036*
	1.25	*0.8961*	*1.2518*	*0.8968*	*0.0775*	*1.2525*	*0.8970*	*0.1087*	*0.0311*

Table 3-1: The different tanα and α angles form the design compared with those measured from the constructed phantom.

3.3.2.4 USAXS phantom

As described in Section 3.2.2.2, paper and colloids, such as PMMA have been used in previous scatter experiments. Paper, although being easily accessible, is not very reproducible due to there being lots of associated variables, such as its density, thickness and the fibre lengths. Colloids, however, can be provided with documented sizes and can be certified for use as standards. This therefore makes them easily reproducible and ideal for use in a USAXS phantom.

As with the absorption and refraction phantoms, a USAXS phantom would be required to give a range of response for a range of different energies. In the paper "Contrast improvements with diffraction enhanced imaging for scattering materials", presented by F. Arfelli et al., a range of scattering was created by varying the thickness of the PMMA. However, it is possible to get colloidal solutions and by diluting them by different amounts may be possible to get a range of USAXS contrast. This is highly reproducible, and also has the advantage that the concentrations could be varied more easily for use in different energy ranges. It is also possible to get colloids of different sizes. This could itself be used to get a

range of USAXS response. Alternatively, by investigating what colloid size gives the most scatter, a phantom which utilised a variety of colloid concentrations could be optimised.

It was not possible to create a USAXS phantom in the same way as was done with the refraction and absorption phantoms, due to investigations into the use of colloids being required first. Two different types of colloids were investigated for use: Ludox HS40, a colloidal silica with diameter of 0.02μm, and polystyrene nanosphere standards with diameters of 0.1μm, 0.5μm and 1μm. The Ludox sample was imaged in a preliminary experiment to examine the viability of the use of colloidal solutions. The polystyrene nanospheres were studied in two further experiments, to look at the feasibility of varying the concentration of the colloidal solutions to get different contrast in the USAXS images and the effect of colloid size on contrast.

CHAPTER 4

4 EXPERIMENTAL METHOD

Several experiments were carried out using different ABI systems. This chapter describes the different systems used and the experiments that were conducted.

4.1 Experimental setups

Three different ABI systems were used, two of which were at the Daresbury SRS, one on Station 7.6 and the other on Station 9.4. A set of experiments were also carried out on ID17 at the ESRF.

4.1.2 Daresbury Station 7.6 ABI system

Station 7.6 is situated on a bending magnet which creates a beam with energy ranging from 10 keV to 25 keV.

The basic system setup is the same as that described in Section 3.2.2, consisting of a crystal monochromator, the sample stage, the analyser crystal and the CCD camera.

The beam size was set using the station shutters and was typically ~1mm in height. The framework for the ABI system was permanently situated on the beam line, however, the optical components were removable. Two sets of silicon [111] channel cut crystals were used (see Section 2.4) which were again mounted in a crystal cage, whose height could be adjusted. Both the analyser and monochromator crystals were controlled by coarse motors.

This is the first use of channel cut crystals as monochromator and analyser in an ABI system. The employment of the channel cut crystals means that the geometry of the system is such that both the sample stage and the detector are simply required to move vertically. This is not the case for systems which use single

crystals, such as the one on ID 17 at ESRF (see Section 4.1.2). The advantage of the channel cut crystals is that they should allow for easier set up of the system.

The sample stage was positioned between the two sets of crystals and was capable of vertical, horizontal and azimuthal motion. The imaging detector used was a Photonic Science Hystar phosphor coupled CCD camera which has an active area of 40mm×40mm and a resolution of ~50μm [49].

In addition to the basic system which has been described, several other pieces of equipment were used. Firstly, a small laser, see Figure 4-1 below, which was lined up with the polychromatic beam, was used to assist in the crystal alignment. An ion chamber (see Section 2.5.2) was also used to aid in the beam alignment and was positioned on the sample stage while in use.

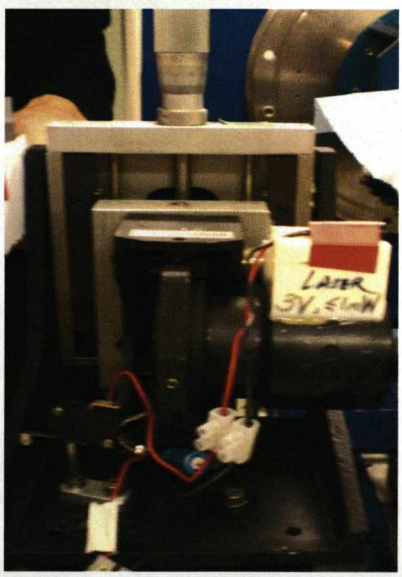

Figure 4-1: A picture showing the laser used for alignment.

Two other detectors were also used, a sodium iodide detector and a small silicon PIN-diode (XR-100). The sodium iodide detector was powered via a NIM HV unit, it was used to measure the rocking curve of the analyser crystal. It was

mounted on the CCD camera, as shown in Figure 4-2. The signal from the detector was passed through a an amplifier then a Single Channel Analyser (SCA) whose logic output was fed into a ratemeter with an audio alarm. The SCA's analogue output was fed into the data logger which recorded the signal. This is shown in Figure 4-3.

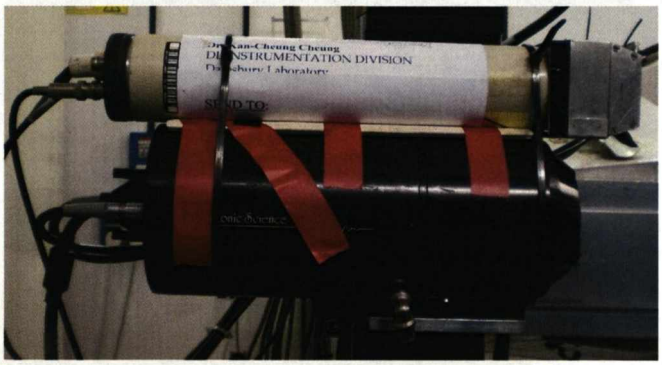

Figure 4-2: A picture showing the sodium iodide detector mounted on the CCD detector.

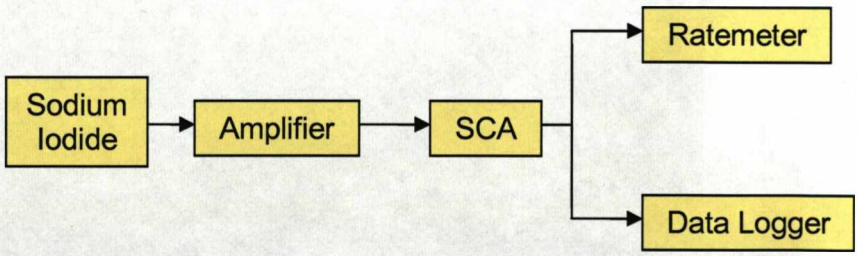

Figure 4-3: A flow diagram showing the processes on the signal from the sodium iodide detector

The silicon diode detector was also used to measure the beam energy after first being calibrated using sealed sources. The detector had a diameter of 3.5mm and was operated in photovoltaic mode. The signal from the detector was amplified and fed into a PC with a Multichannel Analyser (MCA) card and analysis software.

In addition, there was shielding positioned in front of the detectors to stop any scattered x rays from reaching them.

4.1.2 Station 9.4 setup

Station 9.4 is situated on a wiggler and creates a beam with a range of energies from ~15 keV to ~50 keV, meaning there was more potential for imaging thicker samples on this system.

The majority of the system was the same as that used on Station 7.6, including the use of the same CCD camera. The silicon channel cut crystals were used; both were water cooled to aid with stability and they were also controlled by both coarse and piezo-electric motors. The system is shown in Figure 4-4.

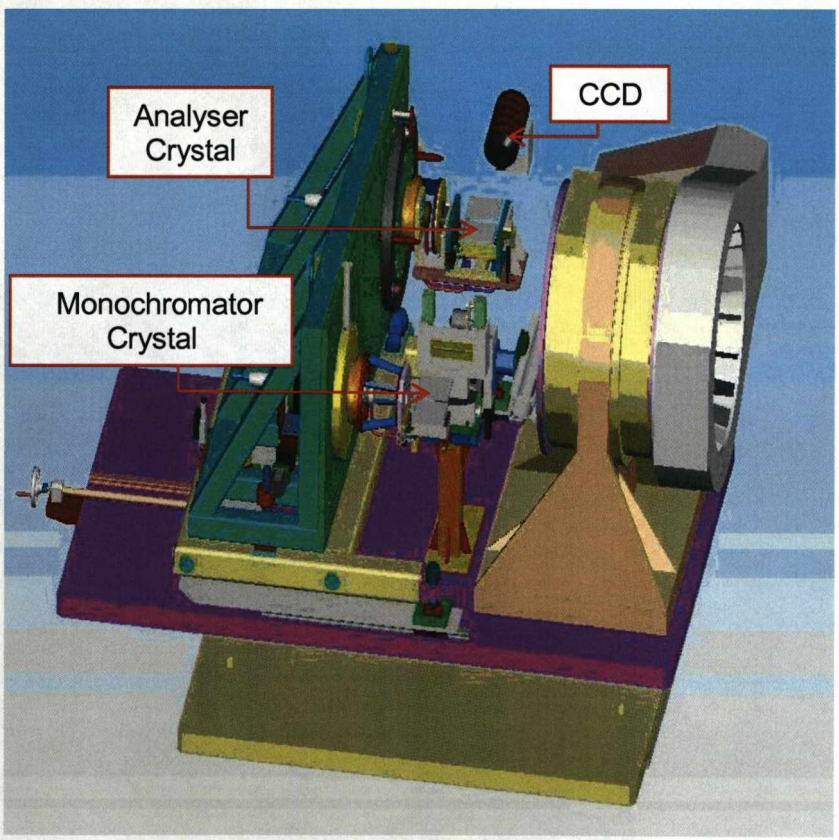

Figure 4-4: Diagram showing the ABI system on Station 9.4

For this system, the rocking curves were measured using the ion chamber, which was mounted beneath the CCD. The reason the ion chamber was used in place of the sodium iodide detector was because the imaging beam could be measured directly, whereas when using sodium iodide detector an attenuator would have had to be placed over the entrance window and the beam size would have had to be reduced in order to stop the detector from saturating. The output from the ion chamber was fed into an amplifier, then a data logger, followed by a PC on which the rocking curves could be plotted directly.

4.1.2 ABI system on ID17

ID17 at the ESRF is situated on a wiggler and has a beam energy ranging from 17-80 keV. The ABI system itself is not permanent and was put in place for the experiment. The basic experimental apparatus was the same as the system described in Section 3.2.2. Unlike the ABI systems at Daresbury SRS, this system used single crystals for the monochromator and the analyser. Two ion chambers were also used to monitor the beam; one was positioned after the monochromator crystal and the other after the analyser crystal. The second of these ion chambers was used to measure the rocking curves. This system used a Frelon camera to record the images, described in Section 2.5.2.1, which had an active input surface of $94\times94mm^2$ and an effective pixel size of $47\times47mm^2$ [10]. The ABI system is shown in Figure 4-5.

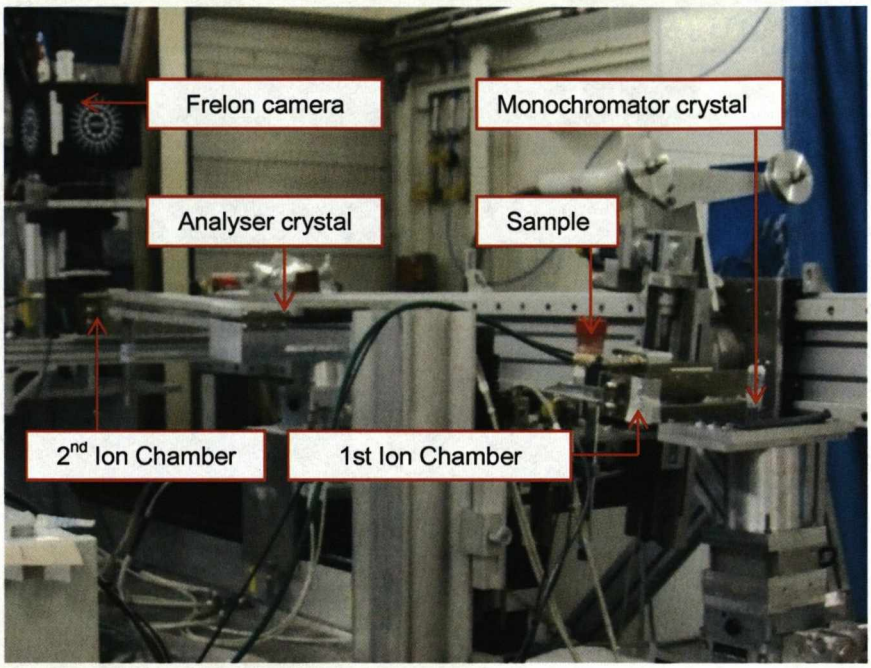

Figure 4-5: The beam line set up at the ESRF, showing the different components of the ABI system.

4.2 **Experiments**

Several experiments were carried out. These can be separated into two categories: those focusing on phantom development and those concentrating on cartilage imaging.

For the different experiments different beam energies were used for the different samples. This energy was selected to provide sufficient penetration of the sample, but not saturate the detector. Related to this was the exposure time which was varied accordingly. In several of the experiments the exposure time was varied for different imaging positions on the rocking curve, this was then accounted for when the raw images were analysed.

4.2.2 Phantom experiments

As mentioned previously, one of the main aims of this work was to develop phantoms to be used on the ABI system. It was therefore necessary to perform a series of experiments.

4.2.2.1 Test phantom

The structure of the test phantom was described in Section 3.3.2.1. The purpose of this experiment was to provide a starting point from which to develop the phantoms. This experiment was also the first that the MIR technique was used at the Daresbury SRS, it was intended that the different components of the phantom would demonstrate the differences between the different sources of contrast.

This experiment was performed at the Daresbury SRS on Station 7.6, sample images and flat field images were taken at ±85%, ±70% and ±50% positions on the rocking curve so that both DEI and MIR analysis could be carried out. At the ±85% position an exposure time of 100s was used and for the ±70% and ±50% positions exposure times of 200s were used.

4.2.2.2 Absorption and Refraction Phantoms

Both the absorption and refraction phantoms, described in detail in Sections 3.3.2.2 and 3.3.2.3, were imaged on ID17 at the ESRF (see Section 4.1.2). A beam energy of 40 keV was used and both of the phantoms were imaged at the peak, ±80%, ±50% and ±30% positions on the rocking curve so that both DEI and MIR images could be created. For the refraction phantom an exposure time of 500ms was used for each imaging position. For the absorption phantom exposure times of: 600ms were used for the peak images; 100ms for the ±80% images; 1200ms for the ±50% images; and 2000ms for the ±30% images.

The refraction phantom was also imaged on Station 9.6 at Daresbury SRS, with a beam energy of 20 keV and the analyser tuned to the peak and ±50% positions on the rocking curves where sample images ands flat fields were taken so that DEI

analysis was carried out. An exposure time of 54s was used throughout this experiment.

4.2.2.3 Colloid samples

As described in Section 3.3.2.4, two types of colloids were used. A Ludox sample, and a set of polystyrene nanosphere samples with a water comparison.

The Ludox sample was imaged on ID17 at the ESRF (see Section 4.1.3) in a preliminary investigation to establish if colloid solutions were capable of producing contrast in the USAXS image. A beam energy of 40 keV was used and images were taken at the peak, ±80%, ±50%, ±30% and ±15% positions on the rocking curve with exposure times of: 500ms at the peak; 700ms at ±80%; 1000ms at ±50%; 1200 at ±30%; 3000ms at ±15%. Images were taken at these positions so that both the DEI and MIR algorithms could be applied

A further two experiments were carried out on Station 9.4 at the Daresbury SRS (see Section 4.1.2), both using a beam energy of 20 keV. The first of these experiments saw a sample of the polystyrene nanospheres, with a diameter of ~1μm in container with a diameter of 25mm alongside a water sample. Images were taken at a series of eleven points on the rocking curve with an exposure time of 6240ms. The raw images were analysed using MIR. In the second experiment three polystyrene nanospheres samples, whose diameters ranged from ~0.1μm to ~1μm (see Section 3.3.2.4), and a water sample were imaged. All samples were imaged simultaneously and were in containers with a diameter of ~7mm. Images were taken with the analyser crystal tuned to seven positions on the rocking curve with an exposure time of 18s at each position.

4.2.2 Cartilage Experiments

A total of five different cartilage experiments were carried out looking at the cartilage in different samples. A variety of different samples were imaged, ranging from slices of cartilage to whole joints, all of which are described in this section.

4.2.2.1 Mice Feet

This experiment was carried out using the ABI system on Station 7.6, as described in Section 4.1.2. The focus of this experiment was the comparison of mice feet with and without osteoarthritis, with the aim of investigating the ability of this technique to image structures in small samples, and to see if it was possible to detect changes in the samples that are linked with osteoarthritis. A beam energy of 15 keV was used.

All the samples used were stored in 10% buffered formalin. Two sets of samples were imaged; each comprised one healthy foot and one arthritic foot. One set was left with its fur on and the other had its fur removed using hair-removal cream. The hair was removed from one set of samples in order to ascertain whether the presence of the fur in the image scattered the x rays and degraded the quality of the image in any way.

The samples were positioned in sample membrane boxes. The furred sample set were imaged in the side view, shown in Figure 4-6, and the de-furred samples were imaged in both side and top view.

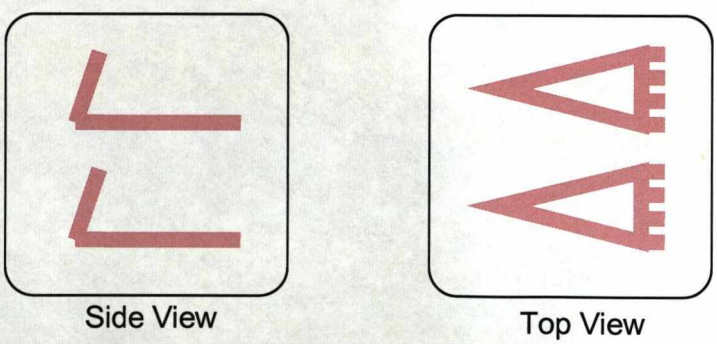

Figure 4-6: Picture showing the orientations that the samples were imaged in.

The sample sets were imaged at ±50% relative intensity position, and peak of the rocking curve in each projection, so DEI analysis could be carried out. The exposure time used for this experiment was 200 ms.

4.2.2.2 Bovine cartilage slice

As with the mice feet experiment this experiment was carried out on Station 7.6 at the Daresbury SRS. The beam energy used was 14.13 keV, as measured using the PIN-diode detector. The aim of this experiment was to establish the ability of ABI techniques to image a small amount of material. This was also the first time the MIR technique (see Section 3.2.2) was used to image a biological sample on this system. For this purpose, sample and flat field image pairs were taken at ±85%, ±70% and ±50% on the rocking curve so that both the DEI and MIR techniques could be applied. Dark field images were also taken. At the ±85% position an exposure time of 100s was used and for the ±70% and ±50% positions exposure times of 200s were used.

A slice from a bovine metatarsal was imaged in this experiment, shown in Figure 4-7, it was ~150mm×150mm and ~1mm thick, and was stored in 10% buffered formalin before imaging. During the experiment the slice was positioned in a sample membrane box.

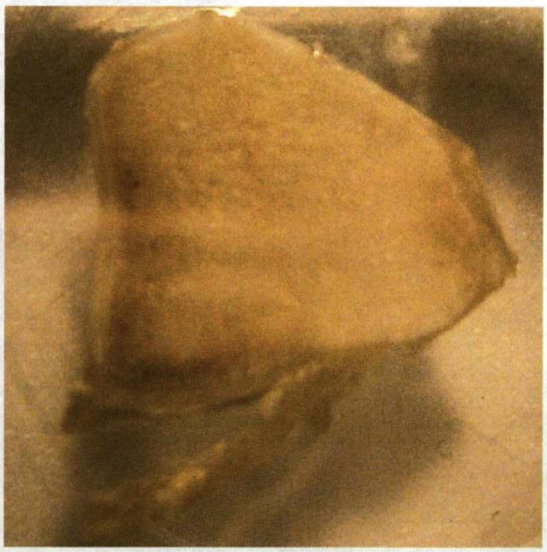

Figure 4-7: Picture of the slice of Bovine cartilage.

4.2.2.3 Pigs trotter

The aim of this experiment was to image a larger whole joint and compare the images to those produced with MRI. The experiment was carried out on Station 7.6 at the Daresbury SRS using the channel cut crystals.

A joint from a pig's trotter was chosen to be imaged due to it being easily obtainable and containing joints of the correct size. Fresh samples were used; when not in use they were stored at <5°C. The samples were positioned in a membrane sample box for imaging. Figure 4-8 a) shows the whole trotter from which the sample was taken and Figure 4-8 b) shows the sample prepared for imaging.

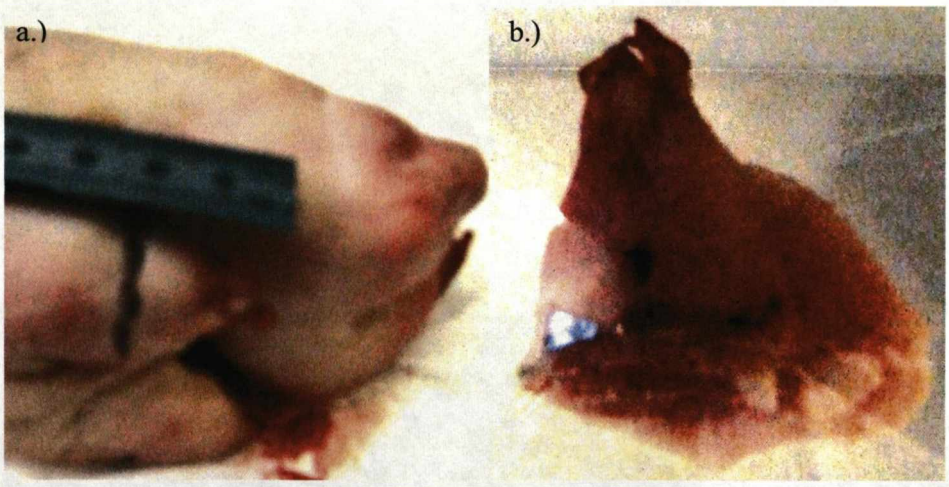

Figure 4-8: Photographs of the sample. a.) The whole trotter to show where the sample was taken from. b.) A picture of the sample as it was imaged.

Due to the size of the sample, a high beam energy was required to penetrate the sample fully. The beam energy used was 26.18 keV and the samples were imaged with the analyser crystal tuned to the peak and ±50% relative intensity positions and an exposure time of 100s was used. The DEI algorithm was applied to create refraction and apparent absorption images.

Magnetic Resonance Image (MR-image) sets were also taken of the sample, in order to identify the structures in the ABI images, and ultimately as a means of comparing the ABI's ability to visualise the cartilage in the sample with an established technique.

4.2.2.4 Canine joint samples

This experiment was carried out on the ABI system on ID17 at the ESRF, described in Section 4.1.2. Three samples were taken from canine knee joints in healthy animals. The first of the three samples was a core taken from one of the joints, shown below Figure 4-9 a) and was ~10mm×10mm in size. The second sample was a disarticulated joint, shown in Figure 4-9 b), and the third was an intact joint which is shown in Figure 4-9 c). All of the samples were kept in a buffered saline solution. They were positioned in plastic containers, where they were held in place with wax. Due to the nature of the samples, a beam energy of 40 keV was chosen to ensure the samples would be penetrated fully.

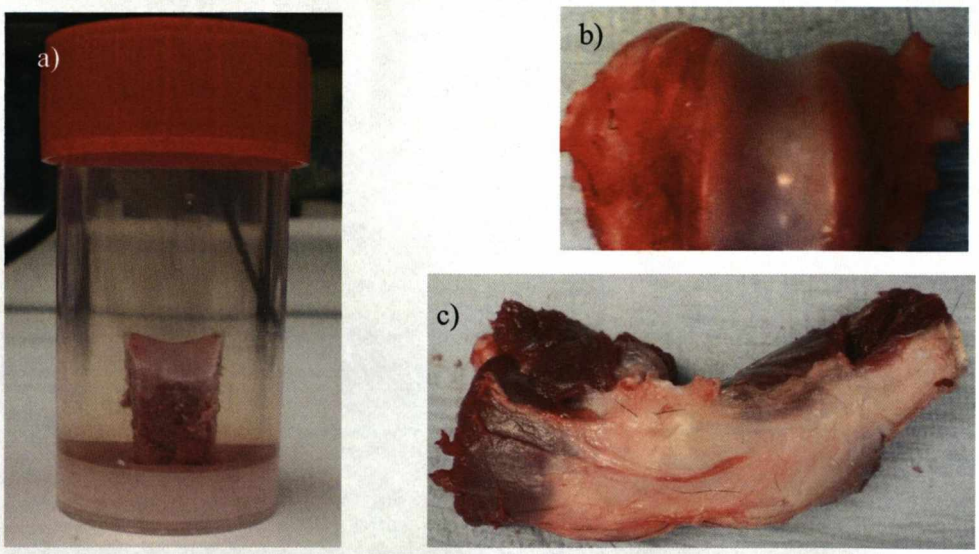

Figure 4-9: Photographs of the canine joint samples. a) The core sample. b) The disarticulated sample. c) The whole sample.

All three samples were imaged at a minimum of seven positions on the rocking curve. These positions were selected from the following: the peak of the rocking curve; peak; ±80%; ±50%; ±30%; and ±15%. These points were used so that both the MIR and DEI algorithms could be applied. Flat field images were also taken at each position, along with two dark field images to go with the data set. The disarticulated sample and the whole sample were also imaged in more than one orientation. The exposure times used were not always the same and ranged from 500ms for images taken at the peak of the rocking curve to 3000ms for imaged taken at the ±15% position on the rocking curve. MR-images were also taken of these samples, as was done in the previous experiment.

4.2.2.5 Human Knee cartilage

This experiment was carried out on Station 9.4 at Daresbury SRS (see Section 4.1.2). The samples were pieces of cartilage from human knee joints, obtained from routine knee replacements that were carried out at Liverpool Broadgreen Hospital. The appropriate ethics approval was acquired prior to the start of the experiment.

Two samples were taken from six patients, giving a total of twelve samples that were imaged; one of these samples is shown below in Figure 4-10 a). Each sample was placed in a sample pot and held in position using wax, an example of this is shown Figure 4-10 b). All of the samples were stored in saline and, when not being imaged, were refrigerated at ~5°C.

Due to the thickness of the samples, which ranged from ~ 20 to 35mm, a beam energy of ~40 keV was used to balance the penetration of the beam through the sample with the potential saturation of the detector. The exposure times used throughout this experiment ranged from 13s to 25s.

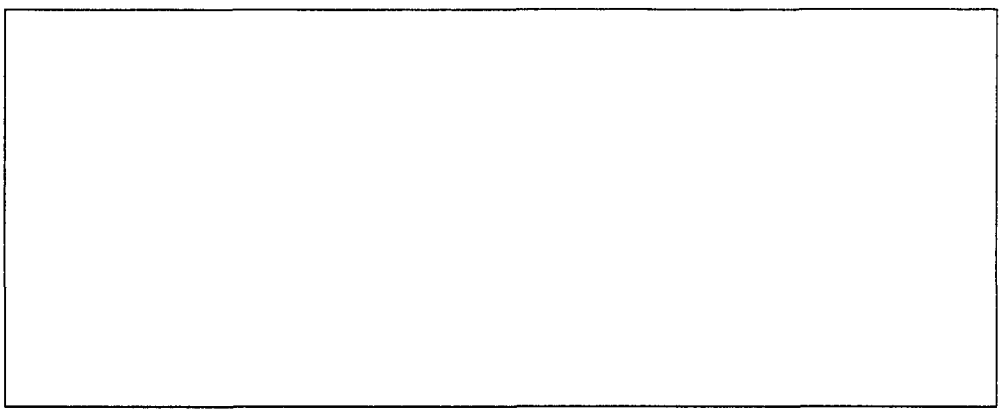

Figure 4-10: Photographs of Sample 003a. a) The sample itself. b) The sample in the sample pot prepared for imaging.

All of the samples were imaged using both DEI and MIR. For the DEI sets, two images were taken, one on either side of the rocking curve at the ±50% relative intensity positions. Flat field images were also taken at both positions. For the MIR set between eleven and thirteen flat field and sample images were taken at regular intervals across the rocking curve. Again, these samples were also imaged using MRI.

Sample 003A was also imaged using DEI-CT. The analyser crystal was tuned to ±50% relative intensities on the rocking curve, and 361 projections were taken over a 180° range.

CHAPTER 5

5 RESULTS FROM THE PHANTOM EXPERIMENTS

The aim of these experiments was to test the phantoms that have been developed for the different sources of contrast to compare the different ABI methods.

5.1 Test Phantom

This was the first phantom experiment and was carried out with a beam energy of 14.13 keV at Daresbury SRS (see Section 4.1.2). The purpose of this experiment was to use the small test phantom to demonstrate the differences between the different sources of contrast and provide a base for the development of the different phantoms.

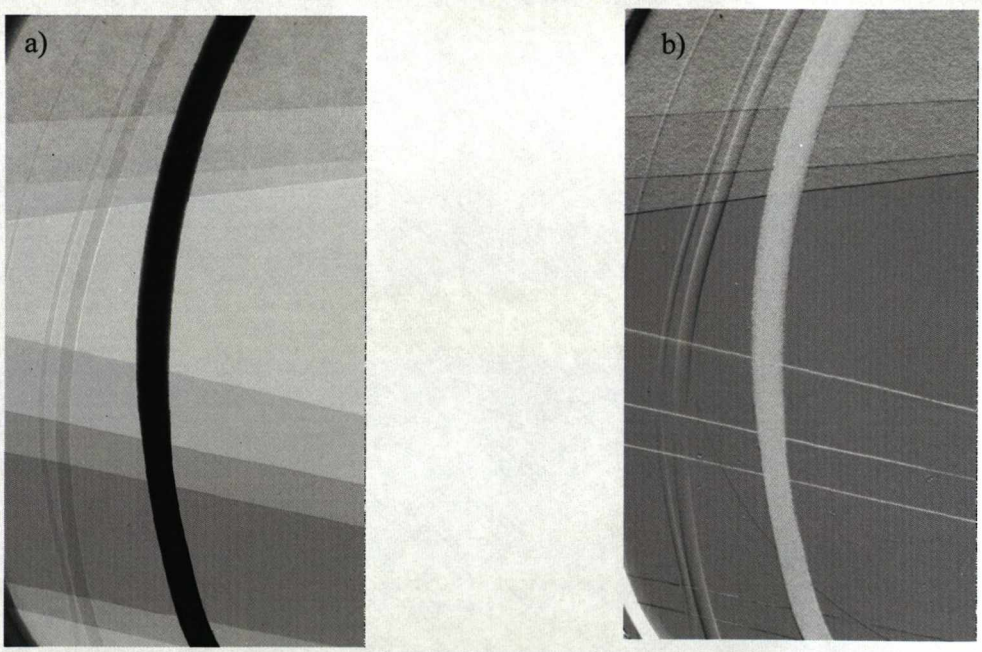

Figure 5-1: The ±50% DEI images of the test phantom. a) The apparent absorption image. b) The refraction image.

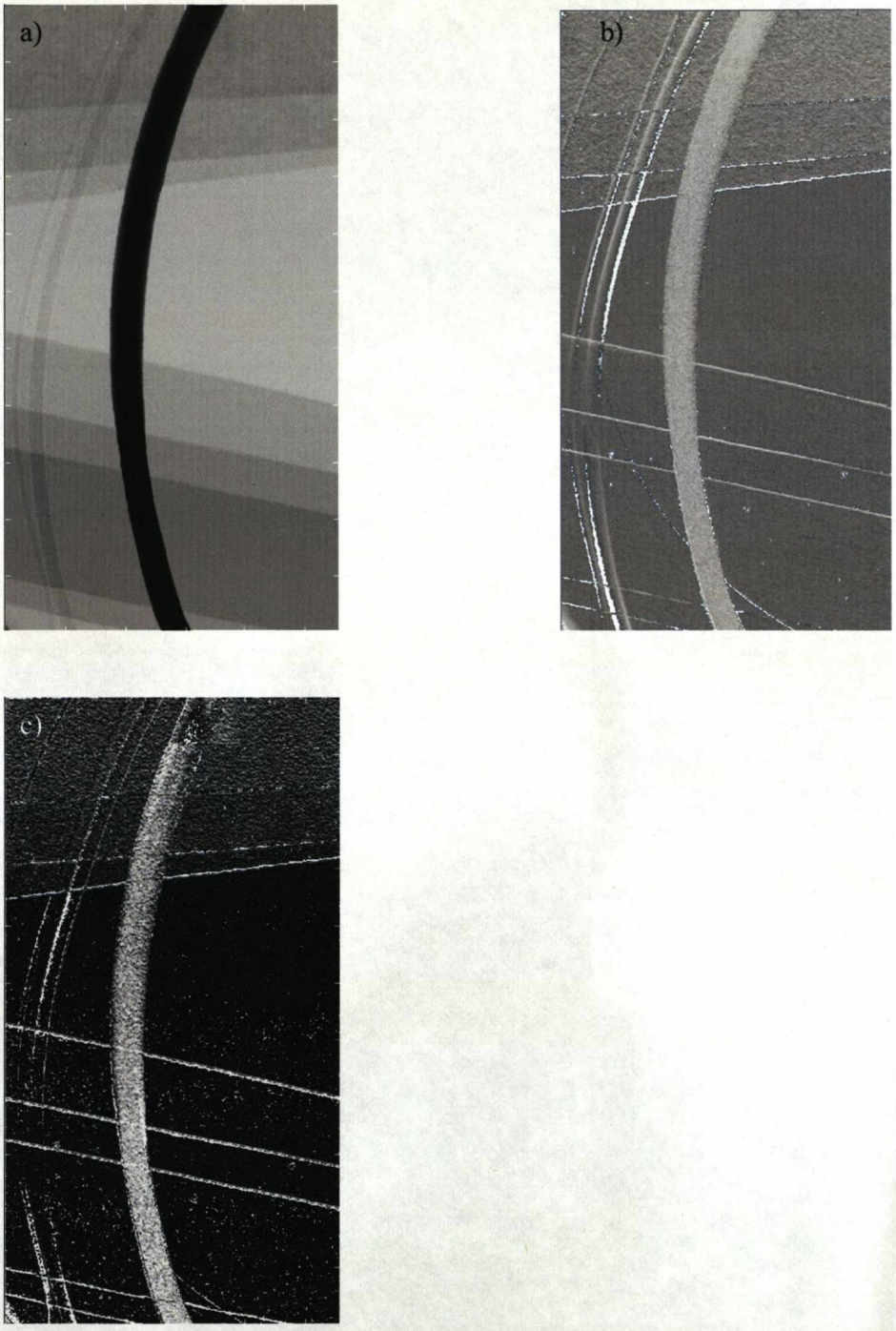

Figure 5-2: The MIR images of the test phantom. a) The absorption image. b) The refraction image c) The USAXS image.

Looking first at the absorption images (Figure 5-1 a) and 5-2 a)), the maximum absorption is given by the piece of elastic. There is also an increase in the amount of absorption with the number of layers of aluminium, as would be expected. Although weaker, this is also the case for the increasing layers of paper, where the absorption images also proved to be sensitive enough to show some of the texture of the paper. The two thickest nylon threads can also be seen clearly, however the thinnest thread is less visible.

In the refraction images (Figure 5-1 b) and 5-2 b)), as in the absorption images the elastic band gives a lot of contrast. The refraction images also show the texture of the paper and a slight increase in refraction contrast with the increasing number of layers of paper. However, unlike the absorption images, the only refraction contrast from the aluminium strips comes from the edges and does not change as the number of layers increases. The visibility of the nylon threads also differs from the absorption images, and all three can be seen clearly due to there almost three dimensional appearance.

The USAXS image, shown in Figure 5-2 c), is more similar to the refraction image than the absorption image. The texture of the paper is very noticeable in this image and clearly shows an increase in contrast with an increasing number of layers. The elastic band also shows a lot of scatter. The contrast from the nylon threads is dissimilar to both the refraction and absorption images and only shows a small amount of contrast at the edges.

5.2 **Absorption Phantom**

The design for this phantom is shown in Section 3.3.2.2. It was imaged in ID17 at the ESRF with a beam energy of 40 keV, with the analyser crystal tuned to the peak, ±80%, ±50% and ±30% relative intensity positions on the rocking curve (see Section 4.2.2.2).

The ±80%, ±50% and ±30% image pairs were used to produce three DEI image sets. Using the MIR method seven sets of images were created, the raw images used to make each set were: the peak, ±80%, ±50% and ±30% images; the peak and ±80% images; the peak and ±50% images; the peak and ±30% images; the ±80% images; the ±50% images; and the ±30% images.

The DEI image set for the ±50% position are shown in Figure 5-3. Looking at the absorption image (Figure 5-3 a)), it can be seen that the contrast increases as the step thickness increases (Figure 5-4). The refraction image (Figure 5-3 c)), on the other hand, shows no visible deviation from the background contrast, no matter what the step thickness. The only signal in the refraction image can be seen at the boundaries and between the sections of the phantom. In both images line artefacts can be seen which were caused by a misalignment in the flat field image. The same result is seen in the DEI images taken at the ±80% and ±30% positions, the images for which are shown in Appendix 1.

In order to perform a more complete analysis of the absorption images the average intensity in the background of the image, I_0, and the average intensity of each step, I, were found and plots of I/I_0 against step thickness were produced. Figure 5-5 shows this plotted for the DEI ±50% absorption image. As can be seen from this plot there is no deviation from theory (see Section 3.3.2.2) for this images. The same result was found for the ±80% and ±30% images, and these plots can be seen in Appendix 1.

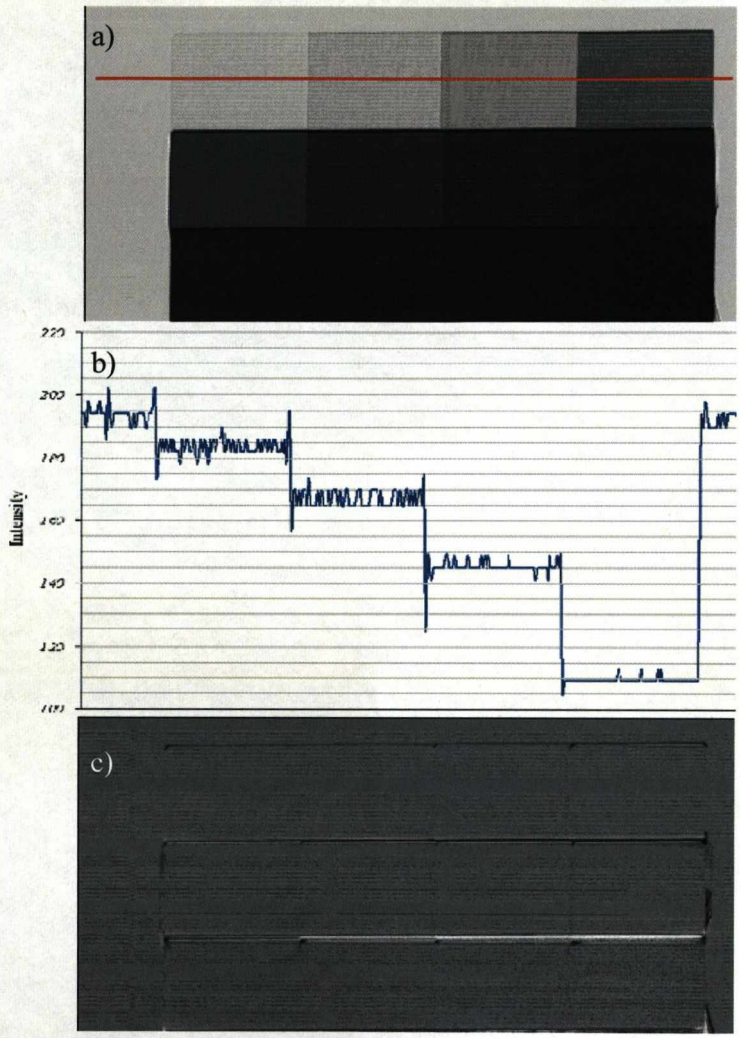

Figure 5-3: The DEI images of the absorption phantom created using the ±50% images. a) The absorption image. The line shows where the line profile was taken b) The line profile of a line through the absorption image. c)The refraction image.

2	5	10	20
30	40	50	60
80	100	120	140

Figure 5-4: Diagram showing the absorption phantom step thicknesses (mm).

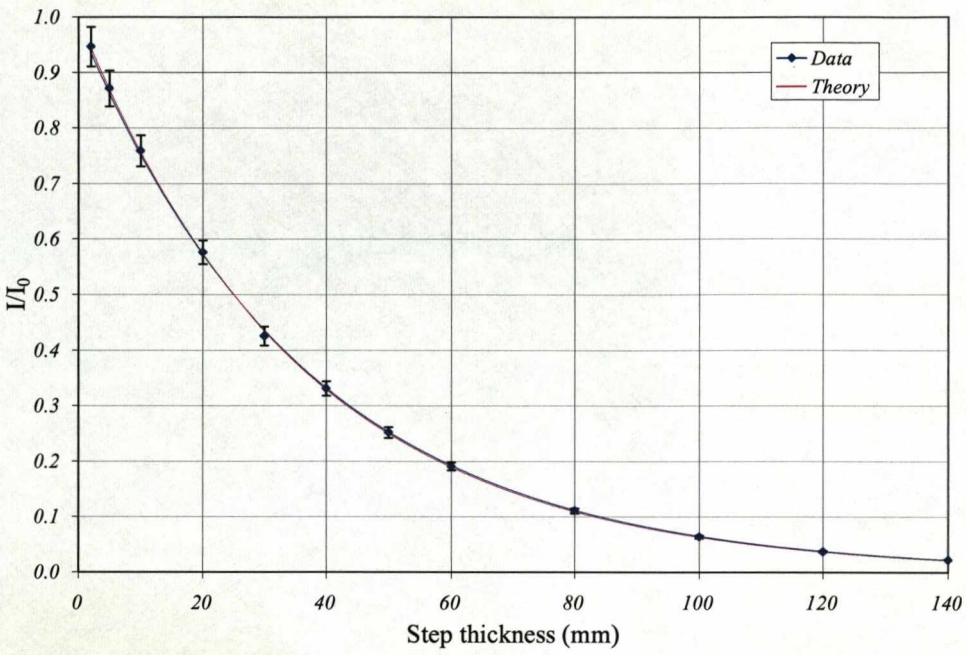

Figure 5-5: Plot of I/I_0 against Step thickness, comparing results from the DEI ±50% image with theory.

The SNR values of the area in each step were found for each of the DEI absorption images, in order to investigate the variation with step thickness (see Section 3.3.1 for the SNR_{AREA} equations). A plot of SNR_{AREA} against step thickness for all three of the absorption images is shown in Figure 5-6. The shape of the lines is as would be expected, the SNR_{AREA} increases as the step thickness increases. This increase is sharp at first and then flattens off at higher step thicknesses as there is very little change in the intensity for the larger steps, a result which corresponds well to what is seen in the DEI images. Comparing the SNR_{AREA} results for the different imaging positions on the rocking curve, it is clear that the ±50% image gives the best SNR_{AREA} profile for the different step thicknesses due to the ±50% position on the rocking curve having the steepest gradient (see Section 3.3.2.2).

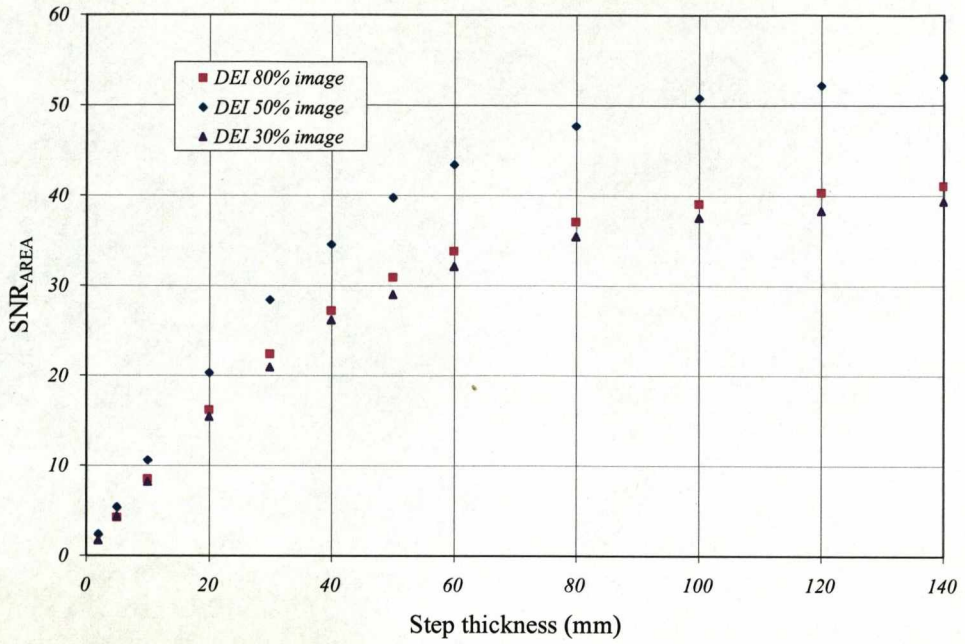

Figure 5-6: A plot of the SNR_{AREA} value for each step against the step thickness (mm) for the DEI absorption images, comparing the results from the ±80%, ±50% & ±30% images.

As was mentioned at the beginning of the section, seven MIR image sets were created, the MIR image set produced using the peak, ±80%, ±50% and ±30% images are shown in Figure 5-7. As with the DEI image (Figure 5-3), the amount of contrast in the absorption image (Figure 5-7 a)) increases with step thickness and the only contrast in the refraction image is at the phantom's section boundaries. Unlike the DEI image set, the MIR method also produced a USAXS image (Figure 5-7d)), which, like the refraction image showed most contrast at the section boundaries. As with the DEI images there were also line artefacts present in the MIR images. The remaining MIR images are shown in Appendix 1.

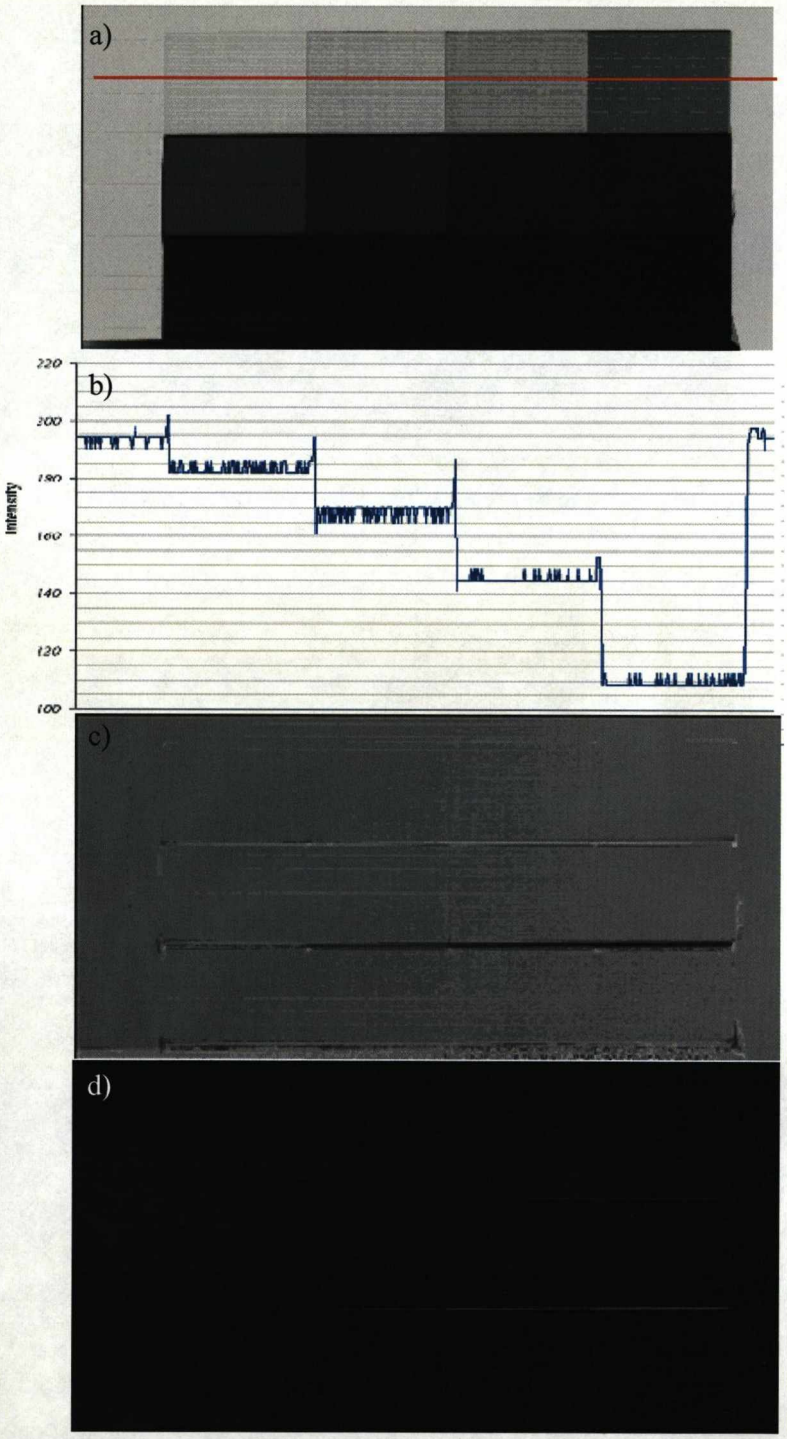

Figure 5-7: The MIR images of the absorption phantom created using ±50% images. a) The absorption image. The line shows where the line profile was taken b) The line profile of a line through the absorption image. c) The refraction image. d) The USAXS image.

As with the DEI images, plots of I/I_0 against step thickness were created for the MIR absorption images. An example of this is shown for the ±50% image in Figure 5-8 a). The results from this image show no deviation from theory for all step thicknesses. Similar results were seen for the other MIR images, which are shown in Appendix 1. A comparison with theory, of the variation of I/I_0 with step thickness for the ±50% DEI image and the ±50% MIR image was also created and is shown in Figure 5-8 b). As can be seen, both sets of results match the theoretical values well and there is very little difference between them.

Plots of the SNR_{AREA} values for each step against step thickness were also created for all of the MIR images. There were two reasons for doing this; firstly to show what effect the imaging position on the rocking curve had on the image quality; and secondly to show how the number of imaging positions affected image quality. Figure 5-9 a) shows such a plot for different imaging positions on the rocking curve. As with the DEI results (see Figure 5-6), the SNR_{AREA} is greater for the ±50% imaging position than either the ±80% or ±30% positions. A comparison of the SNR_{AREA} against step thickness for the two ABI methods is shown in Figure 5-9 b). It can clearly be seen that no matter what the imaging position, the MIR image consistently produced higher SNR_{AREA} values. This is particularly important for the thickest steps where the SNR_{AREA} of each MIR image is approximately twice that of its corresponding DEI image.

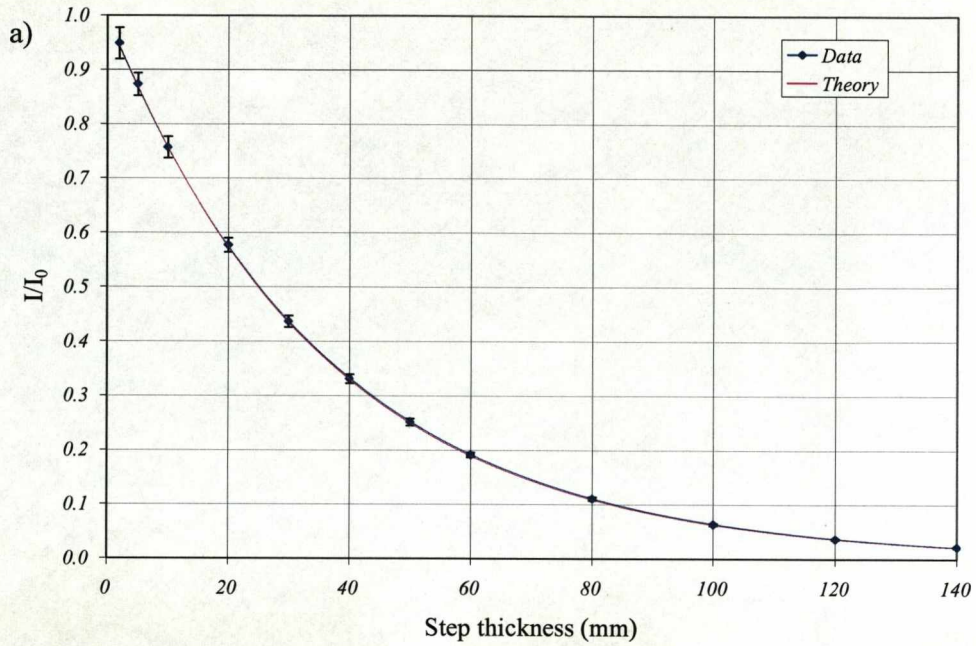

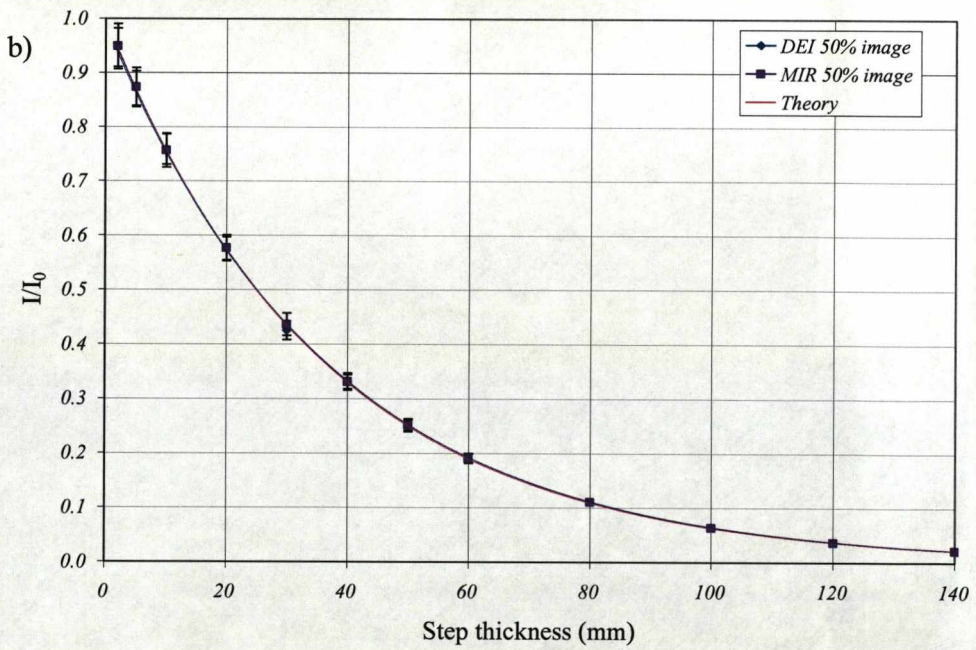

Figure 5-8: Plot of I/I_0 against Step thickness. a) Comparing results from the MIR ±50%, image with theory. b) Comparing results from the DEI ±50% image and the MIR ±50% image with theory.

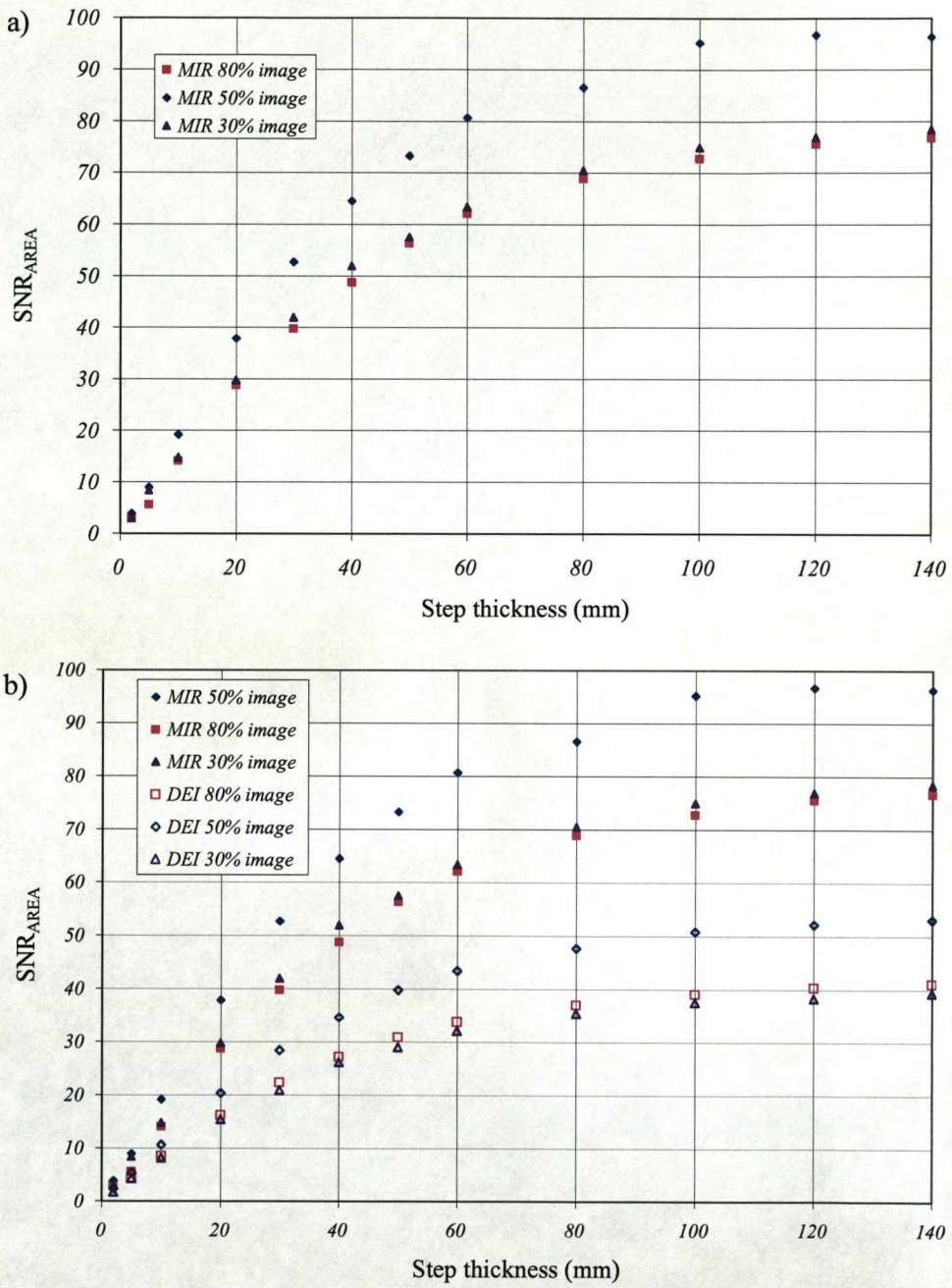

Figure 5-9: A plot of the SNR value for each step against the step thickness (mm). a) The MIR absorption images, comparing the results from the ±80%, ±50% & ±30% images. b) Comparing the 80%, 50% and ±30% results for DEI and MIR.

In order to investigate the effect of increasing the number of imaging positions on the SNR_{AREA} plots comparing the SNR_{AREA} values of the steps for different numbers of imaging positions on the rocking curve were created and are shown in Figure 5-10. The results for the absorption images which used the ±80% images (Figure 5-10 a)), showed that by increasing the number of imaging positions the SNR_{AREA} increased. For the absorption images which used the ±30% images, the peak, ±80%, ±50% and ±30% image gave the largest SNR_{AREA}. However, the results for the other two images gave approximately the same value. In addition the SNR_{AREA} results for the absorption images which used the ±50% images the ±50% image gave the highest SNR_{AREA}. This suggests that by increasing the number of imaging positions on the rocking curve the image quality can be increased. However, this is dependent on other factors, such as the image quality of the component images themselves.

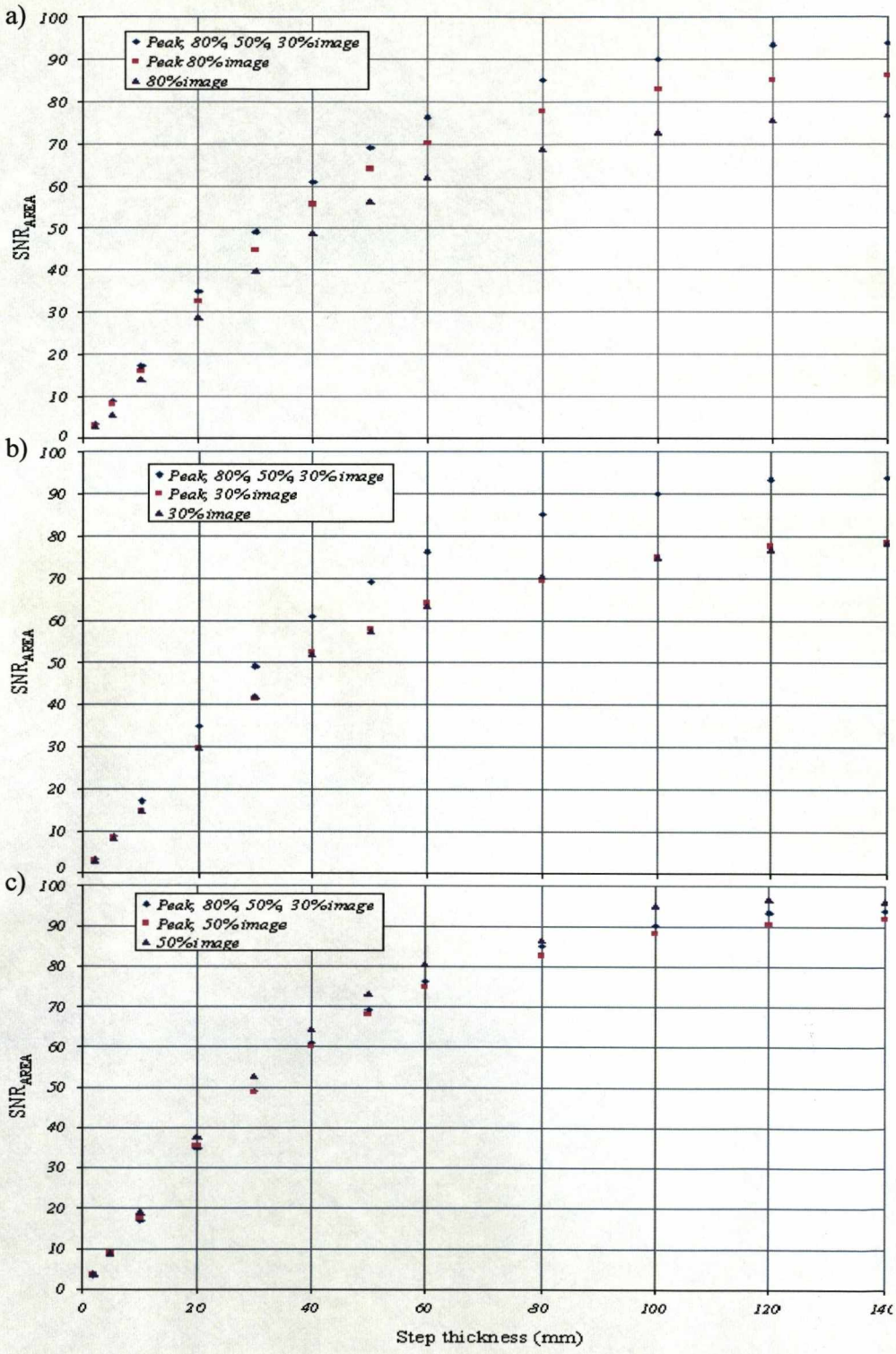

Figure 5-10: Plots of SNR against step thickness comparing the different number of imaging positions on the rocking curve for the MIR technique. a) The image sets using the ±80% images. b) The image set usingthe ±50% images. c) The image sets using the ±30% images.

For completeness, a SNR_{AREA} analysis was carried out for the refraction and USAXS images. Looking first at the USAXS image, it would be expected that as the thickness of the sample increased so would the amount of scatter undergone by the x ray and therefore the SNR of the step would increase. However, the results, shown in Figure 5-11 a), show a lot of variation and such an increase is not visible. Results from the SNR analysis of the refraction images are shown in Figure 5-11 b). As can be seen there is no obvious trend in the results, suggesting that the techniques have separated the refraction and absorption properties effectively.

The results from imaging this phantom have shown that for both techniques ±50% is the best imaging position as was expected. They also show that both techniques perform equally well in terms of giving I/I_0 agree with theory, and also suggest that by increasing the number of imaging positions used for the MIR technique the image quality increases. However, this is also dependent on the image quality of the composite images.

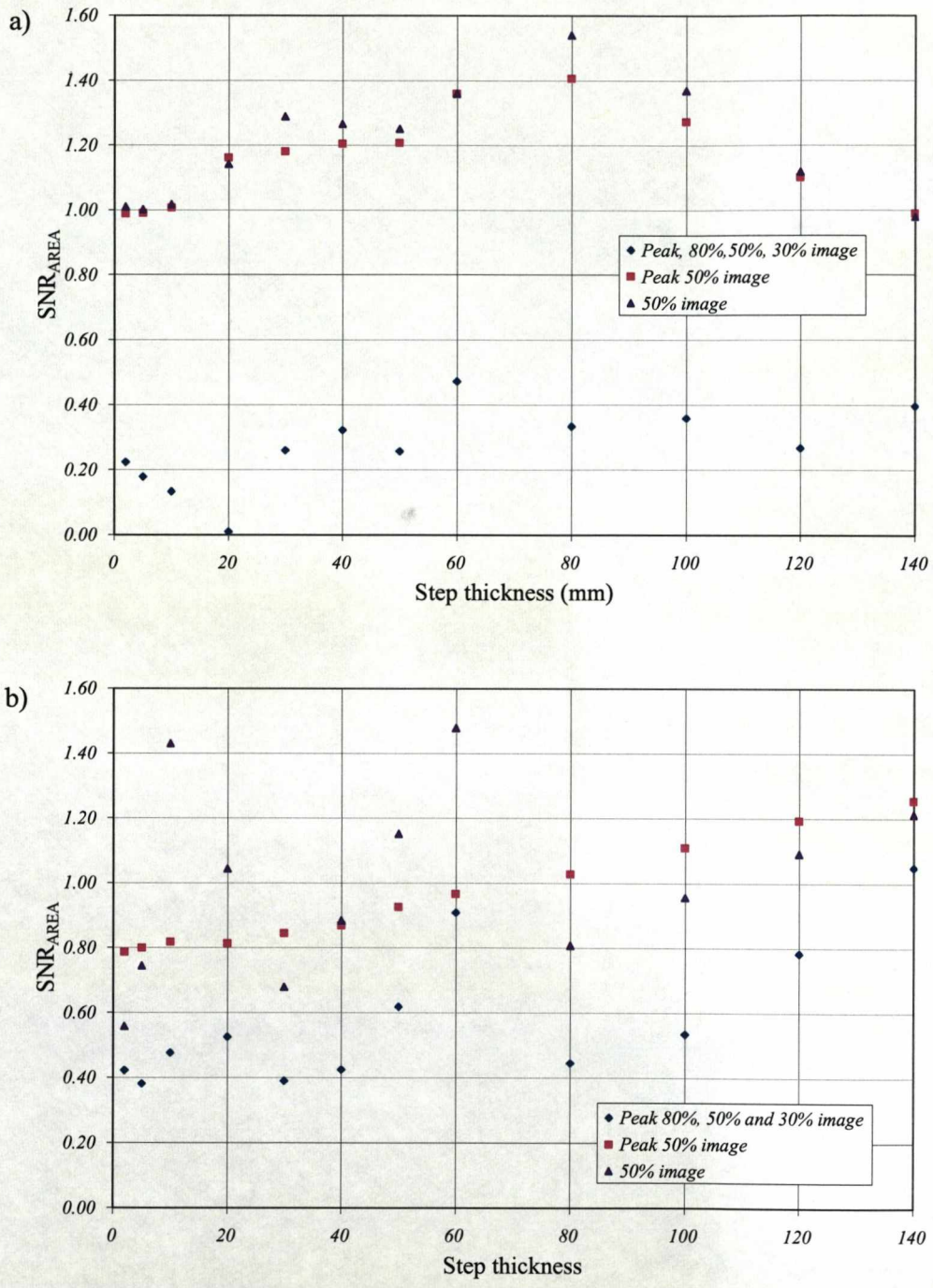

Figure 5-11: Plots of SNR against step thickness. a) Results from the USAXS image. b) Results from the refraction image.

5.3 **Refraction Phantom**

Two experiments were carried out using this phantom; the first at the ESRF using a beam energy of 40 keV, the second at Daresbury SRS using a beam energy of 20 keV.

5.3.2 The ESRF experiment

The refraction phantom was imaged with the analyser crystal tuned to seven positions on the rocking curve: the peak; ±80%; ±50%; 30%; and ±15%. However, due to problems with the images taken at ±50% position, only the images taken at the other positions were used, creating three DEI image sets and seven MIR sets.

The ±80% DEI image set is shown in Figure 5-12. The refraction image (Figure 5-12 a)) shows that on either side of the phantom, where the values of tanα have opposite signs (see Figure 5-13), the faces of the phantom have opposite colour contrast. It also shows that as the values of tanα decrease (see Figure 5-13) the contrast decreases. The absorption image (Figure 5-12 b)), shows the attenuation of the beam through the phantom. The images from the other positions on the rocking curve showed the same results and can be seen in Appendix 1.

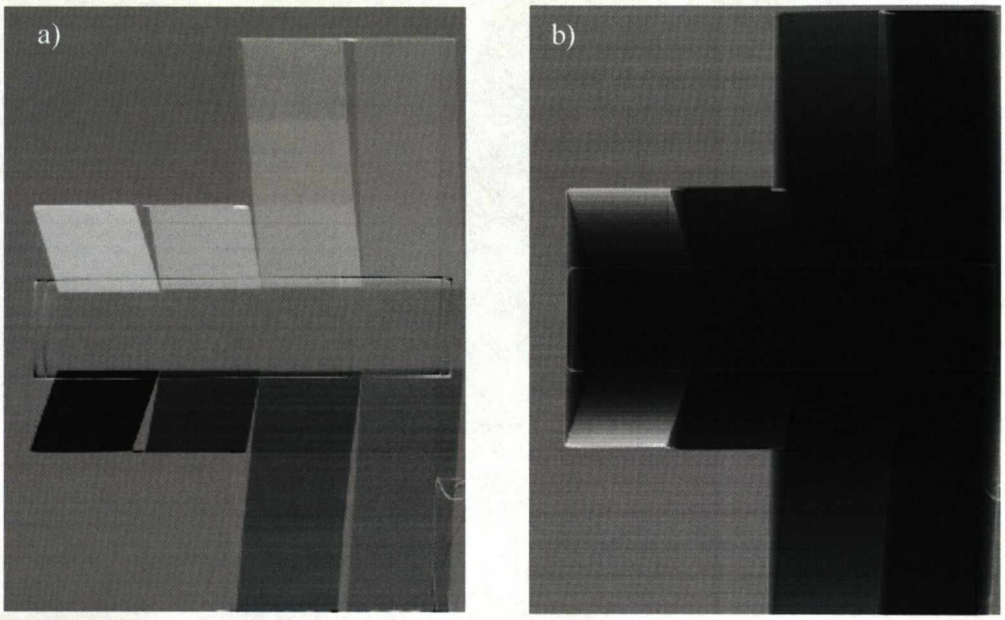

Figure 5-12: The DEI images from the ±80% position on the rocking curve. a) The refraction image. b) The apparent absorption image.

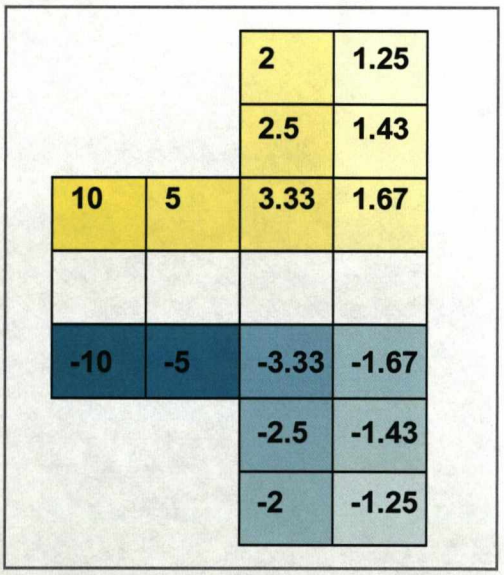

Figure 5-13: Diagram showing all the values of tanα for each face.

Figure 5-14 shows the ±80% MIR images of this phantom. As with the DEI images, the refraction image shows opposite colour contrast for opposite sides of the phantom, this contrast also decreases as tanα decreases. Again, as in the DEI absorption image, the MIR absorption image shows the beam's attenuation through the phantom. The additional USAXS image shows bright regions where the beam has scattered off the surfaces; this contrast decreases as tanα decreases. The line artefacts that have been common throughout these experiments are also noticeable in the USAXS image. Similar results were observed for the other DEI and MIR image sets and can be seen in Appendix 1.

In order to analyse the refraction images more fully, values of $\Delta\theta_z$ were found for each of the phantom's faces and plotted against tanα with the theoretically expected values. Figure 5-15 shows such plots the ±80% DEI refraction images. As can be seen from the theoretical values, the experimental results ought to give a straight line with a positive gradient, crossing the y-axis at zero. However, as Figure 5-15 shows, this is not the case. The line fitted to the data does not have the same gradient as the theoretical prediction and it does not intersect the y-axis at zero. This could be caused by the misalignment of the phantom in the beam.

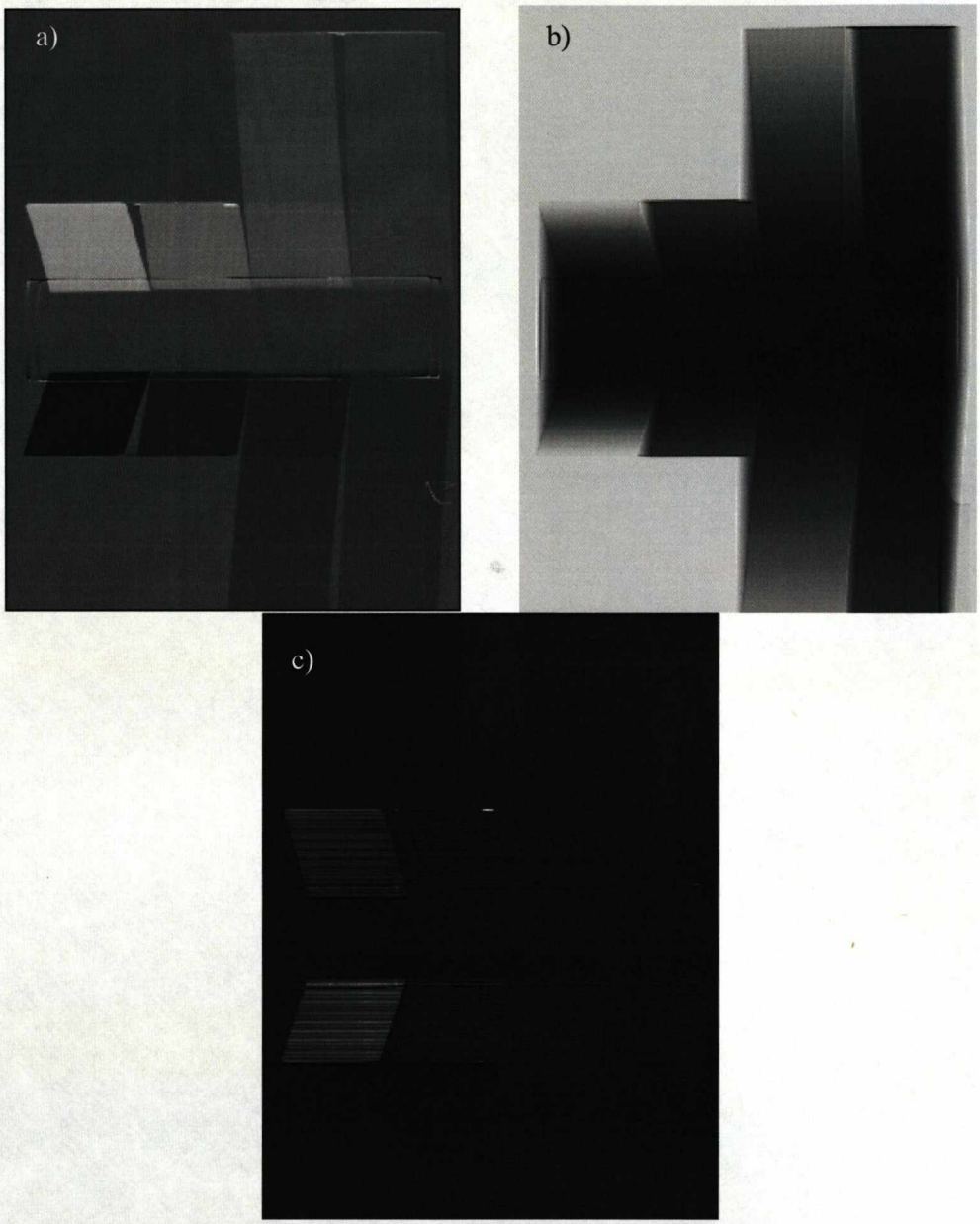

Figure 5-14: The ±80% MIR images of the refraction phantom. a) The refraction image. b) The absorption image. c) The USAXS image.

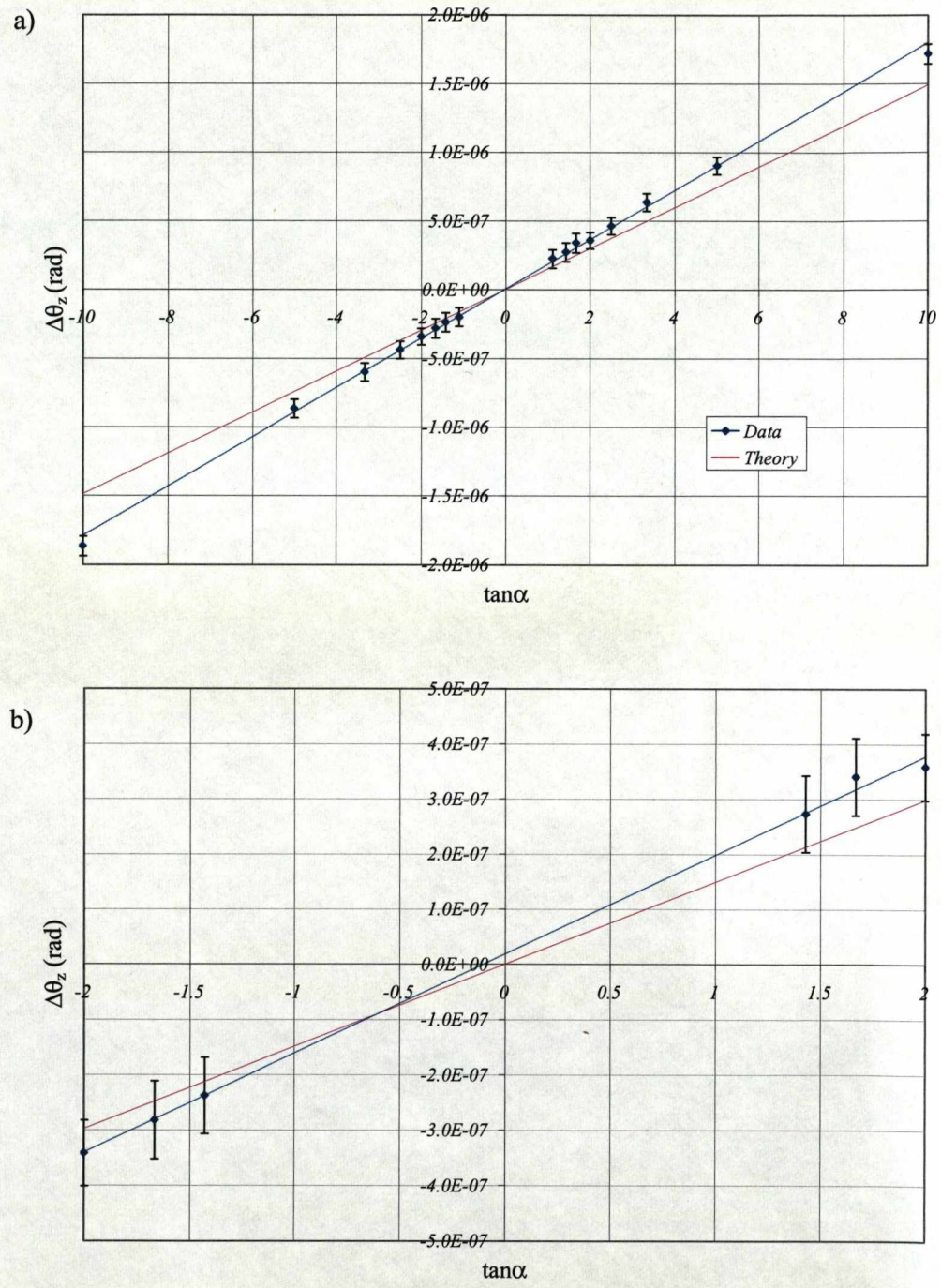

Figure 5-15: Plots of $\Delta\theta_z$ against tanα for the ±80% DEI refraction images. a) For the whole range of tanα. b) For small values of tanα

5.3.2.1 Investigating the effect of phantom misalignment

If the phantom was not positioned so that the faces made the correct angle to the beam, shown in Figure 5-16 a), there would be a slight change in the values of tanα, as shown in Figure 5-16 b). Thus, if the phantom was positioned so that it was facing slightly upwards (as is the case in Figure 5-16 b)), the values of tanα on the top of the phantom would increase slightly and those on the bottom would decrease slightly. The reverse would be true if the phantom was facing slightly downwards.

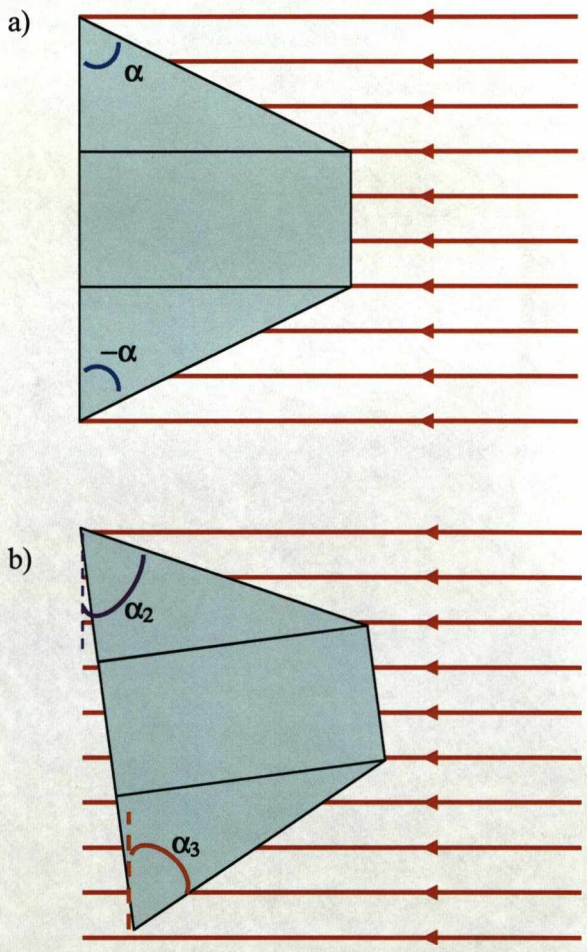

Figure 5-16: Diagram demonstrating the effect of the phantom being positioned at an angle to the beam. a) The phantom positioned correctly. b) The phantom positioned at a slightly upwards facing angle

The effect that the phantom being positioned at an angle has on the plots of $\Delta\theta_z$ against $\tan\alpha$ is shown in Figure. 5-17. The plot of $\Delta\theta_z$ against $\tan\alpha$ in Figure 5-17 a) shows the effect of increasing the angle, α, by small amounts. Figure 5-17 b) shows the effect of decreasing α by small amounts. Comparing these plots with the one showing the real data in Figure 5-15, it can be seen that the region $-10< \tan\alpha <0$, α must have decreased and in the region $0< \tan\alpha <10$, α must have increased. This is consistent with the phantom being positioned so that it faces upwards slightly. An example of the predicted effect that this would have on a plot of $\Delta\theta_z$ against $\tan\alpha$ is presented in Figure 5-18 a), with a close up of the region around $\tan\alpha=0$ shown in Figure 5-18 b), as this plot shows there is a discontinuity in the fitted line at $\tan\alpha =0$. The DEI ±80% results are replotted in Figure 5-19; as would be expected from Figure 5-18, the gradients of the real data are higher than that of the theory and there is a discontinuity at $\tan\alpha=0$. The intercepts of the top and bottom data lines are not equal due to an insufficient background subtraction.

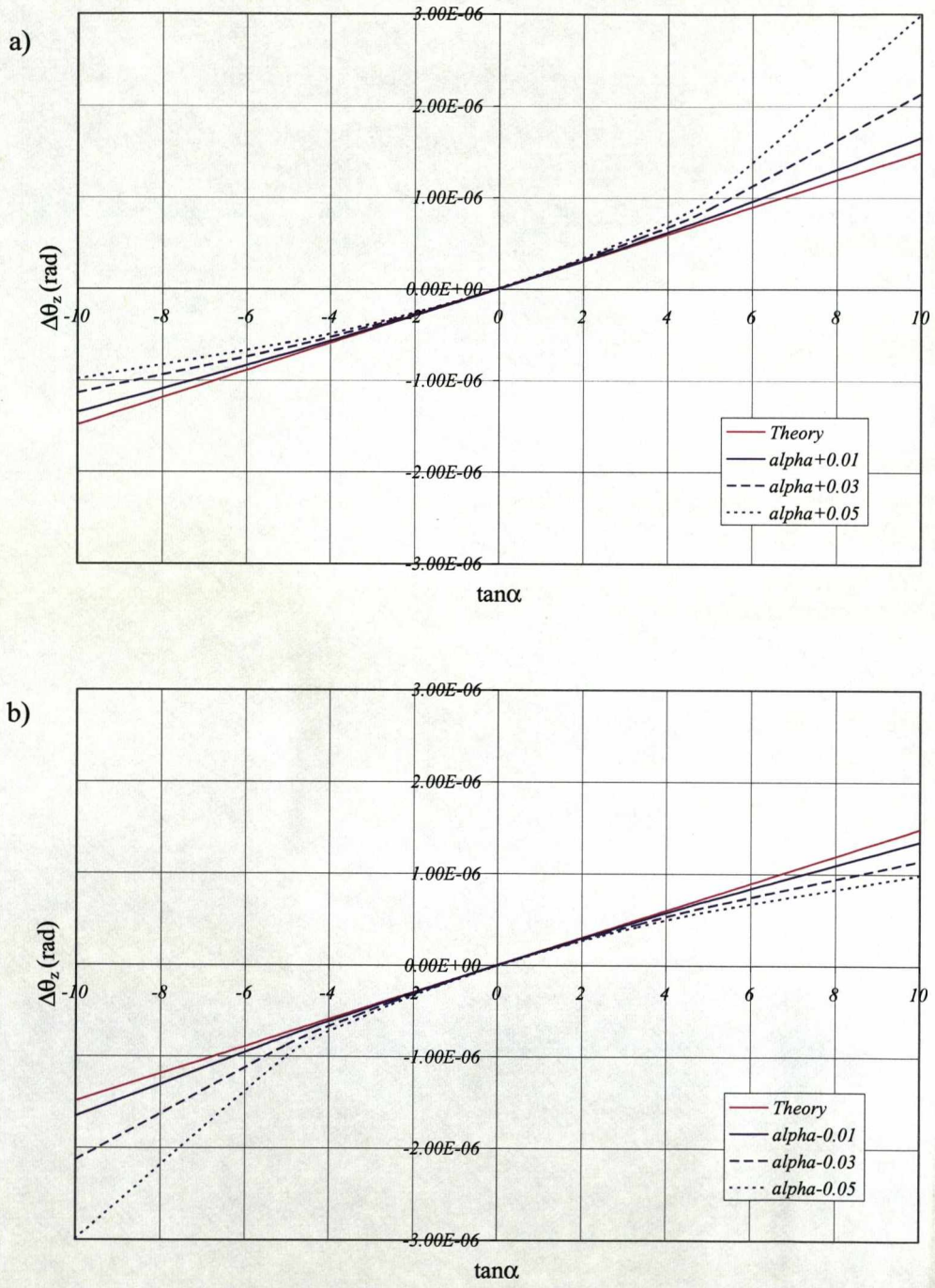

Figure 5-17: Plots of $\Delta\theta z$ against $\tan\alpha$, showing the effects of changing a by a small amount. a) The effect of increasing α. b) The effect of decreasing α.

a)

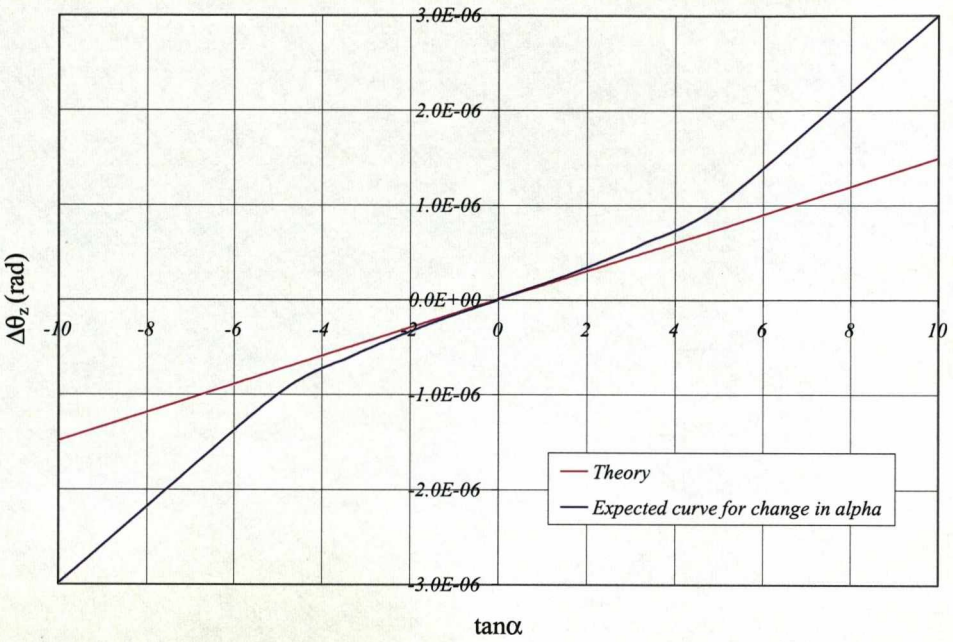

b)

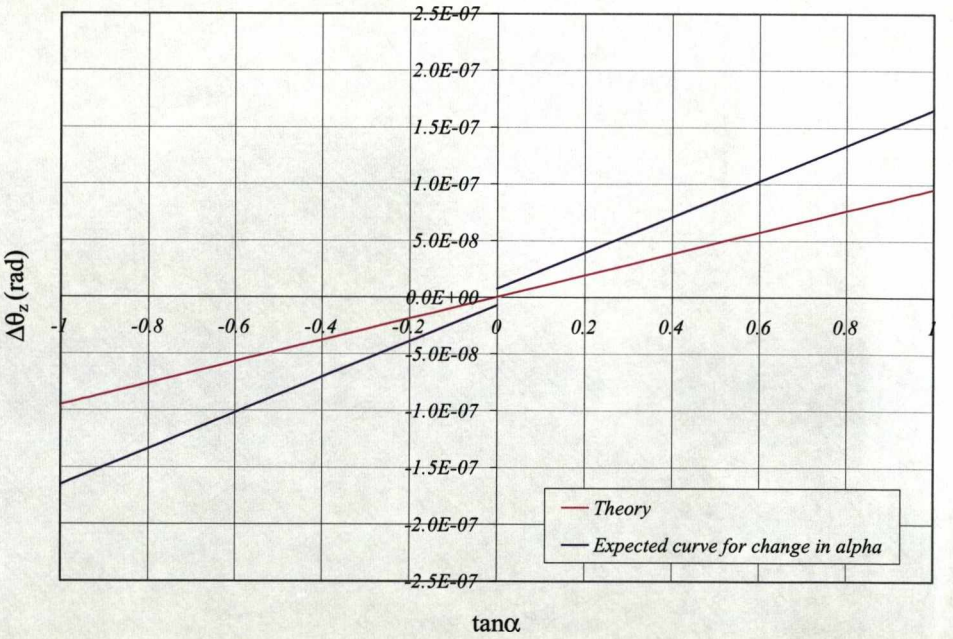

Figure 5-18: Plots of $\Delta\theta z$ against α, with α increased in the region $0<\tan\alpha<10$ and α decreased in the region $-10>\tan\alpha>0$. a) The plot of $\Delta\theta z$ against $\tan\alpha$. b) A close-up of the central region of the plot.

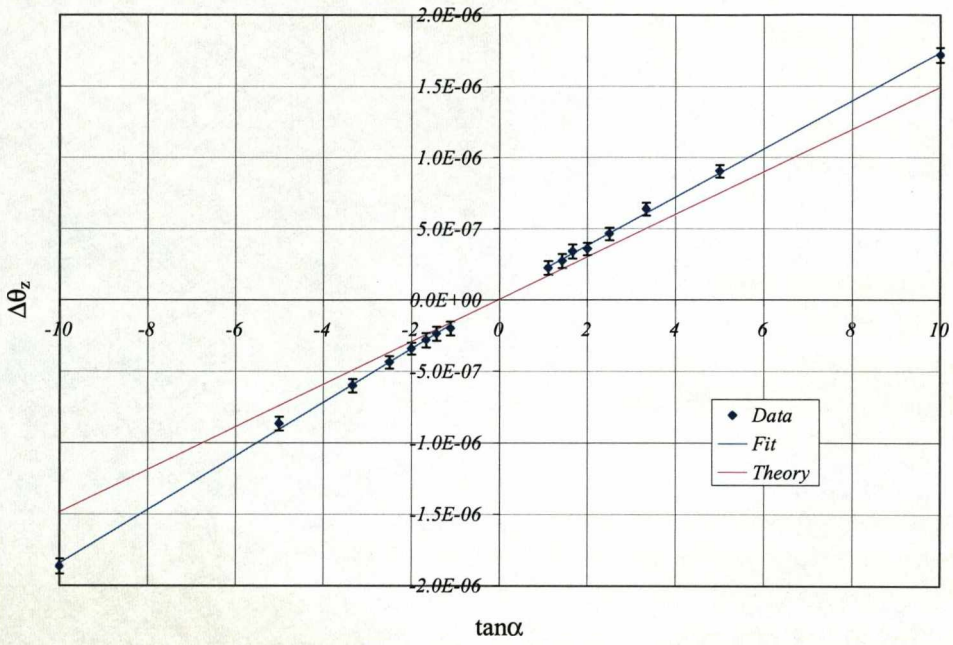

Figure 5-19: Plot of $\Delta\theta z$ against $\tan\alpha$, for the ±80% DEI refraction image, compared with theory.

The plots of $\Delta\theta_z$ against $\tan\alpha$ for the DEI ±30% and ±15% images are shown in Figure 5-20. For both the ±30% and ±15% plots the fitted lines are well within the regions of errors, with the exception of the $\tan\alpha=10$ data point. As with the ±80% plots, the gradients of the real data were greater than that of the theory, and there was a discontinuity around zero. However, as can be seen in Figure 5-20, and shown more plainly in Table 5-1 the gradients for the $+\tan\alpha$ and $-\tan\alpha$, fitted lines do not have the same gradients, which would have been expected. A possible cause of this discrepancy is an inaccurate positioning of the analyser crystal on either or both sides of the rocking curve.

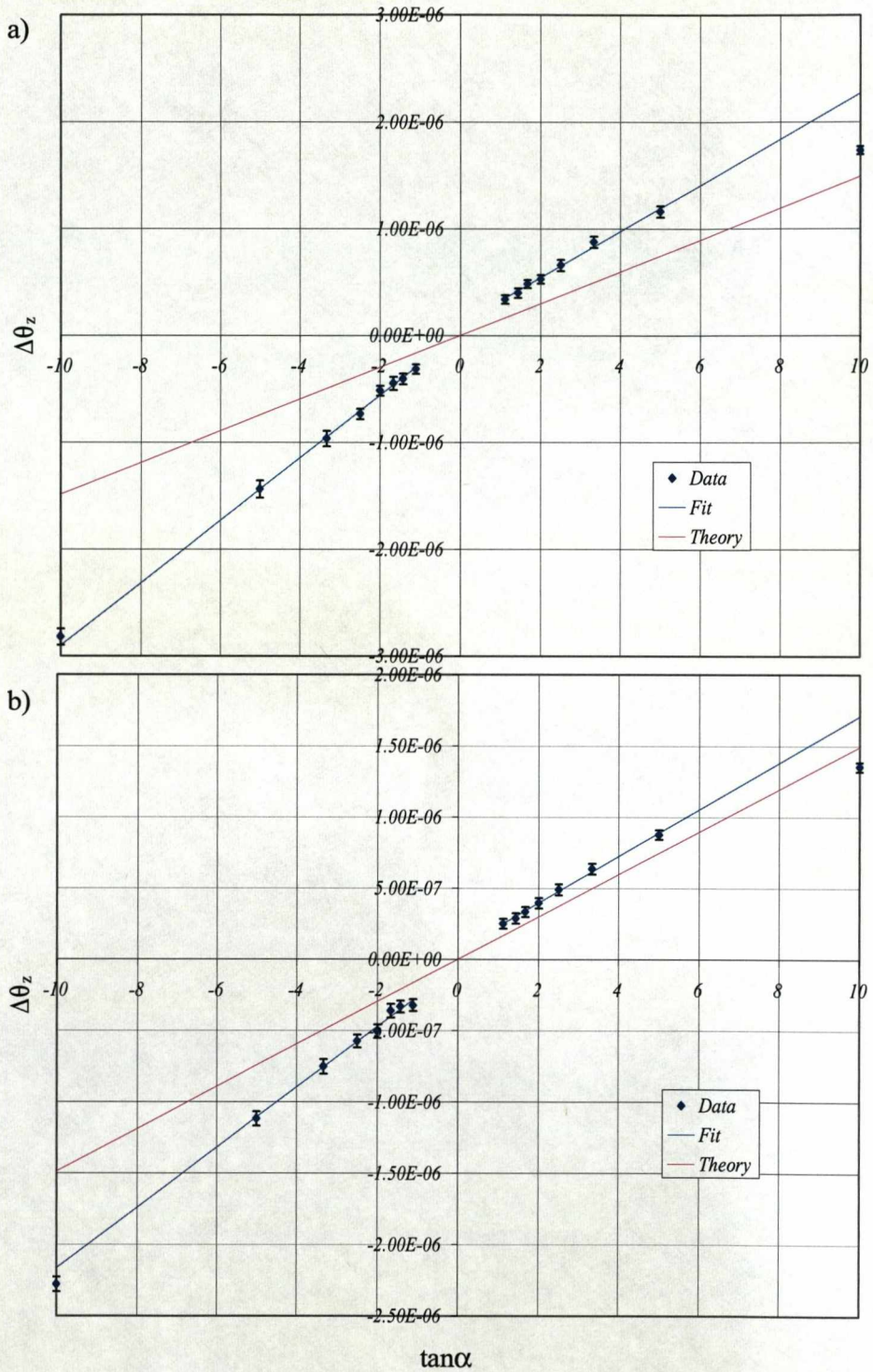

Figure 5-20: The $\Delta\theta_z$ against tanα plots. a) Results from the ±30% DEI images. b) Results from the ±15% DEI images.

		Gradient	$\sigma_{gradient}$	Difference
80%	tanα	1.69×10^{-7}	0.07×10^{-7}	0.19×10^{-7}
	-tanα	1.88×10^{-7}	0.07×10^{-7}	
30%	tanα	2.16×10^{-7}	0.15×10^{-7}	0.77×10^{-7}
	-tanα	2.93×10^{-7}	0.21×10^{-7}	
15%	tanα	1.64×10^{-7}	0.10×10^{-7}	0.48×10^{-7}
	-tanα	2.12×10^{-7}	0.15×10^{-7}	

Table 5-1: The gradients of the lines fitted to the plots of $\Delta\theta_z$ against tanα.

5.3.2.2 The effect of inaccurate positioning on the rocking curve

In order to test what effect positioning the analyser incorrectly on the rocking curve had on plots of $\Delta\theta_z$ versus tanα six more DEI image sets were created. This time with the images from the wrong position substituted into the calculation so as to evaluate the effect.

Figure 5-21 shows the $\Delta\theta_z$ values that were given when images from the wrong positions on the rocking curve were used in the analysis. In Figure 5-21 a), the DEI analysis was carried out for the ±80% imaging position, while, for three of the data sets, images at a lower position (-30%, +30% and ±30% respectively) were substituted in. As this plot shows, for the positive values of tanα, the gradient of the line increases in relation to the line which used the ±80% images. This increase in gradient was greatest when both of the images used were from the lower imaging position. For negative values of tanα, the gradient of the lines increased in relation to the line which used the ±80% images. Again, the gradients which had only one incorrect image showed approximately the same change in gradient, and when two wrong images were used the change in gradient was the greatest. In Figure 5-21 b), the DEI analysis was carried out for the ±30% imaging position, with images at higher positions (-80%, +80% and ±80% respectively) being substituted in. For the positive values of tanα, the gradient of the line decreased, this decrease in gradient was approximately the same when only one incorrect image was used and was greatest when both images were from higher positions on

the rocking curve. For the negative values of tanα, the gradient of the lines also decreased when images from higher positions were substituted in. As before, the change in gradient was similar when only one wrong image was used, and the change was largest when both images used were wrong.

The results presented in Figure 5-21, demonstrated that the inaccurate positioning of the analyser crystal on the rocking curve is the probable cause for the difference in the gradients of the –tanα and +tanα presented in Figure 5-19 and Figure 5-20. This difference in gradient also means that when comparing the imaging position on the rocking curve, shown in Figure 5-22, there are no obvious trends.

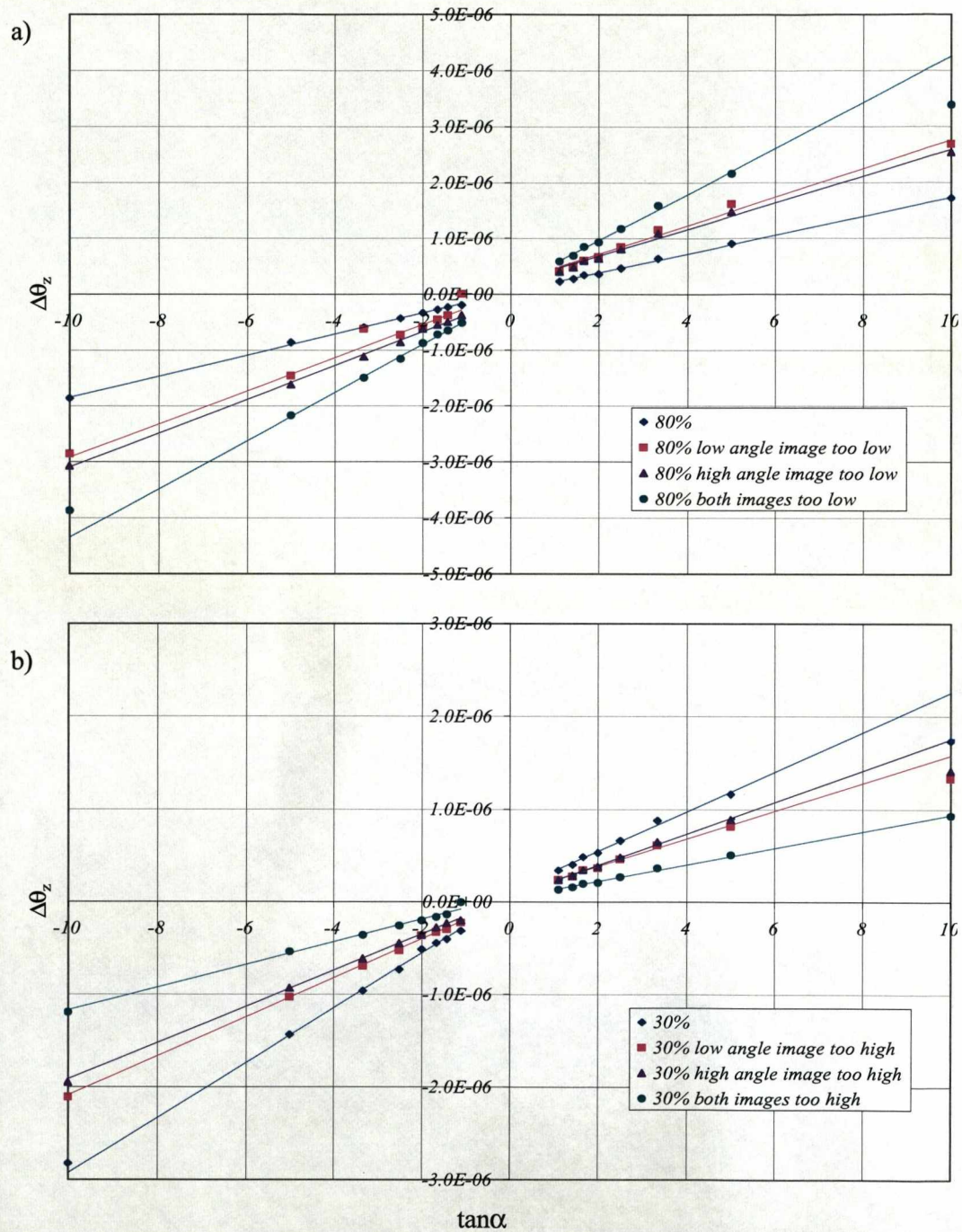

Figure 5-21: Plots of $\Delta\theta_z$ against tanα for showing the effect of inaccurate positioning on the rocking curve. a) The effect of positioning too low on the rocking curve. b) The effect of positioning too high on the rocking curve.

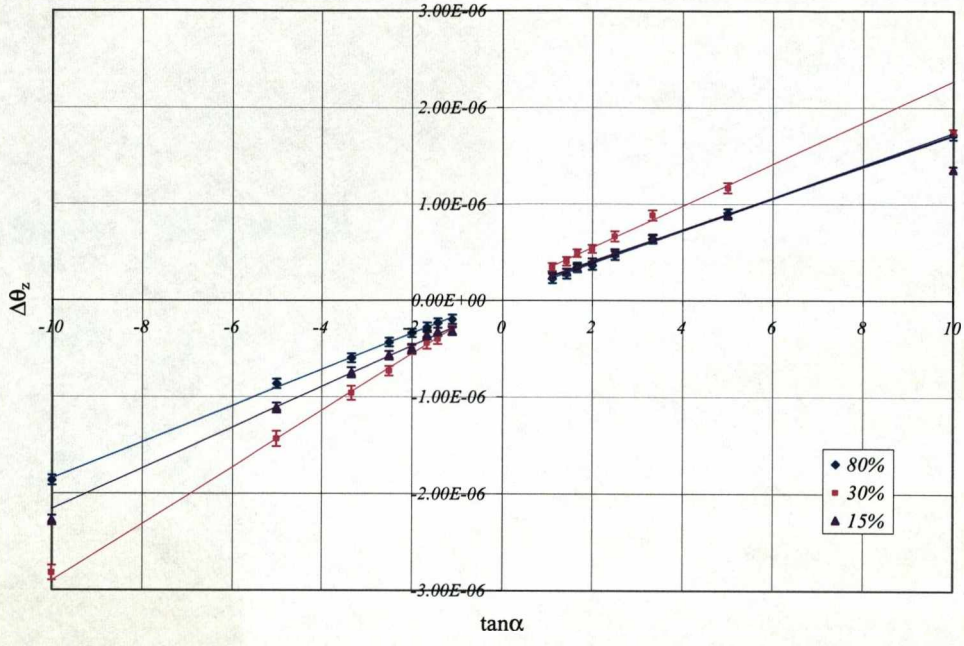

Figure 5-22: Plot of $\Delta\theta_z$ against tanα comparing the imaging position on the rocking curve.

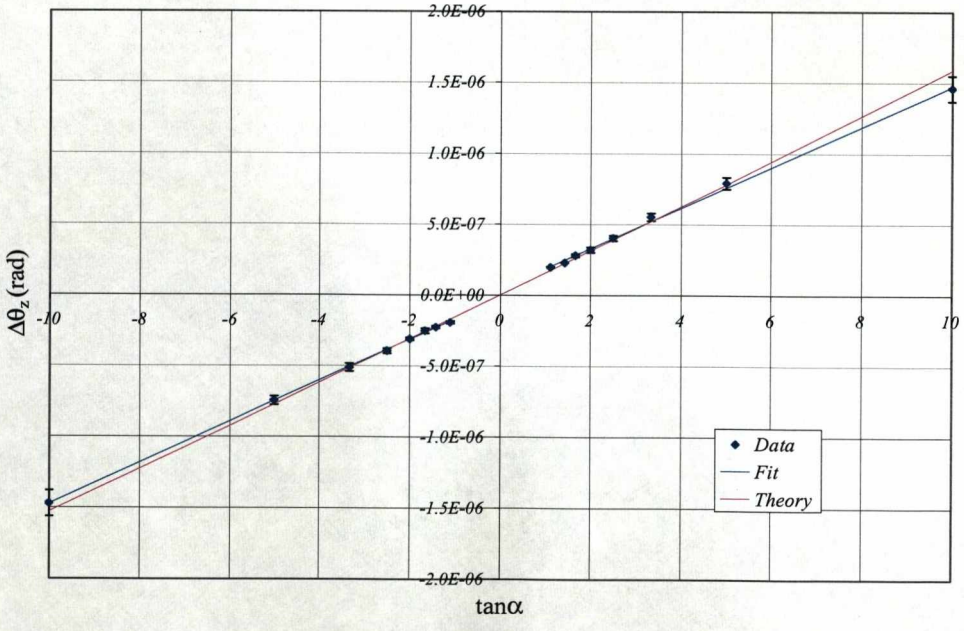

Figure 5-23: Plot of $\Delta\theta_z$ against tanα for the MIR peak, ±80%, ±30% and ±15% image.

As with the DEI images, the values of $\Delta\theta_z$ for each of the phantoms faces were found for all of the MIR images, and plotted against tanα. Figure 5-23 shows such a plot for the MIR peak, ±80%, ±30%, ±15% refraction image. As can be seen, the results were very similar to theory and the fit was within the region of errors for all but the tanα=10 data point.

The results for the other MIR refraction images, however, were not consistent with the findings for this image, as shown in Figure 5-24. Looking first at Figure 5-24 a), a plot comparing the images which used a single image pair in the analysis, the results show that the images lower down the rocking curve gave results furthest away from those predicted by theory. Similar to the DEI results, the ±15% and ±30% results gave lines with gradients higher than theory, as would be expected with the phantom positioned at a slight upwards angle to the beam. The ±80% results, however, although closest to theory, show decreased gradients.

The plot for the MIR images which utilised the peak image in addition to an image pair in the analysis is shown in Figure 5-24 b). The peak ±80% image, as with the ±80% image shows gradients lower than those predicted by theory. The peak 30% and peak ±15% images gave results with gradients higher than theory, as the ±30% and ±15% images did in Figure 5-24 a). Comparing Figure 5-24 a) and b), it can be seen that the peak 30% and peak 15% image results are closer to the theoretical results than the ±30% ±15% image results. This suggests that the accuracy of the MIR analysis increases with the number of imaging positions.

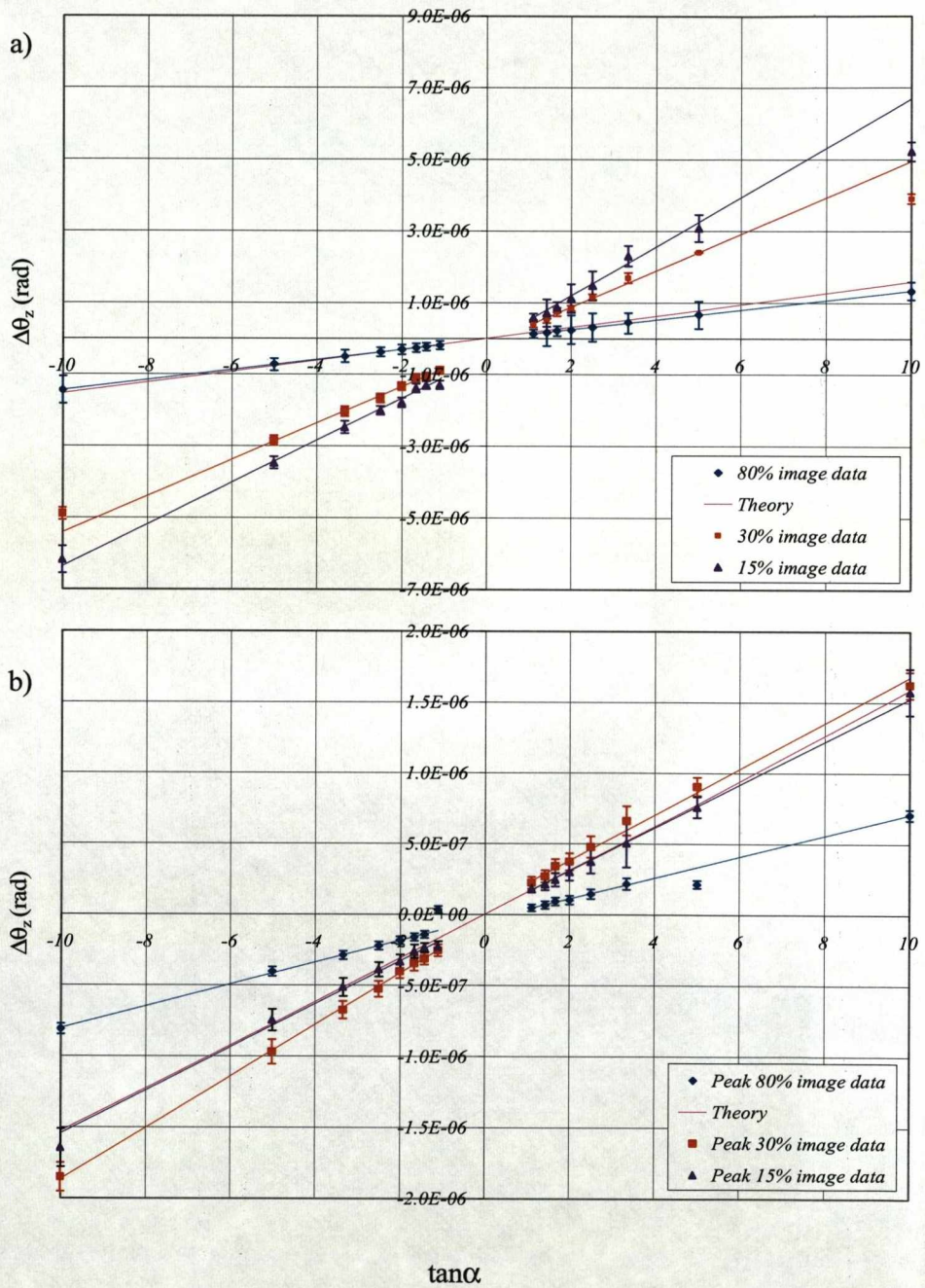

Figure 5-24: Plots of $\Delta\theta_z$ against tanα. a) Comparing the results which utilised single image pairs in the MIR analysis. b) Comparing the results which utilised the peak image and a single image pair in the MIR analysis.

In order to look at the effect of increasing the number of positions on the rocking curve more fully, plots of $\Delta\theta_z$ against tanα comparing increasing numbers of imaging positions on the rocking curve were created and are presented in Figure 5-25. The results for the ±30% and ±15% image sets, shown in Figure 5-25 a) and b), clearly demonstrate that as the number of imaging positions increases the results tend closer to those predicted by theory. The results for the ±80% image sets, shown in Figure 5-25 c), however, deviate from this with the peak ±80% image giving results that are further away from theory than the ±80% image. As was mentioned previously the ±80% and peak 80% images gave results with gradients lower than theory. A possible cause for this is a discrepancy in the positioning on the rocking curve. In order to test this plots of $\Delta\theta_z$ against tanα were created for MIR refraction images which had images from the wrong position on the rocking curve substituted in, these plots are shown in Figure 5-26. The results demonstrate that when the images are at too low a position on the rocking curve, the gradient increases for both ±tanα and when the images are at too high a position on the rocking curve the gradient decreases for both ±tanα. An inaccuracy in the positioning of the images on the rocking curve could therefore account for the discrepancies on the ±80% and peak ±80% image results. As with the DEI results, the lines fitted to the +tanα data and the –tanα data had different gradients, as shown in Table 5-2, as with the DEI results these differences are likely to be due to inaccuracies in the rocking curve position.

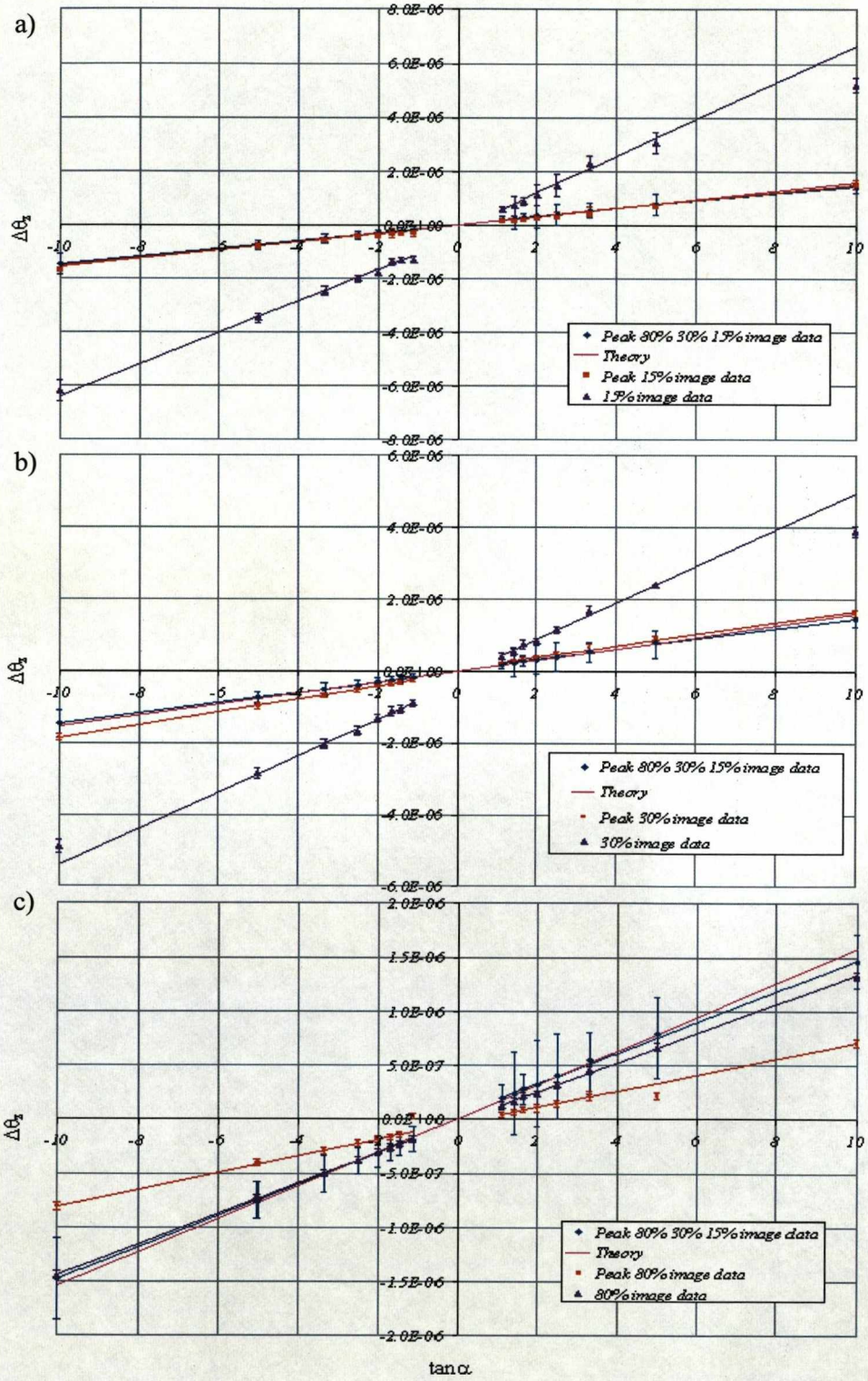

Figure 5-25: Plots of $\Delta\theta_z$ against tanα comparing the number of imaging positions on the rocking curve. a) Results from the ±30% images. b) Results from the ±15% images. c) Results from the ±80% images.

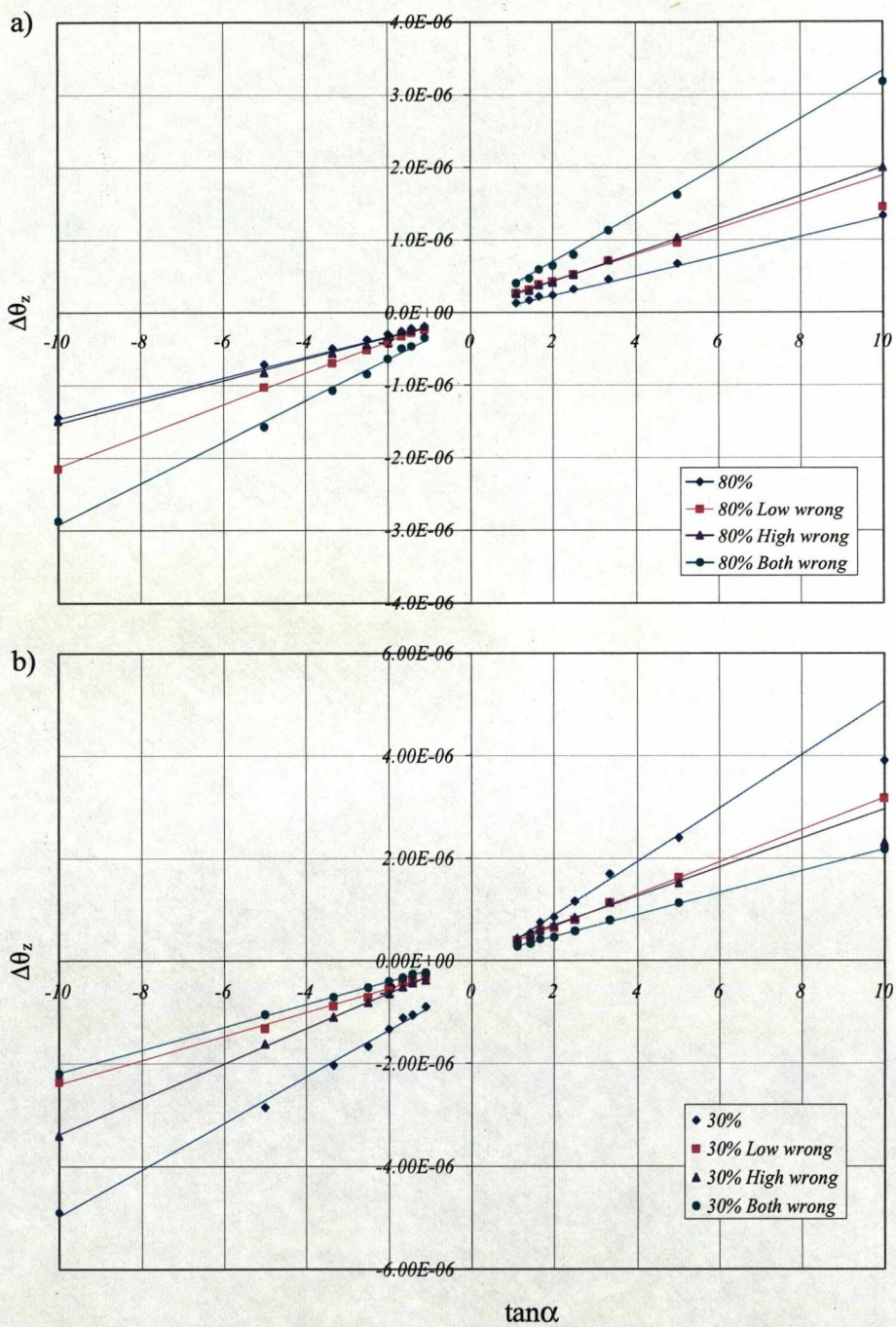

Figure 5-26: Plots of $\Delta\theta_z$ against tanα comparing results from images sets created using images from the wrong position on the rocking curve. a) With images too high on the rocking curve substituted into the calculation. b) With images too low substituted into the calculation.

		Gradient	$\sigma_{Gradient}$	Difference
Peak 80% 30% 15%	$+tan\alpha$	1.43×10^{-7}	0.30×10^{-7}	0.02×10^{-7}
	$-tan\alpha$	1.45×10^{-7}	0.34×10^{-7}	
Peak 80%	$+tan\alpha$	7.44×10^{-8}	0.47×10^{-8}	0.29×10^{-8}
	$-tan\alpha$	7.73×10^{-8}	0.46×10^{-8}	
Peak 30%	$+tan\alpha$	1.62×10^{-7}	0.10×10^{-7}	0.2×10^{-7}
	$-tan\alpha$	1.82×10^{-7}	0.11×10^{-7}	
Peak 15%	$+tan\alpha$	1.52×10^{-7}	0.14×10^{-7}	0.0
	$-tan\alpha$	1.52×10^{-7}	0.12×10^{-7}	
80%	$+tan\alpha$	1.35×10^{-7}	0.06×10^{-7}	0.06×10^{-7}
	$-tan\alpha$	1.41×10^{-7}	0.06×10^{-7}	
30%	$+tan\alpha$	5.09×10^{-7}	0.14×10^{-7}	0.01×10^{-7}
	$-tan\alpha$	5.10×10^{-7}	0.46×10^{-7}	
15%	$+tan\alpha$	6.86×10^{-7}	0.85×10^{-7}	1.01×10^{-7}
	$-tan\alpha$	5.87×10^{-7}	0.46×10^{-7}	

Table 5-2: The gradients of the lines fitted to the plots of $\Delta\theta_z$ against tanα.

5.3.2.3 Finding the angle of misalignment

As was discussed previously, the results presented show that the phantom must have been positioned at an angle to the beam. The equation to find Δθz (Figure 5-27),

$$\Delta\theta_z = 1.3\times10^6 \lambda^2 \rho \tan\alpha, \qquad \text{Equation 5-1}$$

is therefore not complete when the phantom is at an angle and becomes:

$$\Delta\theta_z = K\tan(\alpha+\delta), \qquad \text{Equation 5-2}$$

where $K=1.3\times10^{6}\lambda^{2}\rho$ and δ is the angle that the phantom is tilted at. Rearranging Equation 5-2, in terms of α and δ, it becomes:

$$\tan^{-1}\left(\frac{\Delta\theta_z}{K}\right)=\alpha+\delta. \qquad \text{Equation 5-3}$$

Therefore by plotting $\tan^{-1}(\Delta\theta_z/K)$ against α, it should be possible to find δ, the angle at which the phantom was tilted. These plots were created for both the DEI and MIR images.

The plots of $\tan^{-1}(\Delta\theta_z/K)$ against α for the peak, ±80%, ±30% and ±15% image are shown in Figure 5-27. As can be seen, the results clearly give straight lines, however, the gradients and y-intercepts of the results for both sides of the phantom are not the same. These results and those from the other MIR images are shown in Table 5-3. As this Table shows, the gradients, although they should have been equal to one gave a range of values, the y-intercepts, which should give the value of δ, also gave a range of values.

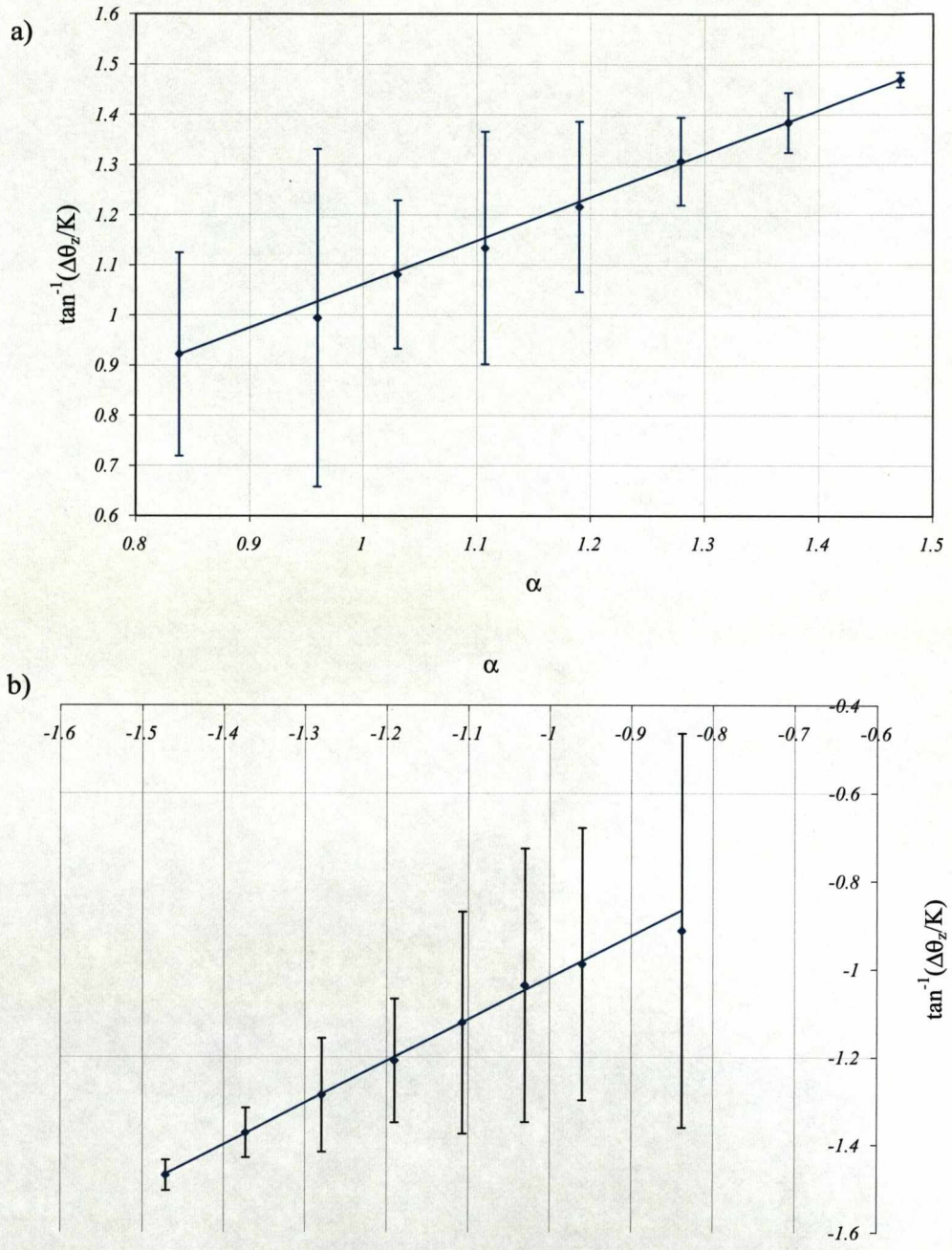

Figure 5-27: Plots of $\tan^{-1}(\Delta\theta z/K)$ against α. a) The positive values of α, the top side of the phantom. b) The negative values of α, the other side of the phantom.

		Gradient	$\sigma_{Gradient}$	y -intercept	$\sigma_{Intercept}$
Peak 80% 30% 15%	+α	*0.87*	*0.24*	*0.30*	*0.32*
	-α	*0.95*	*0.35*	*-0.69*	*0.48*
Peak 80%	+α	*1.31*	*0.18*	*-0.64*	*0.22*
	-α	*2.81*	*0.41*	*2.50*	*0.47*
Peak 30%	+α	*1.12*	*0.13*	*-0.14*	*0.16*
	-α	*0.55*	*0.06*	*-0.67*	*0.06*
Peak 15%	+α	*0.96*	*0.13*	*0.06*	*0.16*
	-α	*0.85*	*0.13*	*-0.21*	*0.16*
80%	+α	*1.20*	*0.19*	*-0.29*	*0.24*
	-α	*0.91*	*0.15*	*-0.12*	*0.19*
30%	+α	*0.46*	*0.08*	*0.89*	*0.10*
	-α	*0.22*	*0.03*	*-1.22*	*0.03*
15%	+α	*0.34*	*0.06*	*1.06*	*0.08*
	-α	*0.16*	*0.02*	*-1.30*	*0.03*

Table 5-3: The y-intercept and gradients values given by the plots of $\tan^{-1}(\Delta\theta_z/K)$ against α, for the MIR images.

In order to establish why there was such variation in the values for the line gradients and y-intercepts, the background values were varied so as to ascertain its affect. Figure 5-28 and Figure 5-29 show how varying the background affected both the gradient and y-intercept. As can be seen in Figure 5-28, when decreasing the background, for the positive values of α, the gradient of the line increased and the intercept decreased, for negative values of α, the gradient of the line decreased and the intercept became more negative. The results for increasing the background are shown in Figure 5-29, for the positive values of α, as the background increased the gradient decreased and the y-intercept increased, for the negative values of α, the gradient increased and the intercept became less negative. This therefore shows that for an inaccuracy in the background the gradient moves away from one and imprecision is introduced to the y-intercept which gives the value of δ.

a)

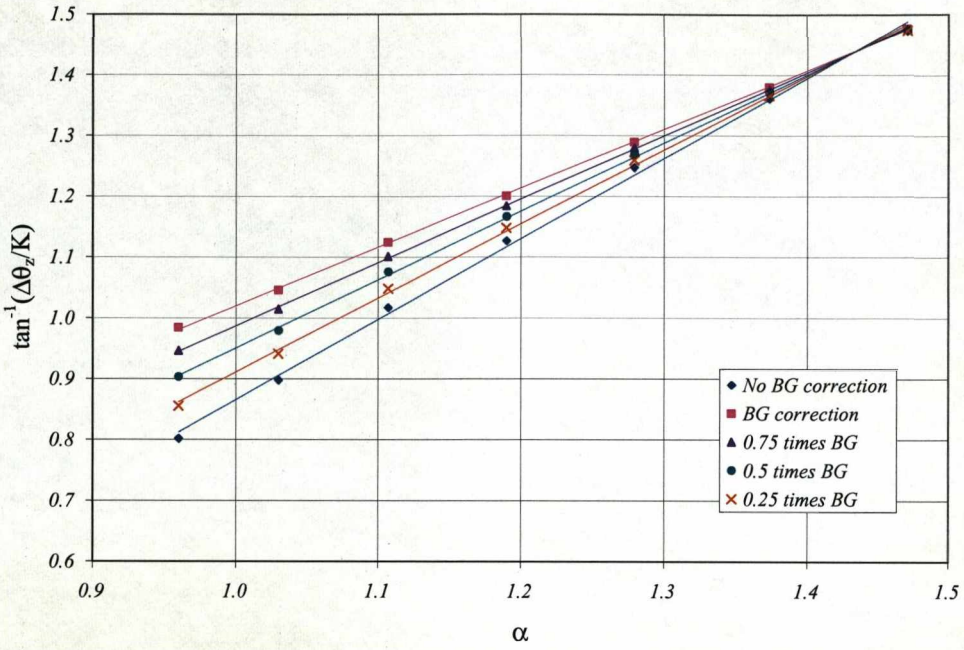

b)

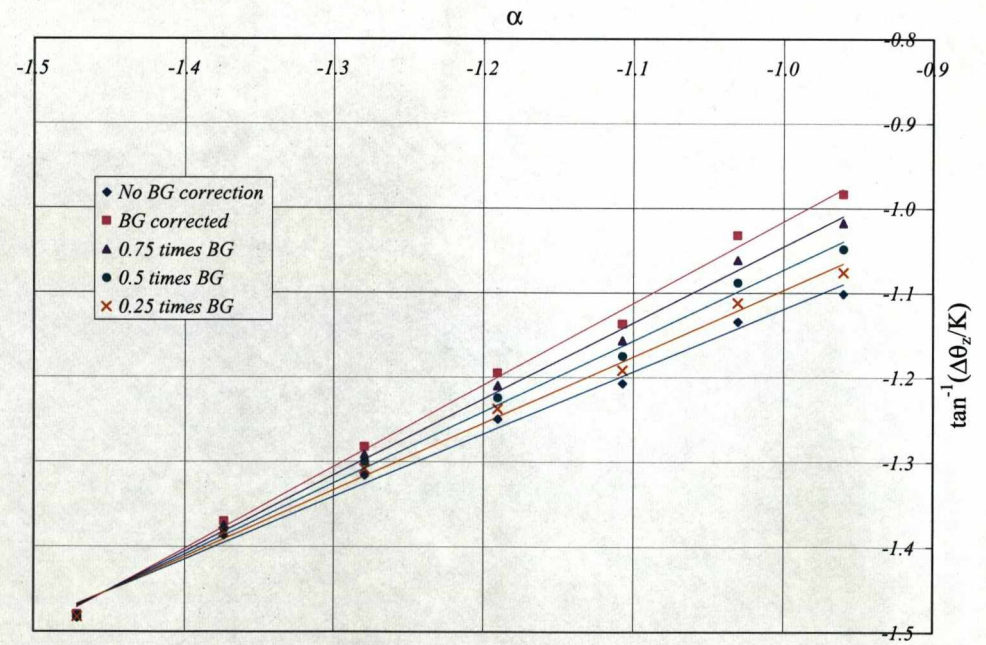

Figure 5-28: Plots of $\tan^{-1}(\Delta\theta_z/K)$ against α for the Peak, ±80%, ±30%, ±15% image data with decreased background. a) For positive values of α. b) For negative values of α.

a)

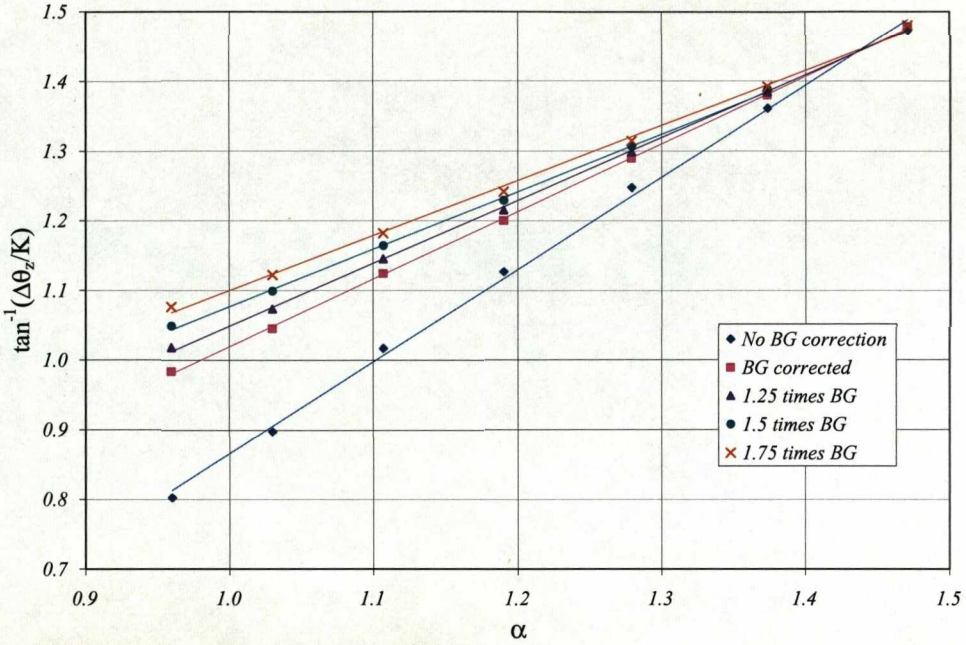

b)

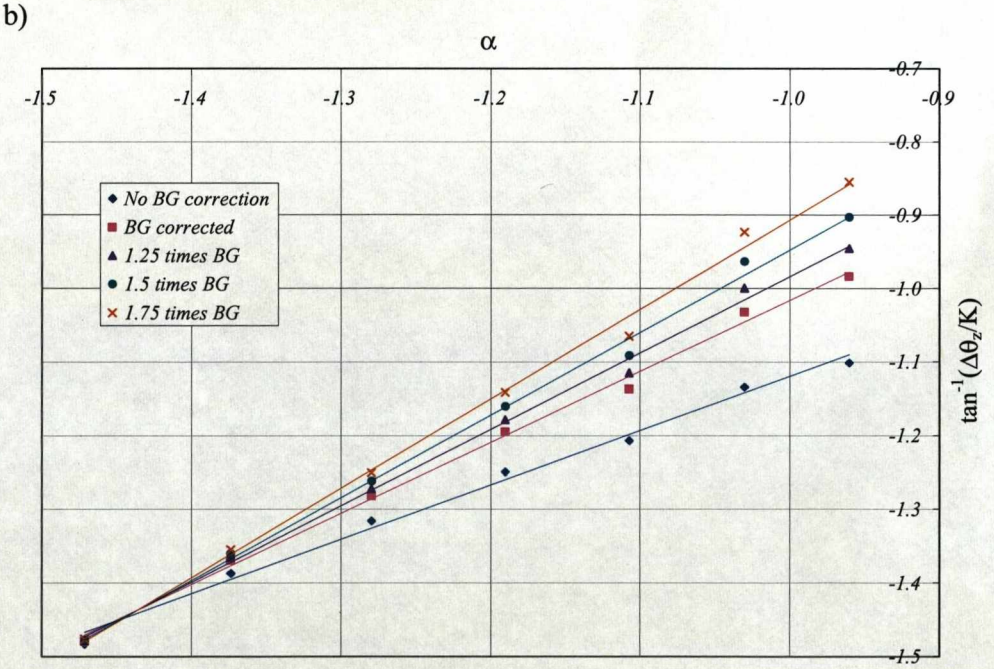

Figure 5-29: Plots of $\tan^{-1}(\Delta\theta_z/K)$ against α for the Peak ±80%, ±30%, ±15% image data with increased background. a) For positive values of α. b) For negative values of α.

In addition to the background there were other factors that could potentially affect the gradients and y-intercepts such as the number of imaging positions on the rocking curve and the position on the rocking curve.

Figure 5-30, Figure 5-31 and Figure 5-32, show the $\tan^{-1}(\Delta\theta_z/K)$ versus α plots, comparing the number of imaging positions for the ±80%, ±30% and ±15% data respectively. In the case of the ±30% and ±15% results where only two images were used (i.e. the ±30% or ±15% image pairs) the results gave gradients with values furthest from one, this was not the case for the ±80% results. Of the images where more than two constituent images were used there was no obvious trend to show that having more images gave better results.

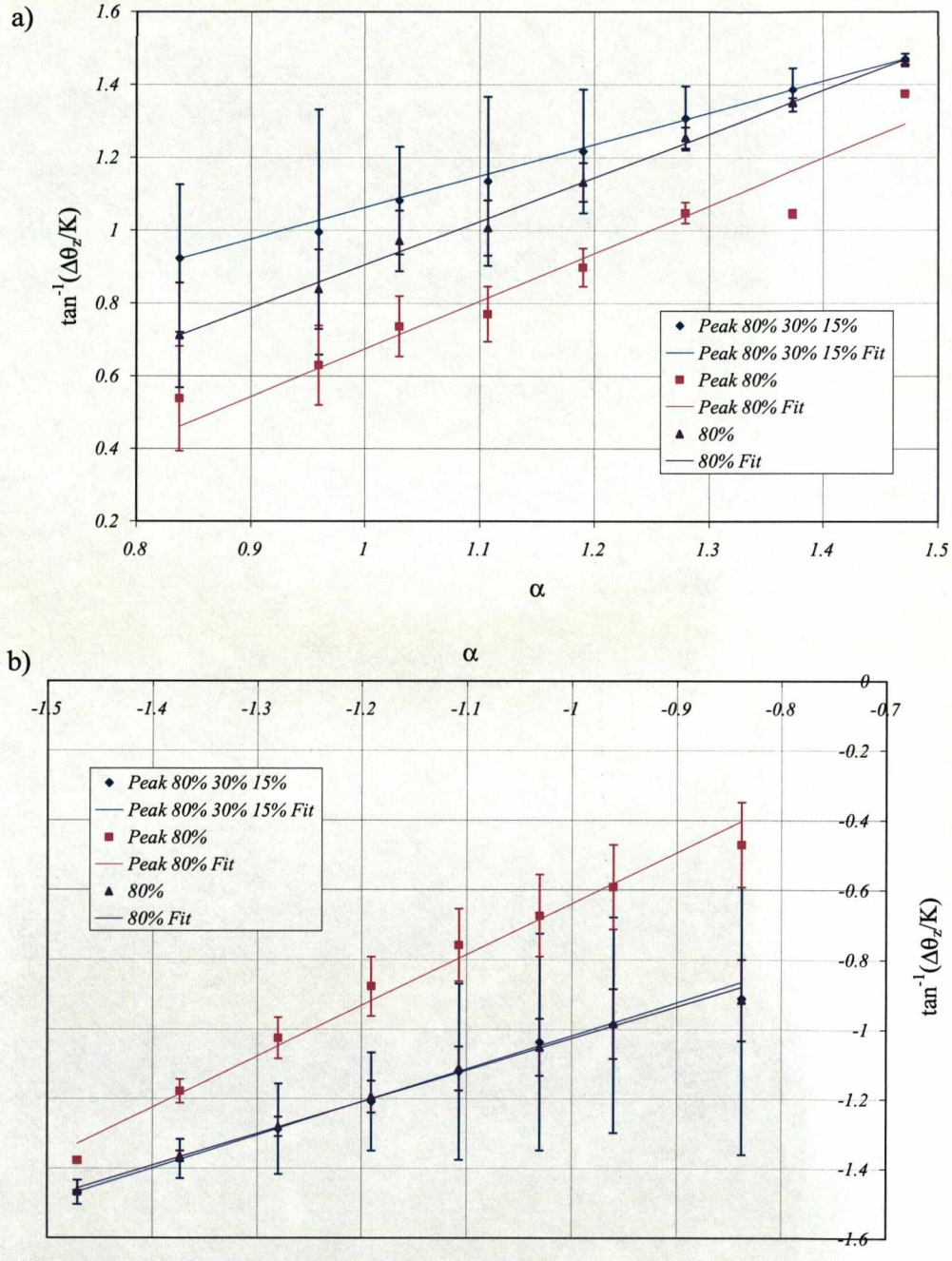

Figure 5-30: Plots of tan-1(Δθz/K) against α for the ±80% data. a) For positive values of α. b) For negative values of α.

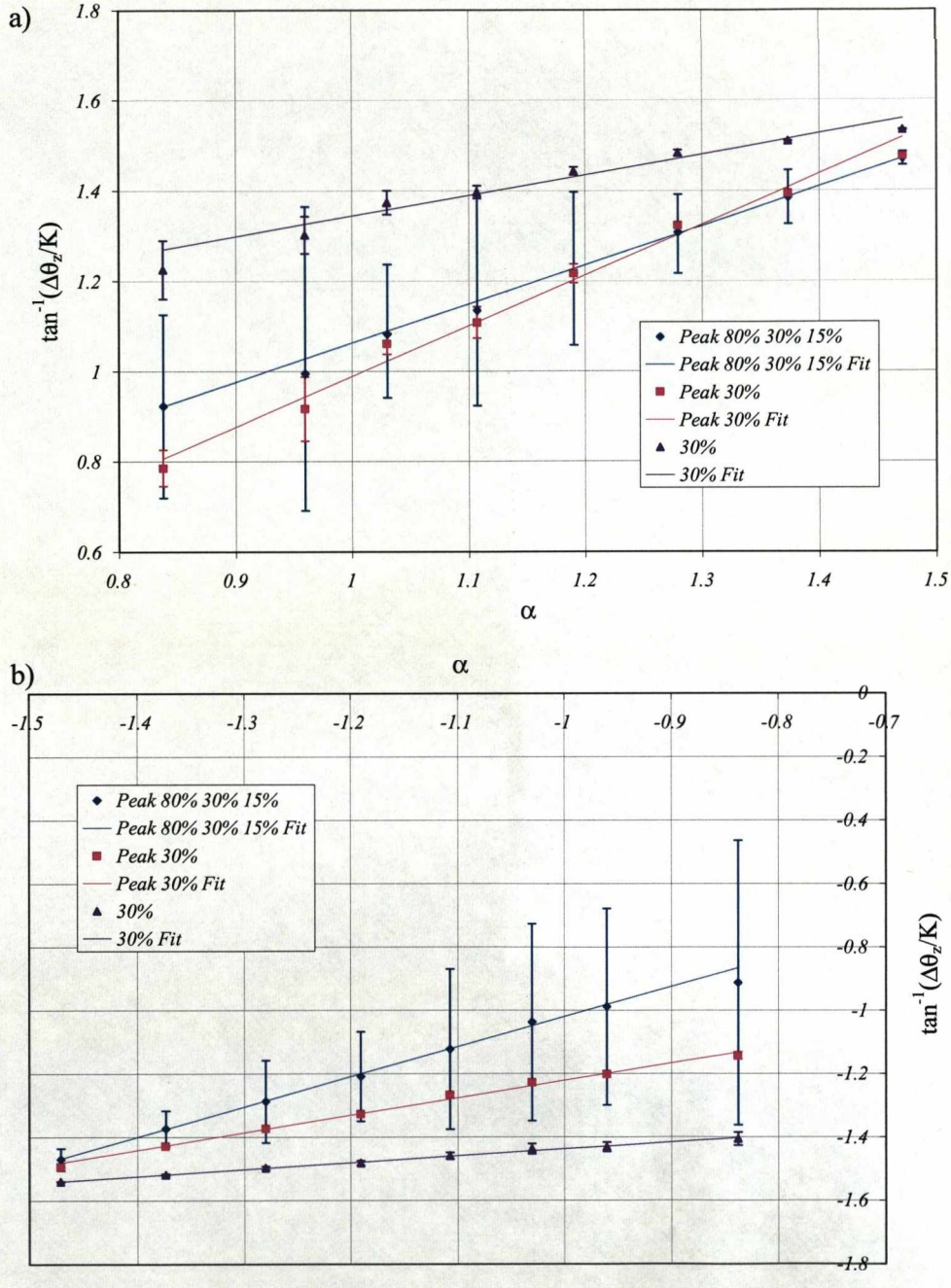

Figure 5-31: Plots of tan-1(Δθz/K) against α for the ±30% data. a) For positive values of α. b) For negative values of α.

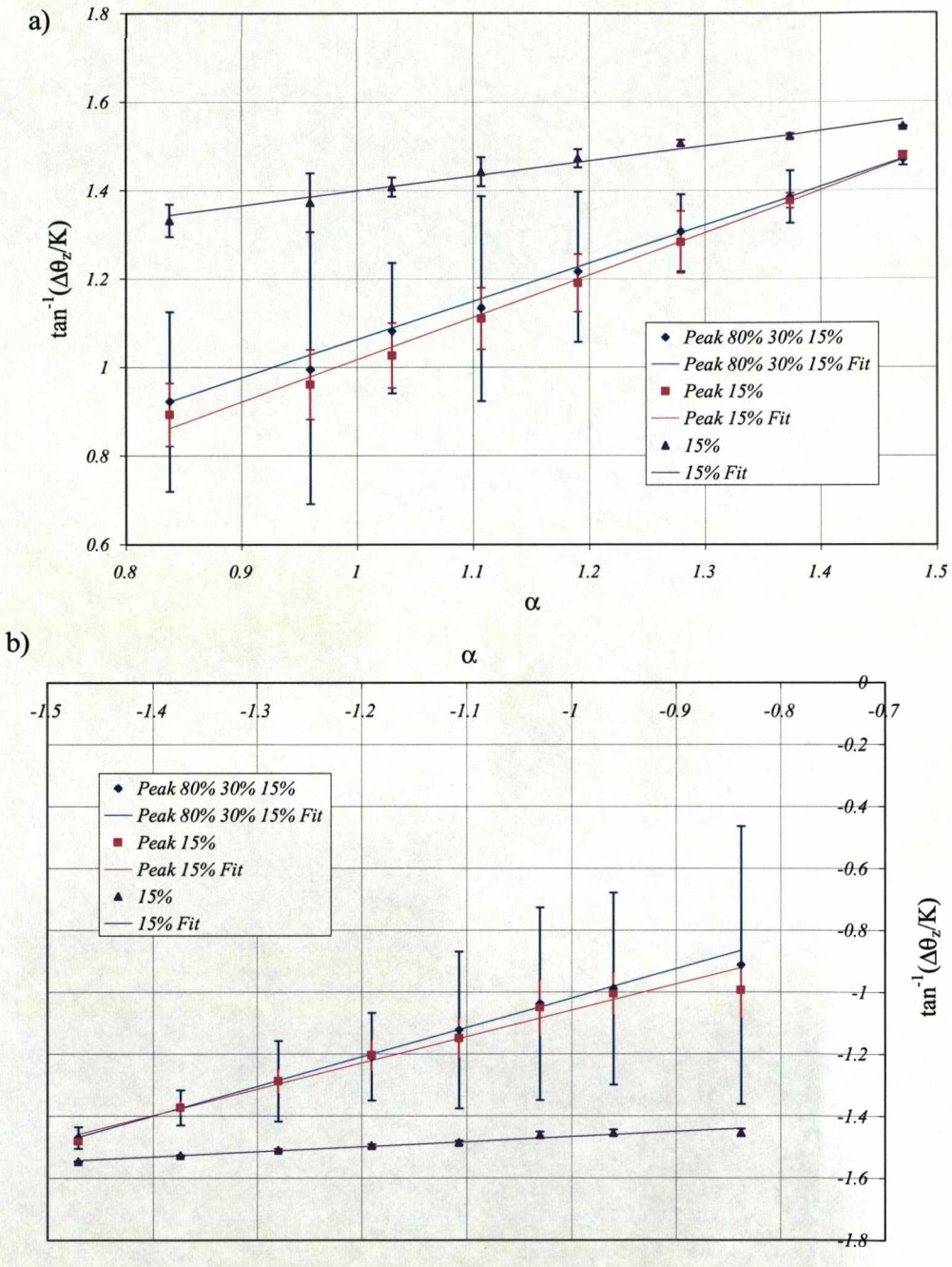

Figure 5-32: Plots of tan-1(Δθz/K) against α for the ±15% data. a) For positive values of α. b) For negative values of α.

Plots of $\tan^{-1}(\Delta\theta_z/K)$ against α were also created for the DEI results and are shown in Figure 5-33. As this Figure shows all the data presented gave straight lines for both $+\alpha$ and $-\alpha$, as was expected. The ±80% results gave values of gradient for $-\alpha$ and $+\alpha$ that were approximately the same, a finding repeated by the ±30% results. However, in a similar manner to the MIR results, none of the lines fitted to the $+\alpha$ and $-\alpha$ results had gradients equal to one, or gave y-intercepts with the same magnitude. The gradients and intercepts of the lines fitted to the DEI data could have been affected by both the background subtraction and the imaging position on the rocking curve, as was the case with the MIR data. Looking at the results shown in Figure 5-33 and Table 5-4, it is clear that there is no obvious trend showing advantages to any of the imaging positions.

The purpose of creating the plots of $\tan^{-1}(\Delta\theta_z/K)$ against α, was to find a value for δ, the angle at which the phantom was positioned to the beam. However, since the results were affected by a variety of factors and it is therefore only possible to give an approximate range in which δ was based on the result presented $0.01<\delta(\text{rad})<1$.

		Gradient	$\sigma_{Gradient}$	y -intercept	$\sigma_{intercept}$
80%	+α	*0.86*	*0.13*	*0.23*	*0.16*
	-α	*0.85*	*0.15*	*-0.24*	*0.18*
30%	+α	*0.52*	*0.17*	*0.72*	*0.24*
	-α	*0.59*	*0.83*	*-0.66*	*0.10*
15%	+α	*0.82*	*0.08*	*0.26*	*0.09*
	-α	*0.56*	*0.05*	*-0.68*	*0.06*

Table 5-4: Comparison of the fits for the DEI plots of $\tan^{-1}(\Delta\theta_z/K)$ against α.

a)

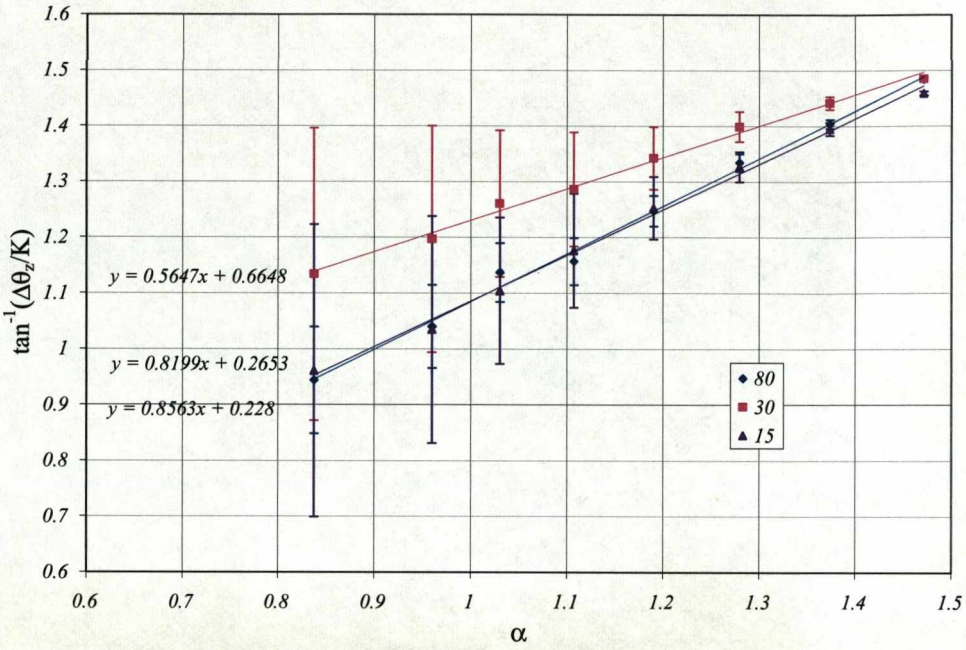

b)

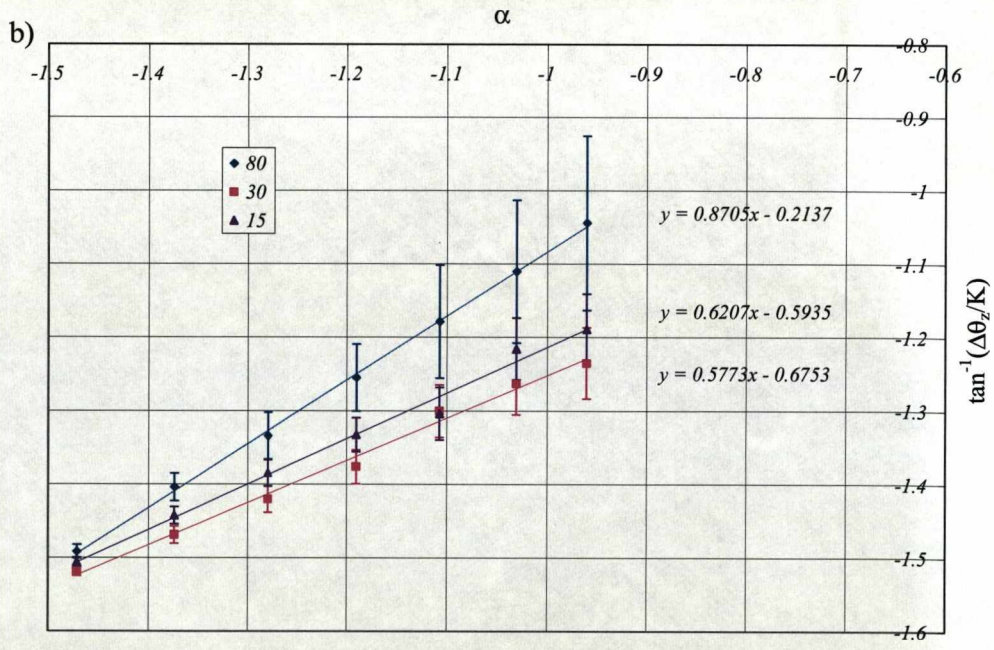

Figure 5-33: Plots of $\tan^{-1}(\Delta\theta_z/K)$ against α for the DEI images. a) For positive values of α. b) For negative values of α.

5.3.2.4 SNR_{AREA} analysis

In addition to calculating $\Delta\theta_z$, the SNR_{AREA} values of the faces of the phantoms were also found. The results for the DEI images are shown in Figure 5-34. It would be expected that either side of $\tan\alpha=0$, the SNR_{AREA} results would give straight lines, for negative values of $\tan\alpha$ the line would have a negative gradient and intercept the y-axis at zero. For the positive values of $\tan\alpha$ the line would have a positive gradient and, again, cross the y-axis at zero. As, can be seen in Figure 5-34, the results from all images give approximately straight lines and all show similar results. With the exception of the result for $\tan\alpha=+10$ for the ±15% image, the maximum SNR values are ~35. For the positive values of $\tan\alpha$, the results show a trend to intercept the y-axis at a value greater than zero, and the results for $-\tan\alpha$ would intercept the y-axis at a value less than zero. This lack of symmetry around $\tan\alpha=0$ is due to the phantom being positioned at a slightly upwards facing angle, resulting in the $+\tan\alpha$ values being larger than they should be, therefore leading to higher than expected values and the $-\tan\alpha$ values being lower than expected.

The same analysis was carried out for the MIR images. Figure 5-35 a) shows the results for the Peak ±80% ±30% ±15%, the peak ±30% and the ±30% images in Figure 5-35 b). As with the DEI results these results show the same lack of symmetry around $\tan\alpha=0$ due to the phantom being positioned at an angle. These results, which are representative of the other MIR images, do not show linear results for either side of $\tan\alpha=0$. Instead, as the magnitude of $\tan\alpha$ reaches larger values there is less change in SNR. Looking at Figure 5-35 a) which shows comparisons for varying the number of positions on the rocking curve, there is no obvious trend to show that increasing the number of imaging positions on the rocking curve would affect the SNR ratio values. The results presented in Figure 5-35 b) compare the imaging position on the rocking curve; they do not show any clear trend to show that one imaging position on the rocking curve is better than another.

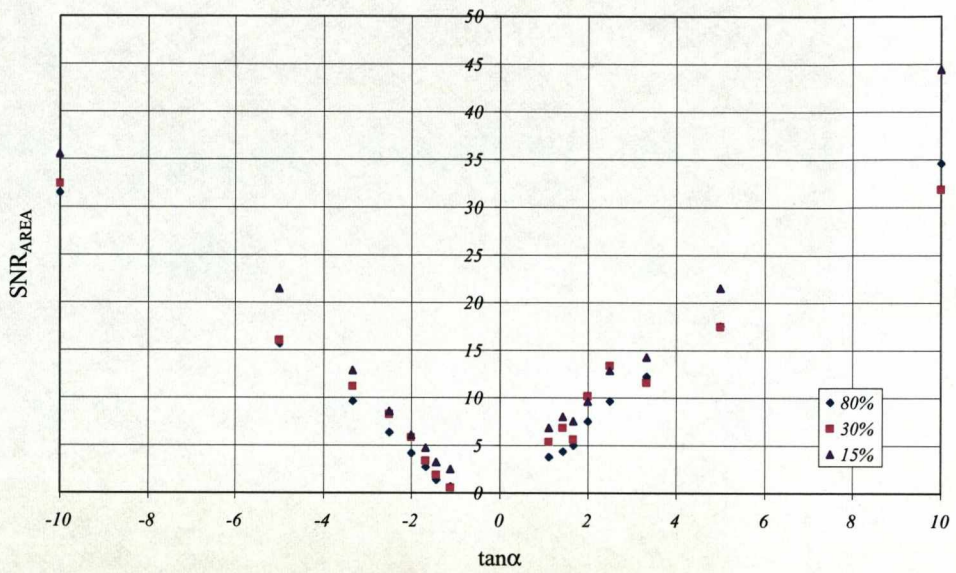

Figure 5-34: A comparison of the SNR_{AREA} values of the faces of the phantom for the different imaging positions on the rocking curve.

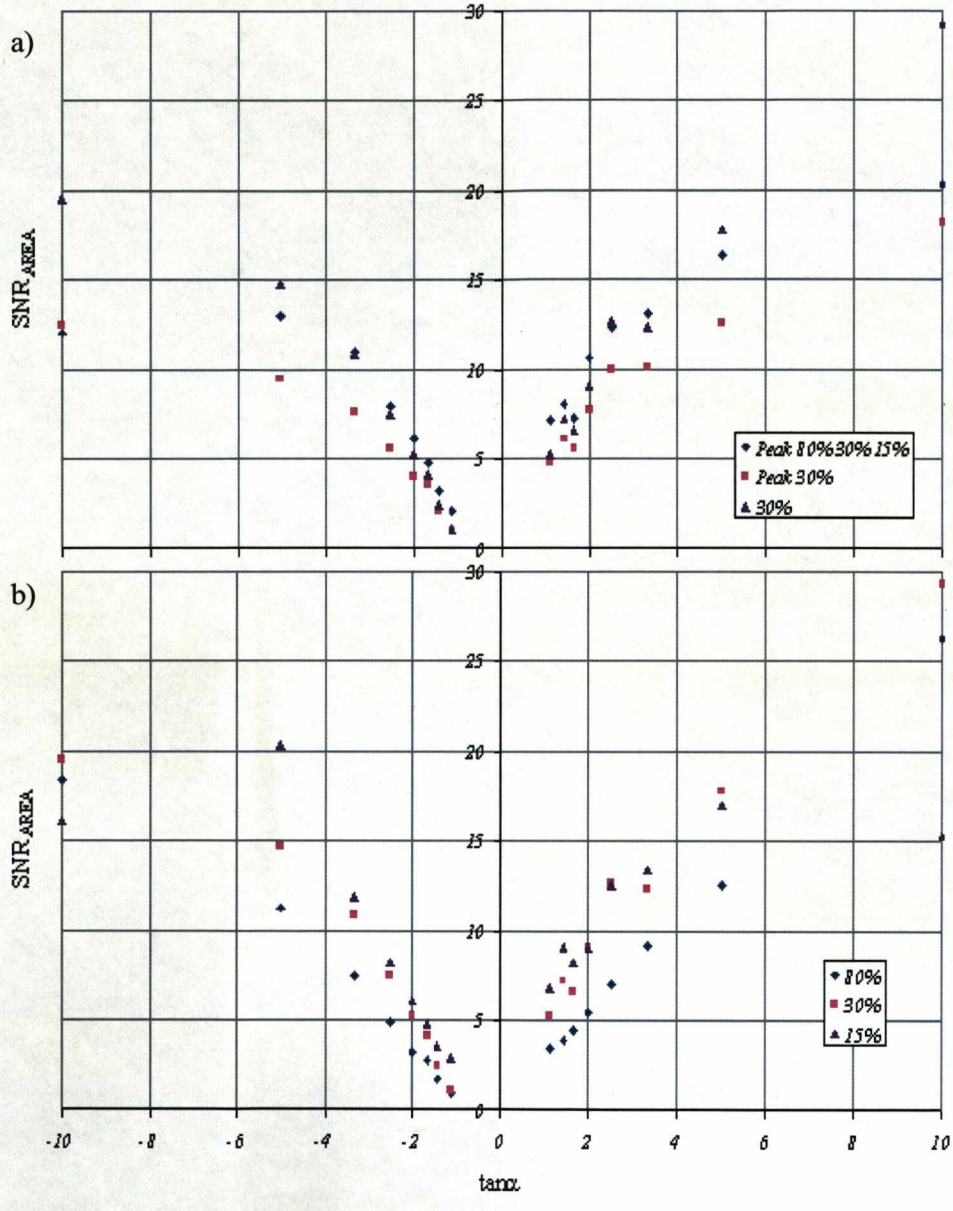

Figure 5-35: Plot of SNR against tanα. a) For data from the Peak ±80% ±30% ±15%, the Peak ±30% and the ±30% MIR images, comparing the effect of the number of imaging positions on the rocking curve. b) For data from the ±80%, ±30% and ±15% MIR images, comparing the effect of the imaging position on the rocking curve.

A comparison of the MIR and DEI analysis is shown in Figure 5-36. As can be seen for small magnitudes of tanα the results for DEI and MIR are very similar. However, as the magnitude of tanα increases the difference between the two sets of results increases and the DEI results are consistently higher than the MIR results.

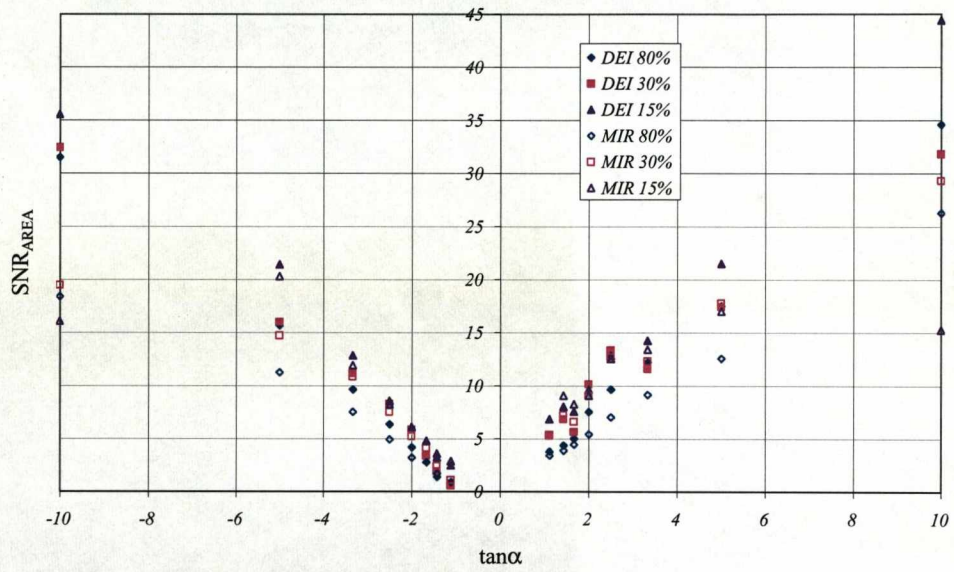

Figure 5-36: Plot of SNR against tanα comparing the DEI and MIR results.

5.3.2.5 Experiment Summary

In this experiment the refraction phantom was imaged for the first time. By calculating the values of $\Delta\theta_z$ for the different faces of the phantom it was possible to compare the experimental results with theory, which showed that the phantom had been positioned in the beam at a slight angle, highlighting the sensitivity of the system. In addition SNR_{AREA} analysis was also carried out, as with the $\Delta\theta_z$ values, these results were also affected by the misalignment of the phantom. They did,

however, reveal a slight difference between the MIR and DEI techniques at large magnitudes of tanα.

5.3.2 The Daresbury experiment

The phantom was imaged with the analyser crystal tuned to the ±50% positions on the rocking curve and DEI analysis was carried out. The resulting images are shown in Figure 5-37. These images show that the DEI method did not separate out the refraction and apparent absorption contrast completely.

Both images also show large differences in contrast in their backgrounds. Looking first at the apparent absorption images this lack of separation can be seen on the faces where tanα=±10, where the edges are brighter than the background. If only apparent absorption contrast were present this would imply that the edges of the phantom were less attenuating than the surrounding air. In the refraction image, the inadequate separation of the sources of contrast is demonstrated by the contrast gradients across the different faces, shown most prominently in the tanα=±10 faces. The values of $\Delta\theta_z$ were also found for each of the faces in the refraction image, and are plotted against tanα in Figure 5-38 which, when compared with the results in the previous section, gives very different results and also shows a lot of spread in the values.

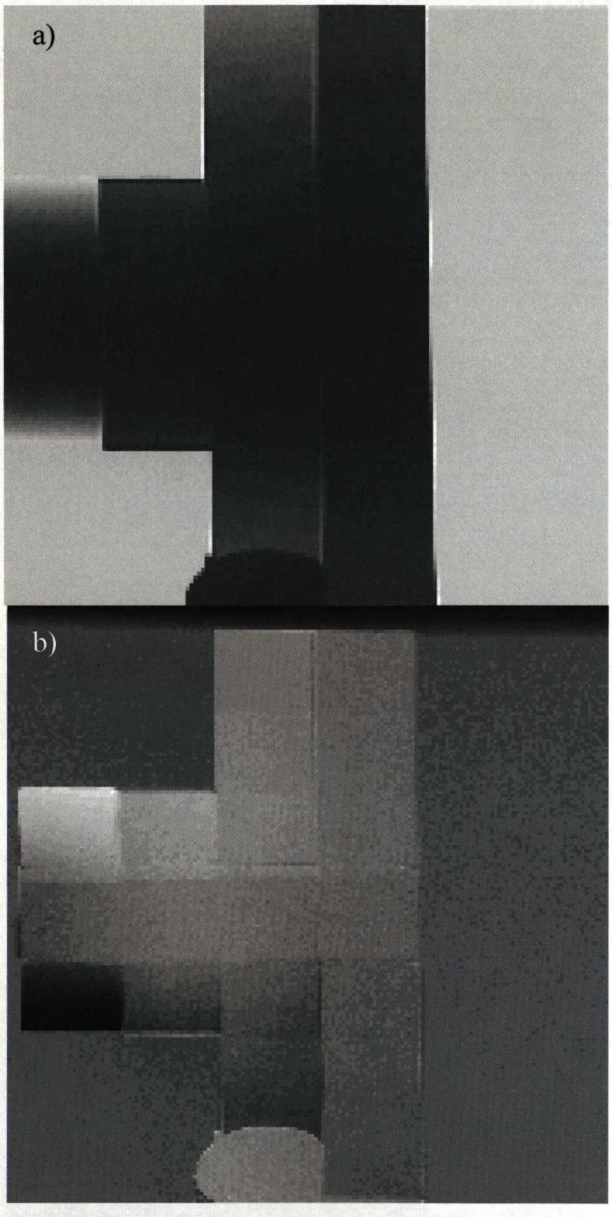

Figure 5-37: The DEI images of the refraction phantom. a) The apparent absorption image. b) The Refraction image.

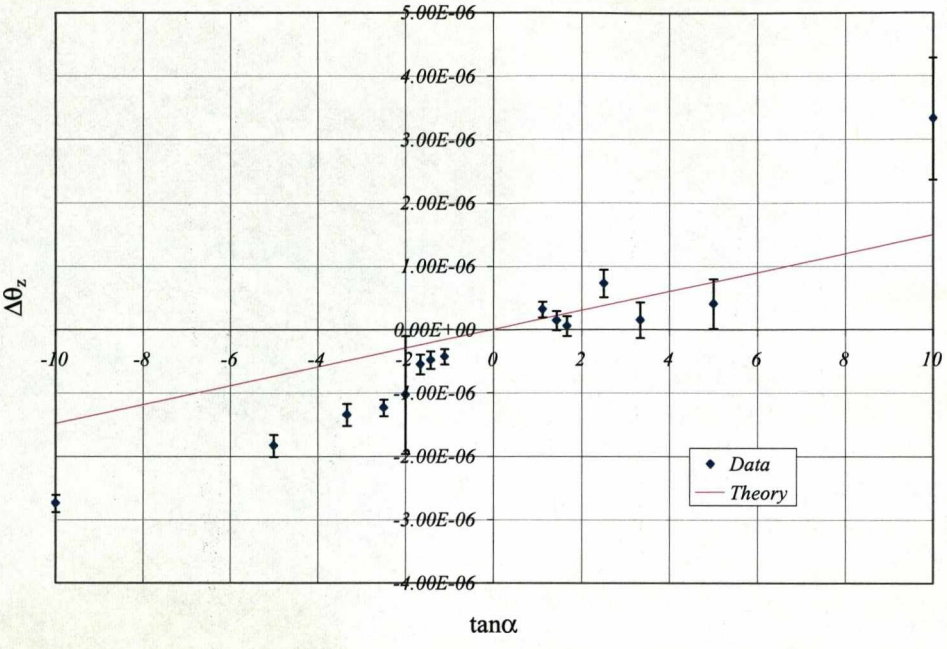

Figure 5-38: Plot of $\Delta\theta_z$ against tanα for the refraction image.

Refraction and apparent absorption images of the phantom, which were created with no flat and dark correction being carried out, are shown in Figure 5-39. As can be seen, despite the presence of some artefacts from the detector, there is an apparent improvement in the separation of the two sources of contrast. This is particularly noticeable when looking at the refraction image, which, unlike the previous refraction image (Figure 5-39 b)), clearly shows opposite contrast on either side of the phantom, as well as each of the faces showing less of a contrast gradient.

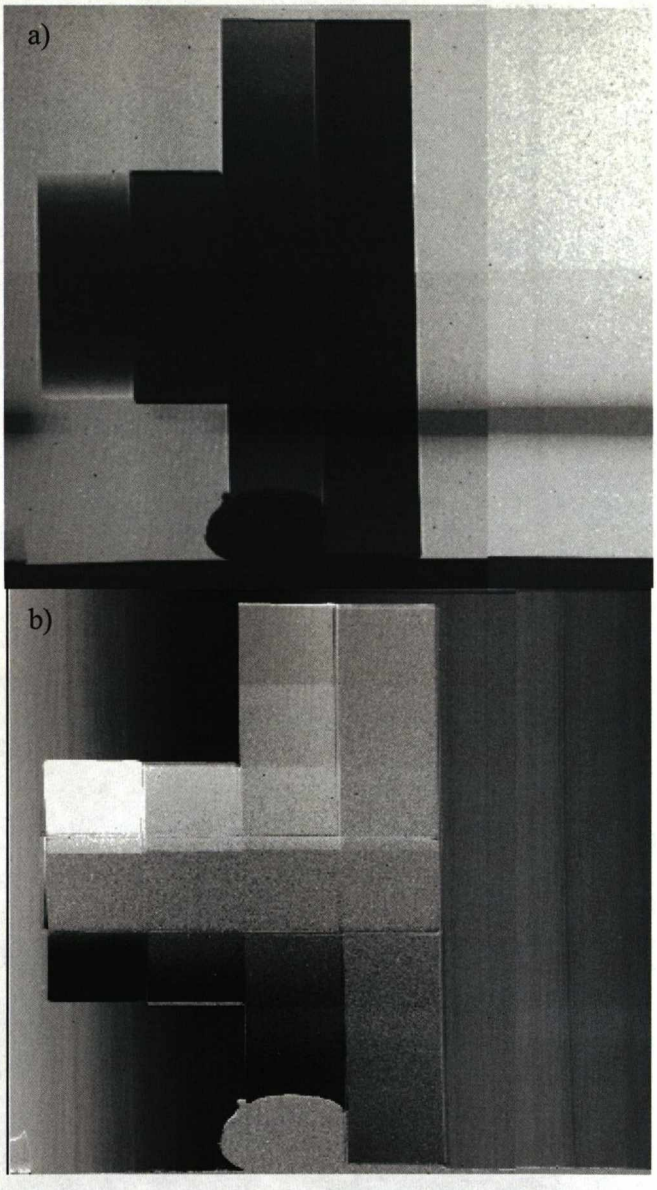

Figure 5-39: The DEI images of the phantom, when no flat and dark subtraction was carried out. a) The apparent absorption image. b) The refraction image.

This improvement of the images when no flat and dark subtraction was carried out indicates that the problems are somehow linked to the flat and dark subtraction. To investigate this problem further, profiles of the images were taken where, in this case, an image profile is a plot of the intensity, averaged over the pixels in the y-direction of the image, against the horizontal pixel number.

Figure 5-40 shows such profiles for the dark corrected ±50% images and flat fields. The first thing that is noticeable is the variation in intensity in the +50% flat field compared with its -50% counterpart. This difference is caused by the analyser crystal having a tilt on it, causing it to diffract the beam with different intensities.

These profiles also show that in the background regions of both images ($20 \leq$pixels ≤ 35 and $1350 \leq$pixels ≤ 2090) the intensity levels are lower than the same regions in the flat field, when they should be the same. This means that there was a discrepancy in the collection of the flat fields and the images. In the phantom region of the images ($135 \leq$ pixels ≤ 350) the flat field profile is followed, however, this is also affected by the thickness of the phantom, as can be seen by comparing the profiles of the region $135 \leq$ pixels ≤ 235, a thinner part of the phantom, with the region $735 \leq$ pixels ≤ 350, a thicker part of the phantom. Figure 5-41 shows a comparison of the flat and dark corrected images. As can be seen obvious gradients have been introduced in the region $735 \leq$pixels ≤ 350. This is due to the discrepancies between the flat field and image profiles caused by the attenuation of the beam. It is worth noting that had there been no tilt on the analyser crystal, the variations in the intensity across the images would not have been so large and this effect would not be as apparent.

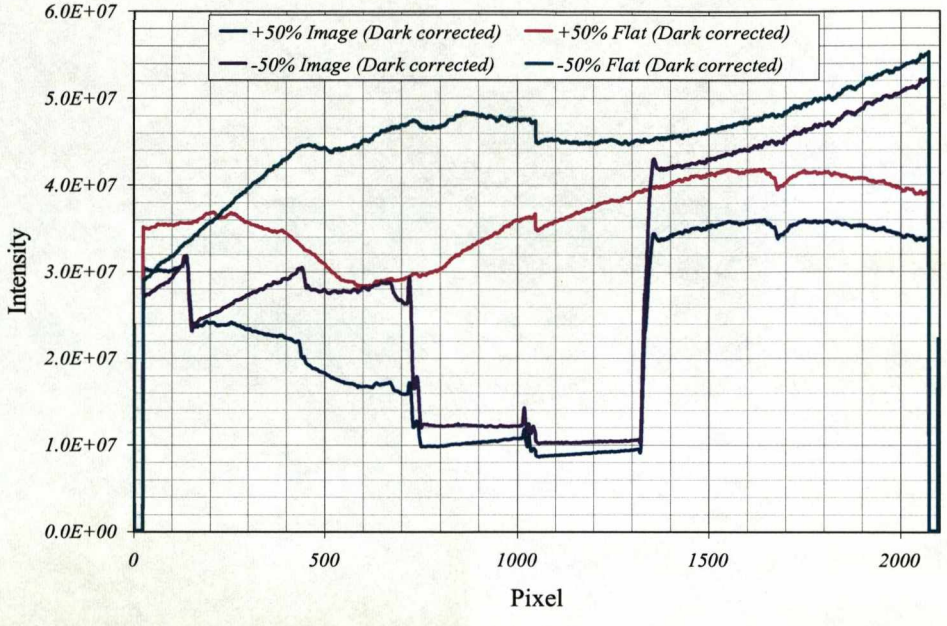

Figure 5-40: The profiles of the dark corrected ±50% images and flats.

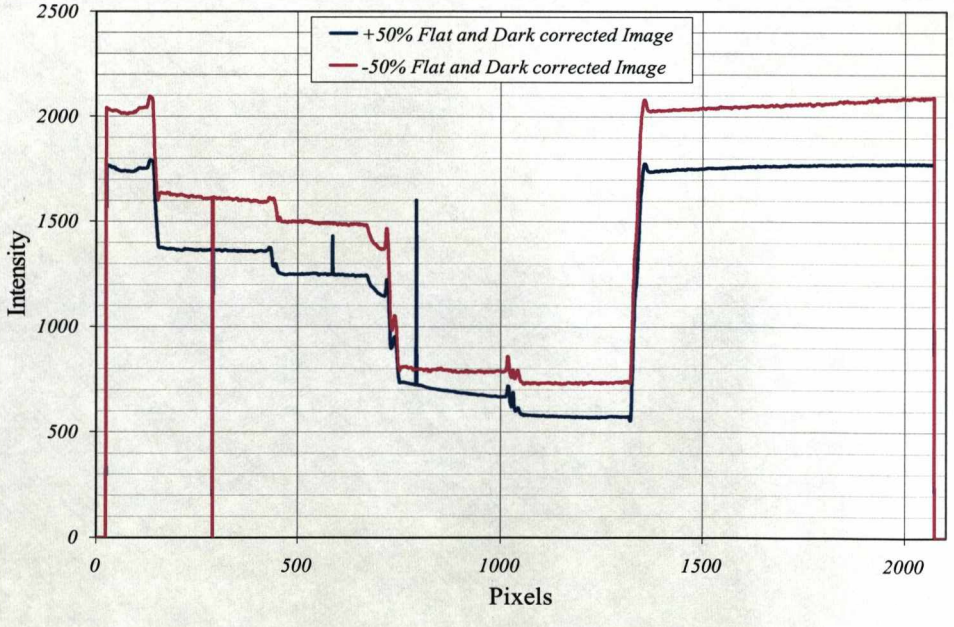

Figure 5-41: The profiles of the flat and dark corrected ±50% images.

Unfortunately the results from this experiment do not provide any more information about the refraction phantom. They do, however, demonstrate the extreme effect that having a tilt on the analyser crystal can have on the ABI images.

The refraction phantom was imaged in two experiments, and although some information was gained about the phantom and the ABI techniques, the predominant outcome has been to see the effects of inaccuracies in the ABI system itself.

5.4 **Colloid samples**

As described in Section 3.3.2.4, the aim of imaging colloid samples was to investigate their potential for use in a phantom designed to characterise the scattering contrast. As part of this work, two preliminary experiments were carried out, one at the ESRF and the other at Daresbury SRS. The results from both experiments are presented in the subsequent sections.

5.4.2 The ESRF experiment

The Ludox sample, described in Section 3.3.2.4 was imaged on ID17 at the ESRF using a beam energy of 40 keV. The sample was imaged at the peak, ±80%, ±50% and ±30% positions on the rocking curve and MIR and DEI analysis was carried out.

The ±50% MIR images are shown in Figure 5-42. The USAXS image, Figure 5-42 a), shows scattering contrast from the meniscus of the solution with no obvious scatter properties in the bulk of the sample. The same is true for the refraction image shown in Figure 5-42 b). The absorption image in Figure 5-42 c), shows the attenuation of beam through the sample.

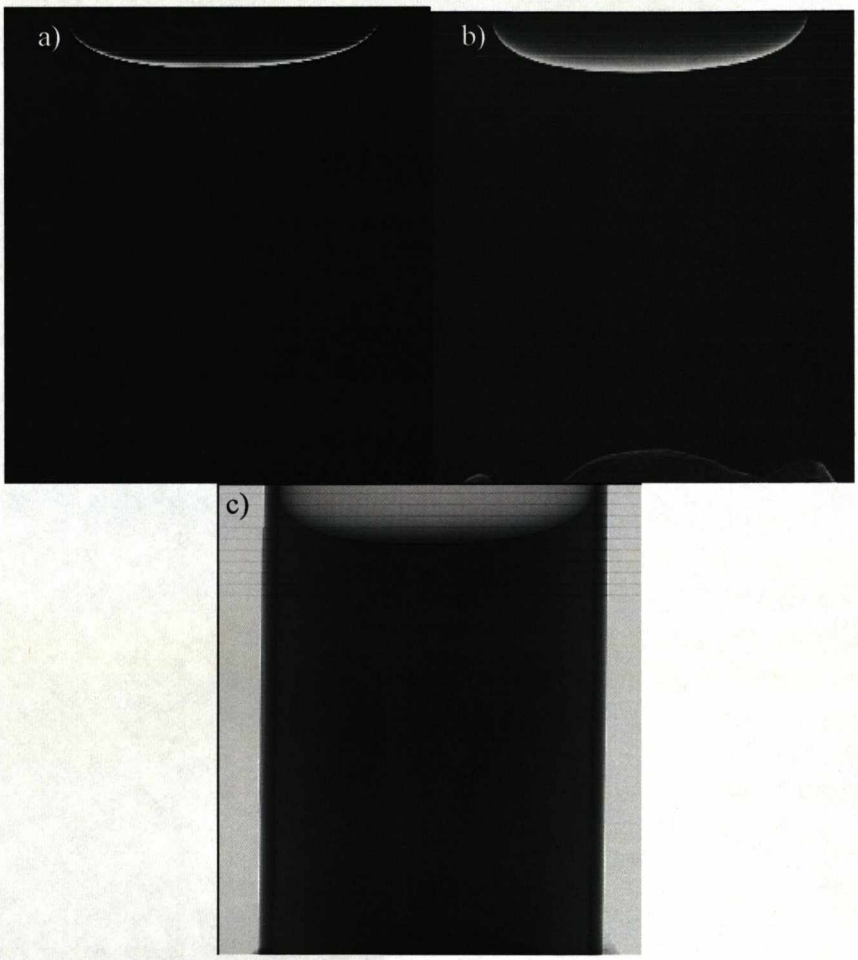

Figure 5-42: The ±50% MIR images of the Ludox sample. a) The USAXS image. b) The refraction image. c) The absorption image.

As with the images from the two phantoms, described in Sections 5.2 and 5.3, SNR_{AREA} analysis was also carried out on this sample. The results comparing the SNR of the sample area for the USAXS images are shown in Figure 5-43. The ±50% position gives the second largest value, followed by the ±80% and ±30% positions. When the additional peak image is used the SNR_{AREA} decreases, because at the peak of the rocking curve the spread caused by the USAXS is very small. The peak ±80% ±50% ±30% image however gave the largest SNR showing that

the as the number of component images increases the SNR_{AREA} increases, although it is influenced by the position on the rocking curve.

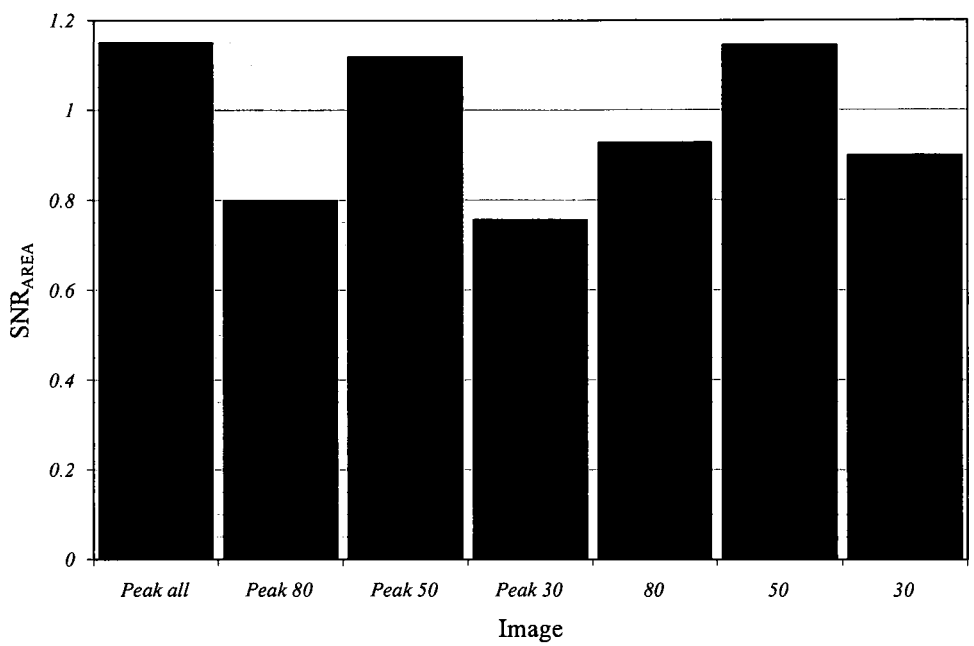

Figure 5-43: The SNR_{AREA} values of the different MIR USAXS images.

Overall the values of SNR_{AREA} for this sample are low, with the highest value at ~1.15. A comparison of the SNR_{AREA} given by the sources of contrast is shown in Figure 5-44, it can clearly be seen that the absorption image gives the largest SNR values, almost ten times greater than the USAXS values. However, looking back at the results from the absorption phantom experiment, for approximately the same thickness of Perspex, the SNR value for the USAXS image is ~0.8, and ~40 for the absorption image. Nevertheless, this is not conclusive in terms of its suitability for use as a scatter phantom.

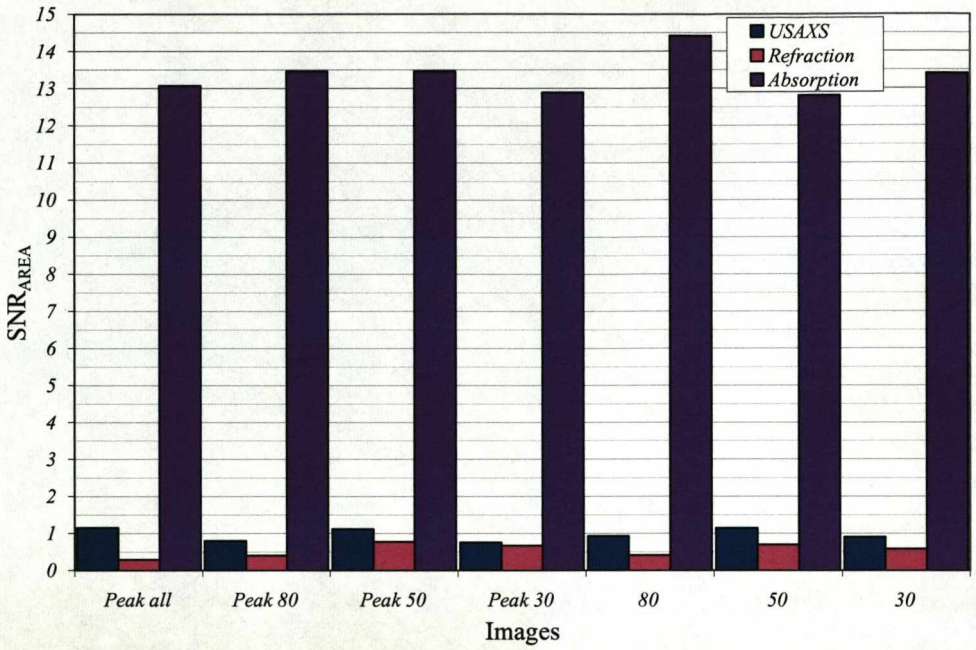

Figure 5-44: A comparison of the SNR values of the different images for the different MIR image sets.

5.4.2 The Daresbury experiments

In these experiments samples of colloidal polystyrene were imaged with water comparisons using a beam energy of 20 keV.

5.4.2.1 900nm polystyrene colloid and water experiment

In this experiment a sample of colloidal polystyrene with a nominal diameter of 900nm, described in Section 3.3.2.4, and a sample of distilled water, were imaged (see Section 4.2.2.3). The samples were imaged simultaneously, with the analyser crystal tuned to eleven positions on the rocking curve. Two MIR image sets were created, one using the images from all eleven positions on the rocking curve (MIR-11) and the other using every other position, six in total (MIR-6).

The two MIR image sets are shown in Figure 5-45 and Figure 5-46. In all images the colloidal sample is on the left hand side and water sample on the right hand side. Looking first at the USAXS image (Figure 5-45 a) and Figure 5-46 a)), high

regions of contrast can be seen in the menisci of the samples. Contrast can also be seen in the bulk of the colloid sample, and to a lesser extent in the water sample. The refraction images, shown in Figure 5-45 b) and Figure 5-46 b), clearly show contrast from the meniscus of the sample. The absorption images (Figure 5-45 c) and Figure 5-46 c)), show contrast in the bulk of the sample, where the beam has been attenuated. The sample containers can also be seen.

Figure 5-45: The MIR-11 images. a) The USAXS image. b) The refraction image. c) The absorption image.

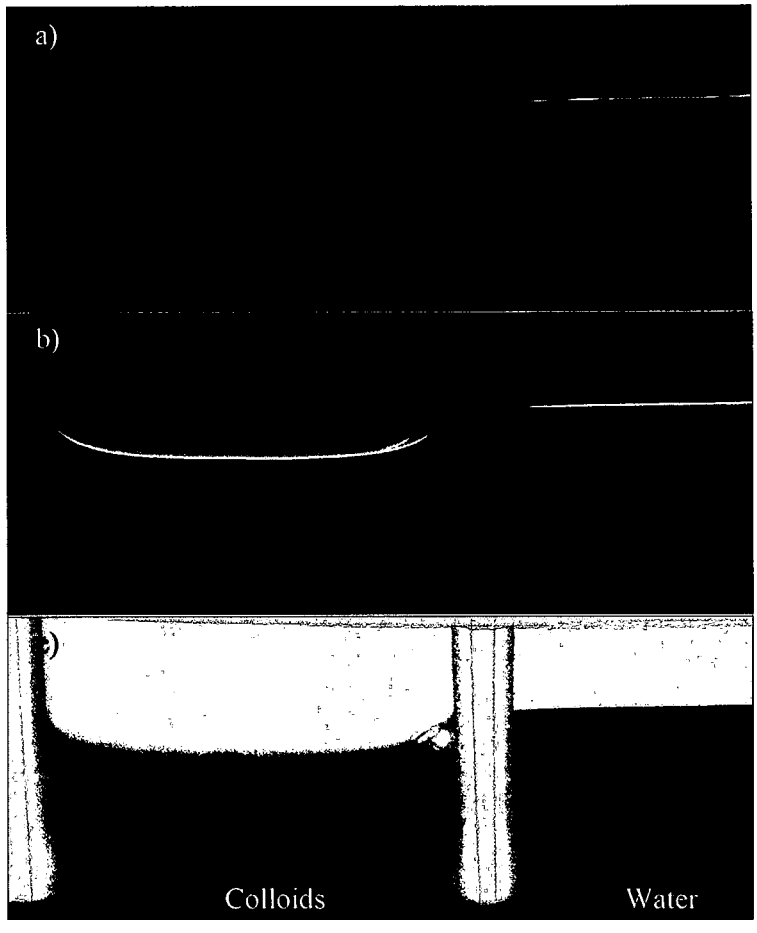

Figure 5-46: The MIR-6 images. a) The USAXS image. b) The refraction image. c) The absorption image.

As with the previous sample, SNR_{AREA} analysis of the sample area was carried out. However, as can be seen in Figure 5-45 and Figure 5-46, the water sample was not fully in the beam. It was therefore necessary to measure the SNR_{AREA} of a small area from what would be the centre of each sample, this is shown by the shaded areas in Figure 5-47.

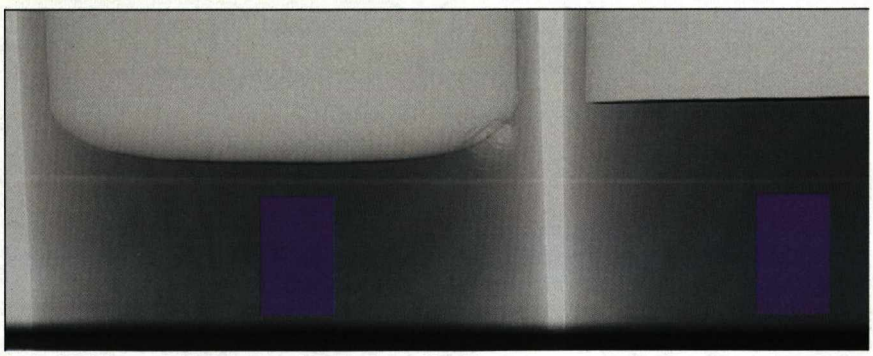

Figure 5-47: An image of the colloidal and water samples, the purple shaded areas represent the areas over which the SNR values were found.

The results of the SNR_{AREA} analysis of the USAXS images are shown in Figure 5-48. It can clearly be seen that the colloidal sample gives greater scattering contrast than the water sample. It can also be seen that with an increase in the number of positions both the colloidal, and the water samples SNR_{AREA} increase, as would have been expected, although the increase in the water samples SNR_{AREA} is not as dramatic as that of the colloidal sample. A comparison of the SNR_{AREA} values of the colloidal samples for the different sources of contrast can be seen in Figure 5-48 b). It is evident that the absorption images give greater SNR_{AREA} values than both the other sources of contrast, although the SNR_{AREA} values of the USAXS images are still significantly greater than those given by the refraction images.

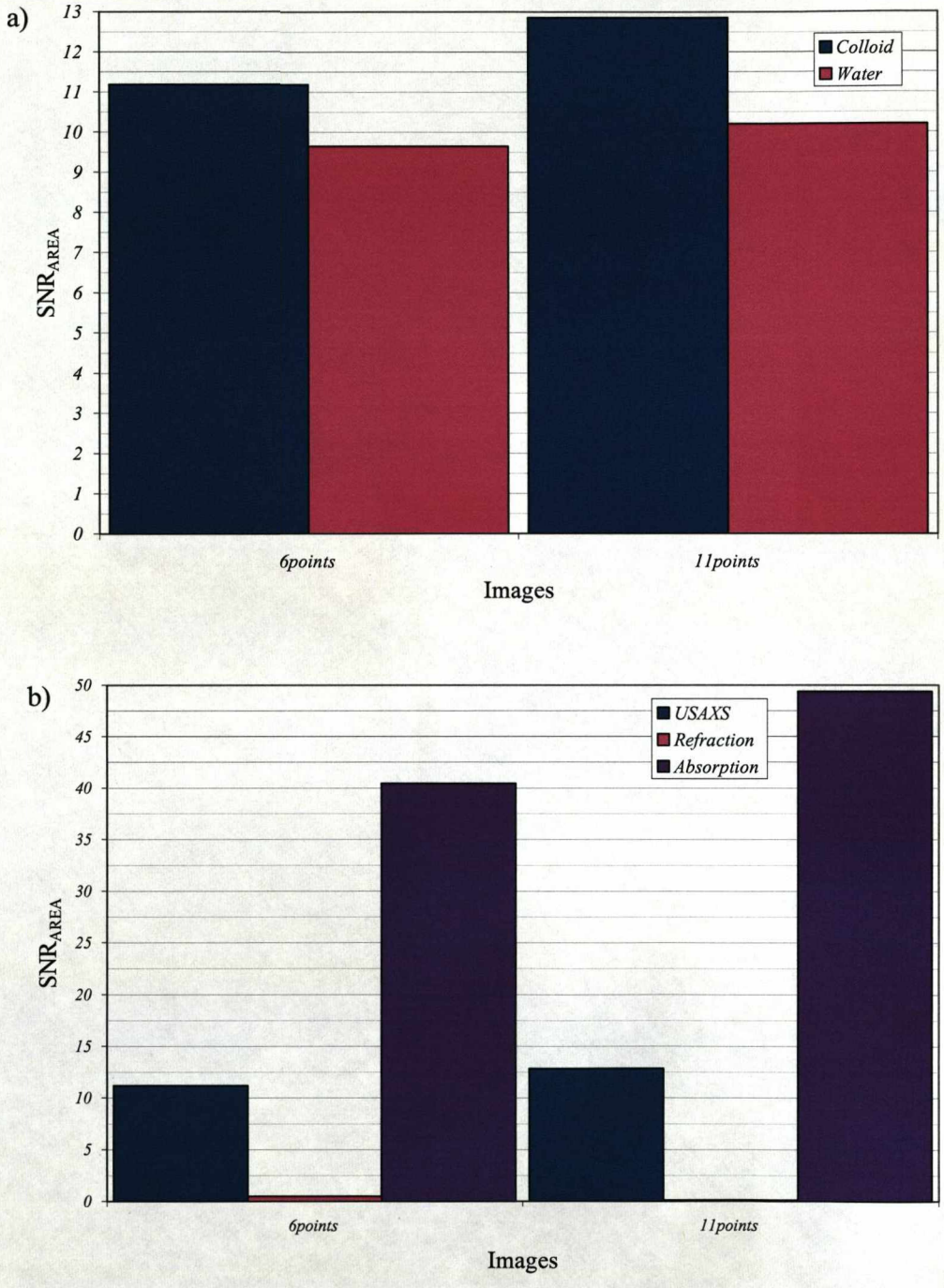

Figure 5-48: Plots showing the area SNR values for the different MIR image sets. a) A comparison of the results for the colloid and water samples from the USAXS images. b) A comparison of the SNR values of the colloidal sample in the different MIR images.

5.4.2.2 Polystyrene colloid samples with a range of sizes

In this experiment, a range of colloidal polystyrene samples were imaged simultaneously along with a water comparison. The polystyrene samples had diameters of 900nm, 500nm and 100nm and the samples were imaged at seven positions on the rocking curve. The raw images were then processed to produce an MIR image set, shown below in Figure 5-49. The 900nm colloid is the sample on the far left of the images, the 500nm sample is the second from the left, the 100nm sample is the third sample from the left hand side and the water sample is on the right hand side of the image.

Looking first at the USAXS image (Figure 5-49 a)) the most noticeable thing that can be seen is the region of the menisci of the colloidal samples. It is possible that there was a higher concentration of the colloids in these regions, therefore leading to higher contrast levels. Slightly higher levels of contrast, compared with the background, are also discernable in the bulk of the samples. However, when compared to the results from the previous colloid experiment (see Section 5.4.2.1, Figure 5-45 a)) the increase in sample contrast from the background is significantly less, for both the colloid and the water samples.

The refraction image (shown in Figure 5-49 b)), as would be expected, does not show contrast in the bulk of any of the samples. It does, however, show more contrast in the region of the menisci of the samples. As with the USAXS images this is thought to be due to a higher concentration of colloids in these regions. Finally, the absorption image in Figure 5-49 c), shows the attenuation of the beam through the bulk of the samples.

As with the previous experiments SNR_{AREA} analysis of the area in the bulk of the samples was carried out. Figure 5-50 shows a plot of the SNR_{AREA} values given for the USAXS image for each of the samples. All three of the colloid samples give a higher SNR_{AREA} value than the water sample with the 500nm sample giving the largest SNR_{AREA} of all.

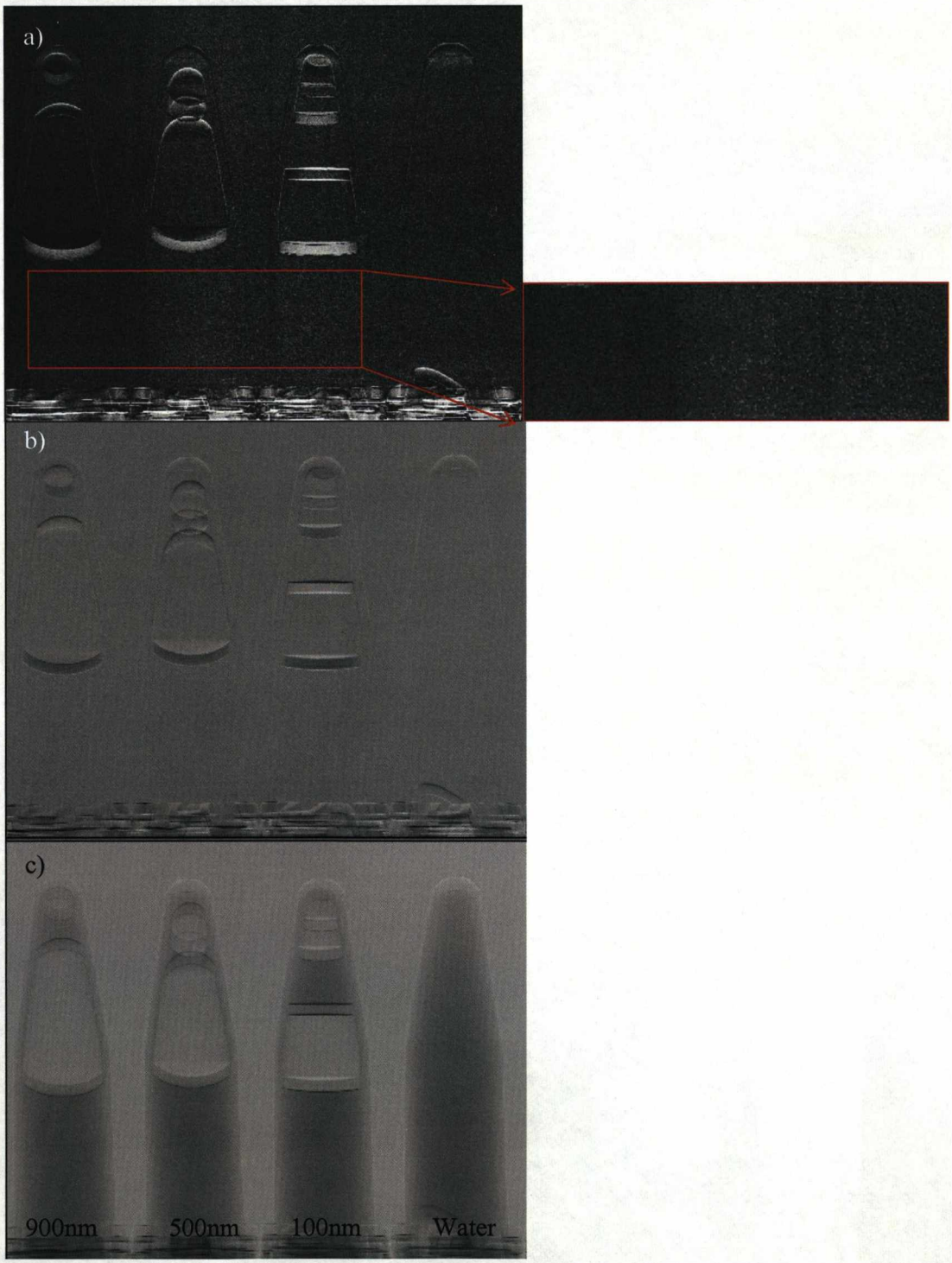

Figure 5-49: The MIR image set of the polystyrene colloids with the water comparison. The samples were contained in up turned epithelial tubes. a) The USAXS image. b) The refraction image. c) The absorption image.

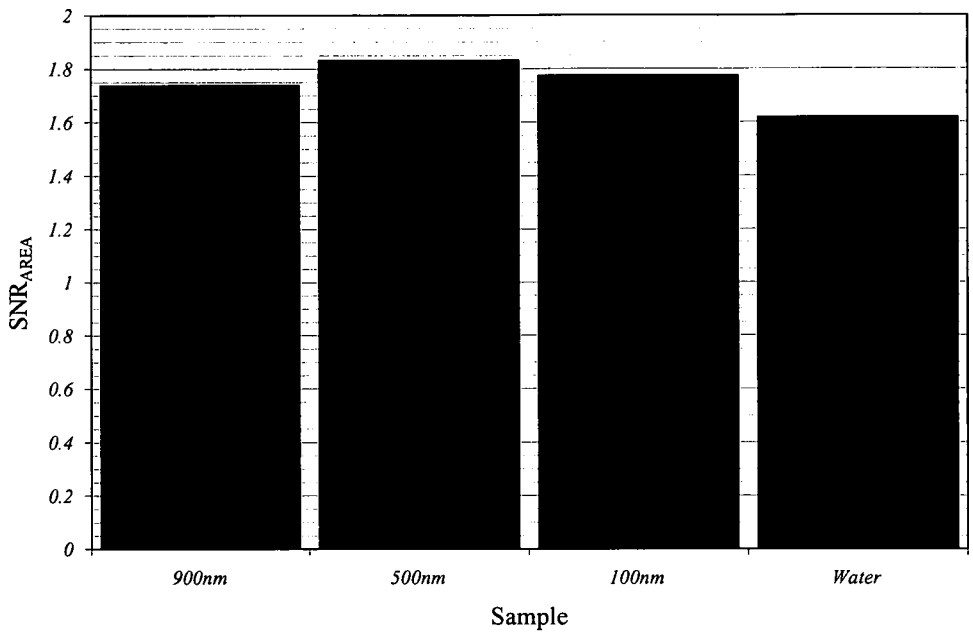

Figure 5-50: A plot of the SNR_{AREA} values given by the colloid samples with a water comparison.

The previous section considered the results from an experiment which compared the 900nm colloid sample with water. Figure 5-51, shows a comparison of the results from the previous section (where six positions on the rocking curve were used), described as Experiment 1, with the results for the 900nm and water samples from this section, described as Experiment 2. The results from Experiment 1, clearly give much larger values than those from Experiment 2. Although the same samples were imaged, there were some differences between the experiments. Firstly, in Experiment 1, the samples were imaged at six positions on the rocking curve, whereas in Experiment 2, the samples were imaged at seven positions on the rocking curve. As can be seen in the in Figure 5-48 in Section 5.4.2.1, there is an increase in SNR when the number of imaging positions on the rocking curve increases. The large change in SNR between Experiments 1 and 2 is therefore not due to difference in the number of imaging positions. The second difference between the two experiments was the average thickness over which the SNR was measured. In Experiment 1 not only was the diameter of the sample

container larger than that in Experiment 2 but the SNR was calculated only in the central and therefore thickest regions of the samples. It is this difference in sample thickness which has led to the results in Experiment 2 being much lower than those in Experiment 1, emphasising the importance of sample thickness for the scattering contrast.

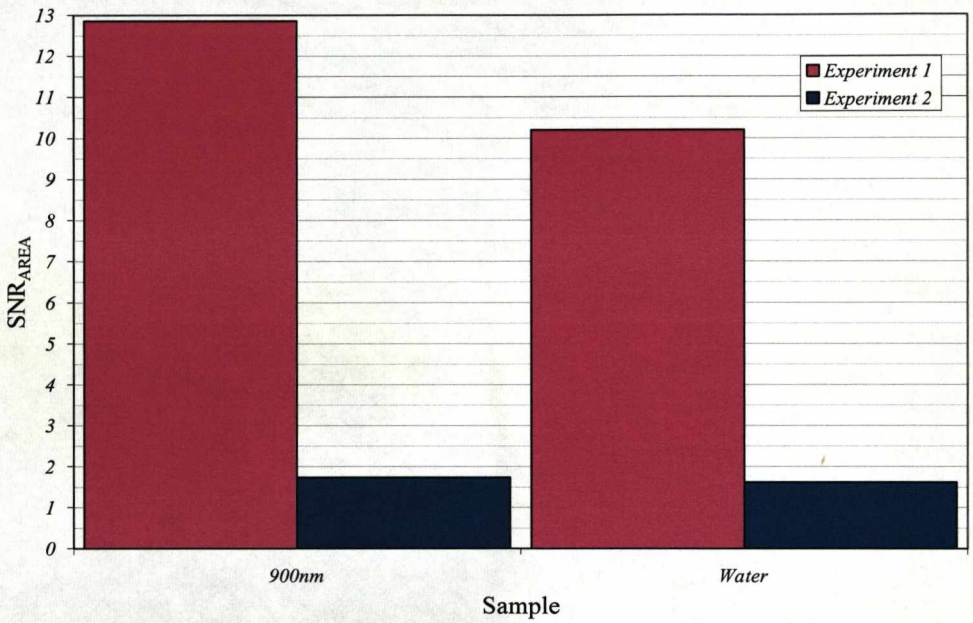

Figure 5-51: The SNR values given by the 900nm and water samples in the two colloid experiments carried out at Daresbury SRS.

In summary, three colloid experiments were carried out to look at the USAXS effects. In the first of these experiments a sample of Ludox was imaged at the ESRF and demonstrated that colloidal solutions gave contrast in USAXS images. The two experiments that were carried out at Daresbury showed that in the USAXS images, the colloidal samples consistently gave SNR values greater than that of the water samples. These experiments also showed that some sizes of colloids will give better SNR values than others, as well as demonstrating the importance of sample thickness for the SNR in the USAXS images.

CHAPTER 6

6 RESULTS FROM CARTILAGE EXPERIMENTS

As shown in Section 4.2.2 five different cartilage experiments were carried out. The ABI images and analysis are presented in the following sections.

6.1 Mice Feet

As described in Section 4.2.2.1, two sets of mice feet samples were imaged, one of which had the fur removed and the other which did not. Each set was made up of one healthy and one arthritic foot and they were imaged at 15 keV in the side view, with the de-furred set also being imaged from the top (see Figure 4-6). The DEI method was used to create refraction and apparent absorption images for all sample sets in all projections. The resulting images are shown in Figures 6-1 to 6-3.

The overall appearance of all the images is good and they are very clear. However, circular marks can be seen in the refraction images which are from the structure of the sample holder. Several droplets of the saline solution which the samples had been stored in are also visible in the images. The membrane of the sample holder also led to artefacts in the refraction images, which were caused by the compression of the sample. The problems with the sample holder were overcome in later experiments by mounting the samples in wax to hold them in position.

When looking at the structures that are visible, the apparent absorption images show the bones but no structure in the soft tissue. The refraction images, however, do show structures in the soft tissues. This is particularly clear in the heels of the samples where tendons are visible, highlighted by the red arrows in the images. In addition the skin can also be seen in the refraction images, particularly in the sole image of the de-furred samples. The structure of the bone itself can also be seen in the refraction images, but is not as visible in the apparent absorption images.

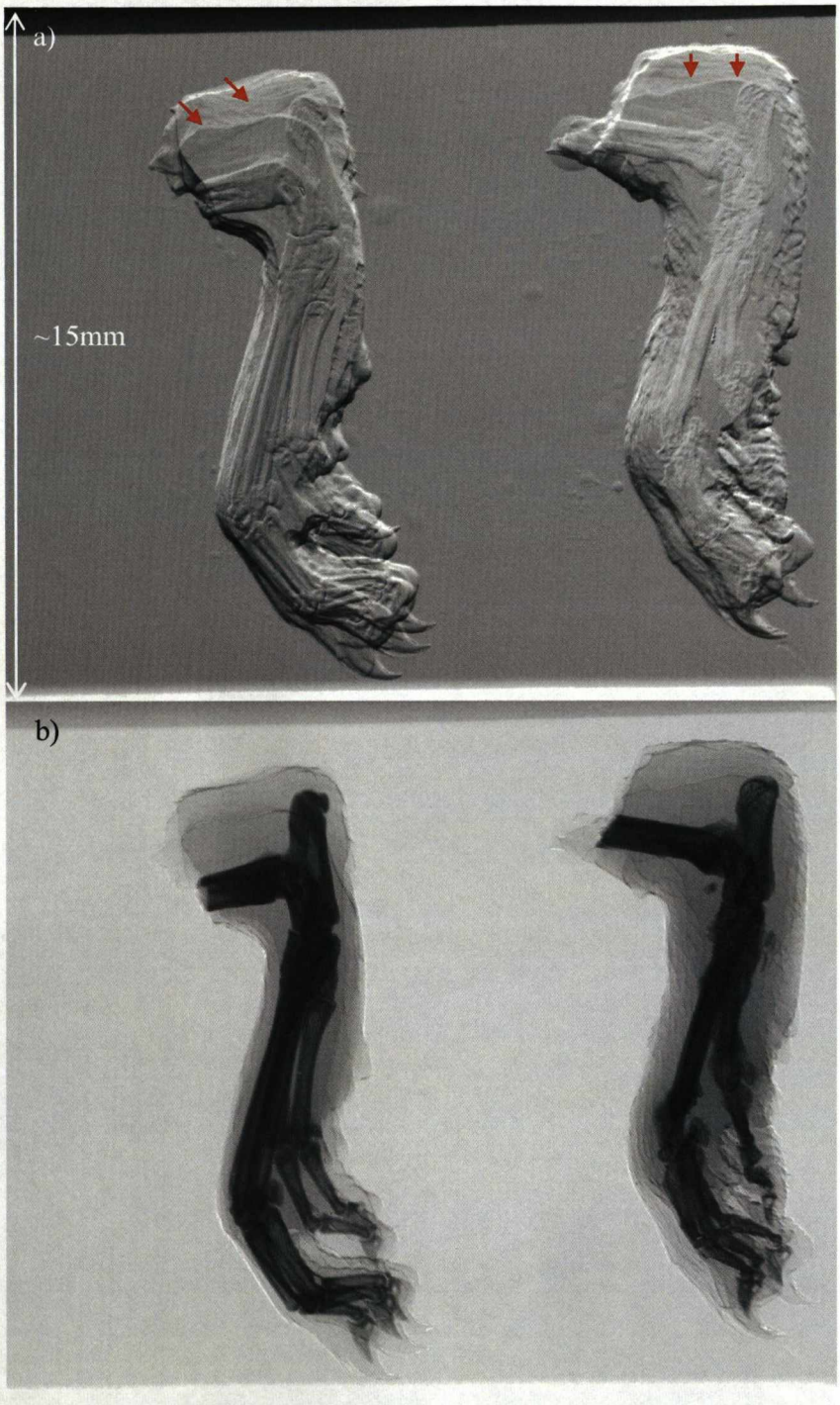

Figure 6-1: The DEI images of the furred sample in the side view, with the healthy foot on the left of the image and the arthritic foot in on the right. a) The refraction image. b) The apparent absorption image.

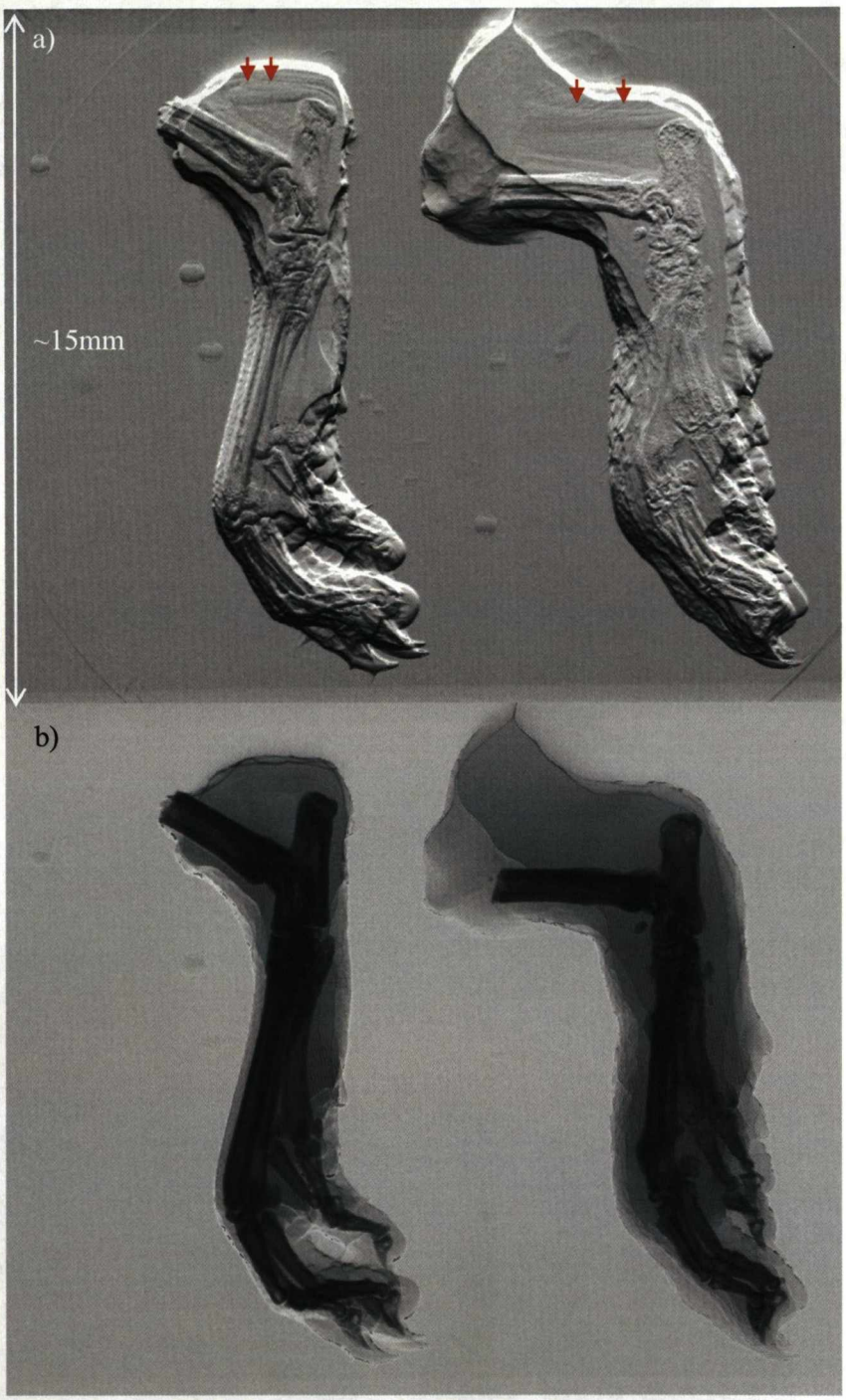

Figure 6-2: The DEI images of the de-furred sample in the side view with the healthy foot on the left of the image and the arthritic foot in on the right. a) The refraction image. b) The apparent absorption image.

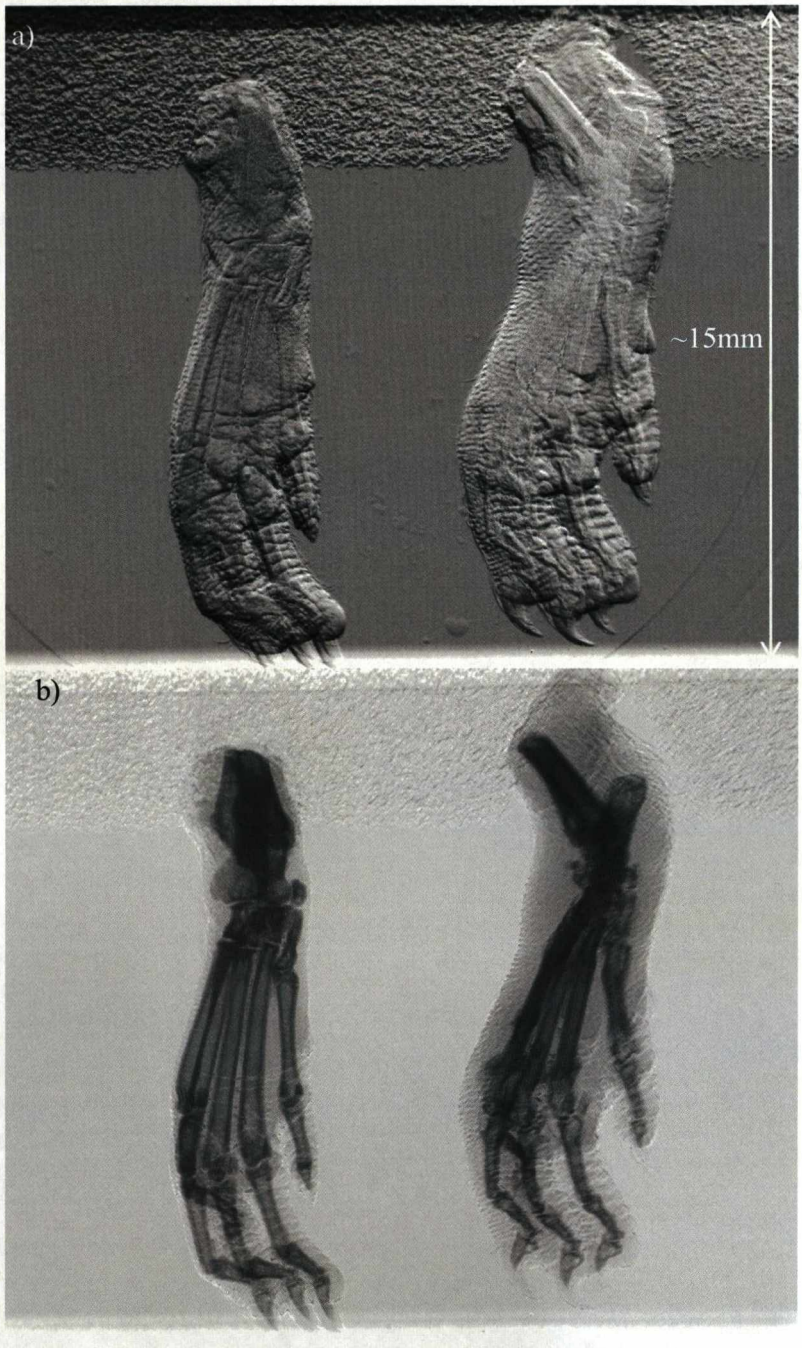

Figure 6-3: The DEI images of the de-furred sample in the top view with the healthy foot on the left of the image and the arthritic foot in on the right. a) The refraction image. b) The apparent absorption image.

Despite the clarity of the refraction images and their ability to visualise some of the soft tissue structures and the bone structure, cartilage is not visible in any of the refraction images. It is most likely that this is due to the small size of the samples as literature has shown that the cartilage can be visualised in larger samples.

When comparing the furred and de-furred images shown in Figure 6-1 and Figure 6-2 the presence of the fur does not obscure the clarity of the underlying structures.

In all of the images the differences in size between the healthy and arthritic feet is clear, this difference is due to the swelling of the arthritic feet. In addition there are visible differences in the structure of the bones in the healthy and arthritic feet which are shown clearly in the refraction images.

6.2 **Bovine Cartilage slice**

The two aims of this experiment were to image a biological sample using MIR and see if it was possible to image such a small sample. As shown in Section 4.2.2.2, the sample was imaged with a beam energy of ~14 keV at several positions on the rocking curve and analysed using both DEI and MIR the resulting images are shown in Figure 6-4 and Figure 6-5.

Comparing the two techniques, both the refraction and apparent absorption DEI images (Figure 6-4 a) and b)) show the same structures and features as the refraction and absorption images created by the MIR method (Figure 6-5 a) and b)). It is unclear, however, whether these structures are from the underlying structure of the sample or are due to the slicing of the sample.

The absorption images (Figure 6-4 b) and Figure 6-5 b)) show the most absorption through in the middle of the sample although different structures can also be seen. The refraction images (Figure 6-4 a) and Figure 6-5 a)) are sharper than the absorption images and show more fine structure, this is demonstrated when looking at the structure of the bone that is visible. The USAXS image differs from

the other images because it highlights a few specific regions of the sample, whereas the other images have some contrast throughout the sample. This means that the outline of the sample is less well defined, but certain features such as the porosity of the bone are shown in detail.

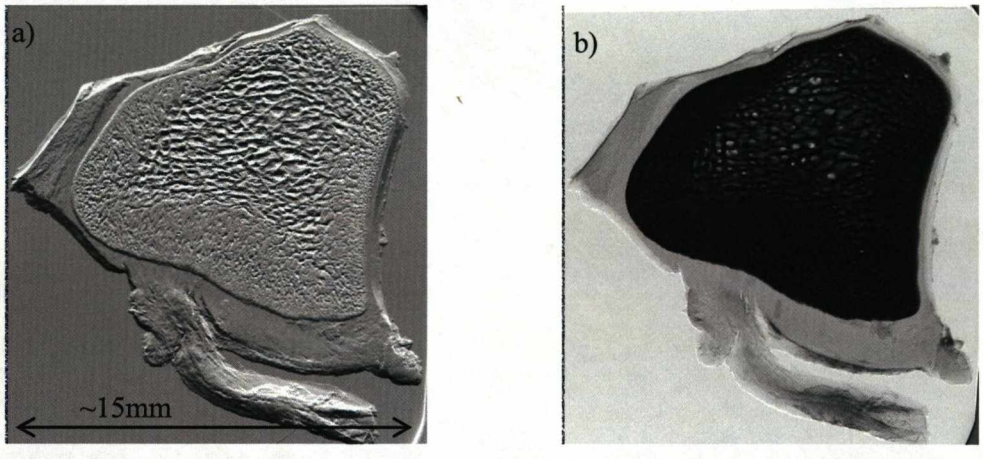

Figure 6-4: The DEI images of the sample. a) The refraction image. b) The apparent absorption image.

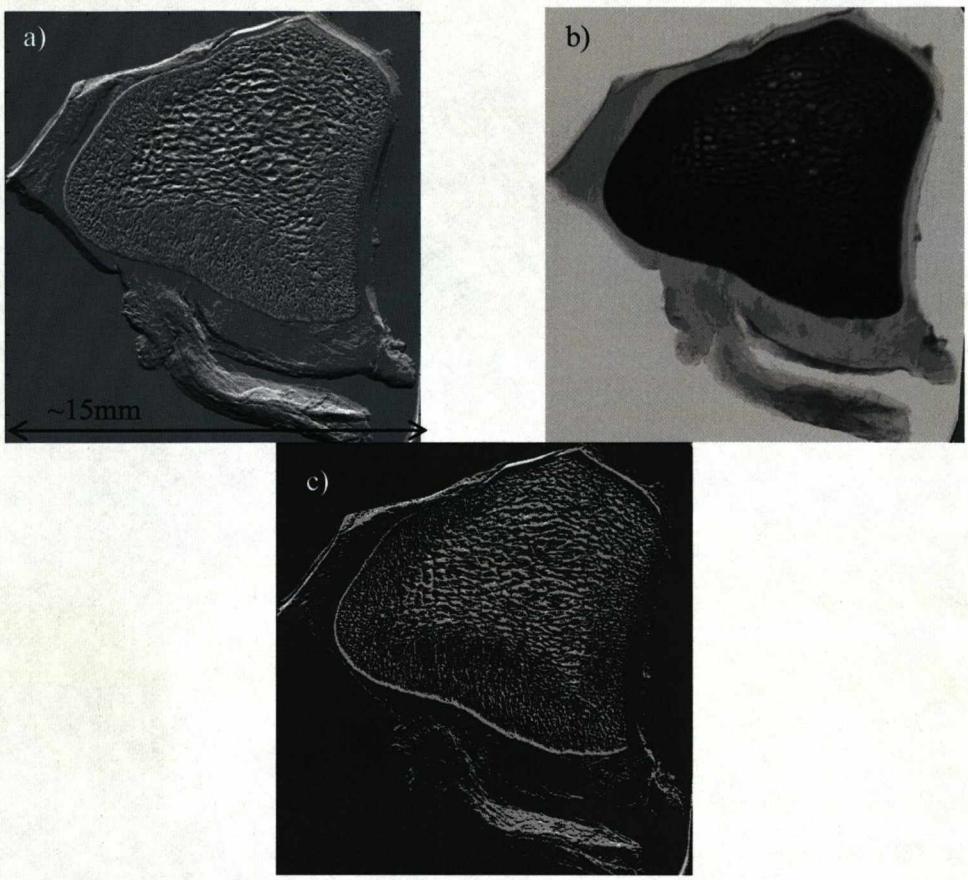

Figure 6-5: The MIR images of the sample. a) The refraction image. b) The absorption image. c) The USAXS image.

6.3 **Pig's trotter**

This experiment was carried out on station 7.6 at the Daresbury SRS using a beam energy of 26.18 keV, as described in Section 4.2.2.3. The aim of this experiment was to image a whole joint in order to establish the ability of the ABI technique to visualise the joint cartilage with the superposition of different soft tissue structures. The DEI method was used and refraction and apparent images were produced.

The DEI images created were very clear and showed both bone and soft tissue structure such as the layers of skin and fat (see Figure 6-6 a) and b)). These structures were visible in the apparent absorption image due to the lack of

scattered x rays and the low energy of the beam. The refraction image also shows the cartilage in the joint, shown more clearly in the close up image. This confirms DEI's ability to visualise joint cartilage through other structures.

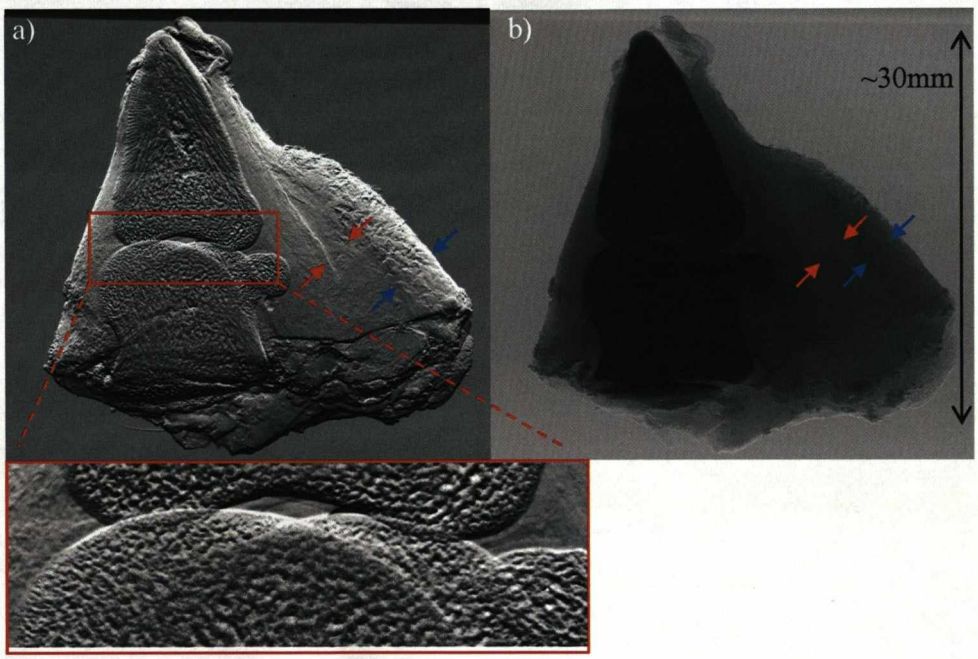

Figure 6-6: The DEI images of the sample. a) The refraction image. b) The apparent absorption image. The red arrows highlight the fat region in the sample and the blue arrow highlight the skin region.

Two of the MR-images taken of the sample are shown in Figure 6-7. It should be noted that the sample will not be in exactly the same projection as the DEI images. As with the refraction images soft tissue structure of the samples can be seen. The joint cartilage is also visible in and shown clearly in the close up in. Unlike the DEI images, however, these MR-images are slices through the sample, whereas the ABI images are projection images and therefore have a superposition of the surrounding structures. Despite this the cartilage can still be seen in the refraction image, although when comparing it with the MRI images, the obvious benefits of imaging the sample in CT, so that slice images through the sample can created is clear.

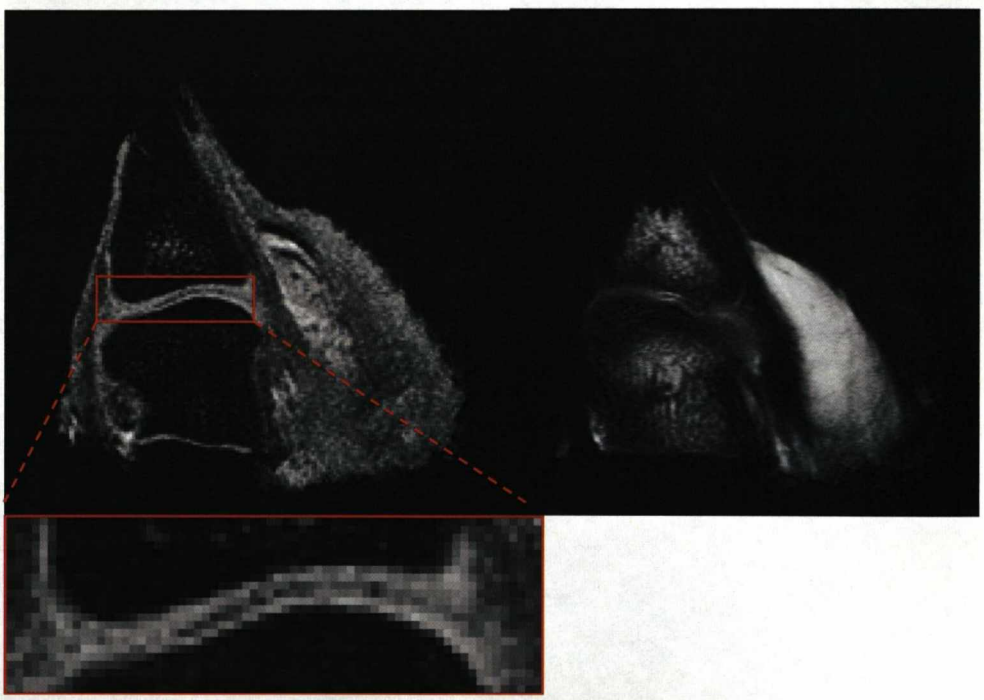

Figure 6-7: MR- images of the sample.

6.4 **Canine Joint Samples**

Three samples were imaged in this experiment; a core sample, a disarticulated sample and a whole sample. As described in Section 4.2.2.4, the experiment was carried out on station ID17 at the ESRF, using a beam energy of 40 keV.

Each sample was imaged at several positions on the rocking curve and DEI and MIR analysis was carried out. The resulting images are presented in the following sections.

6.4.2 The Core Sample

The core sample was imaged at five positions on the rocking curve; the peak, ±80% and ±50%. The ±50% DEI images are shown in Figure 6-8. The apparent absorption image is shown in Figure 6-8 a), the bone structure of the sample is clearly visible. However, the cartilage layer cannot be seen, as shown in the close up of the cartilage region in Figure 6-8 b). The refraction image, shown in Figure 6-8 c), also shows the structure of the bone. However, the refraction image is sharper than the absorption image and overall shows more detail. The cartilage layer can also be seen in the refraction image, this is shown clearly in the close up in Figure 6-8 d).

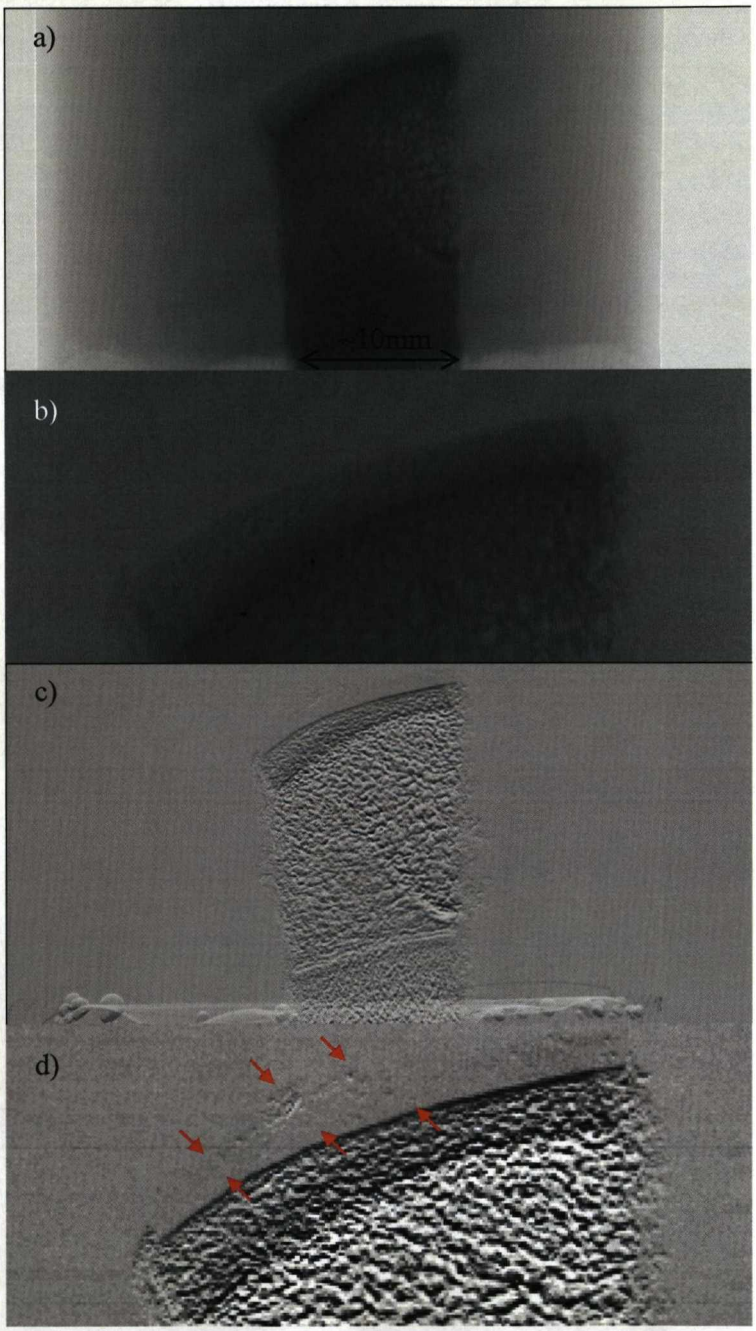

Figure 6-8: The ±50% DEI images of the core sample. a) The apparent absorption image. b) A close up of the cartilage region in the apparent absorption image. c) The refraction image. d) A close up of the cartilage region in the refraction image, the cartilage region is highlighted by the red arrows.

A DEI image set was also created for the images taken at ±80%. These images showed the same results as those presented for the ±50% images and can be seen in Appendix 2.

The ±50% MIR images are shown in Figure 6-9. The absorption image, in Figure 6-9 a), again, shows structure of the bone clearly, however, as with the DEI apparent absorption image, it does not show the cartilage layer. The refraction image, shown in Figure 6-9 b), is a lot sharper than the absorption image and shows the structure of the bone in more detail than the absorption image. The layer of cartilage can also be seen in this refraction image and is shown in close up in Figure 6-9 b). The USAXS image of the sample is shown in Figure 6-9 c), as with the other MIR images, the structure of the bone is clearly visible, however it does not show the cartilage layer. Several other MIR image sets were produced; giving the same results, and are shown in Appendix 2.

In order to compare all the image sets more fully SNR values were calculated for all the images. The SNR results from the DEI images are shown in Figure 6-10. The SNR values are high, all over one hundred. The SNR values for both the refraction and apparent absorption images at ±50% were higher than those at ±80%. This is due to the steeper rocking curve gradient at the ±50% position compared with the ±80% position.

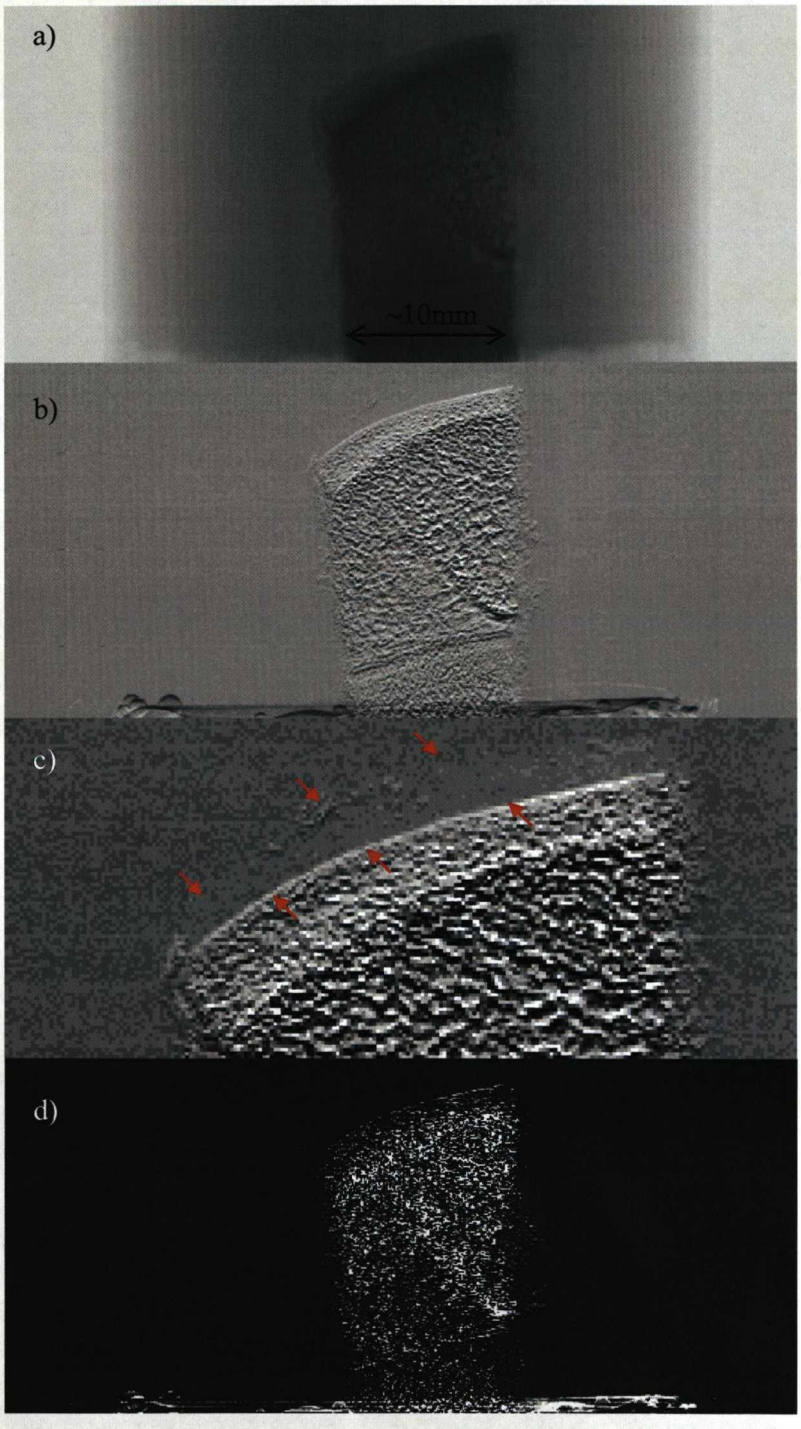

Figure 6-9: The ±50% MIR images of the core sample. a) The absorption image. b) The refraction image. c) A close up of the cartilage region in the refraction image. The cartilage region is highlighted by the red arrows. d)The USAXS image.

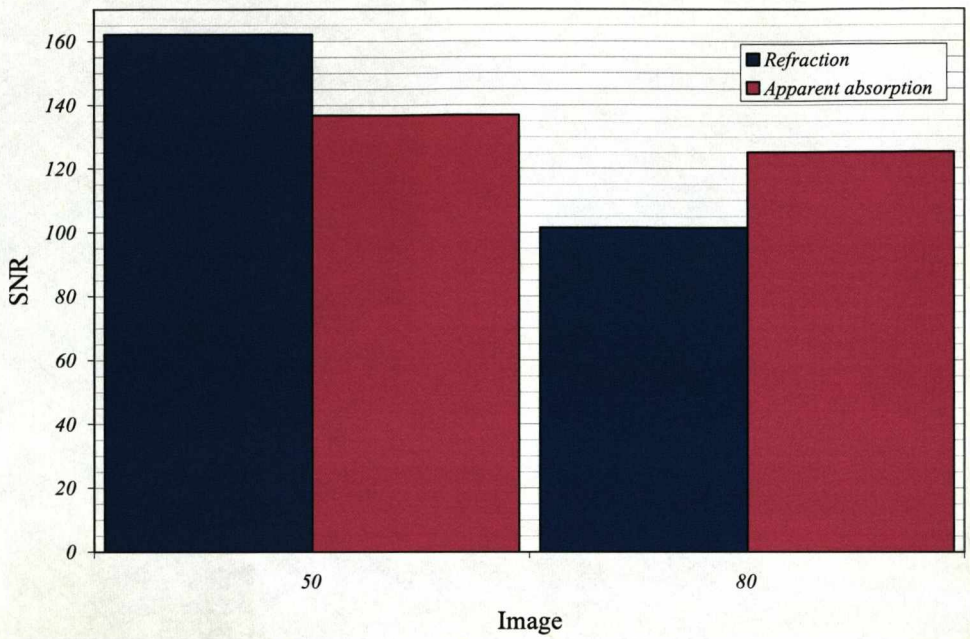

Figure 6-10: The SNR results for the DEI images.

The SNR analysis was also applied to all the MIR image sets, the results of which are shown in Figure 6-11. As can be seen the results from the different types of images are very different. Looking first at the refraction images, all the SNR values are over one hundred, and range from ~102 for the peak ±80% image to ~180 for the peak ±50% image. The results for the absorption images ranged from ~88 for the ±80% image to ~151 for the peak ±80% ±50% image. The USAXS images show the largest variation, ranging from ~340 for the ±50% image to ~42 for the peak ±80%, ±50% image.

The DEI and MIR SNR ±50% and ±80%, results are compared in Figure 6-12. For both positions the MIR refraction images gave higher SNR values than the DEI refraction images. This was not reflected in the results for the absorption images with the MIR absorption image having a higher value than the DEI absorption image whereas for the ±80% images this was reversed.

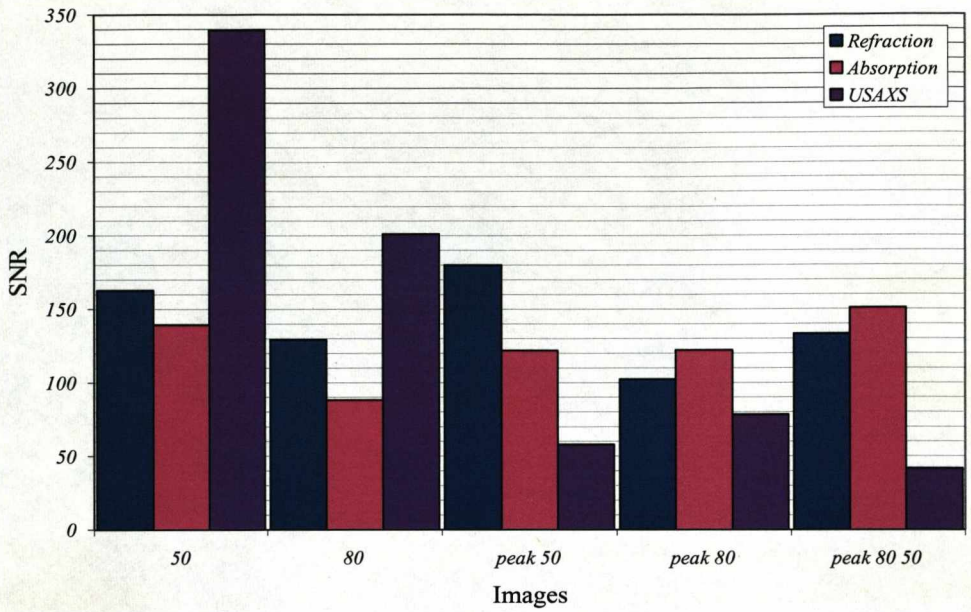

Figure 6-11: The SNR values from the MIR images of the core sample.

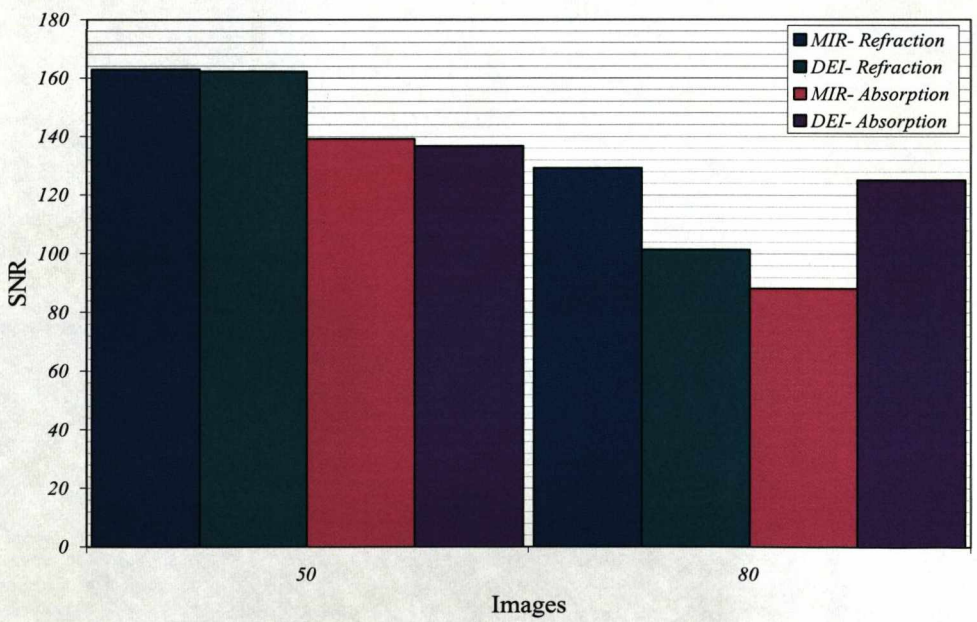

Figure 6-12: A comparison of the SNR values given by the MIR and DEI methods for the ±80% and ±50% images.

6.4.2 The Disarticulated Sample

The disarticulated sample was imaged in two orientations. In each orientation it was imaged with the analyser crystal tuned to the peak, ±80% and ±50% positions on the rocking curve, and both DEI and MIR analysis was carried out.

The ±50% DEI images of the sample in the first orientation are shown in Figure 6-13, and the ±80% DEI images are shown Figure 6-14. The apparent absorption images, in Figure 6-13 and Figure 6-14 a), clearly show the structure of the bone. The refraction images, in Figure 6-13 and Figure 6-14 b), also show the structure of the bone. The layer of cartilage is also visible and is shown more clearly in the close-up. In both the apparent absorption and refraction images line artefacts from misalignments in the flat fields can also be seen.

Five MIR image sets were created. The ±50% MIR images taken in the first orientation are shown in Figure 6-15. The absorption image, as with the DEI apparent absorption image (Figure 6-13 and 6-14 a)), shows the structure of the bone very clearly but has not imaged the cartilage. The refraction image, (Figure 6-15 b)), shows the structure of the bone; however it does so with greater sharpness than the absorption image and the layer of cartilage can also be seen clearly. The USAXS image, in Figure 6-15 c), also shows the bone structure of the sample and as with the refraction image it does so with greater sharpness than the absorption image. Unlike the refraction image however, the cartilage cannot be seen in the USAXS image. Line artefacts due to the flat fields are again present in the images. The remaining MIR images and DEI images showed the same results, and can be seen in Appendix 2.

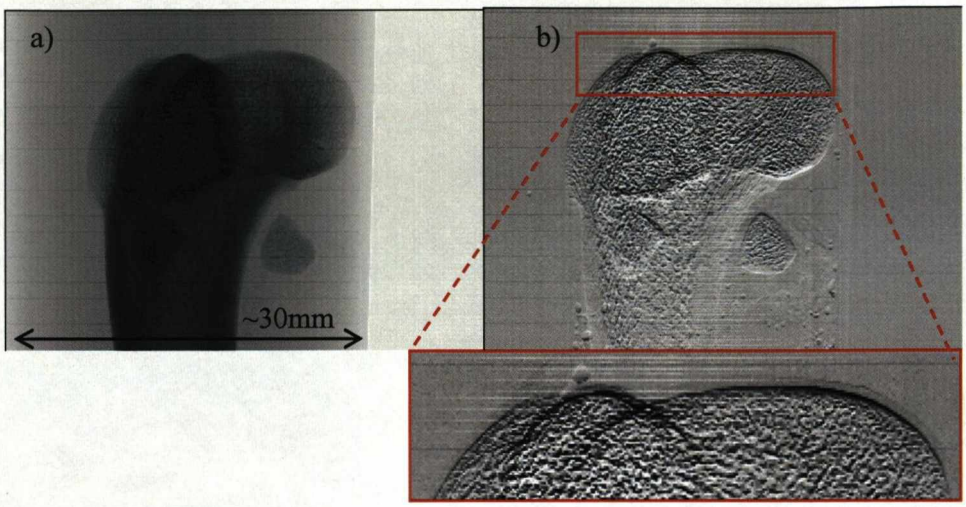

Figure 6-13: The ±50% DEI images of the disarticulated sample in the first orientation. a) The apparent absorption image. b) The refraction image.

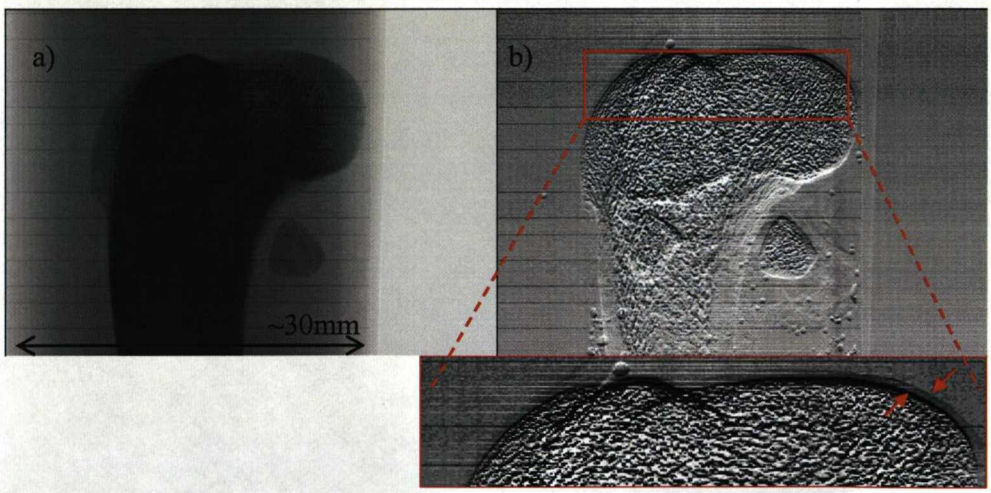

Figure 6-14: The ±80% DEI images of the disarticulated sample in the first orientation. a) The apparent absorption image. b) The refraction image. The cartilage region is highlighted by the red arrows.

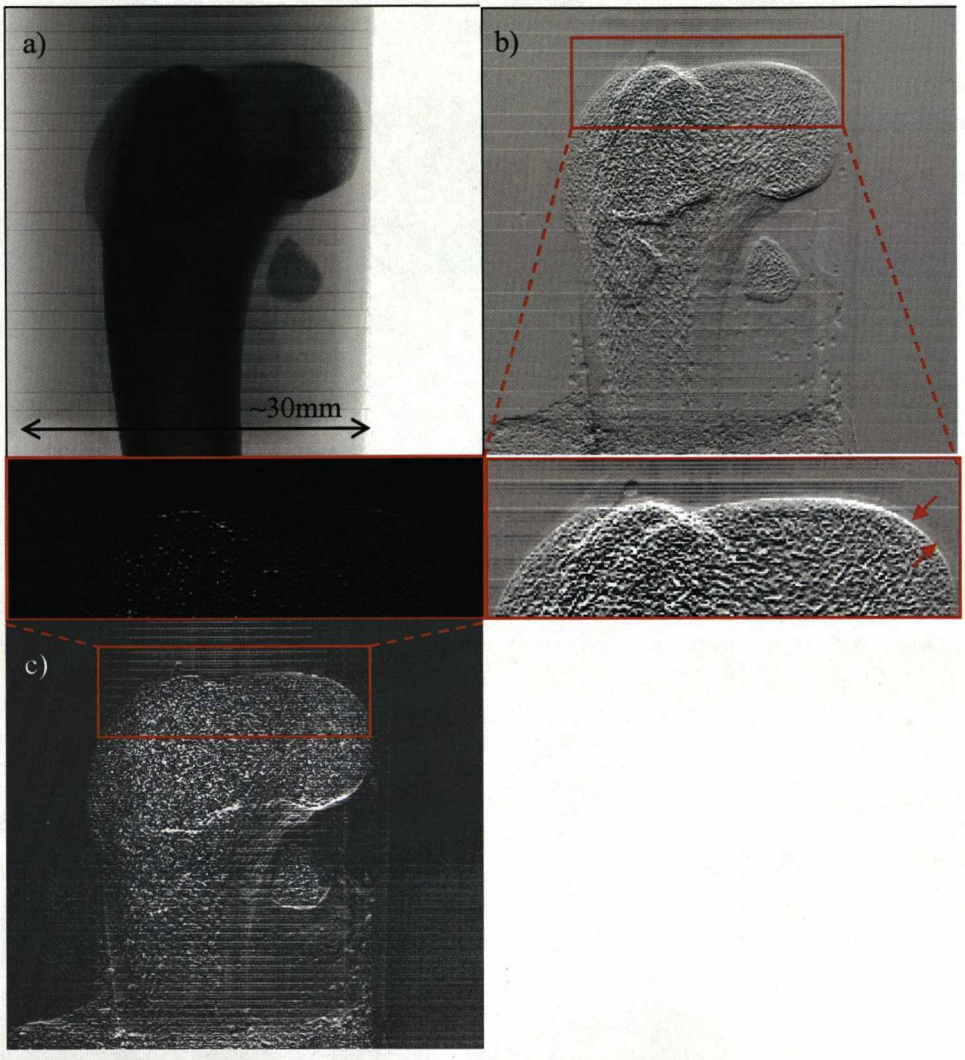

Figure 6-15: The ±50% MIR images of the disarticulated sample. a) The absorption image. b) The refraction image. The cartilage region is highlighted by the red arrow. c) The USAXS image.

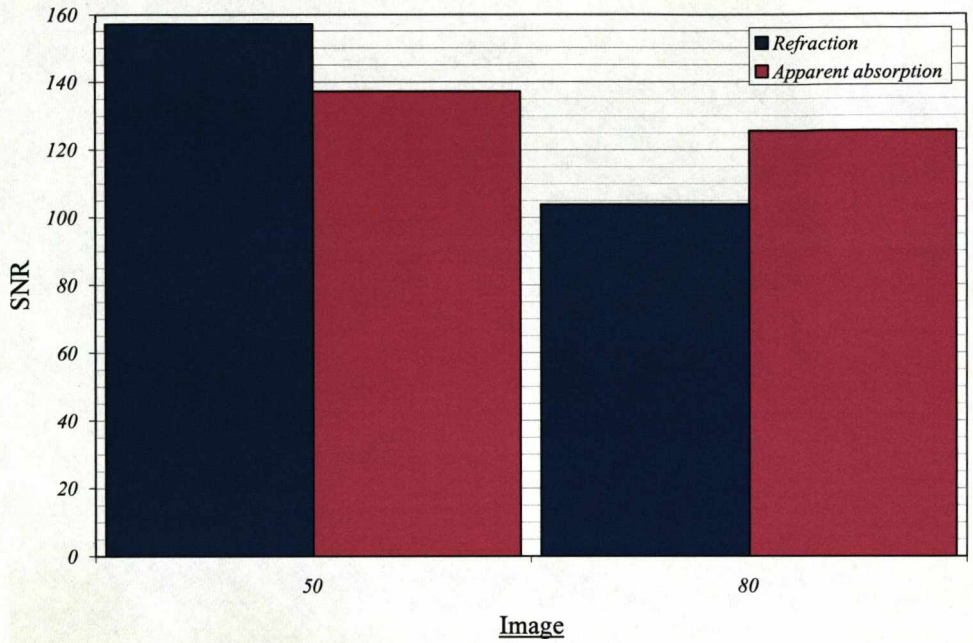

Figure 6-16: The SNR results for the DEI images of the disarticulated sample in the first orientation.

In order to compare the images more fully, SNR analysis was carried out, as was done for the core sample. The SNR results for the DEI images of the sample in the first orientation are shown in Figure 6-16. The SNR values for all the images are high, with the SNR values for the ±50% images being higher than those for the ±80% images. Looking back at the two sets of images, it is clear that the line artefacts are more prominent in the ±80% images compared with the ±50% images therefore resulting in over all lower SNR values for the 80% images. Although the ±50% position would also be expected to give the better results due to the rocking curve having a steeper gradient at this position compared with the ±80% position. The refraction and apparent absorption image values of SNR do not show any continuity, with the SNR value for the ±50% refraction image being higher than that of accompanying absorption image, whereas the ±80% refraction image has a lower SNR value than the ±80% absorption image.

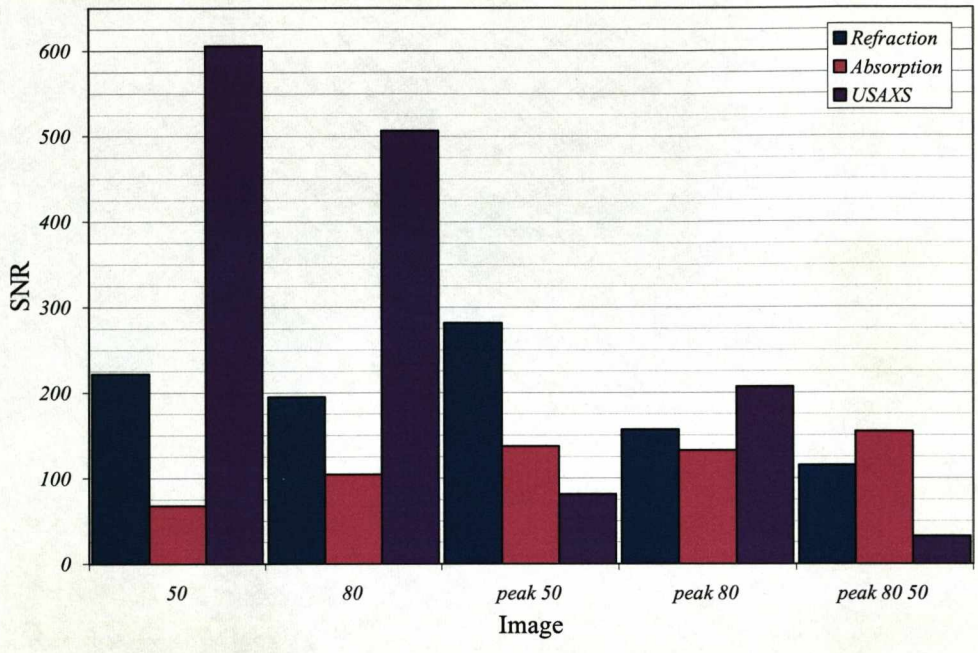

Figure 6-17: A plot showing the SNR given for the different MIR images of the disarticulated sample.

The SNR results for the MIR image sets of the sample in the first orientation are presented in Figure 6-17 and show results spread over a wide range of values. Looking first at the SNR values given by the refraction images, the highest value was from the peak, ±50% image with a value of 281 and the lowest was from the peak, ±50%, ±80% image with a value of 115. This shows that by increasing the number of images used to create the MIR image set it does not necessarily mean that the SNR will increase, but is dependent on the SNR of the constituent images. The values of SNR for the absorption images cover a smaller range of values, the highest, of 154, was given by the peak ±50%, ±80% image and the lowest of 68 was given by the ±50% image. The results for the USAXS images showed the largest variation of all: the highest SNR value was given by the ±50% image with a value of 606, and the smallest, with a value of 33 was given by the peak, ±50%, ±80% image.

A comparison of the SNR values for the MIR and DEI ±50% and ±80% image sets is shown in Figure 6-18. For both the ±50% and ±80% refraction images, MIR gave a significantly larger SNR value than the DEI refraction images. The absorption images did not show a trend, with the MIR ±50% absorption image having a higher SNR value than the DEI ±50% absorption image and the MIR ±80% absorption image having a lower SNR value than the DEI ±80% absorption image.

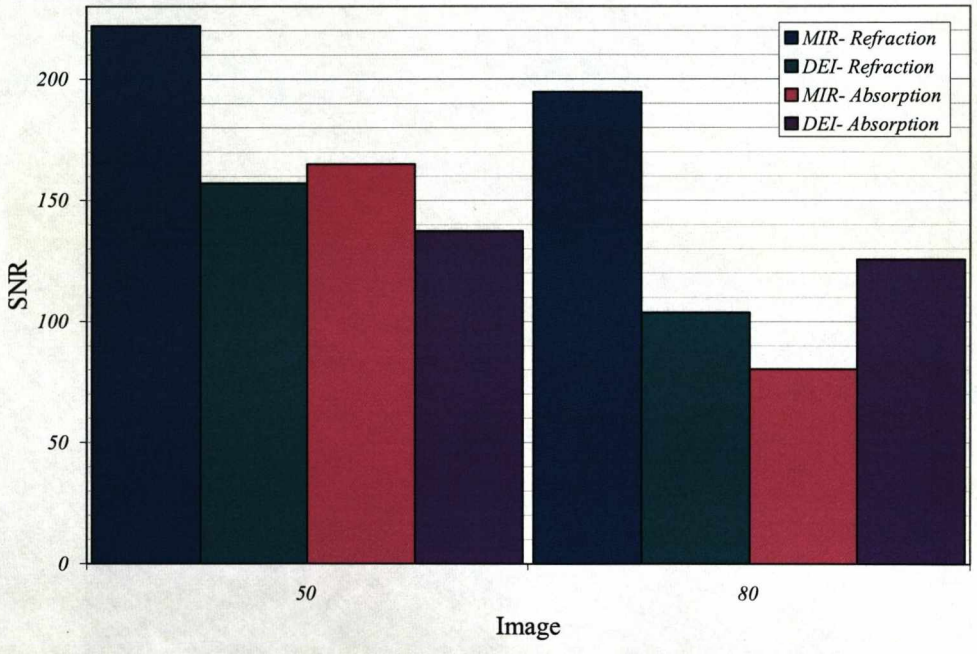

Figure 6-18: A comparison of the SNR values for the ±50% and ±80% MIR and DEI images.

Figure 6-19 shows the ±50% DEI images of the sample in the second imaging position. As with the absorption image from the previous orientation, the absorption image, shown in Figure 6-19 a), shows the structure of the bone but does not show the cartilage layer. The refraction image again shows the structure of the bone more sharply than the apparent absorption image and also clearly shows the cartilage in the sample, which can clearly be seen in the close up image. The same result can be seen in the ±80% DEI images, shown in Figure 6-20.

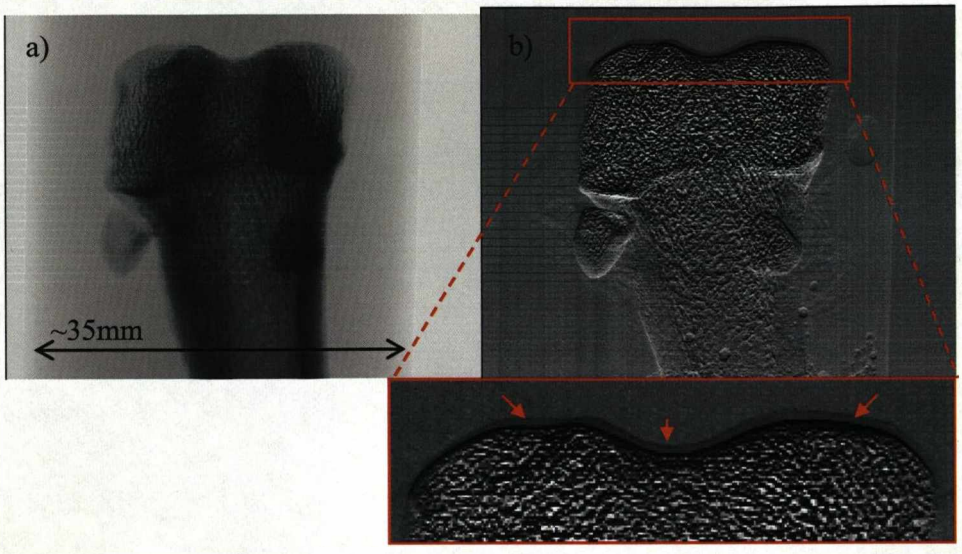

Figure 6-19: The ±50% DEI images of the disarticulated sample in the second orientation. a) The apparent absorption image. b) The refraction image. The cartilage region is highlighted by the red arrows.

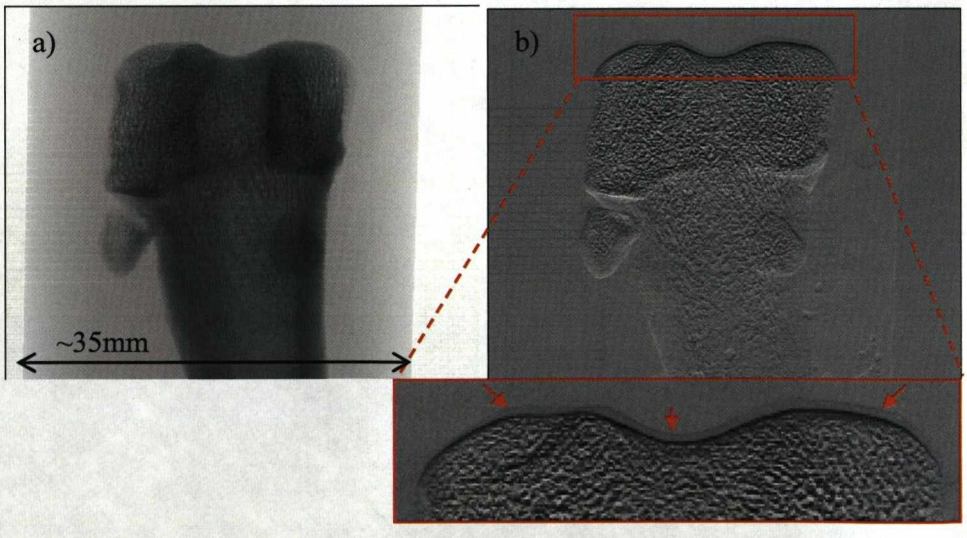

Figure 6-20: The ±80% DEI images of the disarticulated sample in the second orientation. a) The absorption image. b) The refraction image. The cartilage region is highlighted by the red arrows.

The ±50% MIR images can be seen in Figure 6-21. The absorption image in Figure 6-21 a) shows the structure of the bone but does not show the cartilage. The refraction image in Figure 6-21 b), as with the previous results, shows the bone structure clearly and also shows the cartilage, which can be seen clearly in the close up. The USAXS image is shown in Figure 6-21 c) and shows the structure of the bone but like the previous USAXS images does not show the cartilage. As with the images taken in the previous orientation, there are again line artefacts present in all the images due to problems with misalignment of the flat fields. The ±80% MIR images gave the same results and can be seen in Figure 6-22.

A SNR analysis was again applied to both the DEI and MIR images of the sample in this orientation. The results for the DEI images of the sample in the second orientation are shown in Figure 6-23. The results clearly show both the ±50% and ±80% refraction images having higher SNR values than the absorption images. The ±80% refraction image also gave a much higher value than the ±50% refraction image. Looking back to Figure 6-19 and Figure 6-20 b), it is clear that the ±50% image was noisier than the ±80% image. This difference is likely to be due to differences in the merit of the flat alignment. The values of SNR for the absorption images on the other hand are very similar, which reflects that the images themselves, in Figure 6-19 and Figure 6-20 a), show very little difference.

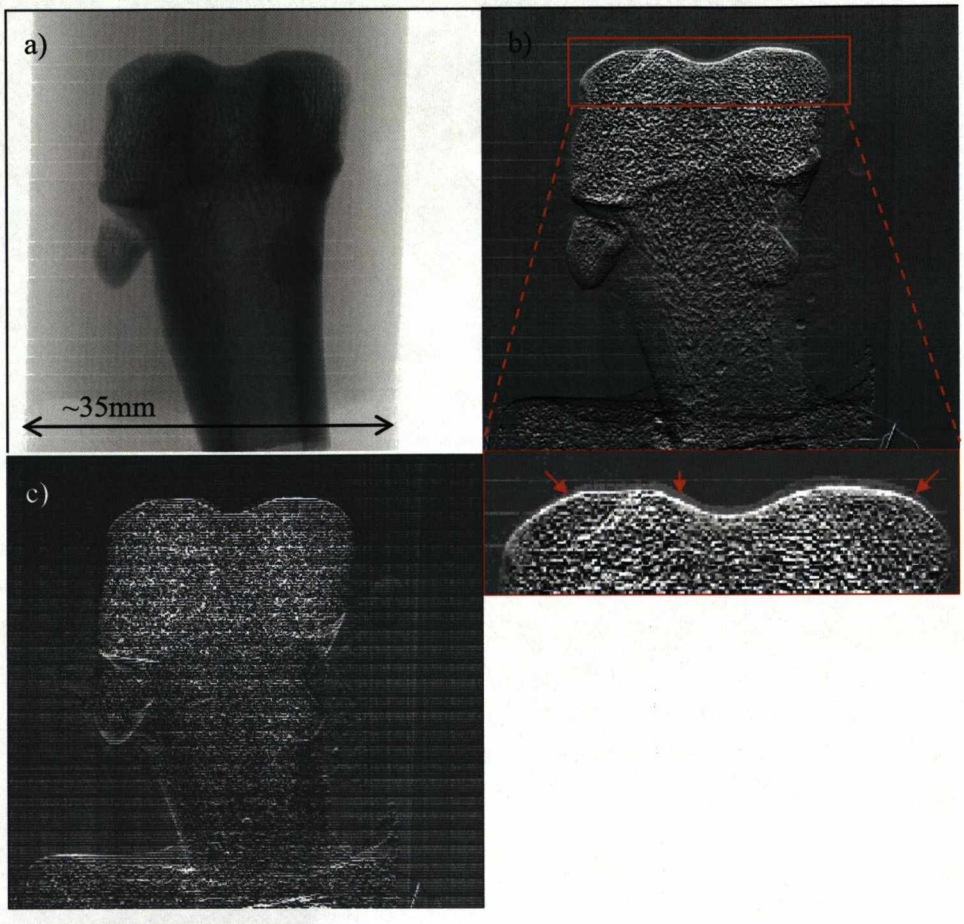

Figure 6-21: The ±50% MIR images of the disarticulated sample in the second orientation. a) The absorption image. b) The refraction image. The cartilage region is highlighted by the red arrows. c) The USAXS image.

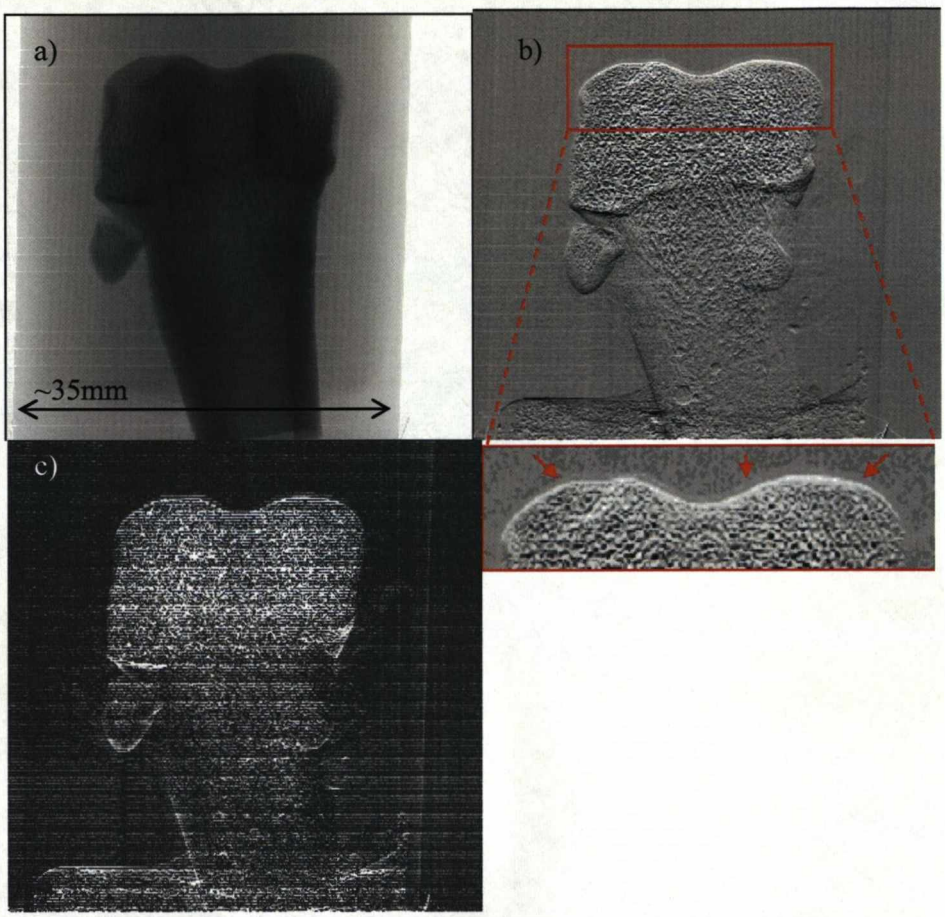

Figure 6-22: The ±80% MIR images of the disarticulated sample. a) The absorption image. b) The refraction image. The cartilage region is highlighted by the red arrows. c) The USAXS image.

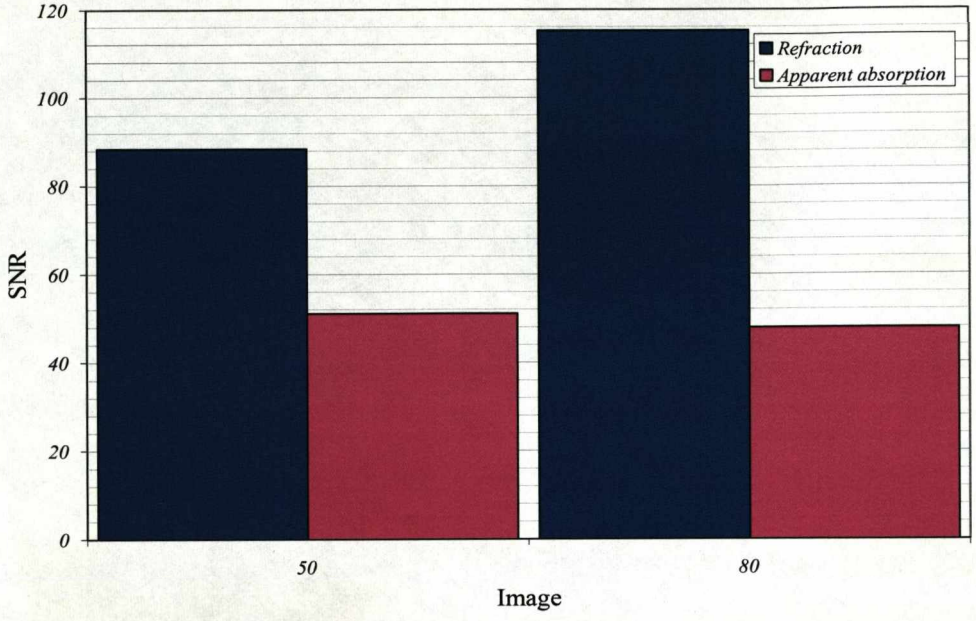

Figure 6-23: The SNR results for the DEI images of the disarticulated sample in the second orientation.

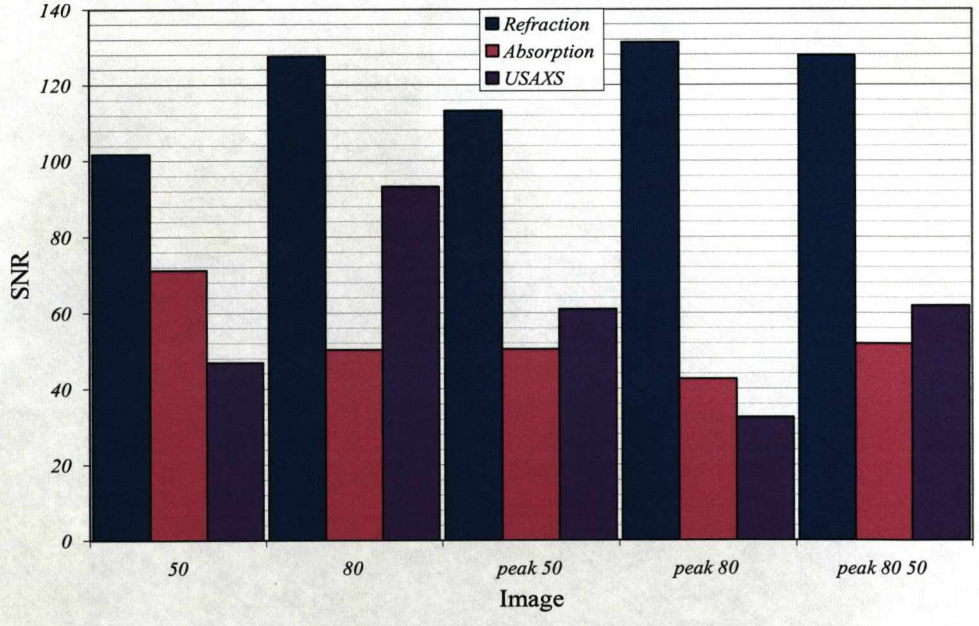

Figure 6-24: The SNR results for the MIR images of the disarticulated sample in the second orientation.

A comparison of the SNR results for the MIR images is shown in Figure 6-24. All the MIR image sets the refraction images consistently gave high SNR values. As with the results from the DEI images, the ±80% refraction image has a higher SNR value than the ±50% refraction image. Again the difference in noise on the images is visible, as shown in Figures 6-21 and 6-22 b). Both the peak, ±80% refraction image and the peak, ±50% refraction image show an increase in SNR from the ±80% and ±50% refraction images, showing that increasing the number of images used can improve the SNR. However, the peak, ±80%, ±50% refraction image gave a SNR value which was lower than the peak, ±80% SNR value, yet higher than the peak, 50% SNR value. This therefore shows that although the SNR value increases with the number of composite images this relies on the images being of the same standard. The SNR results for the absorption images were lower than those of the refraction images and did not show any trend regarding which images were used. Looking at the USAXS results that used the ±50% images, as the number of component images increased so did the SNR, however this was not true for the ±80% results.

The SNR values for the ±50% and ±80% MIR and DEI image sets are shown in Figure 6-25. As can be seen, the MIR refraction images both gave higher SNR values than the DEI refraction images. The same was true of the ±50% absorption images. However, the ±80% absorption images gave very similar SNR results.

The main purpose of imaging this sample was to look at the cartilage. As the images presented in this section show, the cartilage is clearly visible in the refraction images. The line artefacts were less prominent in the images of the sample in the second orientation, as shown in Figure 6-24. Of these images, the peak ±80% refraction image gave the highest SNR value. It is this image that has therefore been looked at more extensively.

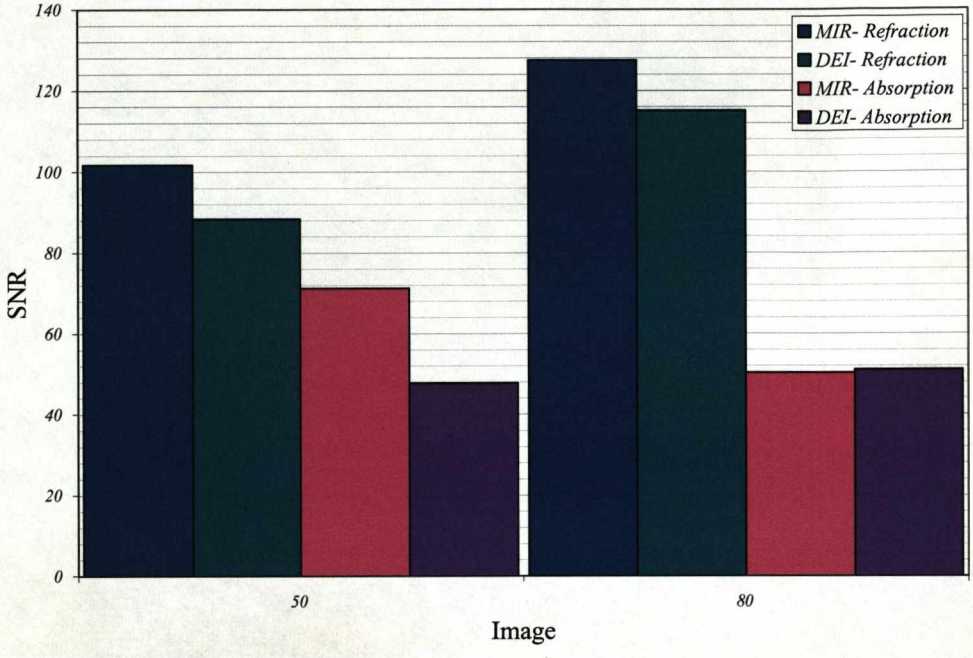

Figure 6-25: A comparison of the SNR results for the MIR and DEI images set of the disarticulated sample in the second orientation.

In order to quantify how visible the cartilage is compared with the background, the SNR_{LINE} of a line going from the background to the cartilage region was found. An example of such a line is shown in Figure 6-26 a). The joint surface was divided into regions, as shown in Figure 6-26 b) and c), and an average SNR_{LINE} value for each region was found. The average SNR_{LINE} values found for each of the regions are shown in Figure 6-27. No values were found for regions 4 and 11 because the line artefacts present in the image were too close to the cartilage surface to take measurements. As can be seen, there is a range of SNR_{LINE} values over the cartilage surface, with an average value of 3.29. The highest SNR_{LINE} value was given by region 12, which had a value of 6.16.

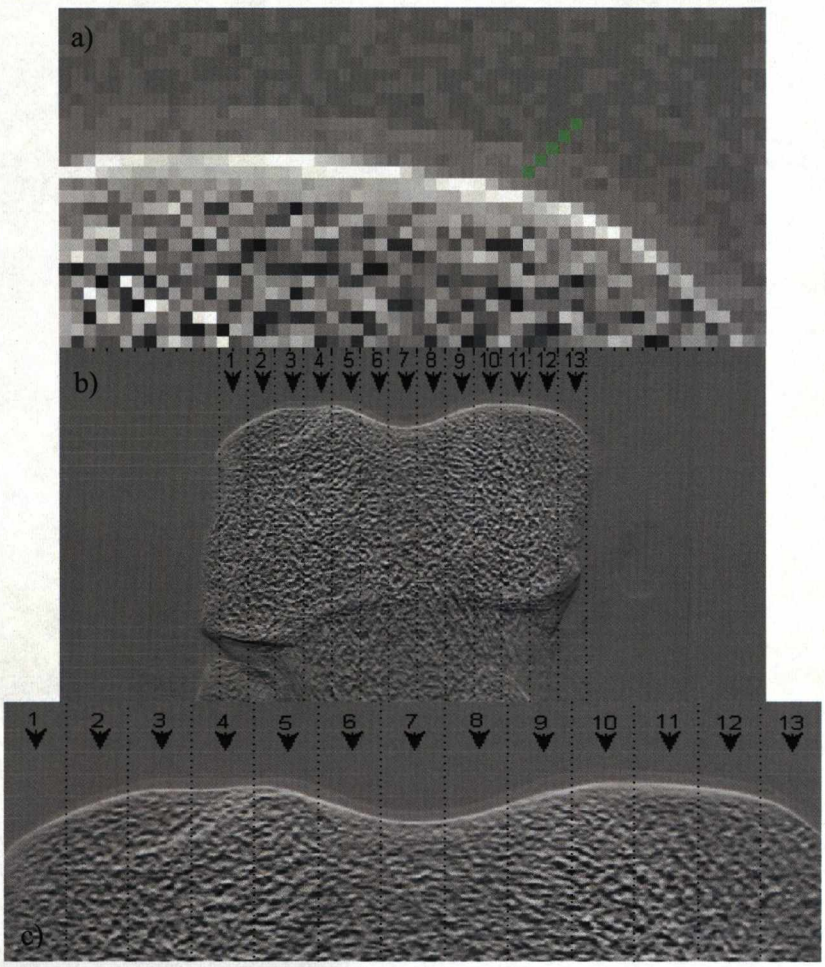

Figure 6-26: a) A diagram showing an example of a line used to calculate the SNR_{LINE} b) The joints surface divided into regions. c) A close up view of the different regions.

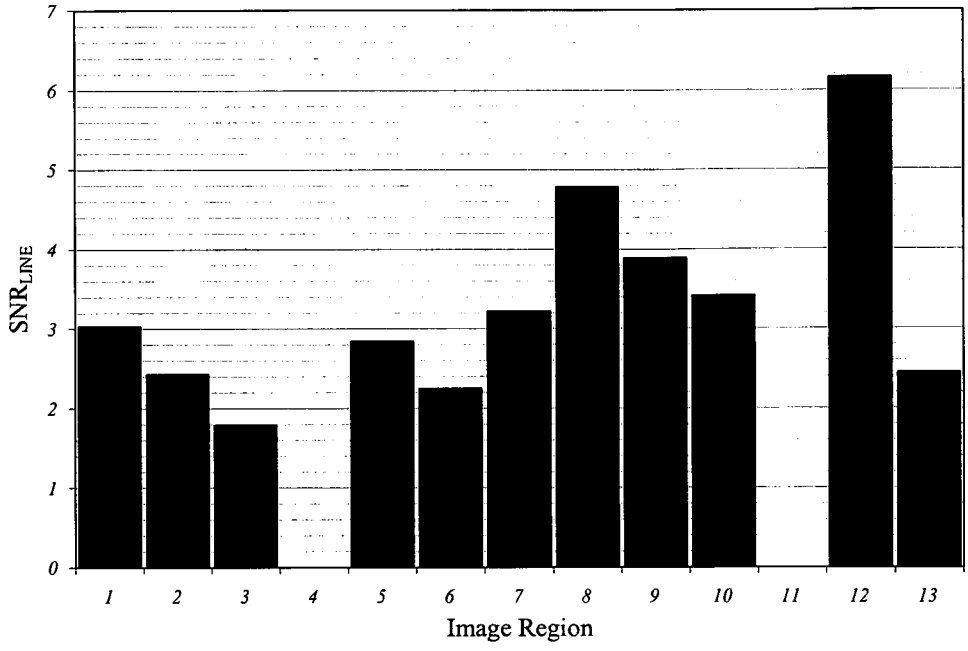

Figure 6-27: The SNR_{LINE} values for the regions in the Peak ±80% refraction image.

In addition to the cartilage showing a difference in contrast from the background in the refraction image, there were also differences in the contrast in the cartilage itself. This can be seen in Figure 6-22 and is demonstrated in greater detail in the series of images in Figure 6-28, which shows close-up images of the cartilage region of the sample. A series of line profiles were taken going from the background region into the bone in Region 12 of the sample (see Figure 6-26), in order to examine this more closely. This region was chosen because, as shown in Figure 6-27, it gave the highest SNR_{LINE} values.

A typical line profile and an image of the corresponding positions in the peak ±80% refraction image are shown in Figure 6-29. There are clear peaks in the profile, which, as shown in Figure 6-29 c), correspond to the different regions of contrast in the image. For example, P1, is a significant peak above the background, as Figure 6-29 b) shows. Matching this peak up with the corresponding pixel in the image, the peak would appear to be due to the structure at the surface of the

cartilage. In a similar manner, the point P2, the largest peak in the profile, corresponds to the point where the profile crosses into the bone region. In addition to these large peaks, two other, much smaller peaks could be seen in the profile, both of these points match with positions in cartilage.

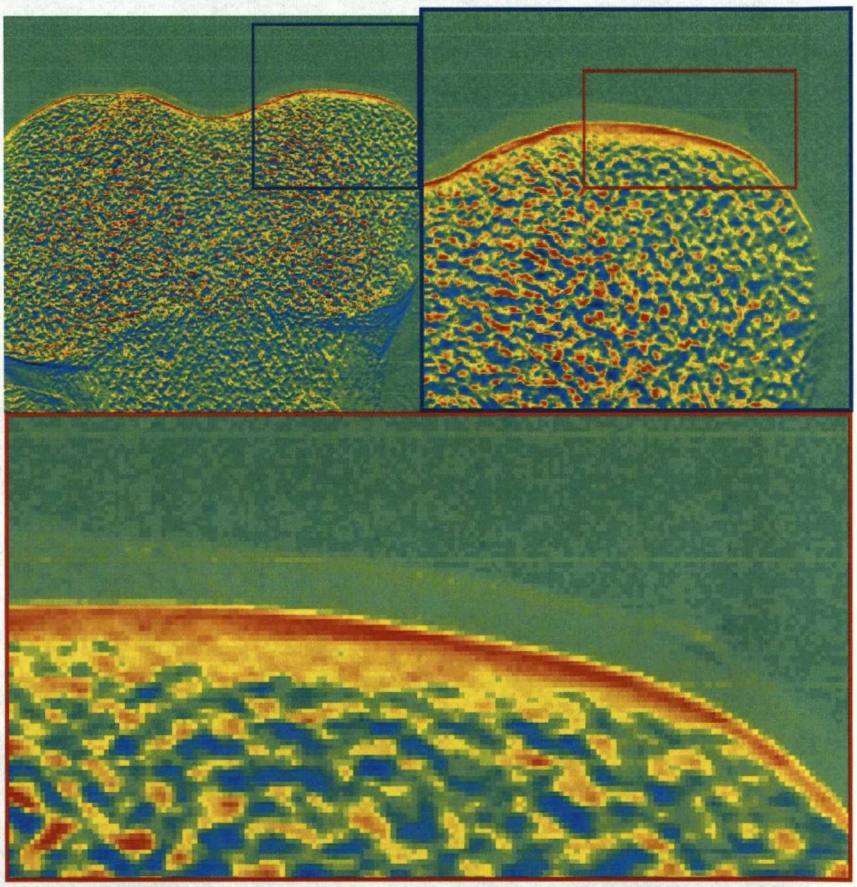

Figure 6-28: A series of close-up images of the cartilage from the peak, ±80%, ±50% refraction image of the disarticulated sample.

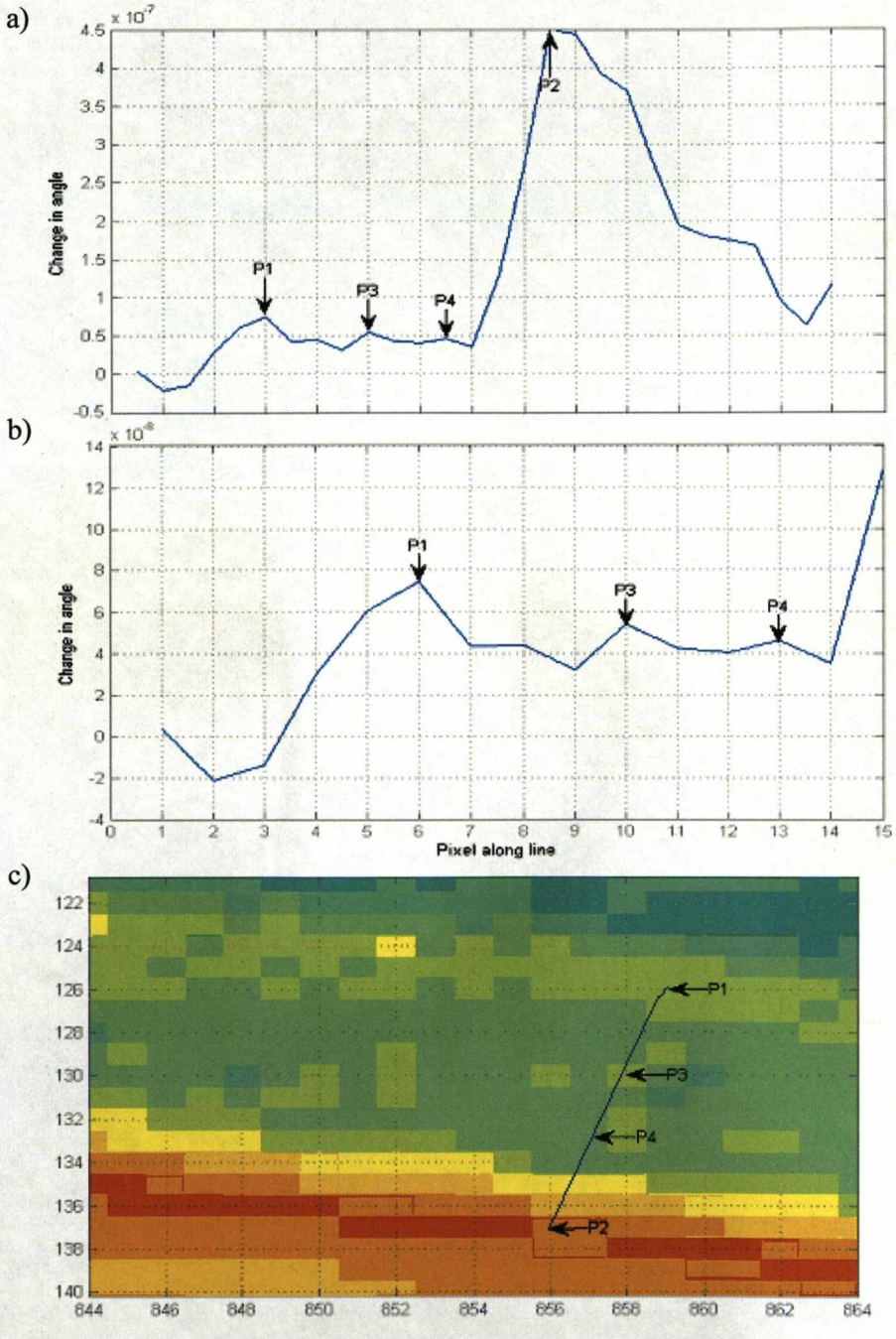

Figure 6-29: A typical line profile taken in Region 12, going from the background of the image through the cartilage to the bone. a) The line profile, a plot of the change in angle ($\Delta\theta z$) against the number pixel along the line. b) A closer look at the start of the line profile, showing the smaller peaks more clearly. c) A close up view of the section of the peak ±80%, ±50% image, with the pixel values shown along the edges.

The sample was also imaged using MRI. Two of the MRI images are shown in Figure 6-30, where Figure 6-30 a) shows the sample in the first orientation and Figure 6-30 b) shows the sample in the second. As was the case for the previous samples with an MRI comparison, the sample is not in exactly the same position as it was in the ABI images and the ABI images were projection images, whereas the MR-images are slices. Comparing the MR-images with the refraction images of the sample, the cartilage can clearly be seen in both. The MR-images have the advantage that they do not have the line artefacts that are present in some of the refraction images, but they were taken at a lower resolution than the ABI images. However, this does not represent the best quality obtainable with this technique.

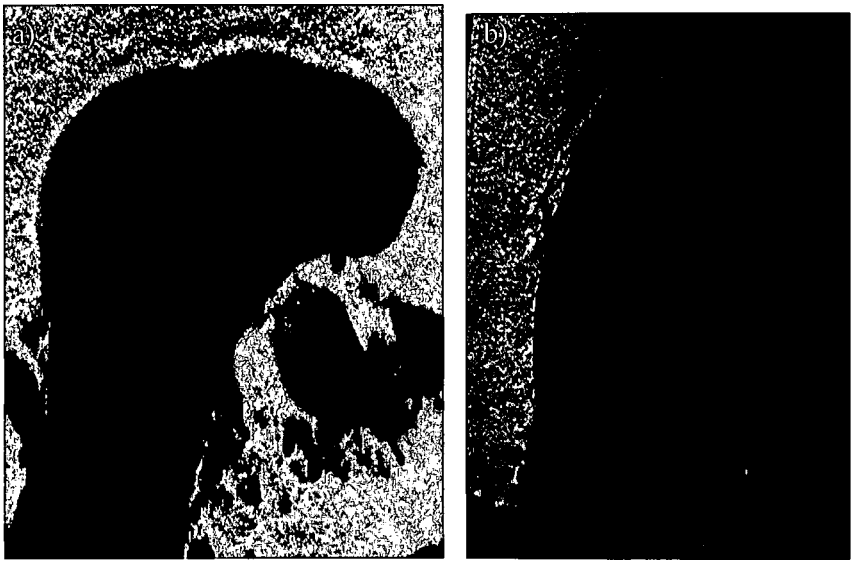

Figure 6-30: The MR-images of the disarticulated sample. a) In the first orientation. b) In the second orientation

6.4.2 The Whole Sample

The whole sample was imaged in three different orientations, once from either side and once from the front of the sample. In the first position the sample was imaged with the analyser crystal tuned to the peak, ±15%, ±30%, ±50% and ±80% positions on the rocking curve. In the second imaging position, images were taken

with the analyser crystal tuned to the peak, ±30%, ±50% and ±80% positions on the rocking curve. In the final imaging position, images were taken with the analyser crystal tuned to the peak, ±50% and ±80% positions on the rocking curve.

The ±50% DEI images of the sample taken in the first two orientations are shown in Figures 6-31 and 6-32. The apparent absorption images are shown in Figure 6-31 and Figure 6-32 a). As with the absorption images of the previous samples, these absorption images again clearly show the bone structure in the sample. The refraction images are shown in Figure 6-31 and Figure 6-32 b). The structure of the bone can be seen and, as with the images of previous samples, the refraction image is a lot sharper in appearance than the absorption image. In the refraction images of the disarticulated sample the cartilage layer was clearly visible. In these refraction images, however, the cartilage layer cannot be seen due to the superposition of the surrounding soft tissues. For the sample in the first orientation, DEI image sets were also created for all the ±15%, ±30% and ±80% data. For the sample in the second orientation ±30% and ±80% image sets were also created, all of these images showed the same results and are presented in Appendix 2.

The ±50% MIR images of the sample in the first orientation and second orientation are shown in Figure 6-33 and Figure 6-34, respectively. The absorption images, in Figure 6-33 and Figure 6-34 a), as with the other absorption images, clearly show the structure of the bone but do not visualise soft tissue structures. The refraction images, in Figure 6-33 and Figure 6-34 b), as with the previous refraction images, show the structure of the bone clearly. However, as with the DEI refraction images the surrounding soft-tissue obscures the cartilage. The USAXS images shown in Figure 6-33 and Figure 6-34 c) both show the structure of the bone very clearly, but the cartilage is not visible. The results shown by these images are replicated by the other MIR image sets of the sample in both orientation and are shown in Appendix 2.

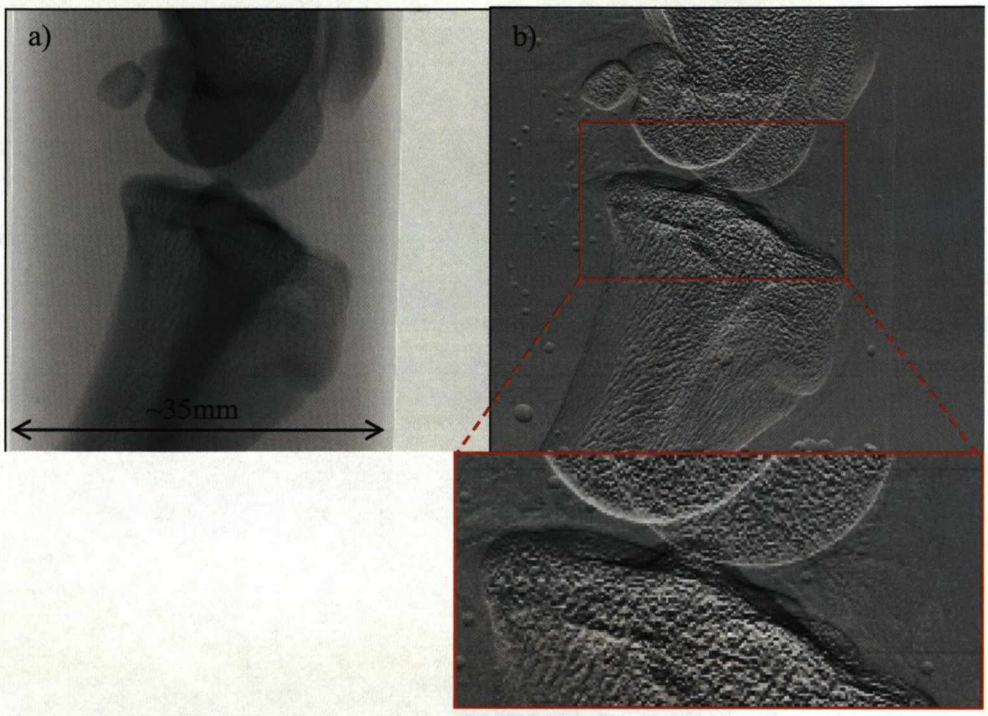

Figure 6-31: The ±50% DEI images of the whole sample in the first orientation. a) The apparent absorption image. b) The refraction image

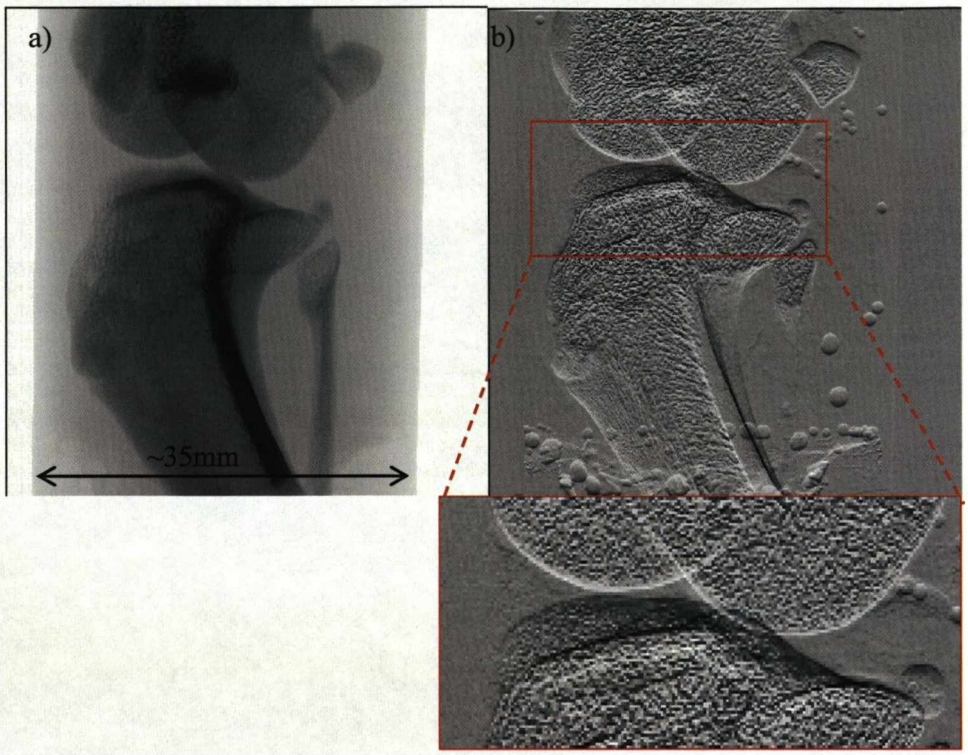

Figure 6-32: The ±50% DEI images of the whole sample in the second orientation. a) The apparent absorption image. b) The refraction image.

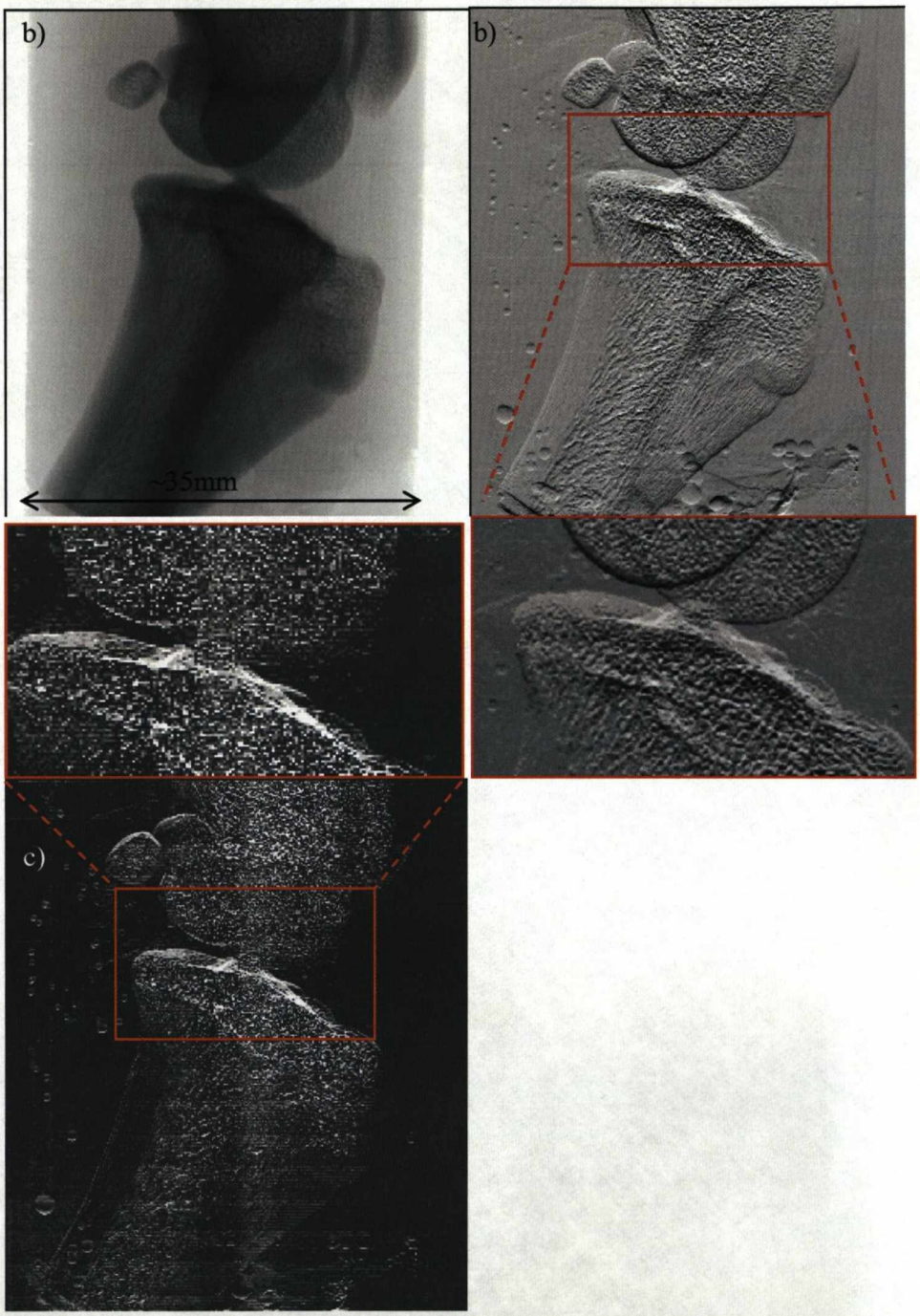

Figure 6-33: The MIR images of the whole sample in the first orientation. a) The absorption image. b) The refraction image. c) The USAXS image.

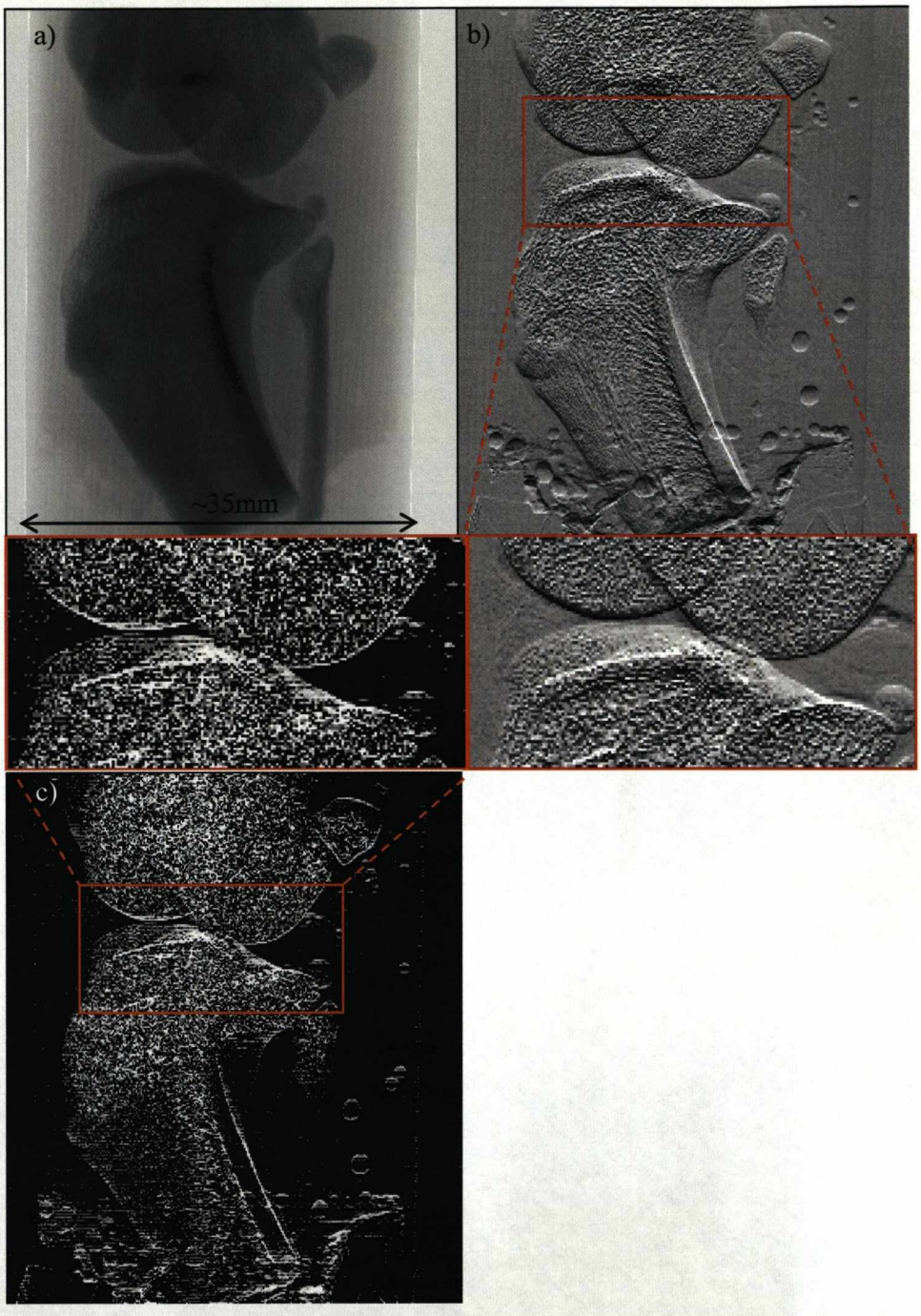

Figure 6-34: The ±50% MIR images of the whole sample in the second orientation. a) The absorption image. b) The refraction image. c) The USAXS image.

SNR analysis was applied to the DEI and MIR images in both orientations. Figure 6-35, shows the SNR values for the DEI images of the sample in the first orientation, which demonstrate an increase as the position on the rocking curve increases, for both the refraction images and the apparent absorption images. The SNR analysis of the DEI images of the sample in the second orientation is shown in Figure 6-36. The SNR values given by the refraction images are all larger than the SNR values of the apparent absorption images. The largest SNR values are given by the ±50% images and the lowest by the ±30% images. Although the ±50% position should give the highest SNR values, the results for these two orientations show this is also dependent on the quality of the images themselves.

Figures 6-37 and -38 show the SNR analysis of the MIR image sets created of the sample in the first and second orientation respectively. Looking first at the results from the first orientation, the lowest set of SNR values is again given by the ±15% images followed by the ±30% images. In the second orientation, where the ±15% position was not used, the lowest SNR values are given by the ±30% image set. The results for the first orientation refraction images show that the ±15%, ±30% and 50% SNR are lower than in the images created using the additional peak image, showing that by increasing the number of composite images the SNR can be increased. However, this was not reflected by the ±80% and peak ±80% refraction images, where there was a decrease in SNR as the number of images increases. This therefore shows that the image SNR is also dependent on the SNR of the component images. The results for the MIR refraction images of the sample in the second orientation also reflect this, although to a lesser degree. The SNR of the absorption images are more varied than the refraction images, although they show an increase as the number of component images increases. The USAXS images show the greatest variation in SNR values, and give the largest and smallest values in both sets of data. This amount of variation means that there are no obvious trends.

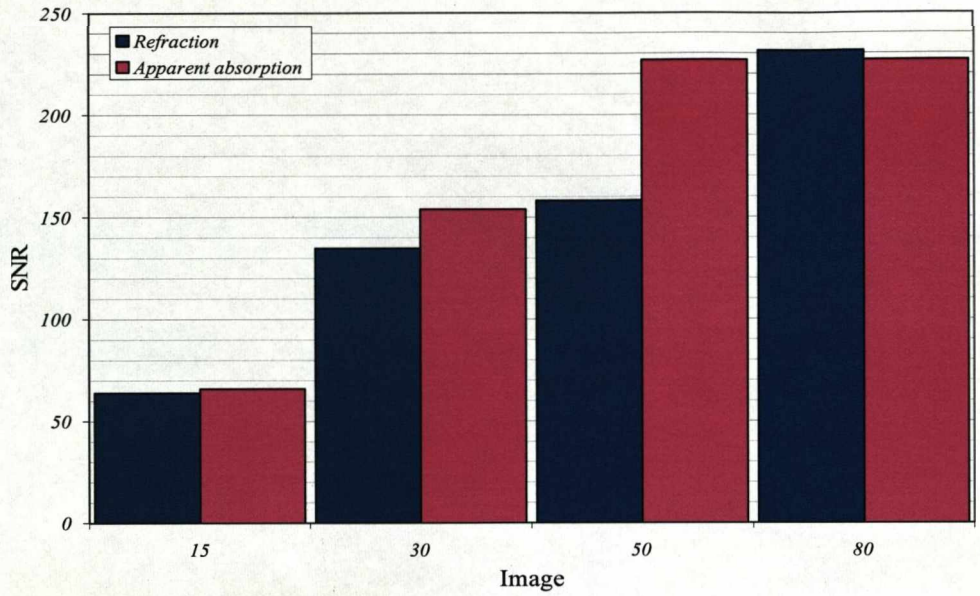

Figure 6-35: The SNR values for the DEI images of the whole sample in the first orientation.

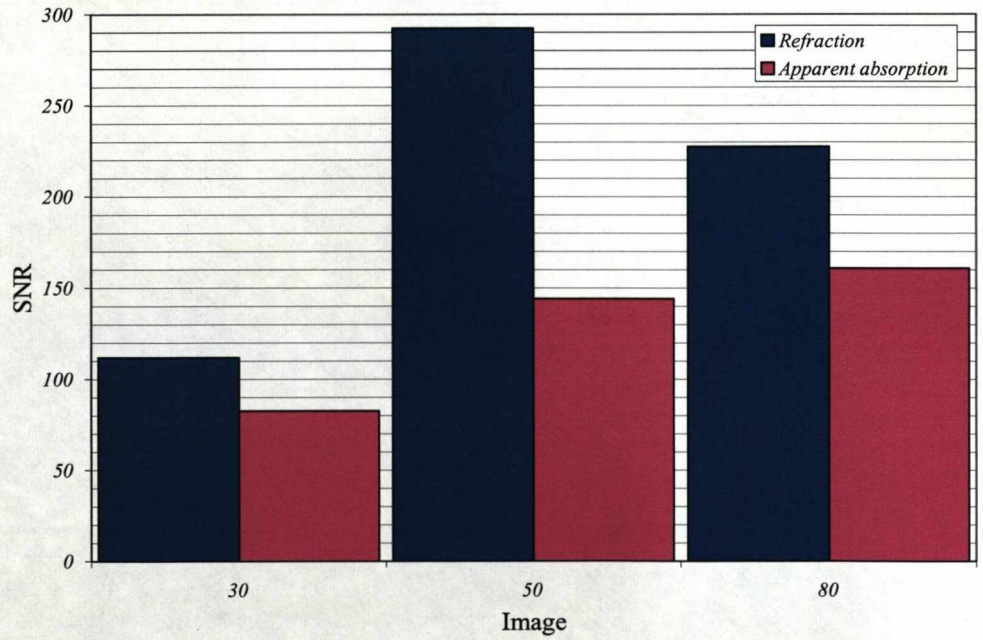

Figure 6-36: The SNR values for the DEI images of the whole sample in the second orientation.

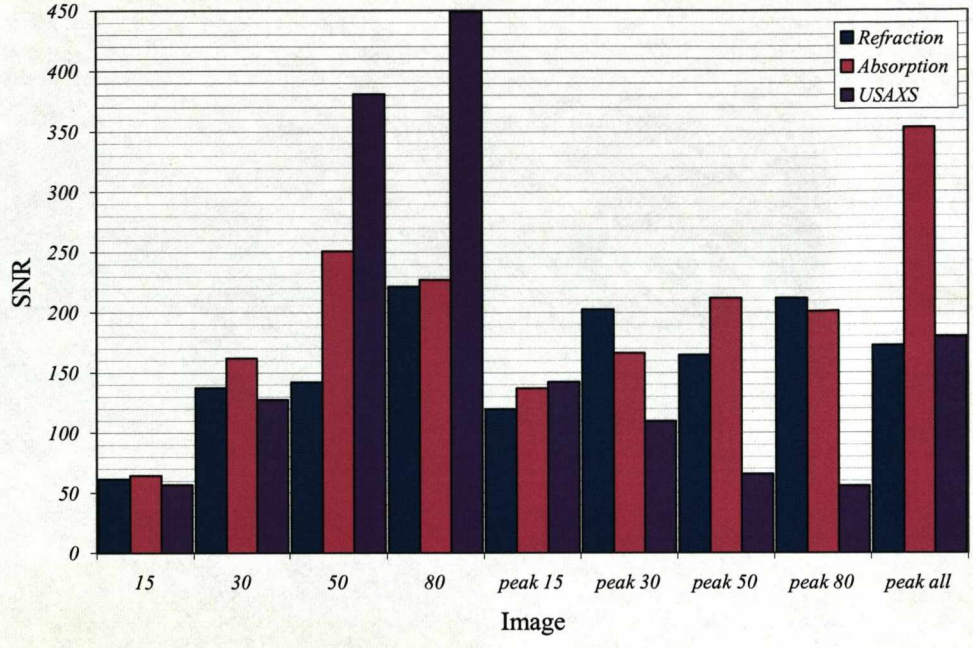

Figure 6-37: The SNR values for the MIR images of the whole sample in the first orientation.

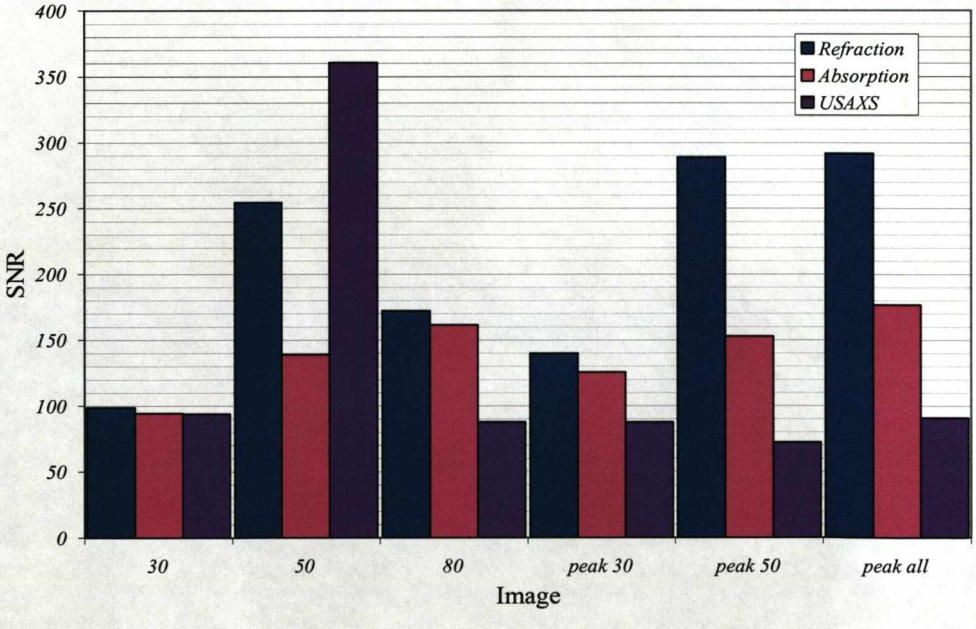

Figure 6-38: The SNR values for the MIR images of the whole sample in the second orientation.

Comparisons of the MIR and DEI results for first and second sample positions are shown in Figure 6-39 and Figure 6-40 respectively. With the exception of the MIR absorption image at ±50%, all the SNR values were very similar for the sample in the first orientation, as Figure 6-39 shows. The results for the second sample position are generally similar. However, the DEI refraction images consistently gave slightly higher SNR than their MIR equivalents.

As mentioned at the start of this section, the sample was also imaged in a third orientation, with the sample facing the beam. The ±50% DEI images of the sample in this position are shown in Figure 6-41 and the ±50% MIR images are shown in Figure 6-42. The absorption images, in Figure 6-41 and Figure 6-42 a), show the structure of the bone, but do not show any soft tissue structure. The refraction images, shown in Figure 6-41 and Figure 6-42 b), as with previous refraction images, show the structure of the bone clearly. Unlike the previous refraction images of this sample, the cartilage in the joint can clearly be seen and is shown in close-up of the joint region. The cartilage is visible in the joint when imaged in this position, not the previous two, because there is less superposition from the surrounding soft tissue. The MIR USAXS image is shown in Figure 6-42 c). As with previous USAXS images this clearly shows the structure of the bone, with more detail than the absorption image. The USAXS image, however, does not show the cartilage.

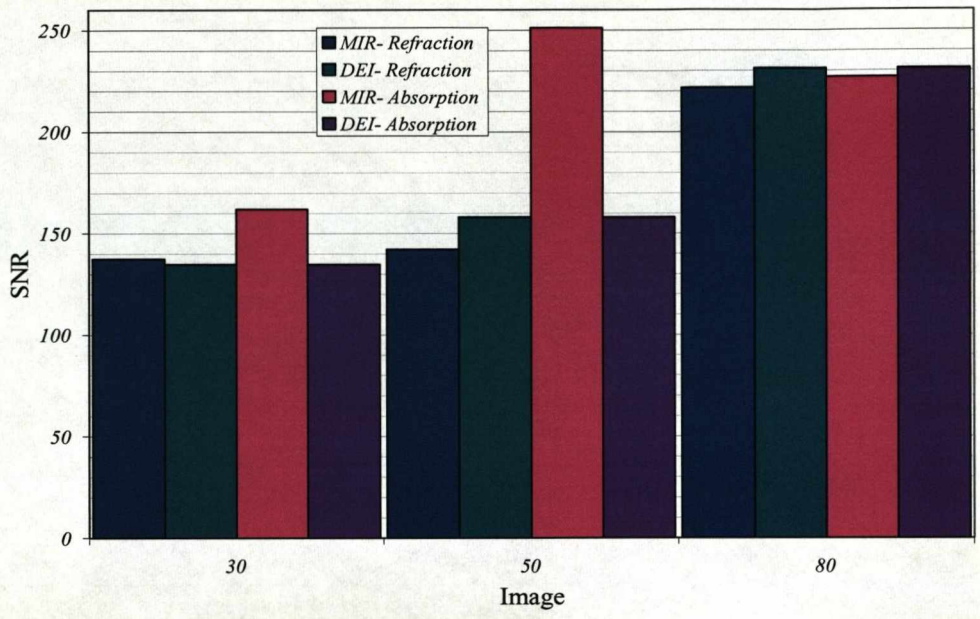

Figure 6-39: A comparison of the SNR values given by the DEI and MIR images of the whole sample in the first orientation.

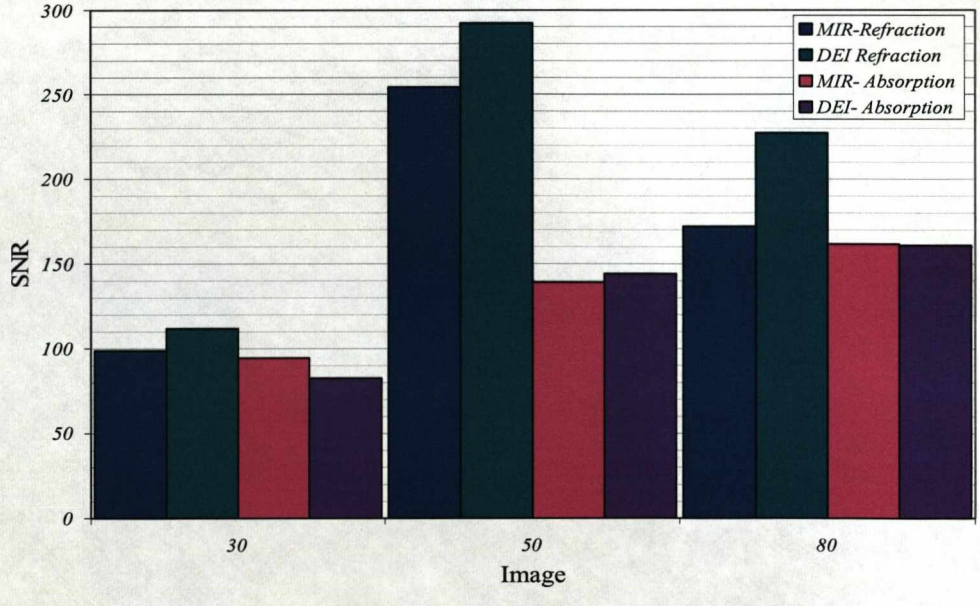

Figure 6-40: A comparison of the SNR values given by the MIR and DEI images of the whole sample in the second orientation.

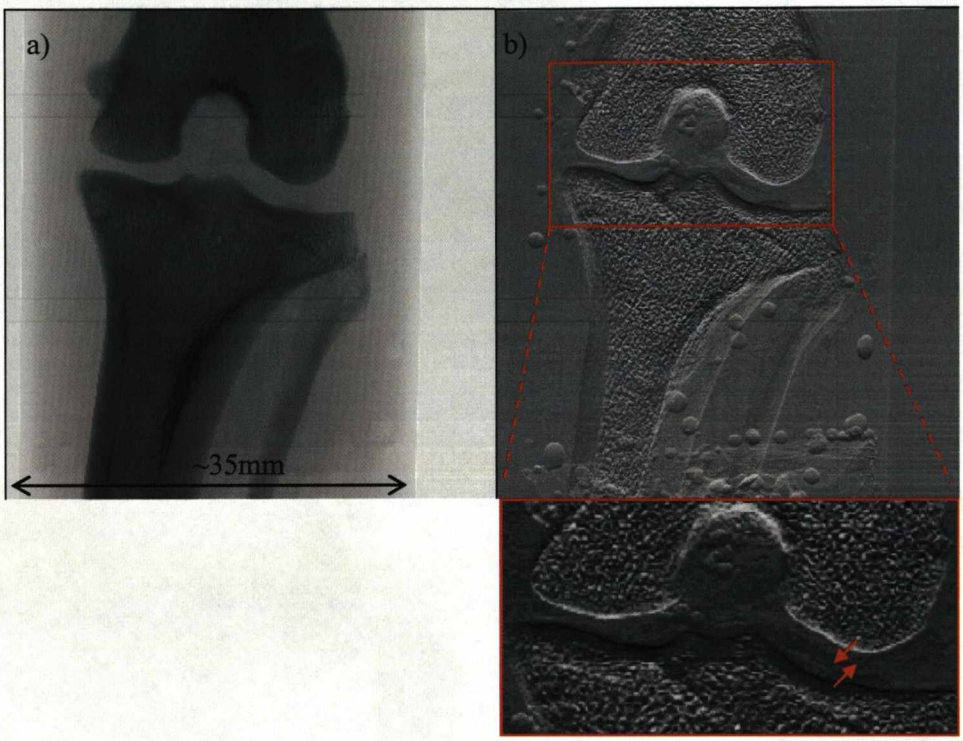

Figure 6-41: The ±50% DEI images of the whole sample in the third orientation. a) The apparent absorption image. b) The refraction image. The cartilage region is highlighted by the red arrows.

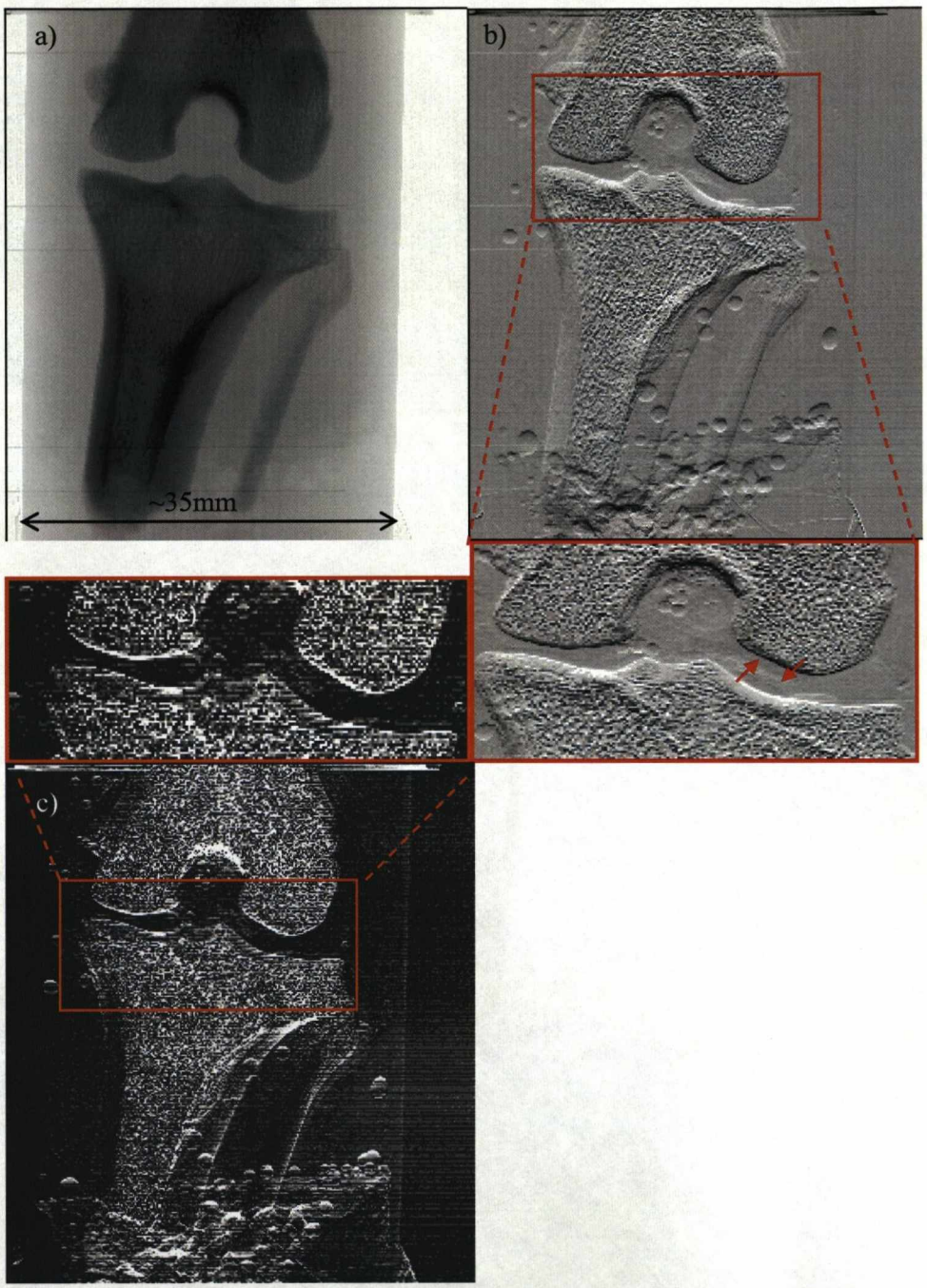

Figure 6-42: The ±50% MIR images of the whole sample in the third orientation. a) The absorption image. b) The refraction image. The cartilage region is highlighted by the red arrows. c) The USAXS image.

The SNR analysis of the DEI images of the sample in this position is shown in Figure 6-43. For both the ±50% and ±80% images sets the refraction images had higher SNR than the absorption image. Figure 6-44 shows the SNR analysis for the MIR image set of the sample in the third orientation. The refraction image SNR values were, with the exception of the results for the peak ±80% image, all higher than the absorption images. The results for the peak ±50% refraction image and ±50% refraction image showed that by increasing the number of component images the SNR increases. The peak ±80% refraction image and ±80% refraction image results showed that this is also dependent on the SNR values of the constituent images. These results were also reflected in the SNR values for the absorption images. The USAXS results however show a lot of deviation and have no clear trend. A comparison of the SNR values for the DEI and MIR images is presented in Figure 6-45 and shows results for both methods are very similar, although the MIR values were generally slightly higher than those for their corresponding DEI image.

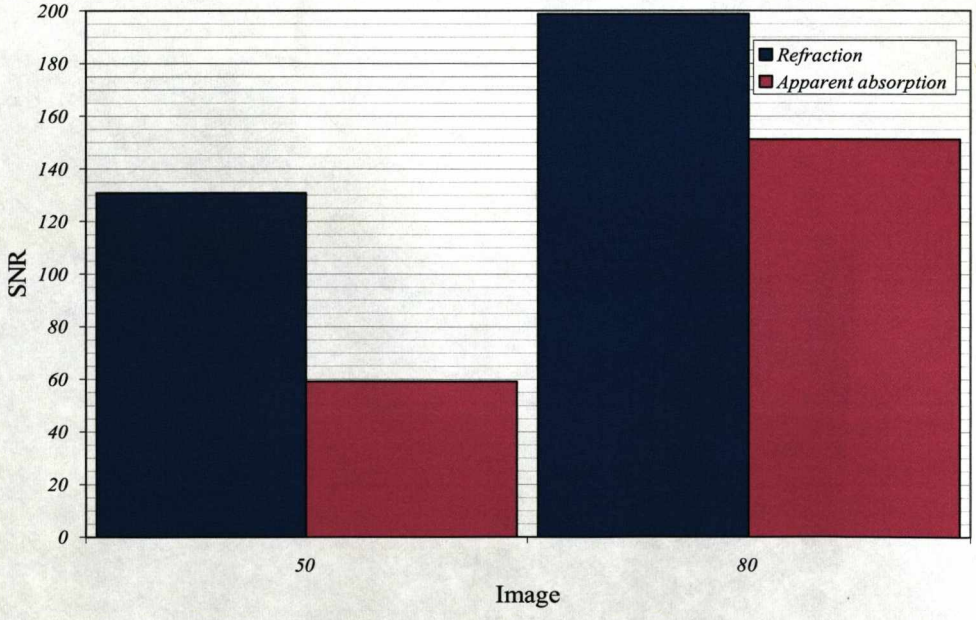

Figure 6-43: The SNR values of the DEI images of the whole sample in the third orientation.

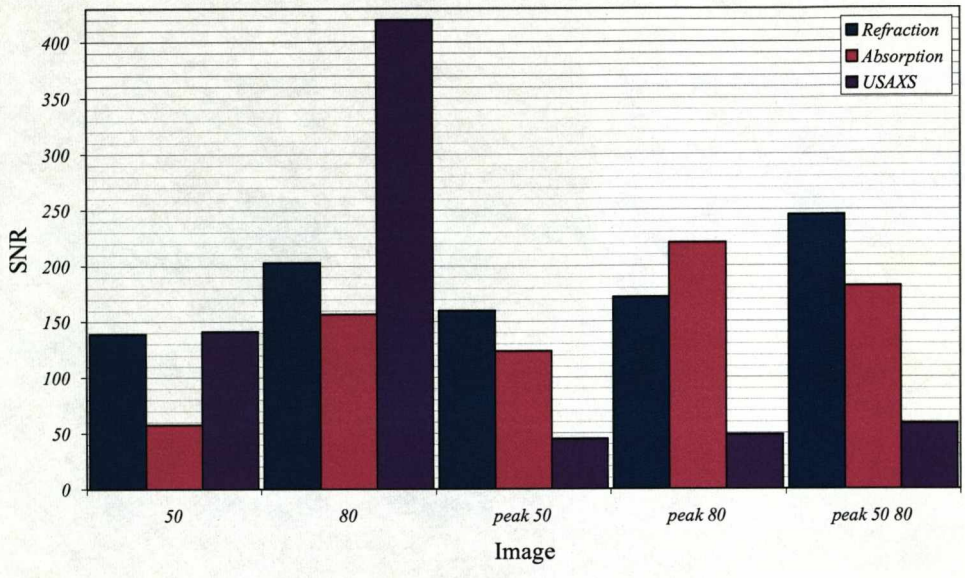

Figure 6-44: The SNR values of the MIR images of the whole sample in the third orientation.

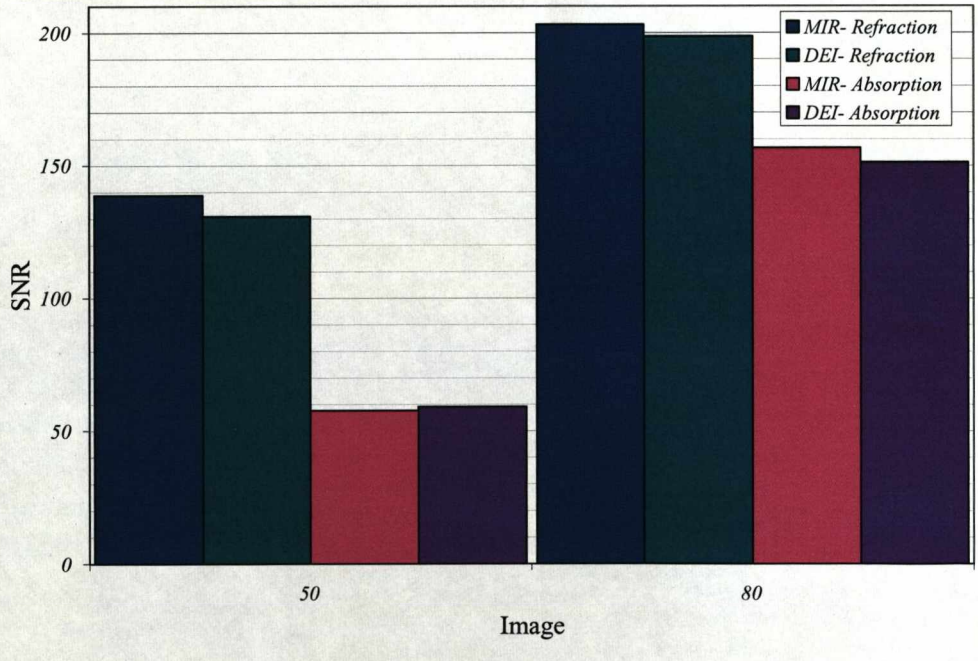

Figure 6-45: A comparison of the SNR results for the DEI and MIR results for the whole sample in the third orientation.

As shown in Figure 6-42, the cartilage can be seen in the refraction images of the joint when the sample was in its third imaging position. Further analysis was therefore carried out. As can be seen in Figure 6-44, the refraction that gave the largest SNR was the peak ±80% ±50% image, therefore it was this image that was used in the investigation. Figure 6-46 shows a close up of the joint, and the cartilage can be seen clearly. To study this more closely, the surfaces of the joint were divided into regions, as shown in Figure 6-47, and the average SNR_{LINE} values were found for each.

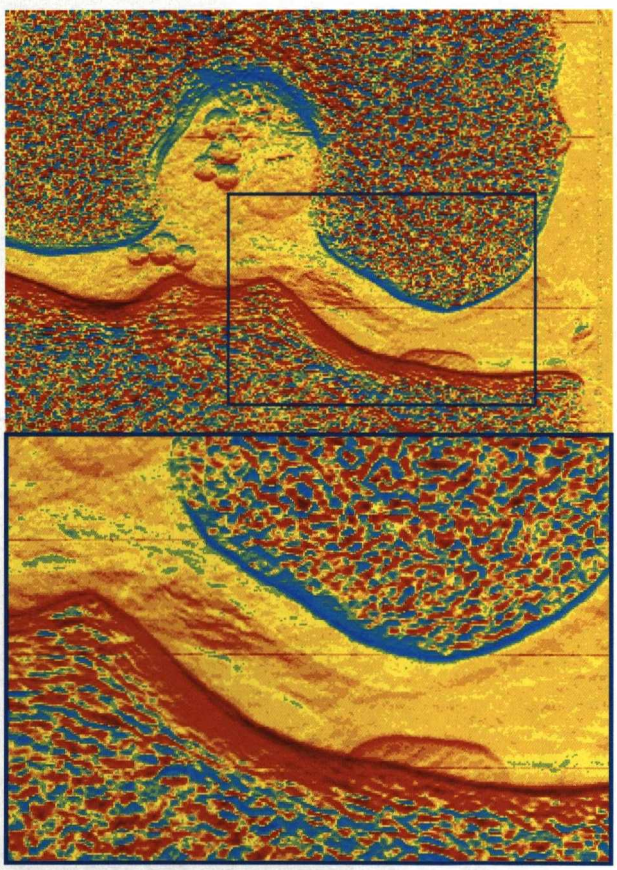

Figure 6-46: Close-up views of the joint region of the peak ±80% ±50% refraction image, showing the joint cartilage.

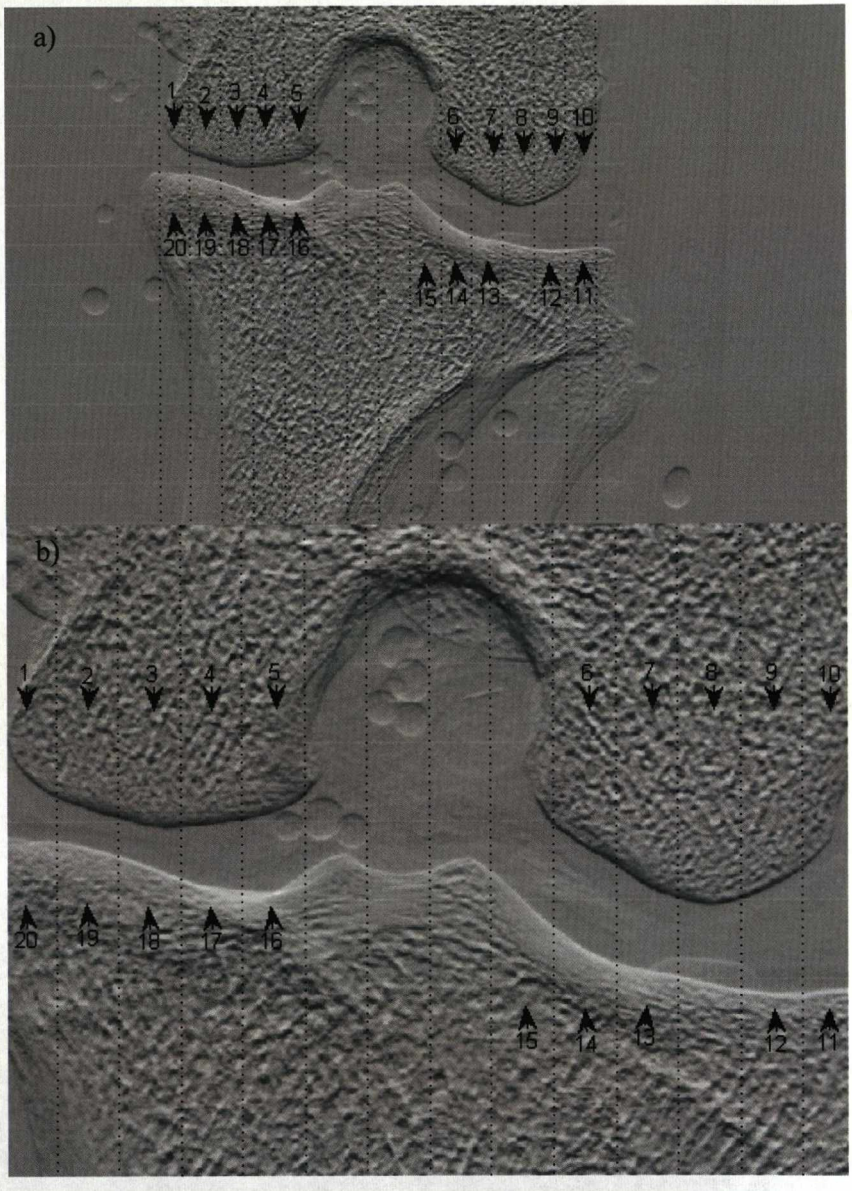

Figure 6-47: Images showing how the joint was divided into regions. a) How showing the whole of the sample. b) A close- up of the joint region.

The results for the SNR_{LINE} analysis of the peak ±80% ±50% refraction image are shown in Figure 6-48. The results gave a wide range of values, from 0.26 in Region 3, to 13.9 in Region 6. The regions which gave high and low SNR_{LINE} values are highlighted in Figure 6-49. As Figure 6-49 shows, the highest values are

given in the regions which are more open and the lowest in the regions which are more enclosed. The only exception to this is Region 1, which was on the edge of the sample.

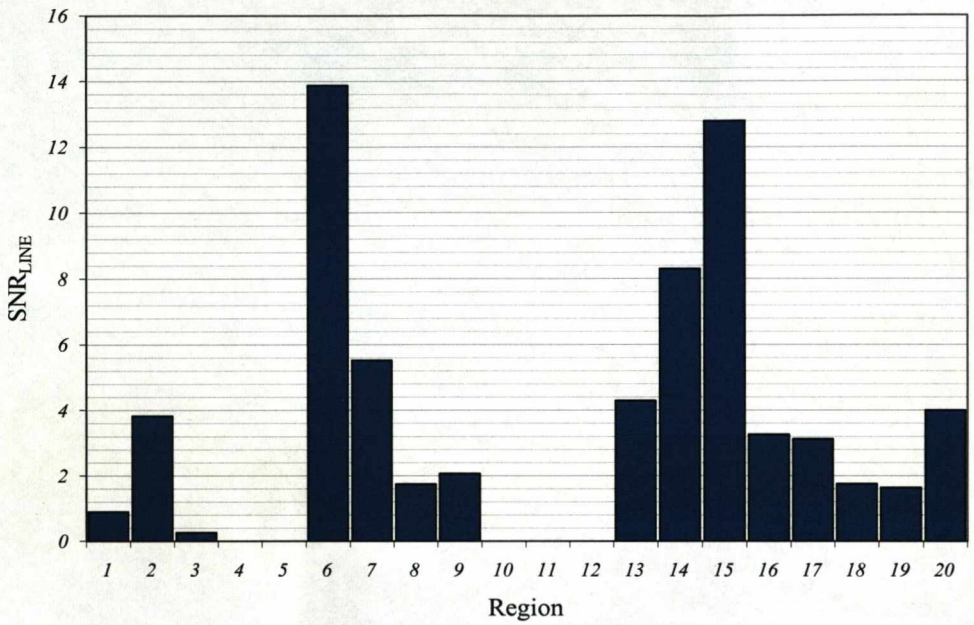

Figure 6-48: A plot showing the SNR_{LINE} values for the different regions in the peak 80% MIR refraction image.

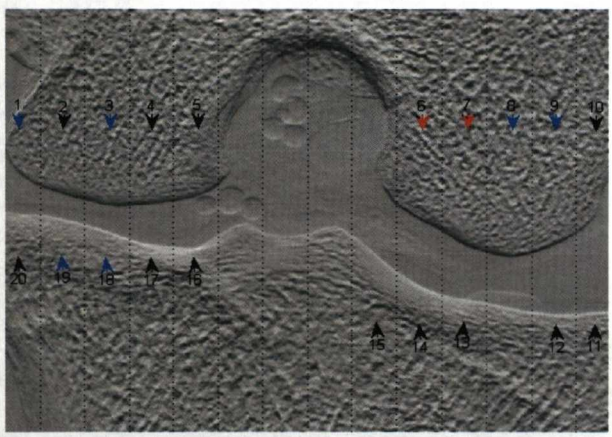

Figure 6-49: An image of the joint showing the different regions. The regions that gave low SNR_{LINE} values are marked in blue and the regions that gave high SNR_{LINE} values are marked in red.

MR-images of the sample are shown in Figure 6-50. Images of the sample were taken from two orientations, the first from the side and the second from the front. The cartilage in the joints is clearly visible in both views of the sample. This was not the case in the ABI images, where the cartilage was more prominent with the sample in the forward facing position. This is due to the MR-images being taken as slices and the ABI-images being projection images causing there to be a superposition of the surrounding structures. When the sample is in the forward facing orientation, there also appears to be a correlation with the high contrast region of the cartilage in the MR-image and the regions of the refraction image that gave high SNR_{LINE} values (see Figure 6-49).

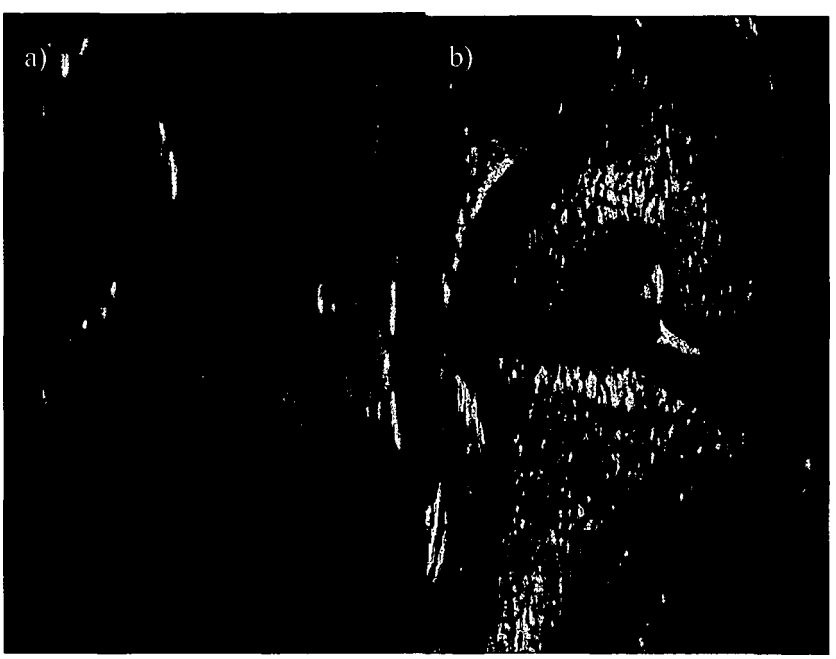

Figure 6-50: MR-images of the whole sample. a) The sample in the first orientation. b) The sample in the second orientation.

6.4.2 Experiment Summary

The results for the canine joint samples have been presented in the previous sections. The samples themselves were imaged with the analyser crystal tuned to a number of different positions and, in case of the disarticulated and the whole

sample, with the sample itself in different orientations. By imaging the samples at different positions on the rocking curve it was possible to create both DEI and MIR image sets. A common feature was the line artefacts that were caused by the misalignments of the flat fields and were present to a greater or lesser extent in all the images.

Both the DEI and MIR methods created absorption images. All the absorption images of all the samples showed clearly the structure of the bone, but did not show any soft tissue structures. The refraction images, also created by both methods, again showed the bone structure for all the samples. However, they did so with greater sharpness than the absorption images. In both of the orientations for the disarticulated sample imaging, the layer of the cartilage was also visible in the refraction image. This was also the case in the refraction images of the whole sample in the third orientation. However, when in the other two orientations, due to the superposition of other structures, the cartilage could not be seen. The cartilage was also visible in the refraction images of the core sample. The USAXS images, as with the previous forms of images, showed the structure of the bone, and, in a similar way to the refraction images, did so more sharply than the absorption images.

SNR analysis was also carried out on the images. The results given showed a lot of variation. The SNR values for the refraction images were dependent on two things: firstly, the noise in the image, mainly how much effect the presence of the line artefacts had; secondly, the imaging position on the rocking curve. As shown in the previous sections, the ±15% image pairs consistently gave the lowest SNR values, followed by the ±30% SNR values. Of the other two imaging positions the ±50% image set would generally be expected to give the highest SNR. However, this was also influenced by how much effect the line artefacts had on the images. For the MIR images, the SNR values of the refraction images were also dependent on the number of component images, and as the number increased so did the SNR. However, this too was affected by the general quality of the constituent images.

A similar result was seen for the absorption images: the ±15% and ±30% images constantly gave the lowest values of SNR respectively; while the ±50% image would give the highest SNR value. However, this was again dependent on the effect that the line artefacts had on the image. The MIR absorption image also followed the general trend of the SNR value increasing with the number of images. This was again affected by the image quality of the component images.

The SNR results for the USAXS showed the most variation. Like the refraction and absorption contrast the USAXS SNR was influenced by several things: the SNR of the component images; the number of images used; and the position in the rocking curve. However, the positions on the rocking curve seemed to have a strong effect meaning it was not always the case of the SNR increasing with the number of imaging positions. This problem occurred because the images were taken at specific positions on the rocking curve, in the colloidal polystyrene experiments where a series of images were taken along the rocking curve the SNR increased as the number of imaging positions increased.

Further analysis was also carried out on the refraction images of the disarticulated sample in the second imaging position, and the whole sample in its third imaging position. This was done in order to look at the cartilage region more extensively. In the case of the whole sample, the cartilage could clearly be seen in the joint and the results of the SNR_{LINE} analysis showed the position in the joint made a difference to how visible the cartilage was. The results from the disarticulated sample showed too that the SNR_{LINE} varied with the position in the joint. Line profiles were also plotted for one of the regions of the cartilage in this sample and showed that there was a clear peak going from the background to the cartilage and again from the cartilage to the bone. They also demonstrated further potential for the seeing more structure in the cartilage.

6.5 **Human Knee samples**

This experiment was carried out at the Daresbury SRS using excised human knee samples, with a beam energy of ~40 keV. A total of twelve samples, from six patients were imaged using both DEI and MIR. Comparative MRI image sets were also taken. Results from two of the samples are presented in this section; the rest can be seen in Appendix 3.

The DEI images of Sample 006B, are shown in Figure 6-51. In the apparent absorption image (Figure 6-51 a)) the structure of the bone can be seen, but no cartilage is visible. In addition, the quadrant boundaries between the top and bottom halves of the detector are very visible. The refraction image (Figure 6-51 b)), also shows the structure of the bone. However, it does so in greater detail than the apparent absorption image as well as visualising the sample's cartilage. As with the apparent absorption image, the quadrant boundaries can be seen; there are also vertical stripes, particularly in the bottom half of the detector, as well as several small bubbles in the solution containing the sample.

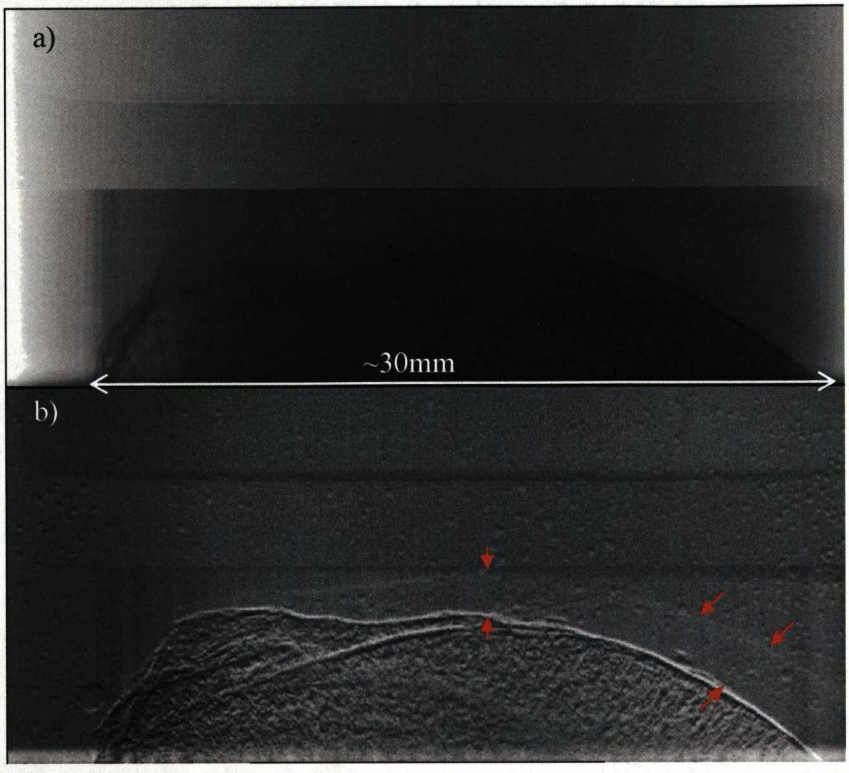

Figure 6-51: The DEI images of Sample 006B. a) The apparent absorption image. b) The refraction image. The cartilage region is highlighted by the red arrows.

The presence of the quadrant boundary and the vertical lines in the images suggest that there was a problem with the flat field subtraction, as was also the case in one of the refraction phantom experiments (Section 5.3.2). In order to establish if this was the case, profiles of the images were created, where the image profile is a plot of the Intensity, averaged over the pixels in the vertical direction of the image plotted against the horizontal pixel number, as shown in Figure 6-52, which shows such plots for the ±50% images and flat fields.

Looking at the profiles for the flat fields, it is clear that there is a large difference in intensity across the profiles, as well as there being a variation between the ±50% flat fields. Both of these factors can be attributed to a tilt on the analyser crystal, resulting in different parts of the beam being diffracted to different intensities, both

across the profiles and on the different sides of the rocking curve. Due to the relatively large size of the samples, the image profiles do not follow the profiles of the flat field images, apart from the very obvious features such as the quadrant boundary.

In addition, from the images in Figure 6-51, the background is only visible on the far left. At this point in the profiles, the flat field and image profiles should have approximately the same intensity. However, as Figure 6-52 shows this is not the case, with the intensity in both the ±50% images being lower than their respective flat fields. In order to correct for this problem average values for the background region in both the images and the flat fields were found. From these averages two constants were found, one for the -50% data and one for the +50% data. These constants were then used to multiply there respective images. The profiles of these corrected images are shown in Figure 6-53, and the resulting DEI images created using them are presented in Figure 6-54.

Comparing the corrected image profiles with the non-corrected profiles, the corrected profiles have approximately the same intensity in the background as the flat field profiles, where as the non-corrected do not. In order to verify that this correction led to an improvement in the resulting DEI images, the overall SNR values of the refraction images which used the corrected and non-corrected images were found. The refraction image using the non-corrected ±50% images, shown in Figure 6-51 b), gave an SNR value of 47.80, whereas the refraction image created using the corrected images, shown in Figure 6-54 b), gave an SNR value of 103.93. This therefore shows that correcting the images had led to an improvement in the refraction image. However, looking at the DEI images the quadrant boundaries and vertical lines are still visible.

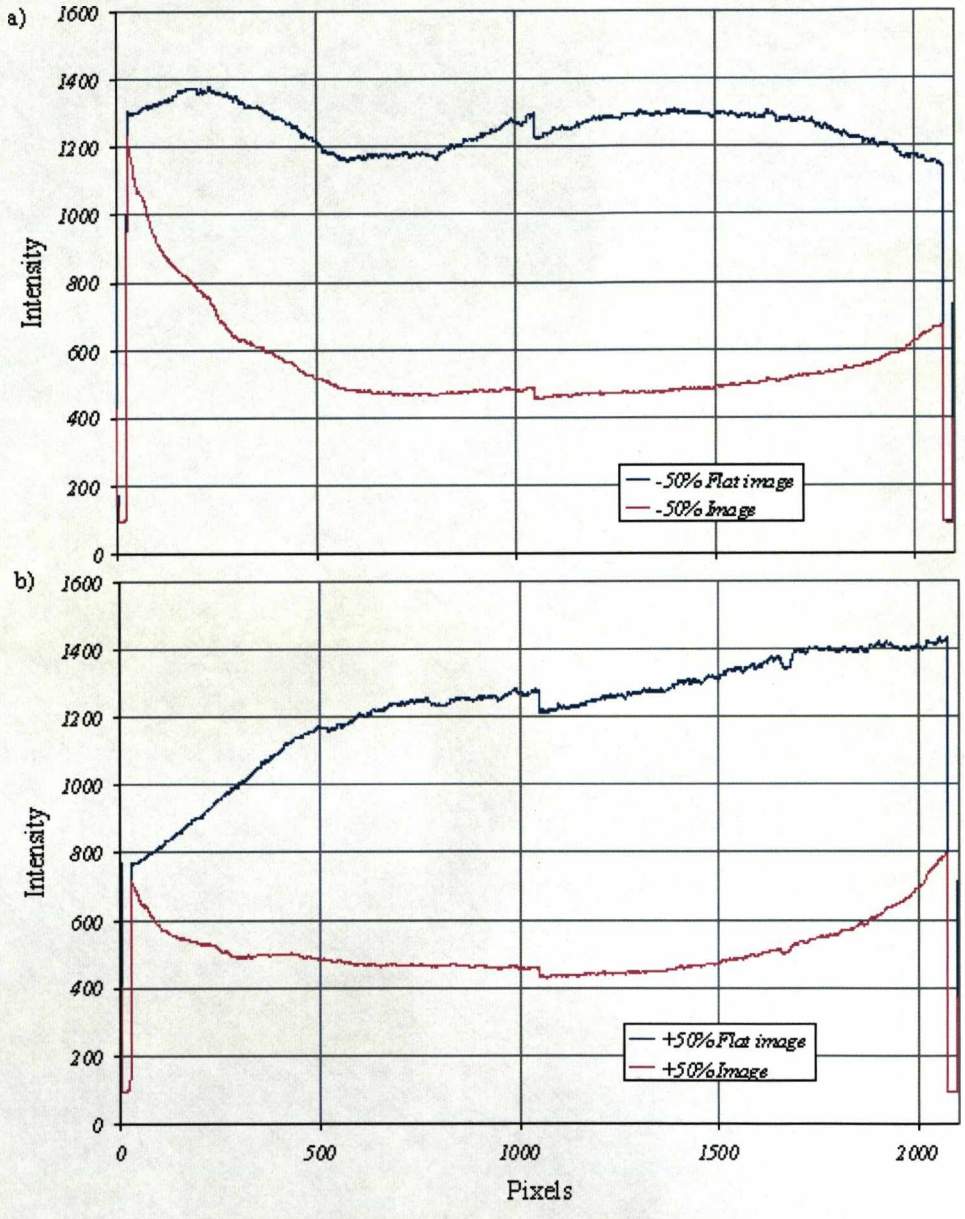

Figure 6-52: Intensity profiles. a) The -50% Flat and Image profiles. b) The +50% Flat and Image profiles.

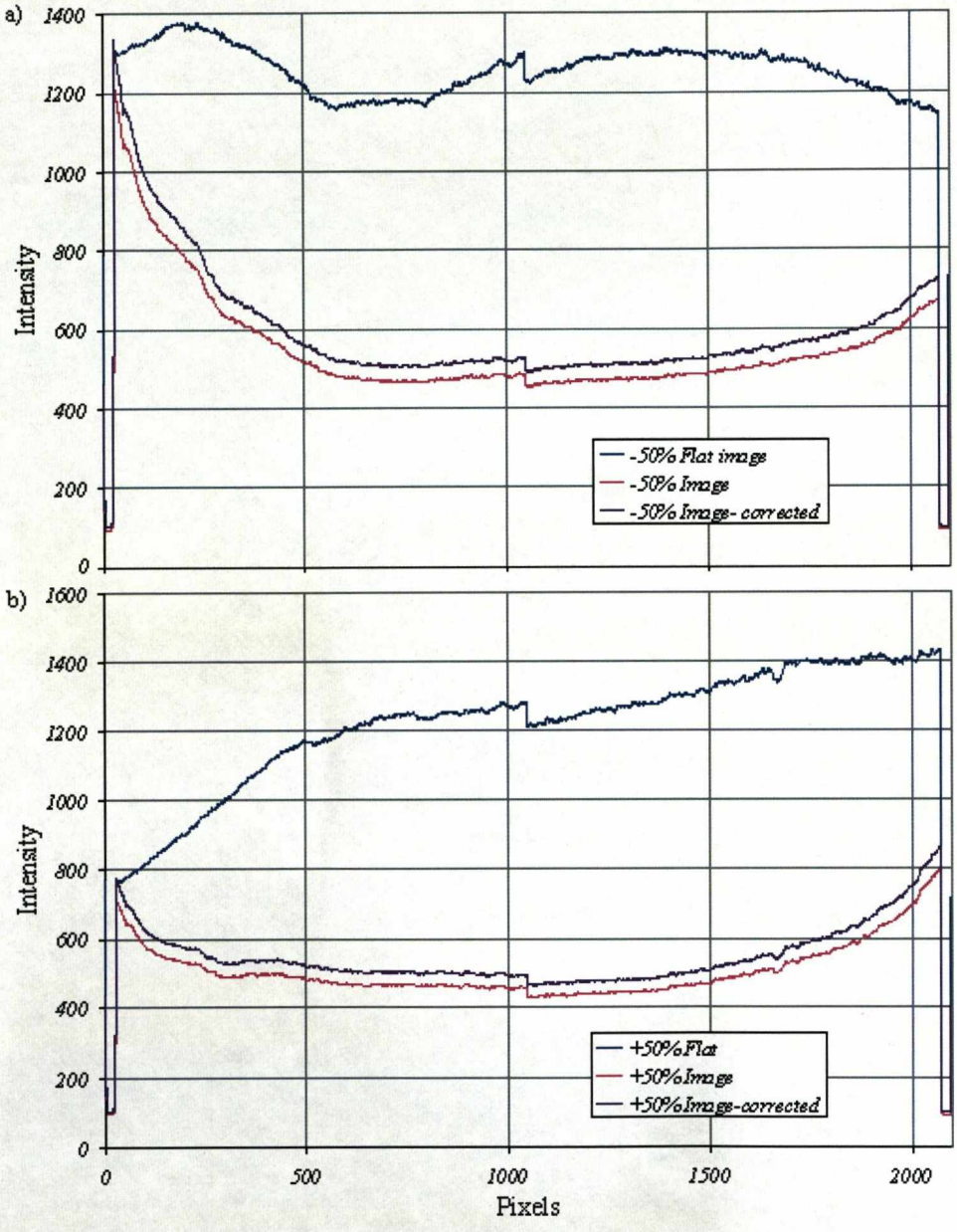

Figure 6-53: The intensity profiles of the corrected images. a) The profiles if the -50% image set. b) The profiles of the +50% image set.

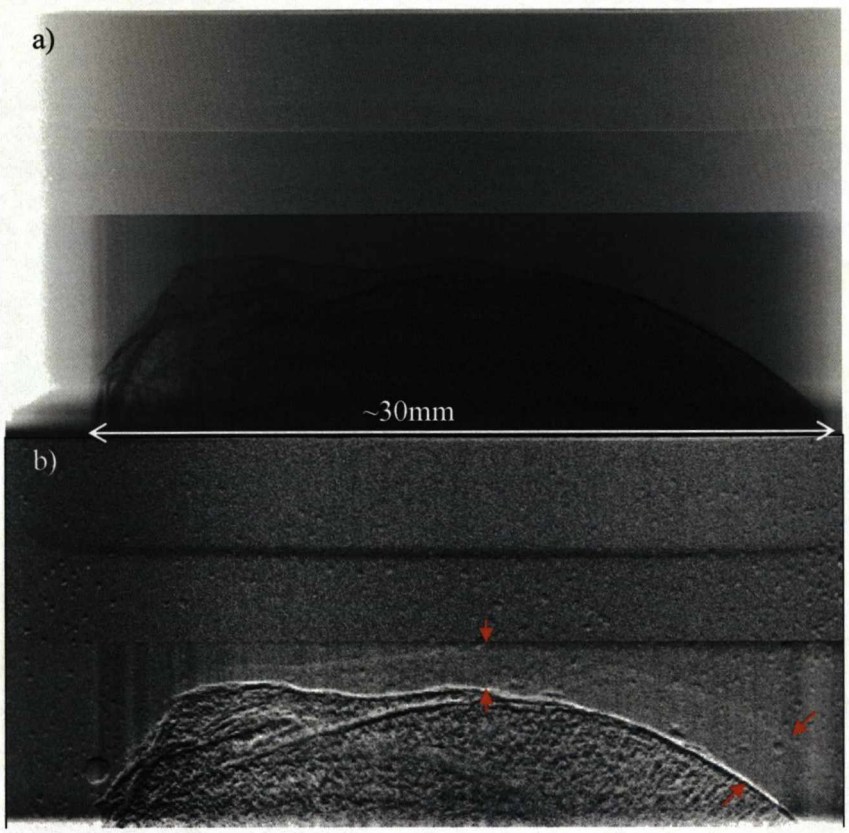

Figure 6-54: The DEI images of Sample 006B using the corrected images. a) The apparent absorption image. b) The refraction image.

In order to examine the presence of the quadrant boundary that cuts horizontally through the image, line profiles were taken along a line which bisected the images vertically, as shown by the red line in Figure 6-55. These profiles were therefore plots of intensity along this line against the pixel number in the y-direction of the image and are shown in Figure 6-56.

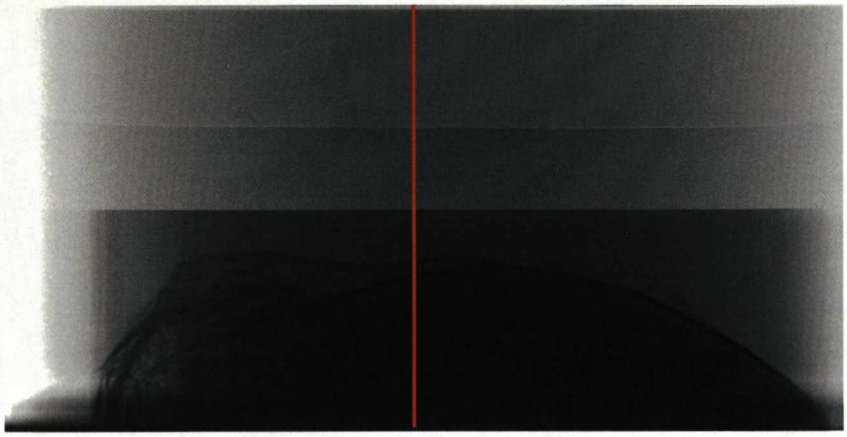

Figure 6-55: Figure showing the positions that the vertical line profile was taken from.

Looking at the profiles created for the flat field images, the quadrant boundary is clearly visible, shown as a step in intensity. In the sample image profiles, however, the boundary is not visible. This is due to the attenuation of the beam through the sample making the step in intensity less prominent. Since the quadrant boundary is present in the flat images and not in the sample images, when the flat field corrections are carried out a step in intensity is introduced as an artefact in the flat corrected images of the sample.

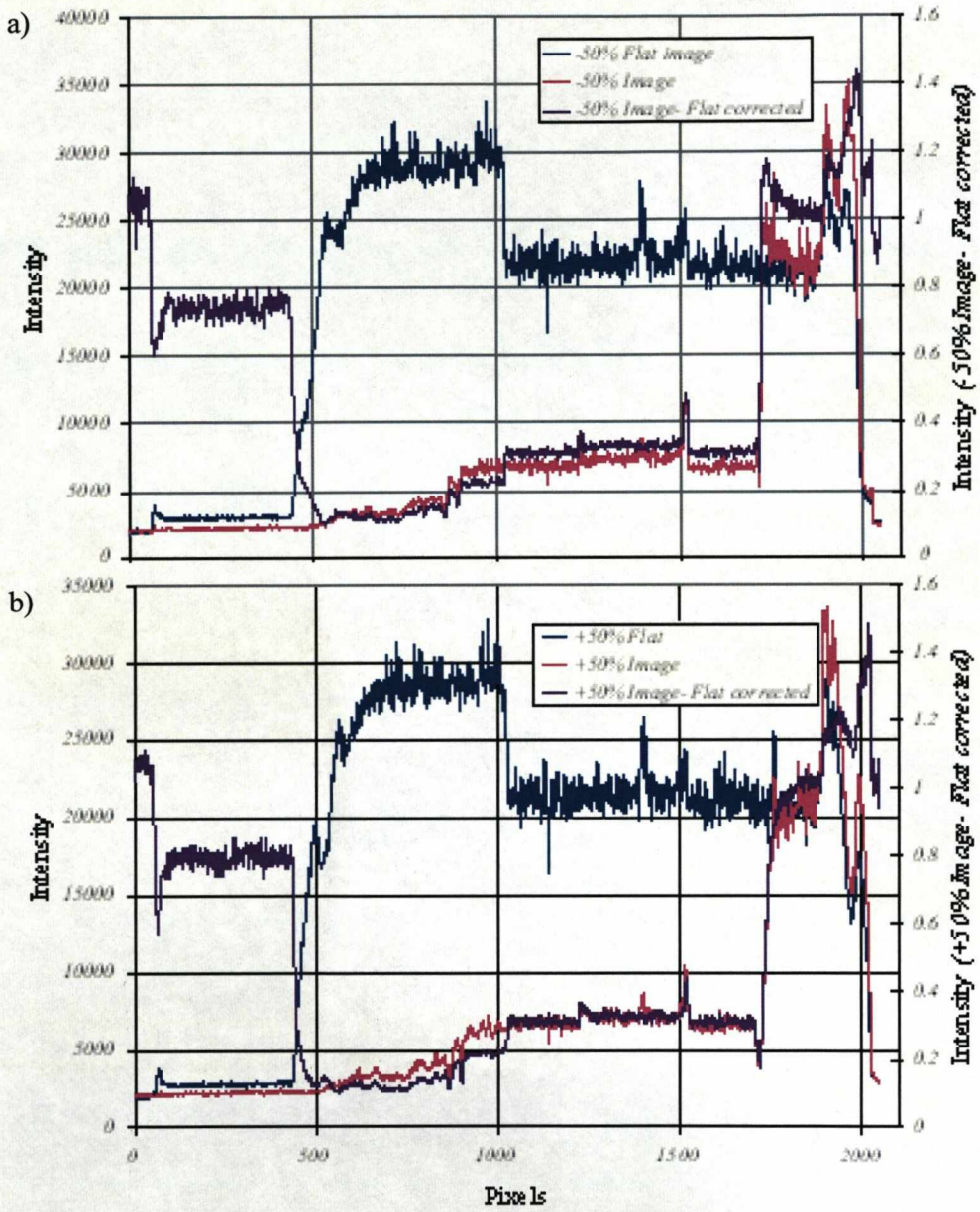

Figure 6-56: Vertical line profiles. a) The -50% image set. b) The +50% image set.

The second artefact that was visible in the DEI images was the vertical lines (see Figure 6-51) which were caused by the tilt on the analyser crystal. As the images show, the vertical lines are more prominent in one half of the detector, this is due

to the bottom half of the detector seeming to have a better response to the intensity variations and is likely to be caused by the same fault with the detector that caused the step in intensity between the two quadrants.

Examining the image profiles has therefore shown that the artefacts that are present in the DEI images were introduced through inaccuracies in the flat field subtraction. There are two reasons why the artefacts are so prevalent in this experiment compared with to previous ones. Firstly, the samples were very thick, leading to high levels of attenuation of the beam. This by itself would not have led to the increased levels of artefacts. However, it was combined with the fact that there was a lot of variation in intensity across the flat fields. The intensity variations had two causes: the tilt on the analyser crystal which led to there being high and low regions in intensity across the images; and problems with the detector which as demonstrated clearly in Figure 6-56, led to steps in the intensity across the images at the quadrant boundaries.

MIR images of the sample were also created. Figure 6-57 shows the MIR set which used all of the series of thirteen images that were taken along the rocking curve.

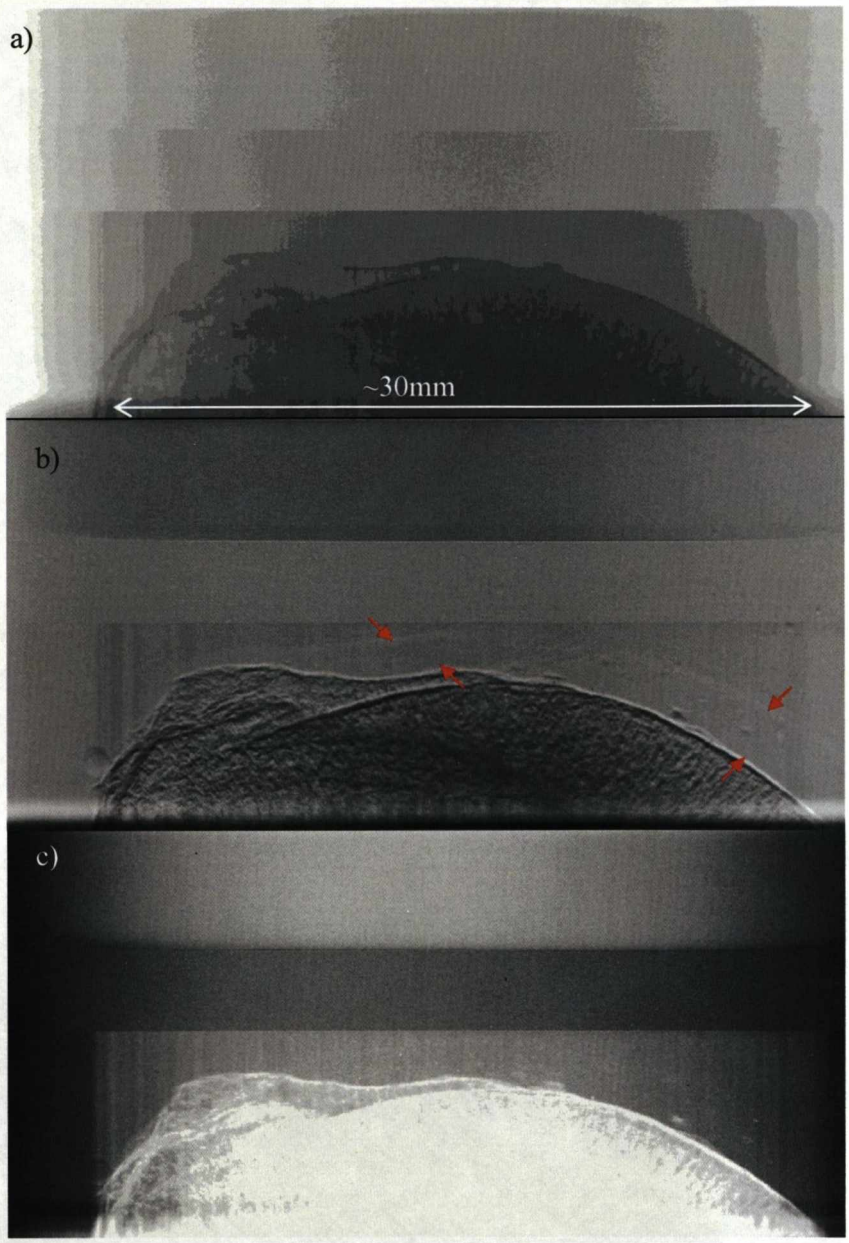

Figure 6-57: The MIR images of sample 006B, created using 13 images taken along the rocking curve. a) The absorption image. b) The refraction image. The cartilage region is highlighted by the red arrows. c) The USAXS image.

The absorption image, Figure 6-57 a), shows the structure of the bone. However, as with the DEI absorption image, it does not show the presence of the cartilage.

The refraction image, Figure 6-57 b), also clearly shows the structure of the bone, as well as visualising the cartilage in the sample. The additional USAXS image produced by this method also clearly shows the structure of the bone, the cartilage, however, is not visible although structures in the cartilage region can be seen. All three MIR images show the quadrant boundary of the detector and faint vertical lines, the same artefacts that were present in the DEI images.

An additional MIR set was also created, this time using just five of the images that were taken along the rocking curve. Visually, these MIR images showed the same results as those created using thirteen constituent images, but, in order to compare the images quantitatively the overall SNR of each image was found. The SNRs of the DEI images were also found so as to compare the two methods. The results are presented in Figure 6-58. It can clearly be seen that the MIR image set using thirteen constituent images (MIR-13) consistently gave the best SNR values for all three types of images. The results also show that both the MIR refraction images gave better SNR values than the DEI images and for the absorption images the MIR-13 values was a lot better than the MIR-5 (the MIR set created using five component images) refraction image and the DEI refraction image, where the MIR-5 image and the DEI image gave very similar values. The results also show that for both the MIR sets and the DEI set, the refraction images gave higher SNR values than their absorption equivalent. Looking at the USAXS results it can be seen that the number of imaging positions and the SNR values are strongly linked for this type of image.

The refraction image, Figure 6-57 b), also clearly shows the structure of the bone, as well as visualising the cartilage in the sample. The additional USAXS image produced by this method also clearly shows the structure of the bone, the cartilage, however, is not visible although structures in the cartilage region can be seen. All three MIR images show the quadrant boundary of the detector and faint vertical lines, the same artefacts that were present in the DEI images.

An additional MIR set was also created, this time using just five of the images that were taken along the rocking curve. Visually, these MIR images showed the same results as those created using thirteen constituent images, but, in order to compare the images quantitatively the overall SNR of each image was found. The SNRs of the DEI images were also found so as to compare the two methods. The results are presented in Figure 6-58. It can clearly be seen that the MIR image set using thirteen constituent images (MIR-13) consistently gave the best SNR values for all three types of images. The results also show that both the MIR refraction images gave better SNR values than the DEI images and for the absorption images the MIR-13 values was a lot better than the MIR-5 (the MIR set created using five component images) refraction image and the DEI refraction image, where the MIR-5 image and the DEI image gave very similar values. The results also show that for both the MIR sets and the DEI set, the refraction images gave higher SNR values than their absorption equivalent. Looking at the USAXS results it can be seen that the number of imaging positions and the SNR values are strongly linked for this type of image.

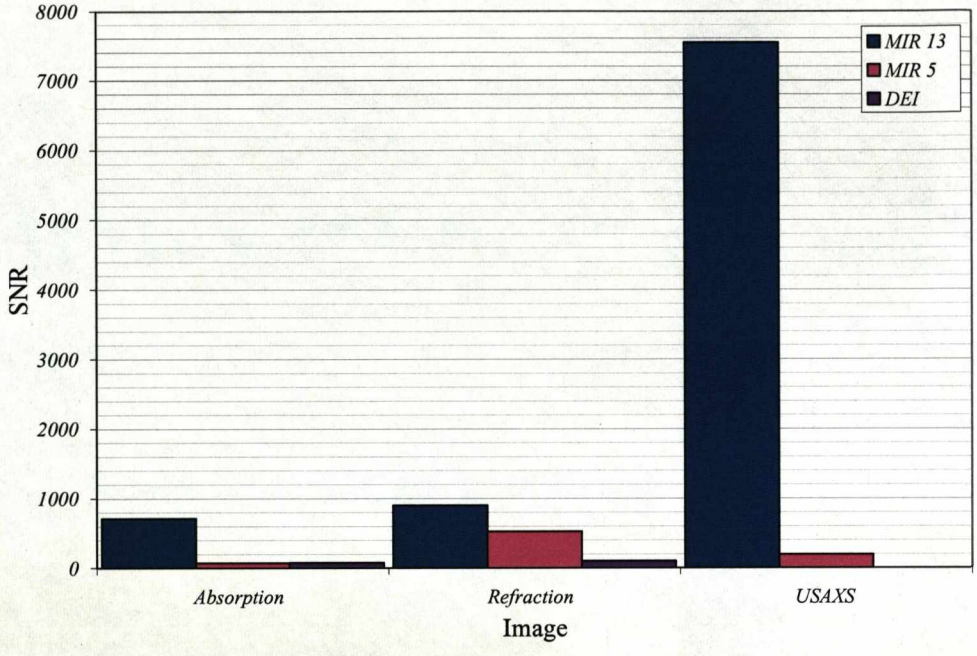

Figure 6-58: Chart showing the SNR of the images so as to compare the image quality of the two methods and to show the variation of in quality given by varying the number of points on the rocking curve using the MIR method.

The main aim of this experiment was to evaluate the ability of the ABI techniques to visualise the cartilage and its structures. As mentioned previously, the refraction images were the only ones which clearly showed the cartilage in the sample. Of these images the refraction image from the MIR image set created using thirteen images on the rocking curve was looked at more closely as it had the best SNR value (see Figure 6-58). This refraction image is shown in Figure 6-59 a). As was noted before the cartilage layer is clearly visible. More structure can be, such as the damaged region in the large red rectangle, and shown in the close-up of the region in Figure 6-59 b). There are also several smaller points which can be seen in the cartilage, one of which is highlighted in the small red square in Figure 6-59 a) and in close-up in Figure 6-59 c). Due to the inaccuracies caused the intensity differences over the images; it was not possible to take SNR_{LINE} for the edge of the

cartilage as was done for two of the canine samples, it also meant that it was not possible to visualise any further structure in the cartilage.

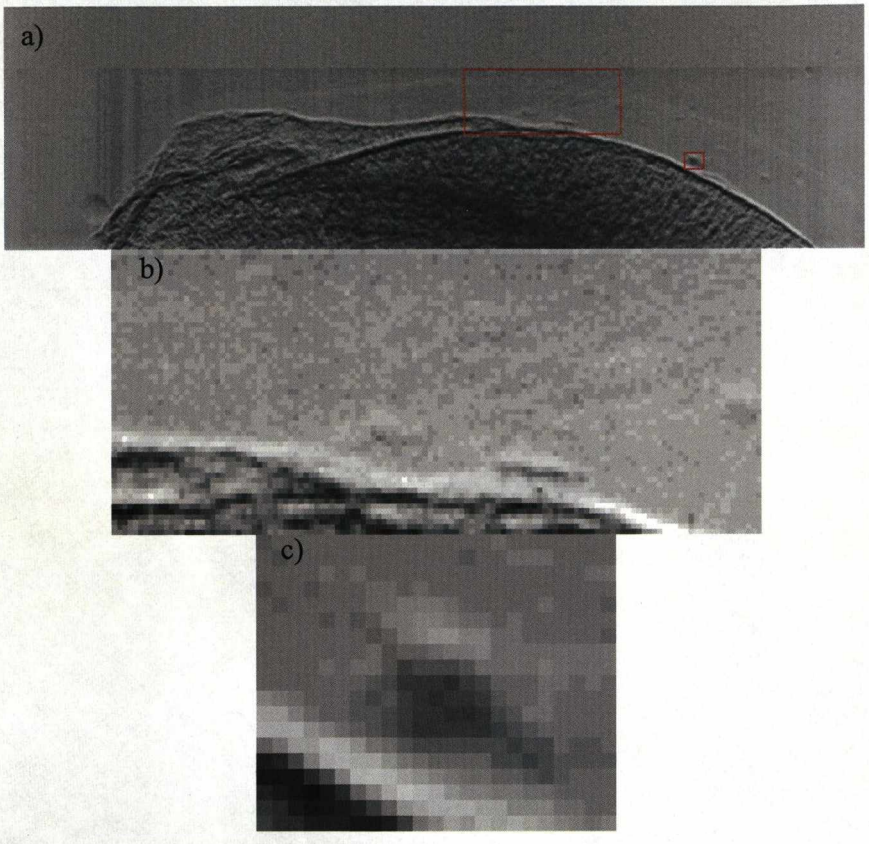

Figure 6-59: a) The MIR-13 refraction image with regions of interest in the cartilage marked. b) A close-up of a region in the cartilage showing damage. c) A close-up of a feature in the cartilage region.

An MR-image of this sample is shown in Figure 6-60, in which the cartilage is clearly visible. Again the MR-image is a slice image through the sample, whereas the ABI images are projection images and the sample will also not be in exactly the same orientation. Despite this, the same defect seen in the ABI images, highlighted in Figure 6-60, is also shown in the MR-image. The cartilage layer is more visible in the MR-image than the refraction images. However, due to the prominence of the artefacts that were present in the refraction images caused by

the ABI system, it is not a fair comparison of the techniques, and does not reflect the true potential of the ABI methods.

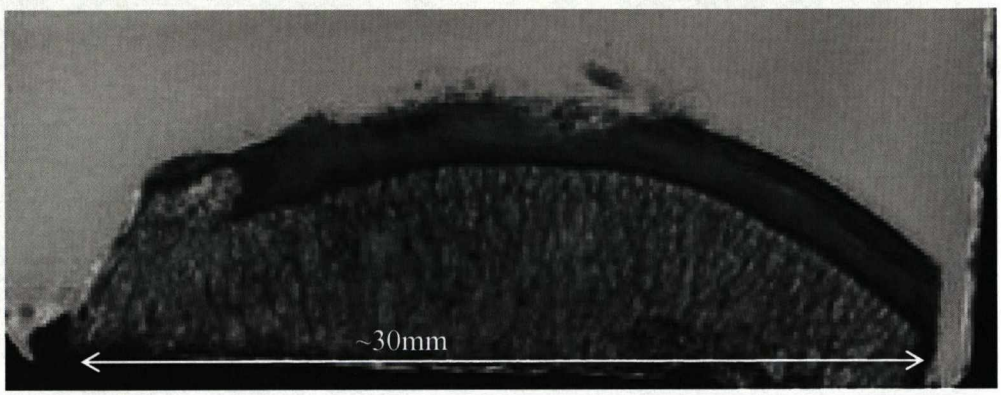

Figure 6-60: MR-image of sample 006B.

The second of the two samples to be described in this section was also imaged using both DEI and MIR. The DEI images of the sample are shown in Figure 6-61. The flat fields were corrected, in the same way as for the previous sample, to create these images. The apparent absorption image, as with the previous absorption images shows the structure of the bone but no cartilage. The refraction image shows the structure of the bone, but the outline of the cartilage can also be seen. Also visible are lots of bubbles in the solution. As with the previous sample, the same artefacts are still present: the vertical lines and the segment boundary.

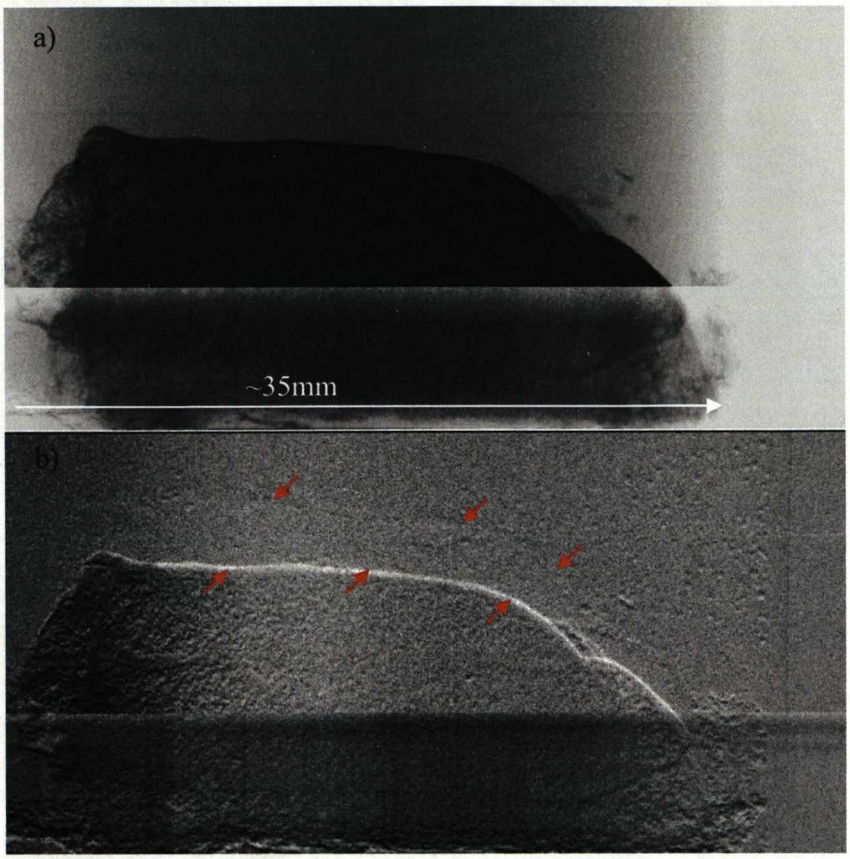

Figure 6-61: The DEI images of Sample 003A. a) The apparent absorption image. b) The refraction image. The cartilage region is highlighted by the red arrows.

MIR images were also created of this sample and those created using thirteen constituent images (MIR-13) are shown in Figure 6-62, although another set was also produced using five component images (MIR-5) which showed the same results. As with the DEI images, the same artefacts are again present in these images. The absorption image, as with the other absorption images, shows the structure of the bone, which can be seen in more detail in the refraction and the USAXS images. The cartilage can also be seen in the refraction images and other defects in the cartilage can be seen in both the refraction and the USAXS image. There is also a subtle increase in contrast in the cartilage region of the USAXS image.

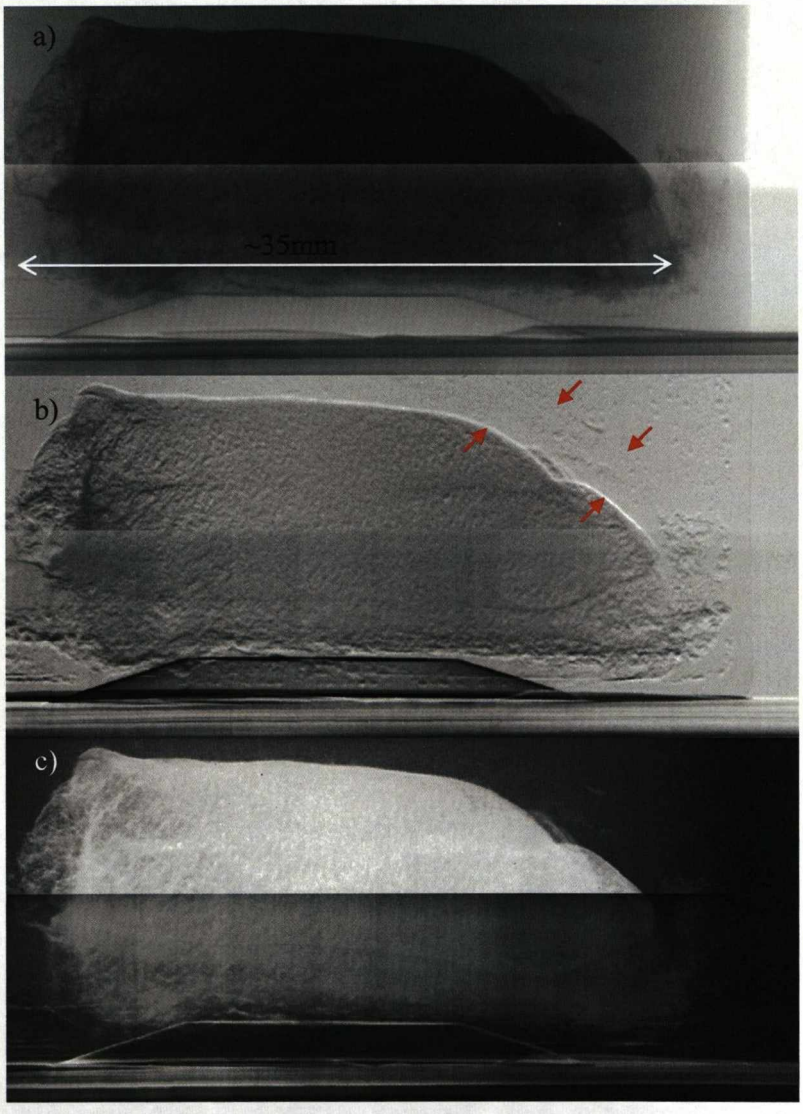

Figure 6-62: The MIR-13 images of Sample 003A. a) The absorption image. b) The refraction image. The cartilage region is highlighted by the red arrows. c) The USAXS image.

The SNR values of each of the images were found in order to compare them quantitatively, as was done with the previous sample and the results are presented in Figure 6-63. As with previous results the refraction images gave higher SNR values than their absorption of USAXS equivalents and the MIR results were consistently higher than the DEI results. Looking at the values for the MIR sets, it can also be seen that for the refraction and USAXS images the MIR-13 images

were higher than the MIR-5 images, whilst the absorption images had approximately equal values SNR confirming that on the whole increasing the number of images taken along the rocking curve increases the image quality.

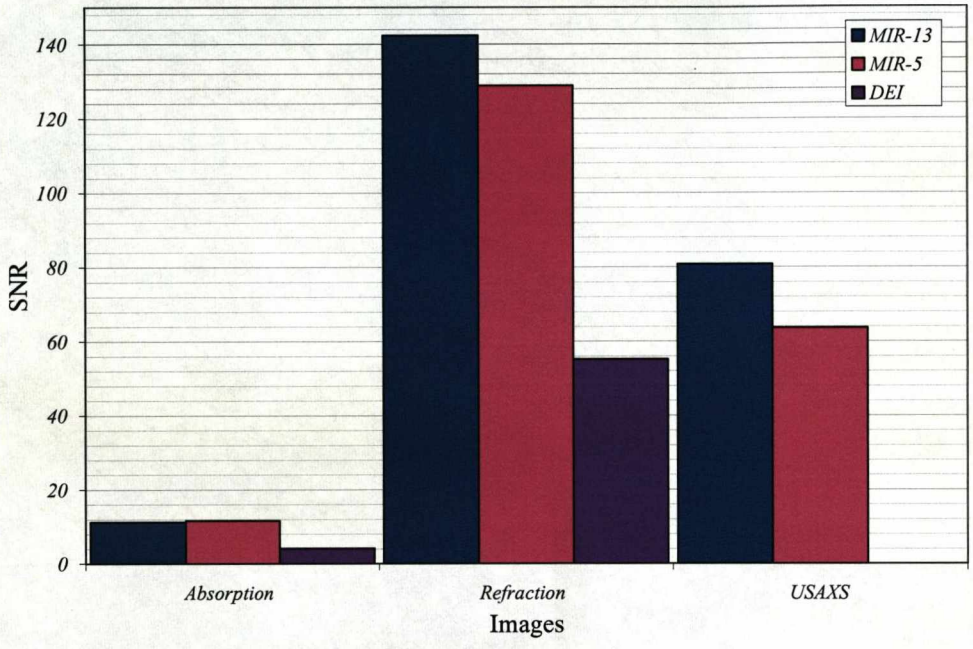

Figure 6-63: A plot comparing the SNR values of each of the images of Sample 003A.

Like the previous sample the artefacts in the images made it impossible to examine the structure of the cartilage further than inspecting the images. Looking at a close up of the cartilage region of the MIR-13 refraction image (the image with the best SNR value) the outline of the cartilage can be seen, highlighted by the red arrows in Figure 6-64, along with small defects, one of which is circled in blue in the refraction image and can also be seen in the USAXS image.

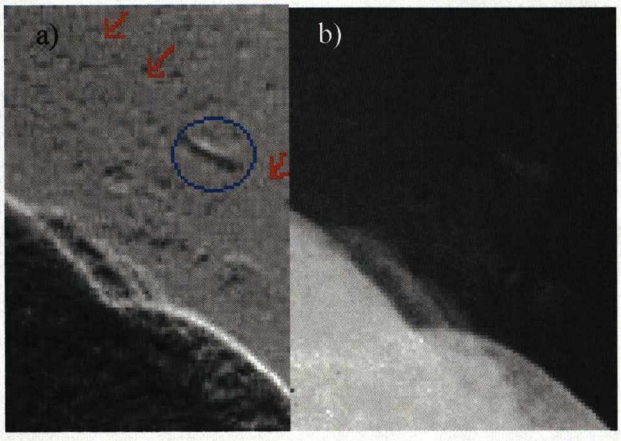

Figure 6-64: Close ups of images of Sample 003A, showing the cartilage region.
a) A close up from the refraction image. b) A close up from the USAXS image.

One of the MR-images of this sample is shown in Figure 6-65. The sample was resized between being imaged using ABI and imaged using MRI. There was not a lot of detail in the sample by which to compare the two imaging modalities, the ABI images were also not wholly representative of the techniques abilities. The MR-image, however, does demonstrate the quality of image that MRI is capable of producing, showing not just the cartilage, but its structure, therefore showing how high the bar has been set for emerging techniques such as ABI.

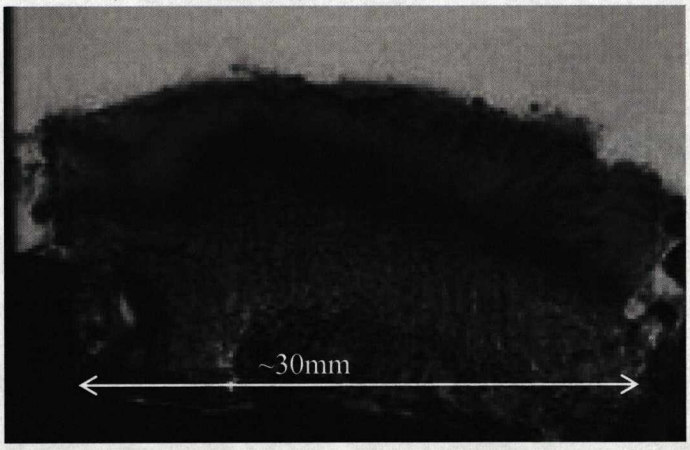

Figure 6-65: MR-image of Sample 003A.

As mentioned in Section 4.2.2.5, sample 003A was also imaged using DEI-CT, however, due to unforeseen problems the data is still under analysis.

The overall aim of this experiment was to establish the ability of the different ABI techniques to visualise cartilage damage, as well as potentially its structure. However, due to problems with the system the results did not show as much as had been hoped. Nonetheless, they did provide further information on the system and highlighted areas of improvement, such as the detector.

CHAPTER 7

7 CONCLUSIONS AND FUTURE WORK

The work for this thesis was carried out as part of a larger project which aimed to develop the ABI system at the Daresbury SRS. As part of this work, channel-cut crystals were used for the first time on such a system and the first experiments utilising them are reported in this thesis. My work on this project fell into two main areas; firstly, to develop phantoms which are specific to the different sources of contrast used in the ABI techniques; and secondly, to investigate the potential areas of interest in biological imaging, specifically cartilage imaging.

7.1 **Phantom development**

There were several different factors to be considered in developing the different phantoms: firstly, they should be capable of characterising different sources of contrast, therefore requiring them to provide a range of contrast values; secondly, the phantoms should work over a wide energy range; and thirdly, they should be easily reproducible, to provide continuity between experiments.

No phantoms had previously been imaged using ABI with the specific aim of looking at the absorption contrast. The experiment presented in this thesis was therefore the first to do so and a simple step phantom design was used. The absorption phantom was imaged in one experiment, using a 40 keV beam on ID17 at the ESRF, and several DEI and MIR image sets were created. The plots of I/I_0 versus step thickness for both of the ABI techniques were good, deviating very little from the theoretical prediction which was well within region of error, showing the accuracy of both techniques for this source of contrast. The SNR_{AREA} against step thickness plots showed that for the DEI image sets the ±50% gave the best results over all the step thicknesses. This was also true for the MIR results when comparing the image sets which utilised a single image pair. The MIR image

results also consistently gave better SNR_{AREA} values than their DEI equivalents, therefore suggesting MIR to be the better technique for absorption contrast. The effect on the SNR_{AREA} of increasing the number of component images in the MIR analysis was also looked at and showed that as the number of component images increased the SNR_{AREA} increased, altough this was also dependent on the component images themselves.

Different groups have imaged refraction phantoms using ABI techniques in the past, including a wedge phantom with slopes in the range $-0.8 \leq \tan\alpha \geq 0.8$ used by Z. Zhong et al. The refraction phantom used in this work was also a wedge phantom which, unlike the previous one, had slopes of a much larger range $-10 \leq \tan\alpha \geq 10$. In the first of the two refraction phantom experiments, the phantom was imaged using a beam energy of 40 keV on ID17 at the ESRF, and several DEI and MIR image sets were created. The refraction images produced by both techniques gave the expected results. Plots of $\Delta\theta_z$ against $\tan\alpha$ for these images were created and compared with theory. The experimental results, however, did not follow those predicted by theory. Instead experimental findings were consistent with the phantom being positioned at a slight angle to the beam. These plots also highlighted the effects of inaccuracies in the positioning of the analyser crystal on the rocking curve. Both of these findings therefore show the sensitivity of the techniques and need for accuracy in positioning the sample and the analyser crystal. The MIR results also showed an improvement in accuracy with increasing the number of component images, albeit dependent on the accuracy of these images.

Plots of $\tan^{-1}(\Delta\theta_z/K)$ against α were created, from which a value of the angle to which the phantom positioned to the beam could be calculated. These plots were found to be strongly affected by the background subtraction, the number of imaging positions and the position on the rocking curve. Because of this only an approximate range for δ, of $0.01<\delta(\text{rad})<1$, could be found.

Plots of SNR_{AREA} versus tanα did not give the expected results due to the inaccuracy in positioning of the phantom. The SNR_{AREA} results for the DEI images showed that ±80% was the best imaging position, but since ±50% results were not available, this should be repeated. The MIR results on the other hand, did not show a trend as to the best imaging position on the rocking curve or show a variation of the SNR_{AREA} with increasing the number of imaging positions. They did, however, show a lack of linearity at larger magnitudes of tanα, which, when comparing the two ABI techniques meant that the DEI images gave consistently better results for these values and suggests that if large values of tanα are present in a sample DEI may be the ABI technique of choice. However, this would need to be looked at more thoroughly.

The second of the two refraction phantom experiments was carried out on Station 9.4 at the Daresbury SRS and a ±50% DEI image set was created. The images produced did not show the contrast that had been expected. This problem was found to be due to the variation in intensity across the imaging field, which was itself caused by the presence of a tilt on the crystal.

In terms of investigating the USAXS contrast, two different materials have been used previously: paper and colloids. The aim of this investigation was to establish if it is possible to create a range of contrast in by diluting colloidal solutions, something which has not been done previously. Different sizes of colloids were also investigated.

Three preliminary colloid experiments were carried out. In the first a Ludox sample was imaged using a 40 keV beam on ID17 at the ESRF. The SNR_{AREA} analysis of the USAXS images showed that there was some signal from the sample. However, the contrast in the actual image was very small which could have been due to two things: firstly, the colloids themselves could have been of an inappropriate size; secondly, the beam energy used may not have been optimum. Further investigation would be required to establish this.

The other colloid experiments were carried out on Station 9.4 at Daresbury SRS, using a 20 keV beam. In the first of these experiments a sample of 900nm colloidal polystyrene and a sample of distilled water were imaged simultaneously, and MIR-11 and MIR-6 image sets were created. The USAXS images clearly showed contrast in the colloid sample, which was visibly greater than the contrast from the water sample. The SNR_{AREA} values of the colloid samples were greater than those of the water sample for both USAXS images, meaning the use of a range of concentrations of colloids to create a range of contrasts is plausible. As would be expected the SNR_{AREA} values also showed a noticeable increase as the number of imaging positions increased, this increase was also far more significant for the colloid sample than the water sample. This suggests that to get a good USAXS signal the number of imaging positions should be optimised.

In the final of the colloid experiment, three colloid samples of different sizes and a water sample were imaged. The USAXS images showed only slightly higher levels of contrast in the bulk of the sample than was visible in the background. The SNR_{AREA} values of the samples were lower than those seen in the previous experiment, suggesting that an optimum thickness of sample should also be investigated. The SNR_{AREA} results also showed that the 500nm sample was the best colloid size to be used as it had the highest SNR_{AREA}. However, a more conclusive result could be given if larger sample volumes were imaged, as in this experiment the SNR_{AREA} values were small and there was not a lot of difference between all the results. Another issue raised by this experiment was that there were high levels of contrast in the USAXS images in the menisci region, which is potentially due to a separation if colloids from their solution, which could be important in future experiments.

The aim of this part of my work was to develop phantoms which were specific to the different sources of contrast. As can be seen, this was done for the absorption and refraction contrast. The phantoms worked as they were designed to by providing a range of contrast values, although further testing at different energies

would be beneficial. For the USAXS contrast, the preliminary findings demonstrated that it should be possible to utilise colloidal solutions in a USAXS phantom, although further work is still required.

The phantom experiments not only gave information about the phantoms, but also the systems and the ABI techniques. Both of the refraction phantom experiments showed something about the ABI systems. In the first experiment, carried out at the ESRF, the experimental values of $\Delta\theta_z$ did not align with the theoretical predictions. This was shown to be due to a misalignment of the phantom in the beam, therefore demonstrating the sensitivity of ABI. In the second of the refraction phantom experiments the effect of a tilt error on the crystals was highlighted.

The results of the absorption phantom experiment showed that MIR images consistently gave higher SNR_{AREA} values than their DEI equivalent, showing the strength of this technique in terms of this source of contrast. The SNR_{AREA} analysis carried out in the ESRF refraction phantom experiment uncovered a discrepancy between the MIR and DEI images at large magnitudes of $\tan\alpha$. Although this matter needs to be studied further, this result does suggest that DEI may be the best option when imaging samples that have structures with large magnitudes of $\tan\alpha$. A general theme from all of the phantom experiments was that for the MIR images the SNR_{AREA} was improved by increasing the number of imaging positions, something shown most prominently in the first of the Daresbury colloid experiments, the result also showed that this has a strong dependence on the quality of the constituent images.

7.2 **Cartilage imaging**

The starting point for this work was to explore the potential biological applications for ABI. There were two main areas that had been investigated previously by other groups; mammography and cartilage imaging. It was decided that cartilage imaging should be the focus of the work since mammography had been more

extensively studied. Diseases such as osteoarthritis also meant that there are possible applications for ABI techniques.

In work carried out by other groups it had been shown that cartilage could be clearly visualised in the ABI refraction images, in both whole and disarticulated samples, for animal and human models. They have also shown in some cases that they are capable of visualising the structure of this cartilage.

A total of five different cartilage imaging experiments were carried out over the course of this work. The first three of these experiments were carried out on Station 7.6 at the Daresbury SRS where mice feet samples, a slice of bovine cartilage and a joint from a pig's trotter were imaged. These were the first biological samples to be imaged using channel cut crystals in an ABI system.

In the mice feet experiment, arthritic and non arthritic mice feet were imaged simultaneously. The resulting DEI refraction images visualised some of the soft tissue, such as the tendons. However, due to the small size of the samples the joint cartilage could not be seen. The refraction image also showed the structure of the bone more clearly than the apparent absorption image. The presence of swelling and a poorer quality of the bone structure made the healthy and arthritic samples easily discernible.

The purpose of the bovine slice sample experiment was to look at the ability of the ABI techniques to image such a small sample, this was also the first time that MIR had been used to look at a biological sample on the system. The resulting MIR and DEI images both showed the same structures. The refraction and USAXS images also showed the bone structure of the sample with greater clarity than the absorption images.

The pig's trotter was imaged with the intention of using DEI to visualise joint cartilage through the superposition of the surrounding soft tissue. As with the work carried out previously by other groups, the cartilage in the joint was visible, as well

as other soft tissue structure, such as the skin. This was corroborated by the MR-images of the sample.

In another of the experiments, core, disarticulated and whole samples were imaged on ID17 at the ESRF, and several DEI and MIR images sets were created for each sample. MRI comparisons were also taken. For all three samples the absorption images showed the structure of the bone. However, the cartilage was not visible, as was also the case in the USAXS images. The refraction images of all three samples also showed the structure of the bone. However, the images of the core sample, the disarticulated sample and the whole sample, in one of its three imaging orientations, also visualised the cartilage. The cartilage could not be seen in all of the whole sample's imaging orientations, because in the other positions there was greater superposition of the surrounding structures.

The results of the SNR_{LINE} analysis for the whole sample showed that the SNR_{LINE} values varied for different regions, and that there was a possible link between regions of the cartilage which gave high SNR_{LINE} values and regions of the MR-images which gave high contrast. The results for the disarticulated sample, also showed a variation in the SNR_{LINE} values for different regions of the cartilage. For this sample line profiles for the cartilage region which gave the highest SNR_{LINE} values, were also taken. These profiles showed that there were variations in $\Delta\theta_z$ throughout the cartilage, suggesting that the techniques may be sensitive to the different layers that are present in the cartilage, something that should be investigated in greater detail.

As with results from other experiments, the SNR analysis of the images demonstrated that MIR gave higher SNR values on the whole than there equivalent DEI images. They also showed that for the MIR images the SNR increases with the number of constituent images. However, this is dependent on the quality of these images.

In the final cartilage experiment a total of twelve samples were imaged on Station 9.4 at Daresbury SRS using both MIR and DEI, with a beam energy of ~40 keV. MRI comparisons were also taken of the samples.

The results from two of the samples, 006B and 003A were presented. As with previous experiments, the absorption images and the USAXS images showed the structure of the bone. However, the USAXS images did so with greater sharpness than the absorption images and also showed some structures in the cartilage region. The refraction images, as with the USAXS images, showed the structure of the bone more sharply than the absorption images. They also showed the cartilage, and, in the case of the 006B sample, clearly showed the presence of a defect in the cartilage, which could also be seen in the MRI image of the sample and is consistent with what has been seen previously by other groups.

SNR analysis of the overall images was also carried on the images and showed that the MIR images created using the most constituent images gave consistently higher SNR values than the MIR images which used fewer images. The MIR images also gave higher SNR values than the DEI images. The most noticeable point about these images, however, was the artefacts caused by the presence of a tilt on the crystals and a fault in the detector. These artefacts were worsened by the large thickness of the samples.

The reason for carrying out this work was to look at the capabilities of the ABI techniques for looking at cartilage. The results from the pig's trotter, canine joint sample and human knee sample experiments corroborated what had been demonstrated previously, that the cartilage is visible in the refraction image, and that it can be imaged through the surrounding soft-tissue. However, as shown by the results from imaging the whole sample in the canine joint experiment, this can also be dependent on the orientation of the sample, and therefore highlighted the necessity of DEI-CT

The SNR_{LINE} analysis that was carried out showed that there was variation in the SNR_{LINE} values for different regions of the cartilage. The results from the whole sample also showed a link between regions of high contrast in the MR-images and cartilage regions in the refraction image which gave high values of SNR_{LINE}, earmarking this as a potentially useful analysis tool in future experiments. The line profiles taken from the refraction images of the disarticulated sample also showed that although not clearly visible in the refraction images themselves, different layers in the cartilage could be detected, although this requires further investigation.

As with the phantom experiments, the results from these experiments also identified points about the system and the ABI techniques. The most prominent example of this was the human knee sample experiment, which was hindered by the variations in intensity across the imaging field due to the tilt on the crystals, and also a defect in the detector. The ABI techniques themselves were compared through the SNR values of the images. The results from the cartilage experiment support the previous findings that the MIR images generally give higher SNR values than their equivalent DEI images, also that the SNR of the MIR images increases as the number of component images increases, although this is again dependent on the quality of these images.

7.3 **Future work**

Although several things have been accomplished in this work, including the use of channel-cut crystals on an ABI system for the first time, there are still several areas where further investigation would be beneficial.

In terms of the development of the phantoms, although the absorption phantom was shown to work well it should also be tested using both higher and lower x-ray beam energies in order to establish whether these good results can be replicated under such conditions and therefore prove or disprove the usefulness of the phantoms design over a range of energies.

The refraction phantom also needs further work. Firstly, in order to evaluate the effect of positioning the phantom at an angle to the beam, several DEI or MIR image sets should be taken of the phantom with the angle that the phantom makes to the beam varied for each. The refraction phantom, as with the absorption phantom, should also be imaged at different energies, in order to test the phantom's design over a range of energies. As was discussed in the previous section, the results from the SNR_{AREA} analysis of this phantom also showed discrepancies between the DEI and MIR results for large values of $\tan\alpha$. In order to investigate this further a series of experiments should be undertaken.

The colloid experiments reported in this thesis were merely preliminary investigations. As mentioned in the previous section, the experiment undertaken using the polystyrene colloids of different sizes should be repeated, with greater thickness' of samples, to ensure better results and make it possible to identify which colloid size gives the best SNR_{AREA} value. Once this has been done different thicknesses of the colloid should be tested in order to establish a suitable sample thickness for the USAXS phantom. A prototype USAXS phantom can then be constructed and tested, using a range of dilutions of colloidal solutions, this should be done using a range of energies.

There are some areas in the cartilage work where further work would be valuable. Firstly, the experiment that was carried out on the human knee samples should be repeated when the problems with the system have been corrected. As was mentioned in previous chapters, some DEI-CT was also taken of some of the samples. However, due to unforeseen problems there were no reconstructed images to be presented. Further work is required to overcome these problems and make DEI-CT available for future experiments. The work that was carried out using SNR_{LINE} analysis of the cartilage boundaries, also showed promise in links between high SNR_{LINE} values and regions of high contrast in the MR-images of the same part of the sample. It would therefore be useful to investigate this further and confirm the presence of such a relationship, explore the reason behind it and

investigate its potential uses. There is also potential for layers in the cartilage to be seen in profiles of the cartilage region in the image, this too needs further investigation.

The main area where extra work is required is the ABI system on Station 9.4 itself. As was shown in the refraction phantom and human knee sample experiments carried out on this station, the presence of tilt on the crystals was problematic. It is therefore necessary to investigate the source of this tilt thoroughly; firstly, to establish if it was coming from one or both of the crystals, and if it is added to by the fact that the crystals are channel-cut crystals; secondly to establish if there is a way of minimising the tilt prior to each experiments; and finally to implement a means of correcting for the effects. As was shown in the human knee sample experiment, faults with the detector also caused problems. The source of this fault should therefore be identified and either fixed or a different detector should be used in future experiments.

APPENDIX 1

Further images and plots from the absorption and refraction phantom experiments are shown in this Appendix.

1 ABSORPTION PHANTOM RESULTS

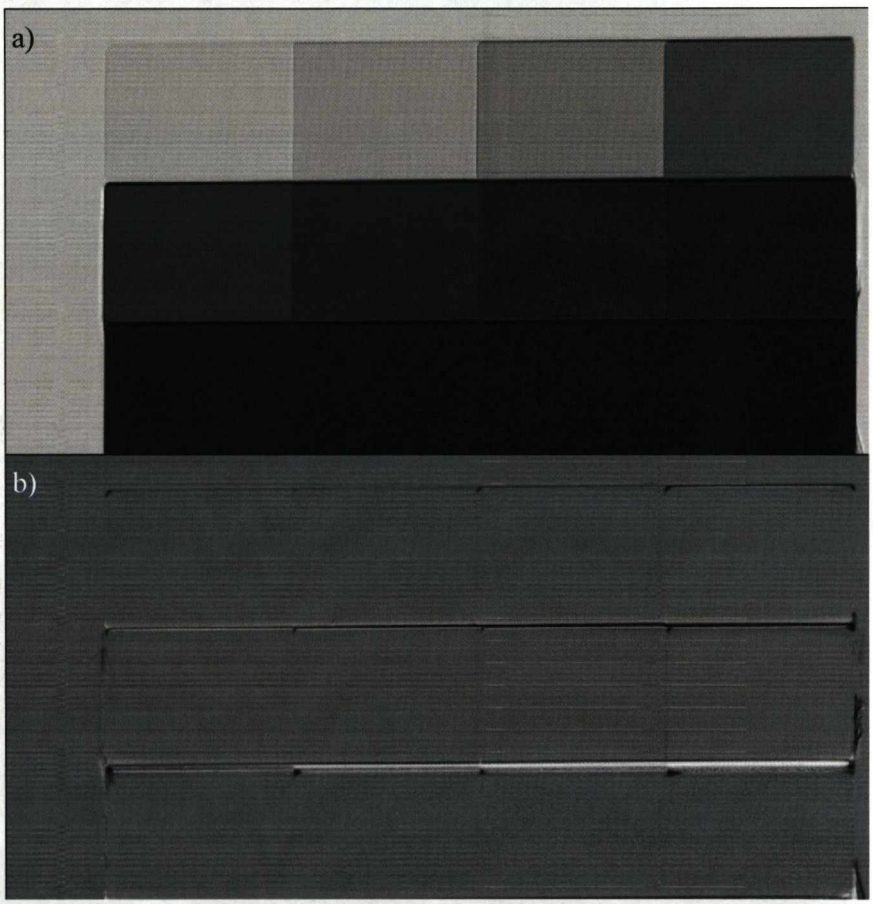

Figure A1-1: The DEI images of the absorption phantom created using the ±30% images. a) The apparent absorption image. b) The refraction image

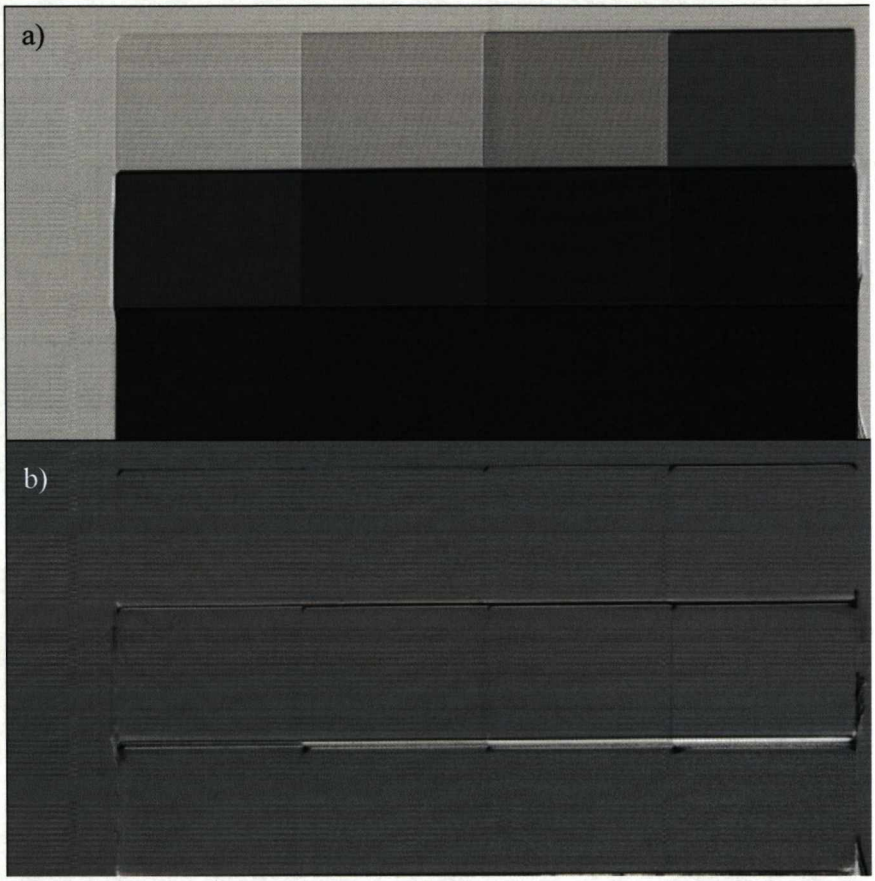

Figure A1-2: The DEI images of the absorption phantom created using the ±80% images. a) The apparent absorption image. b) The refraction image.

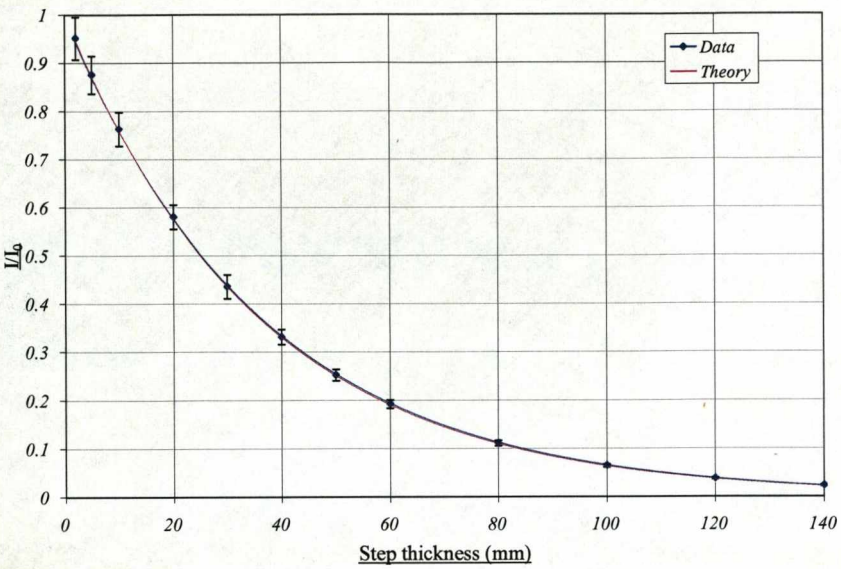

Figure A1-3: Plot of I/I_0 against Step thickness, comparing results from the DEI ±80% image with theory.

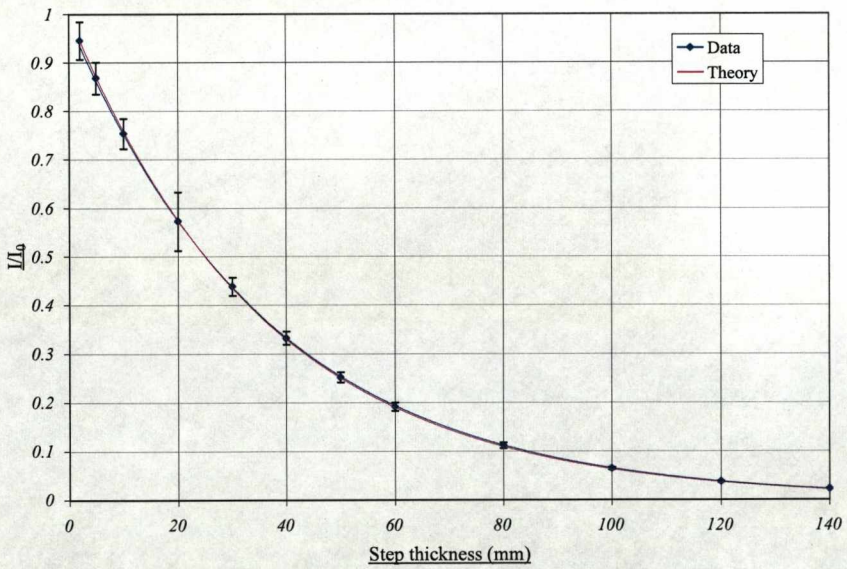

Figure A1-4: Plot of I/I_0 against Step thickness, comparing results from the DEI ±30% image with theory.

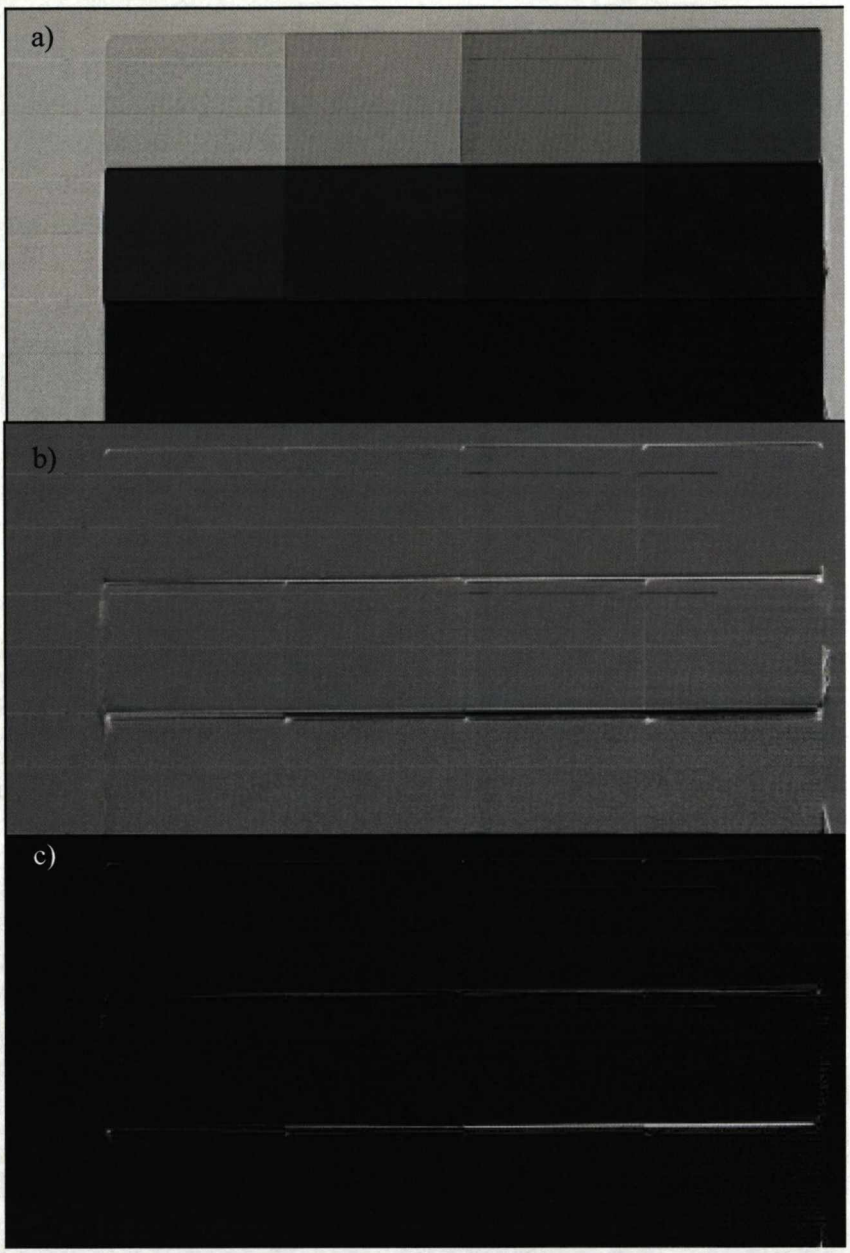

Figure A1-5: The MIR images of the absorption phantom created using the ±30% images. a) The absorption image. b) The refraction image. c) The USAXS image.

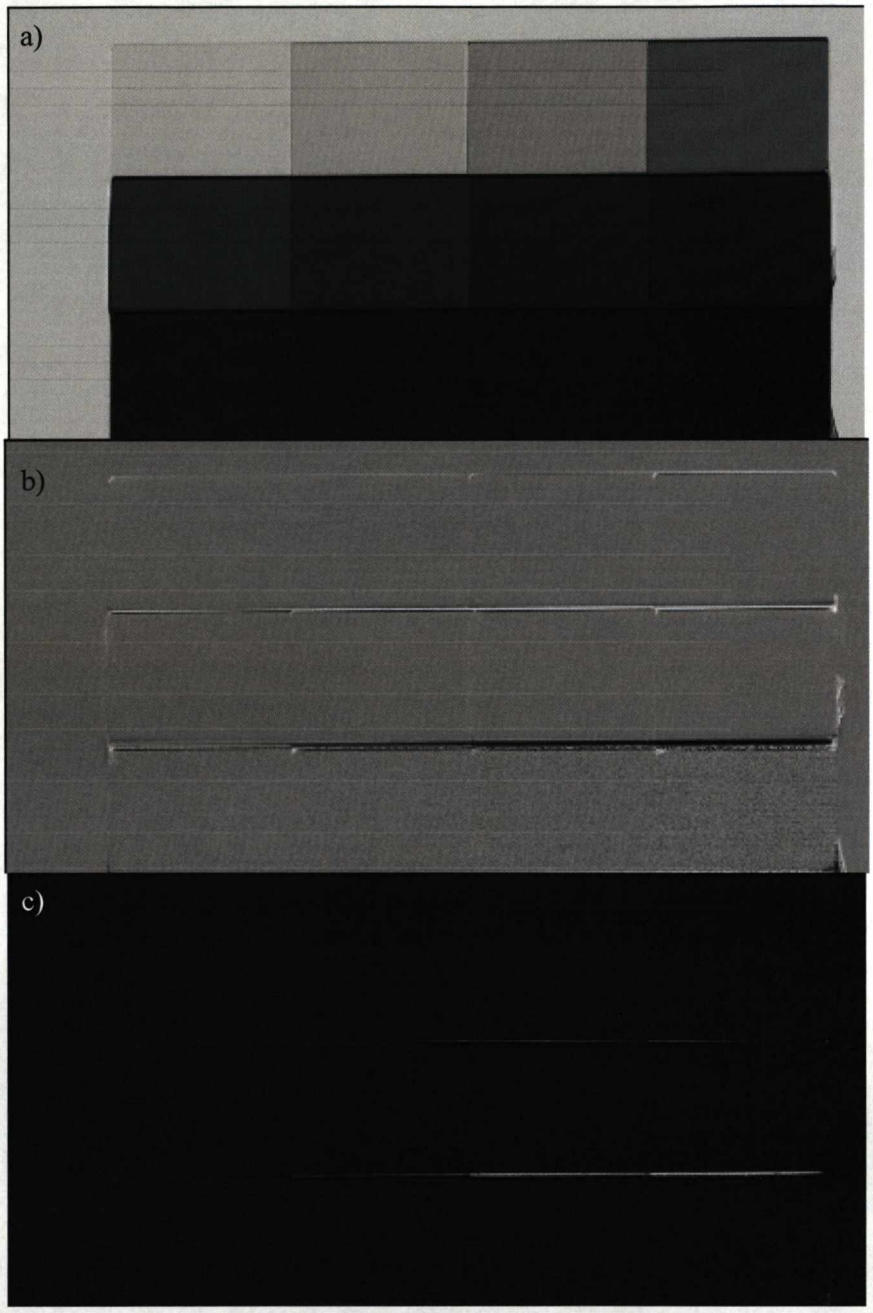

Figure A1-6: The MIR images of the absorption phantom created using the ±80% images. a) The absorption image. b) The refraction image. c) The USAXS image.

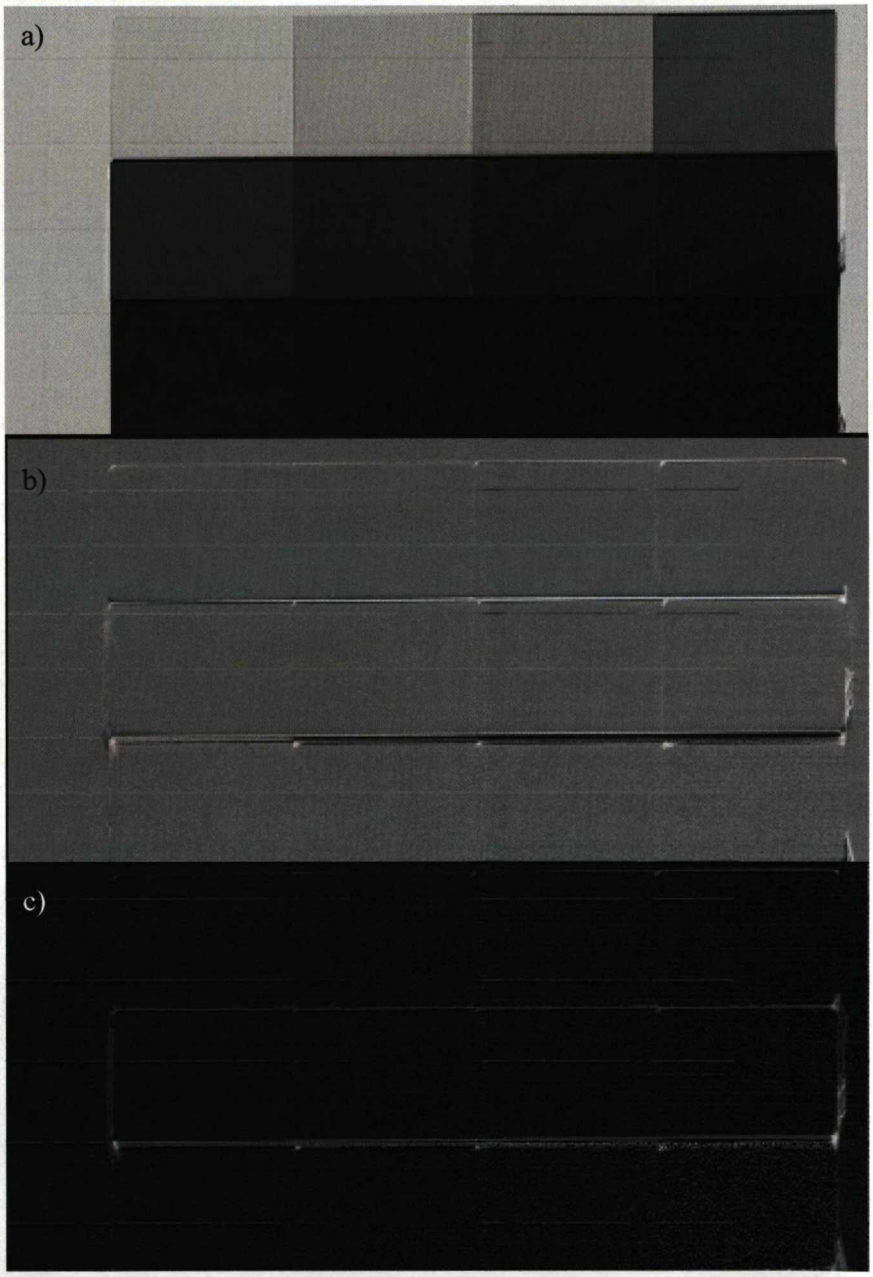

Figure A1-7: The MIR images of the absorption phantom created using the Peak and ±30% images. a) The absorption image. b) The refraction image. c) The USAXS image.

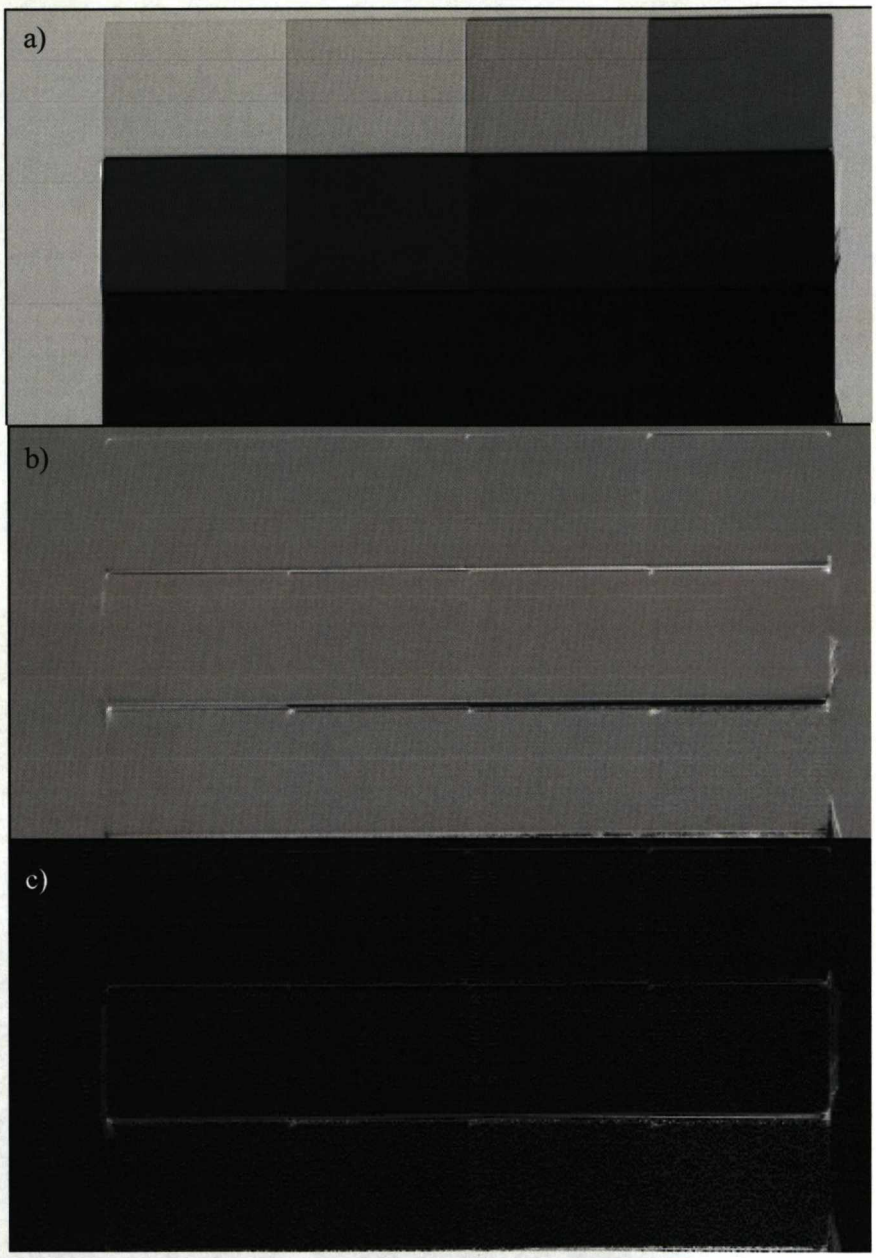

Figure A1-8: The MIR images of the absorption phantom created using the Peak and ±50% images. a) The absorption image. b) The refraction image. c) The USAXS image.

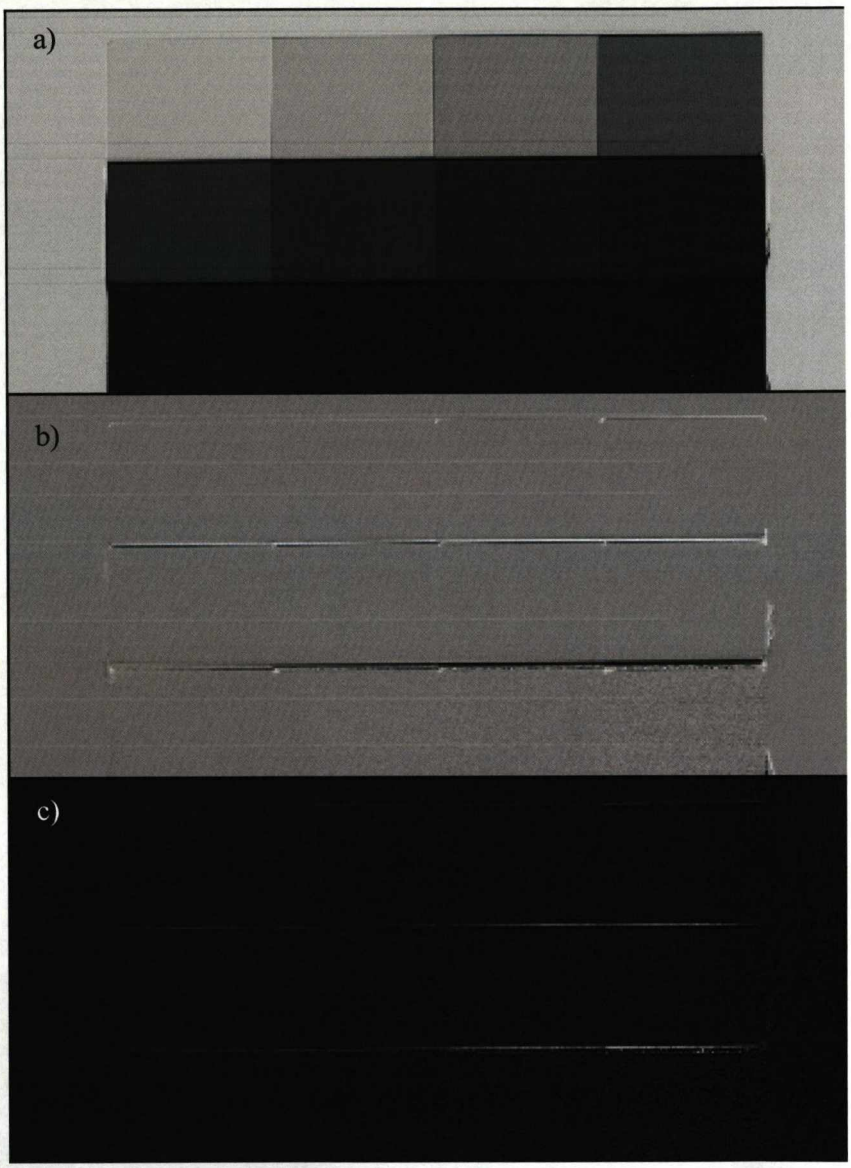

Figure A1-9: The MIR images of the absorption phantom created using the Peak and ±80% images. a) The absorption image. b) The refraction image. c) The USAXS image.

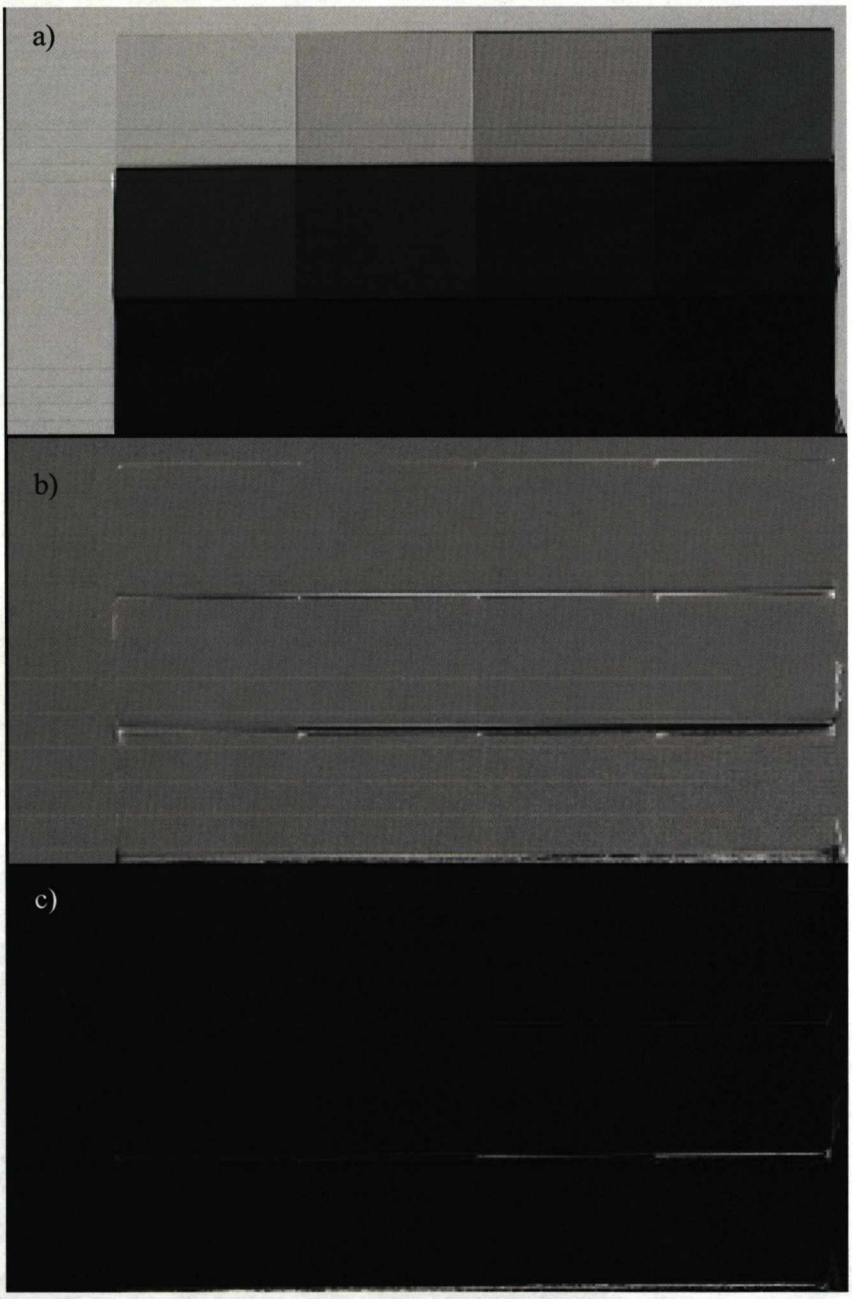

Figure A1-10: The MIR images of the absorption phantom created using the Peak, ±80%, ±50% and ±30% images. a) The absorption image. b) The refraction image. c) The USAXS image

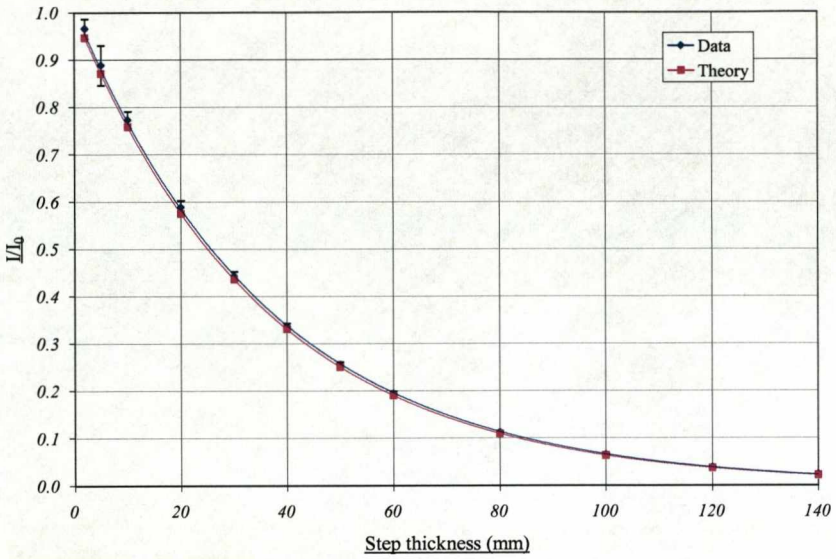

Figure A1-11: Plot of I/I_0 against Step thickness, comparing results from the MIR ±30% image with theory.

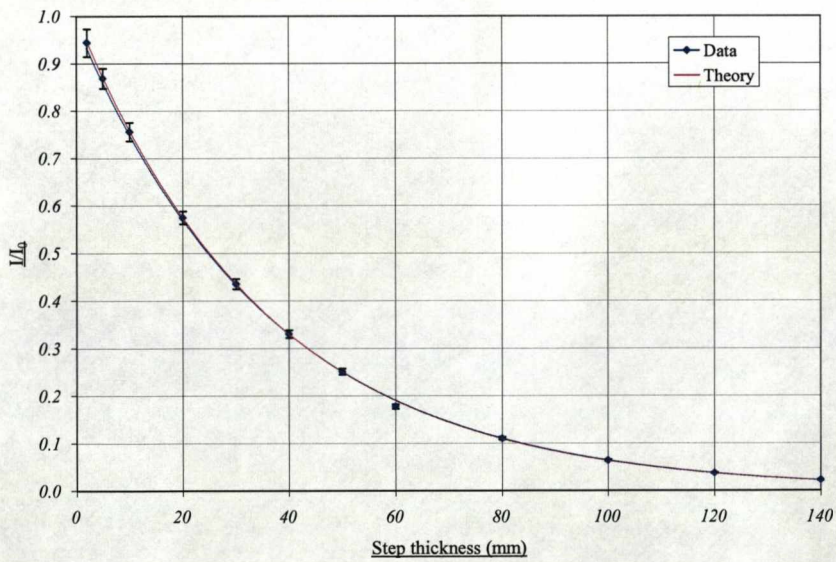

Figure A1-12: Plot of I/I_0 against Step thickness, comparing results from the MIR ±80% image with theory

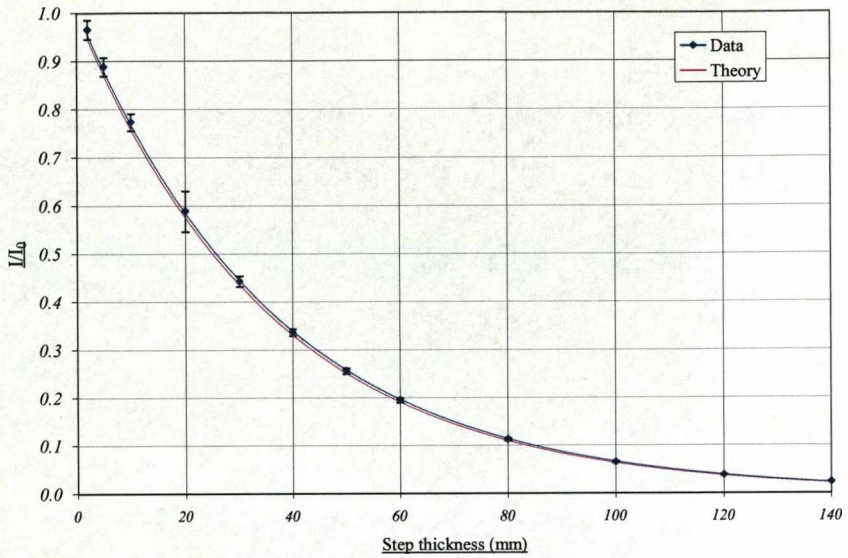

Figure A1-13: Plot of I/I_0 against Step thickness, comparing results from the MIR Peak, and ±30% image with theory.

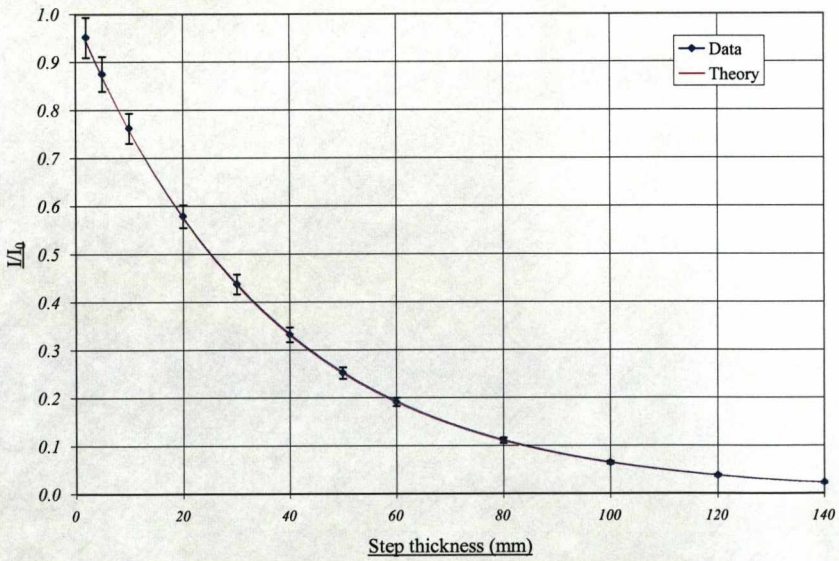

Figure A1-14: Plot of I/I_0 against Step thickness, comparing results from the MIR Peak, and ±50% image with theory.

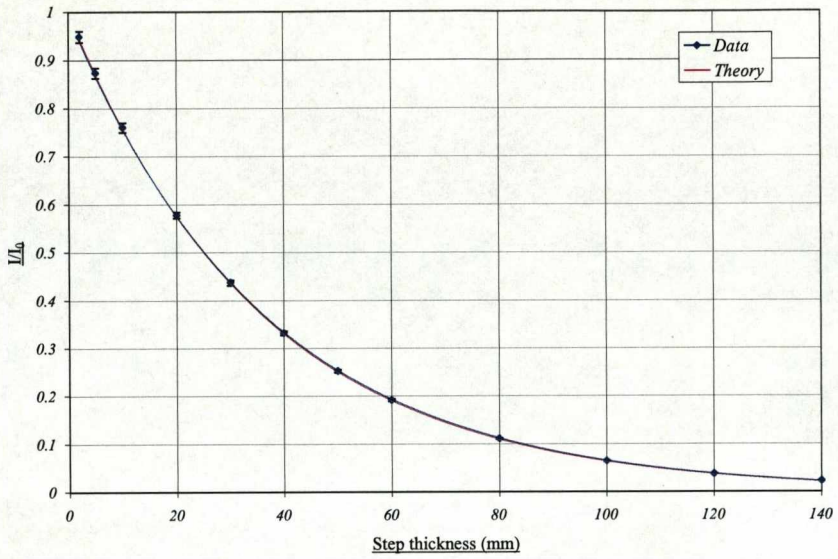

Figure A1-15: Plot of I/I_0 against Step thickness, comparing results from the MIR Peak, and ±80% image with theory.

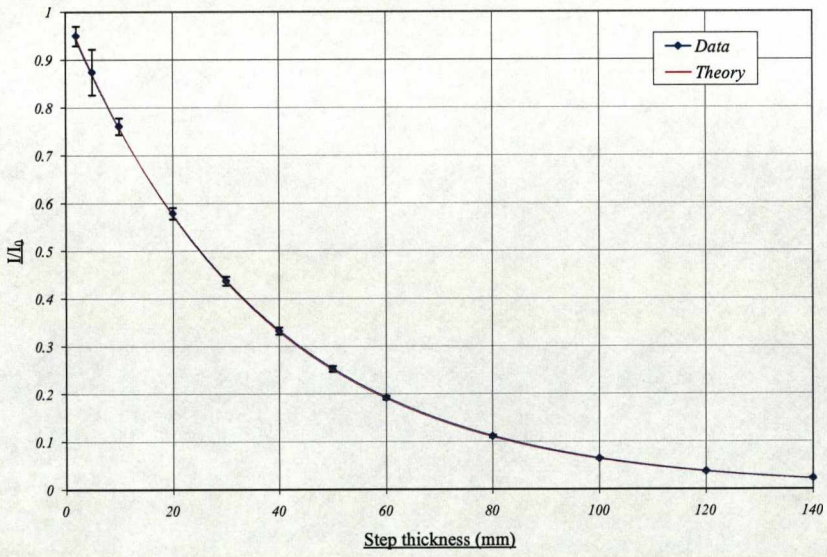

Figure A1-16: Plot of I/I_0 against Step thickness, comparing results from the MIR Peak, ±80%, ±50% and ±30% image with theory.

2 REFRACTION PHANTOM RESULTS

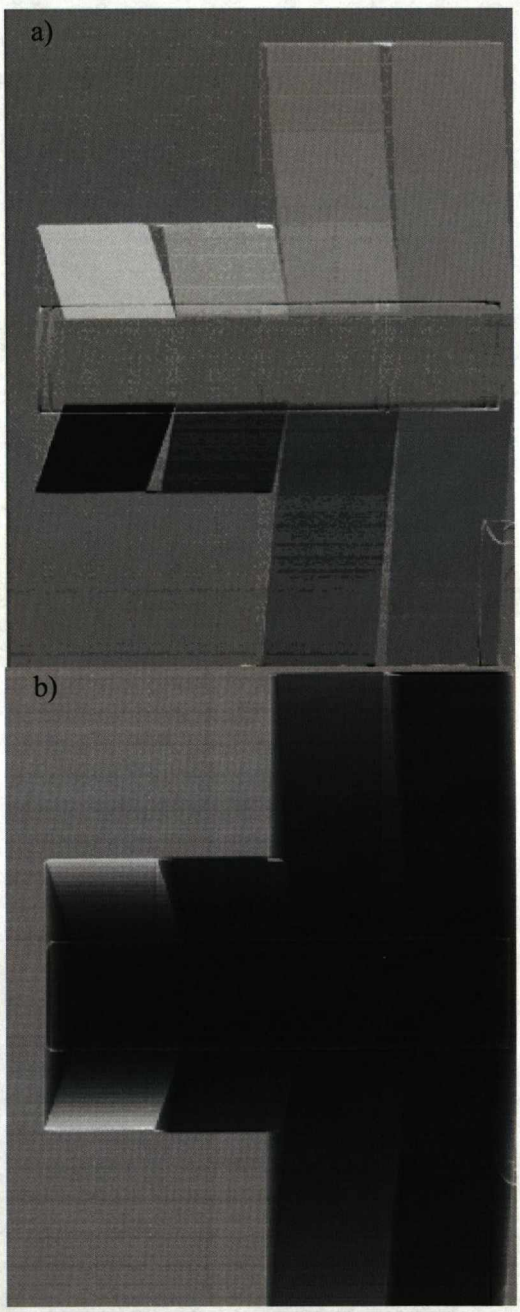

Figure A1-17: DEI images of the refraction phantom, taken at the ±15% position on the rocking curve. a) The refraction image. b) The apparent absorption image.

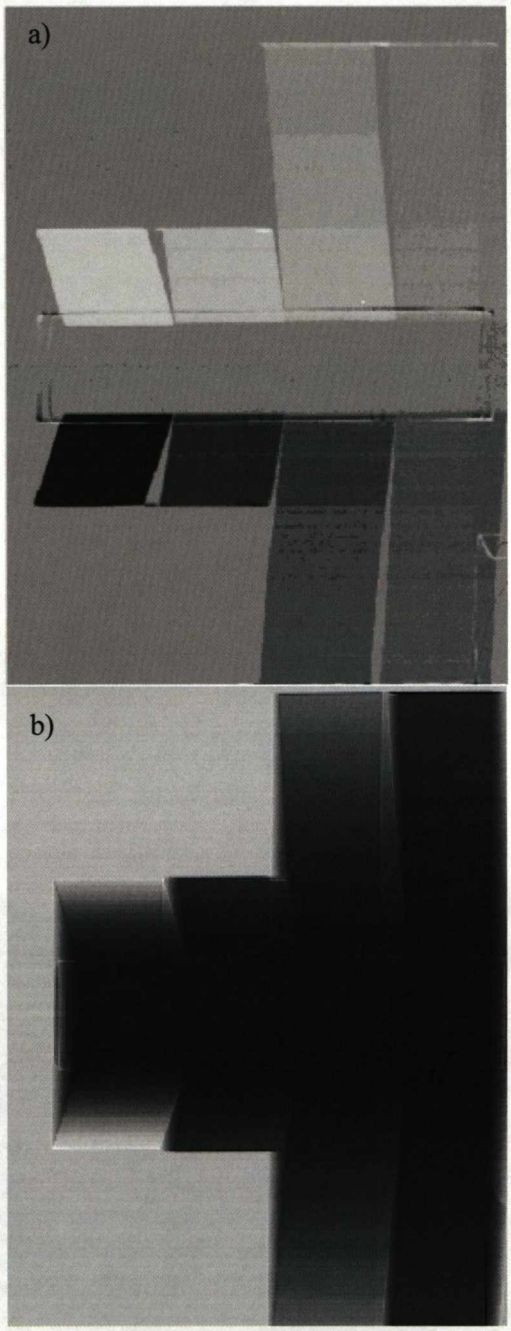

Figure A1-18: DEI images of the refraction phantom, taken at the ±30% position on the rocking curve. a) The refraction image. b) The apparent absorption image.

APPENDIX 2

Further results from the Canine joint sample experiment.

1 CORE SAMPLE RESULTS

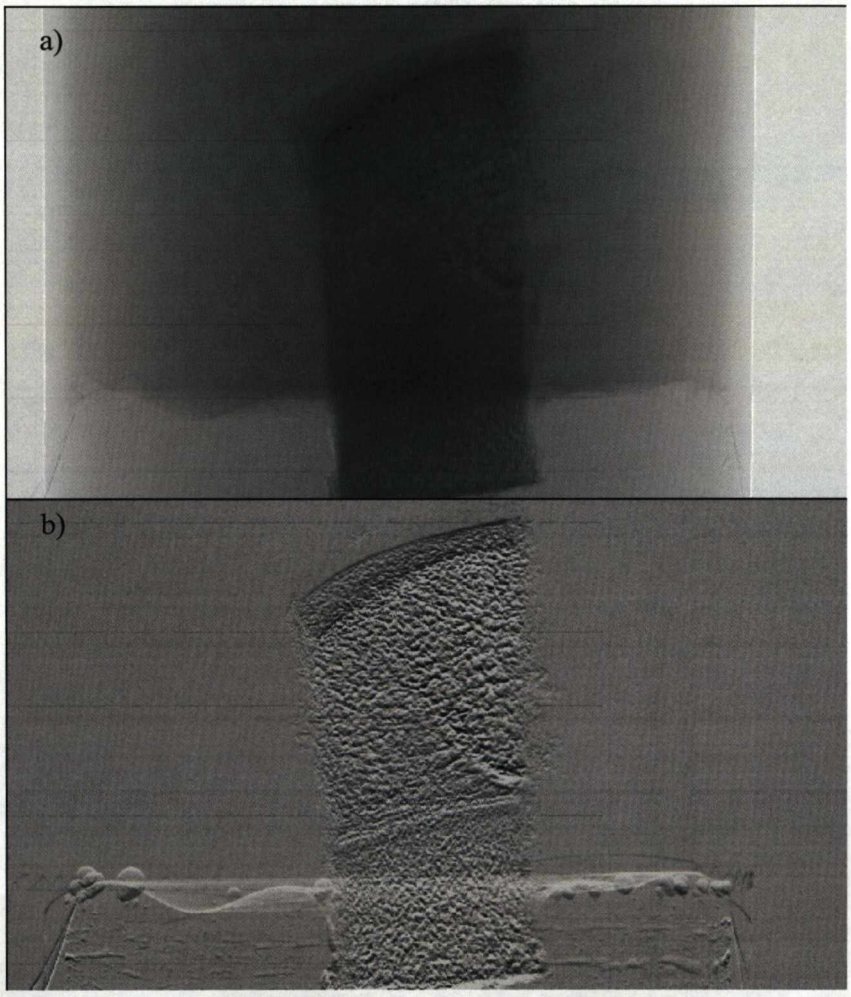

Figure A2-1: The DEI image at ±80%. a) The apparent absorption image. b) The refraction image.

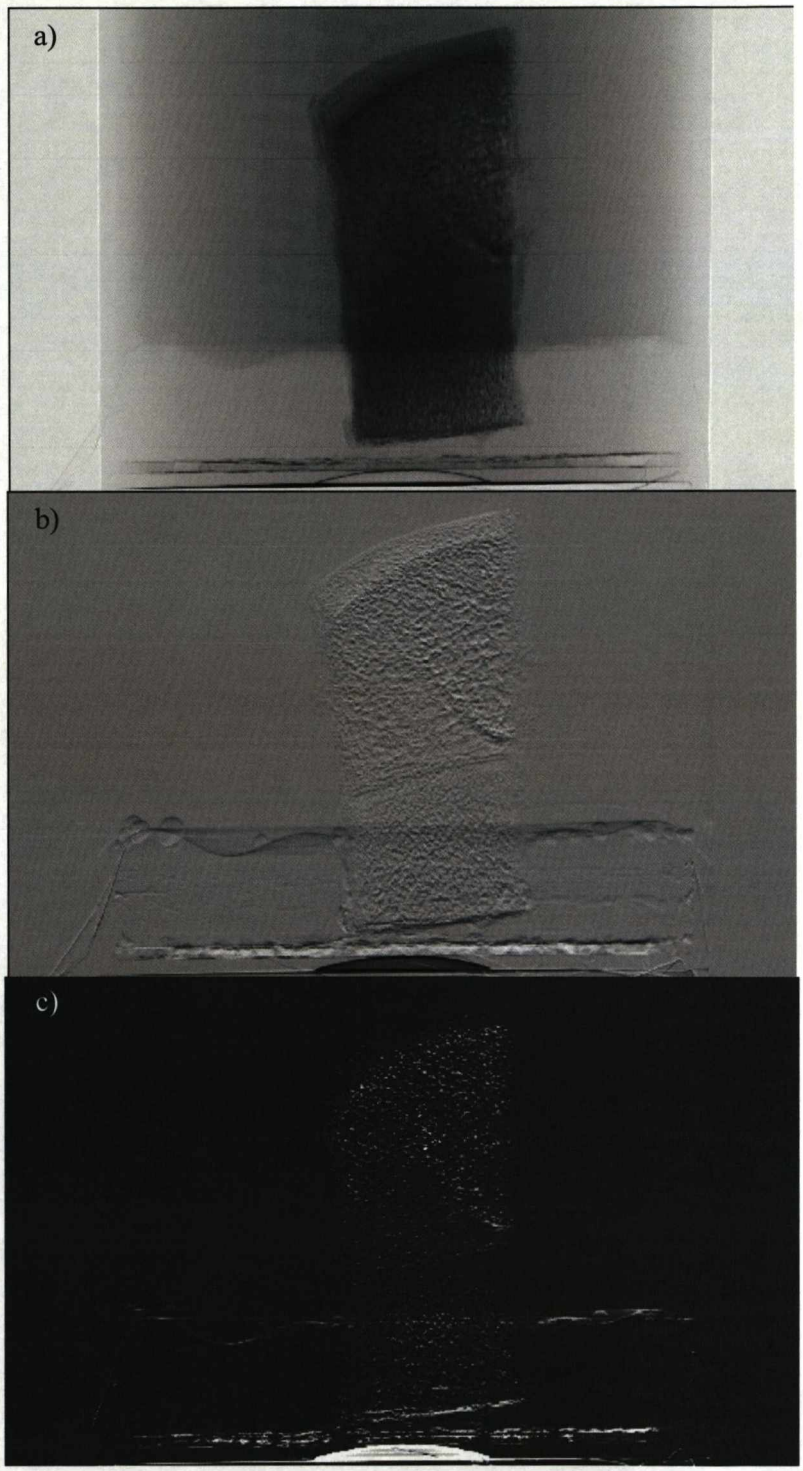

Figure A2-2: The MIR images of the Core sample taken at ±80%. a) The absorption image. b) The refraction image. c) The UXAXS image.

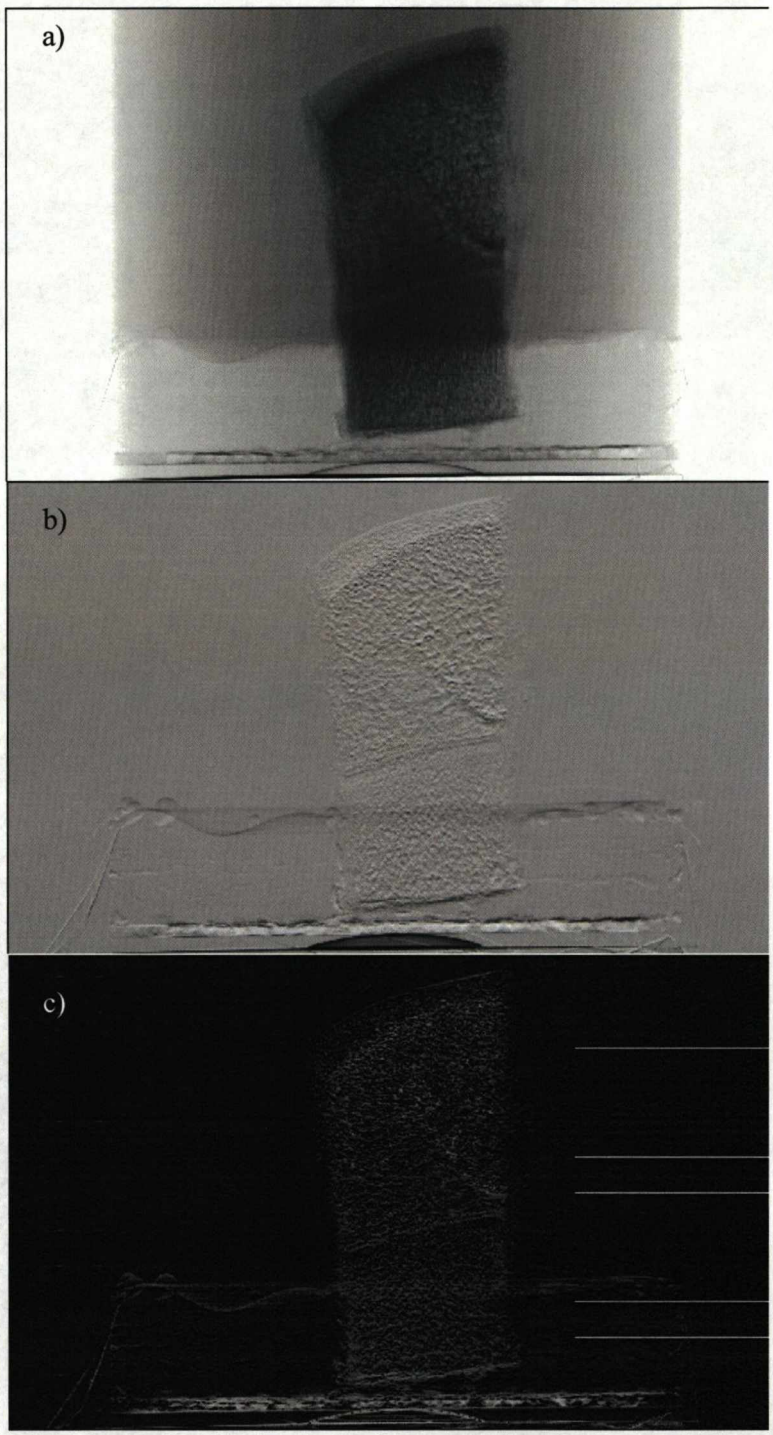

Figure A2-3: The peak, ±50% MIR images of the Core Sample. a) The absorption image. b) The refraction image. c) The USAXS image.

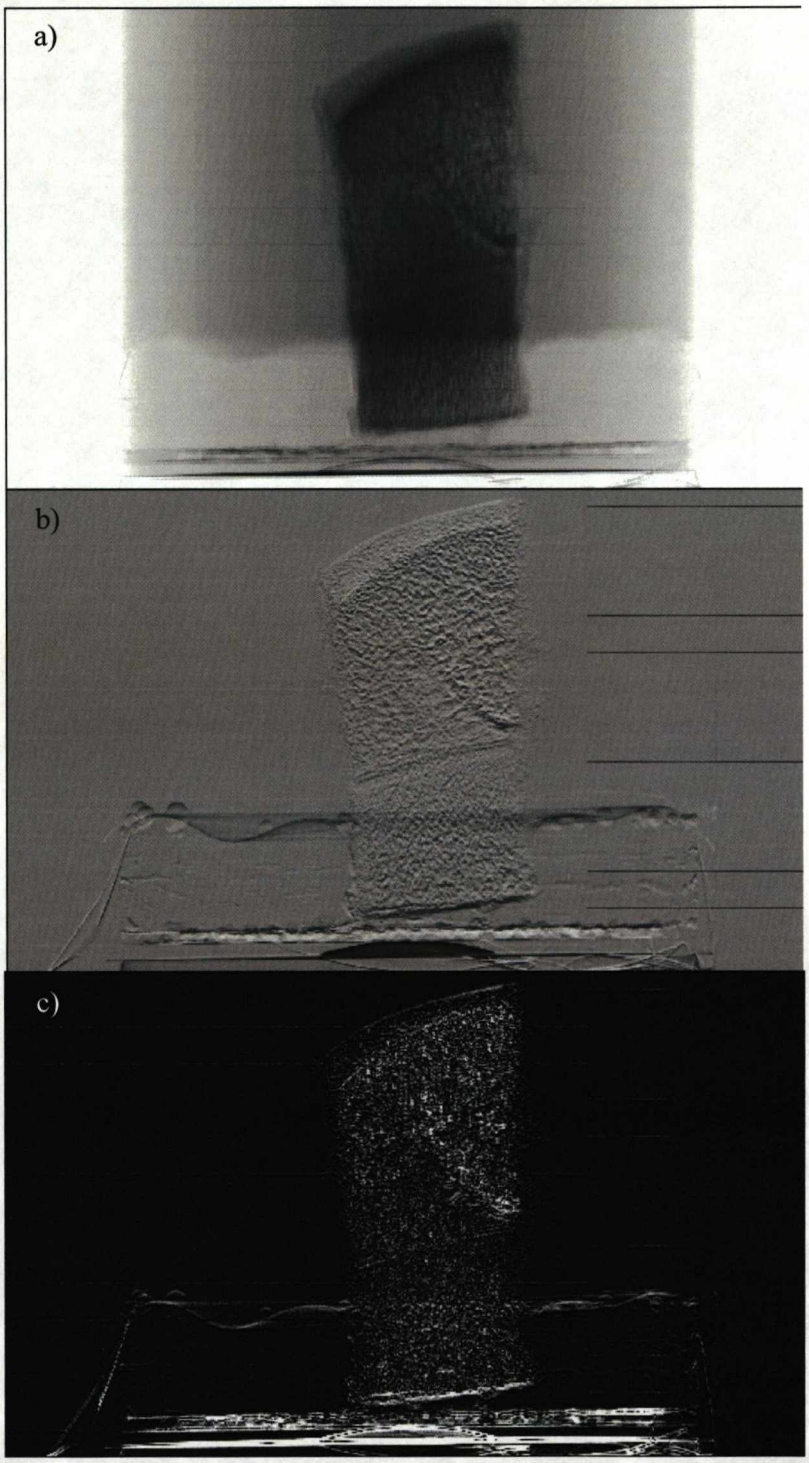

Figure A2-4: The peak, ±80% MIR images of the Core sample. a) The absorption image. b) The refraction image. c) The USAXS image.

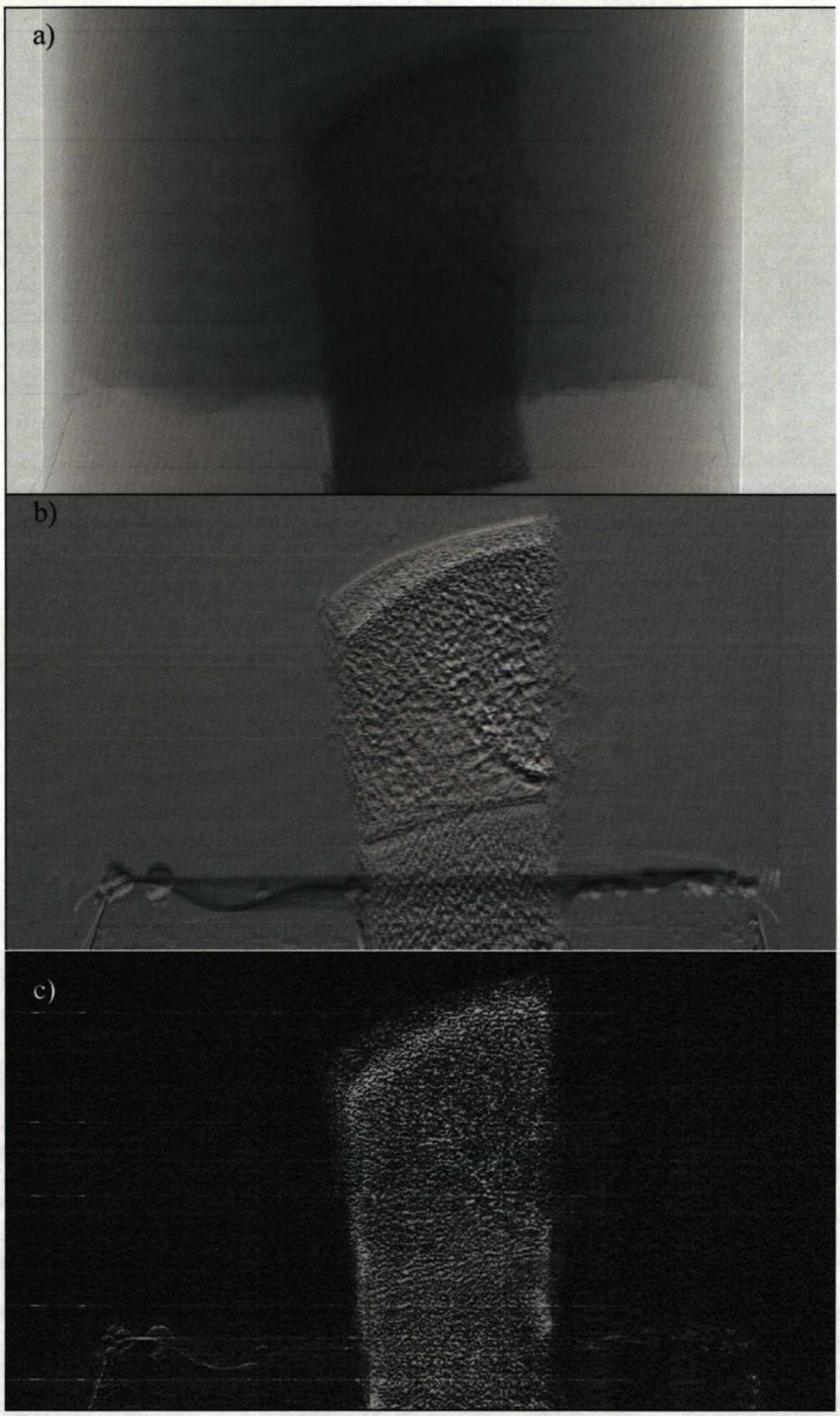

Figure A3-5: The Peak, ±50%, ±80% MIR images. a) The absorption image. b) The refraction image. c) The USAXS image.

2 DISARTICULATED JOINT SAMPLE RESULTS

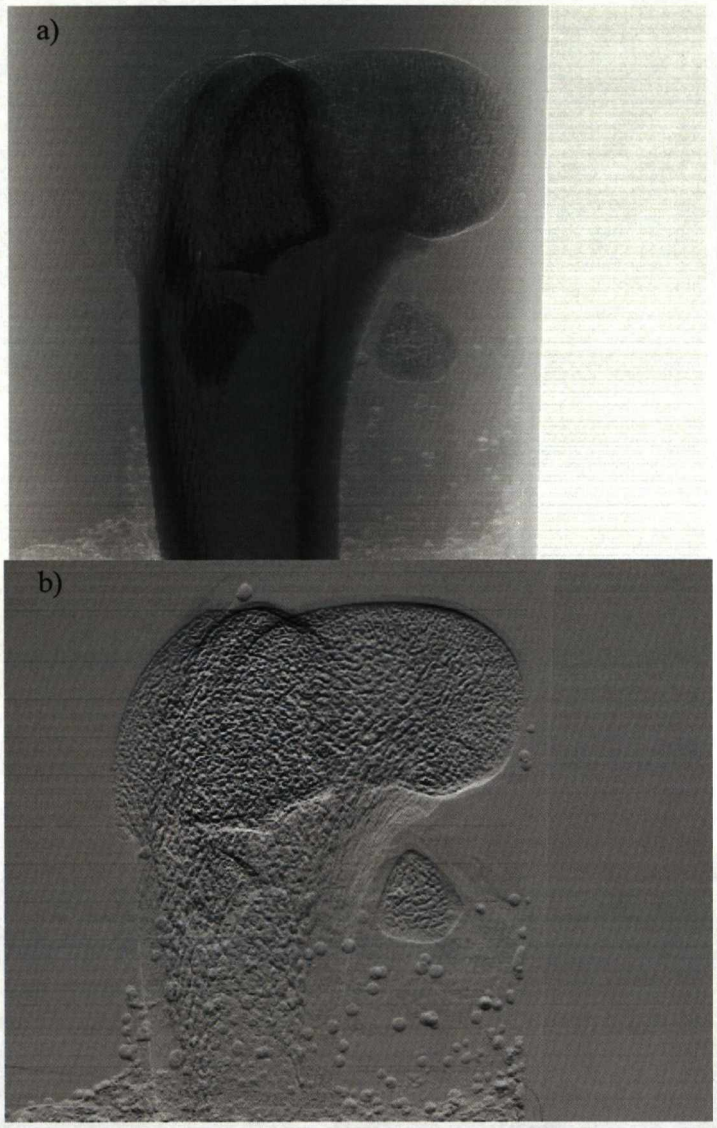

Figure A2-6: The ±15% DEI images of the disarticulated sample in the first orientation. a) The apparent absorption image. b) The refraction image.

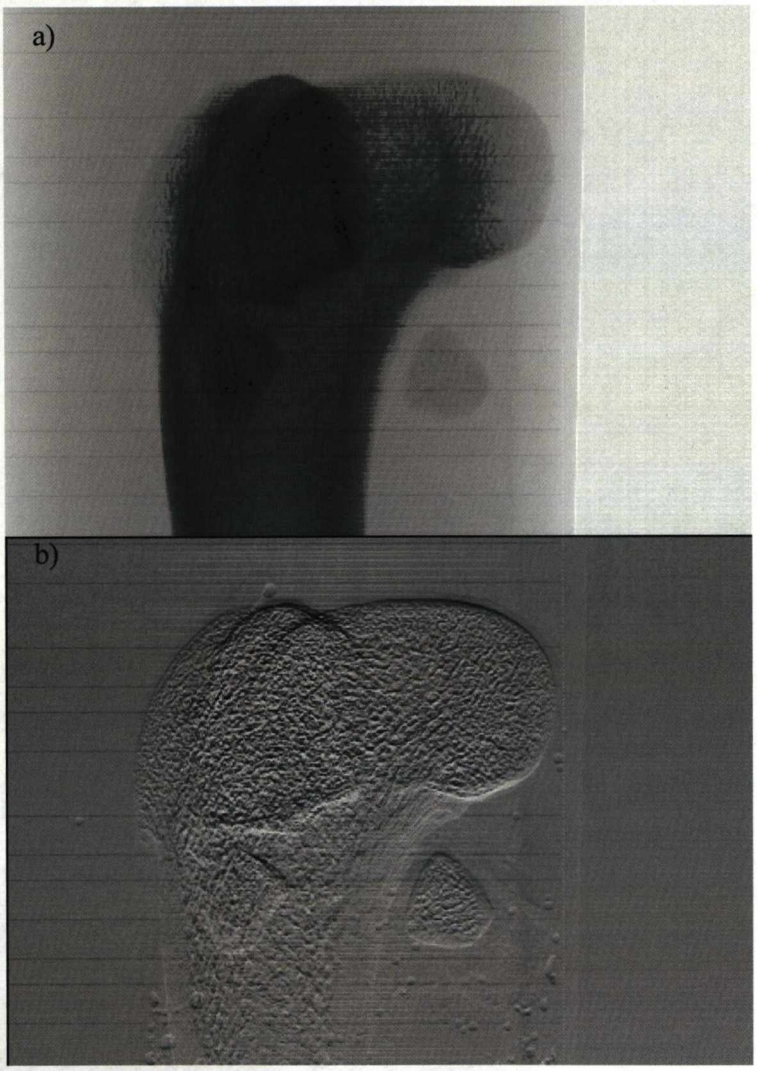

Figure A2-7: The ±50% DEI images of the disarticulated sample in the first orientation. a) The apparent absorption image. b) The refraction image.

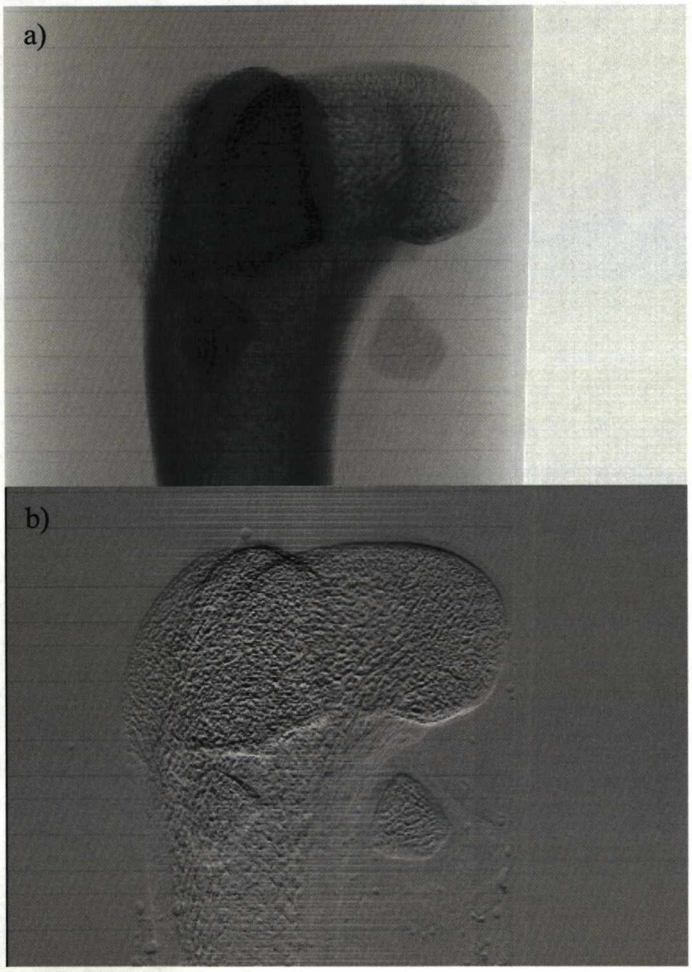

Figure A2-8: The ±80% DEI images of the disarticulated sample in the first orientation. a) The apparent absorption image. b) The refraction image.

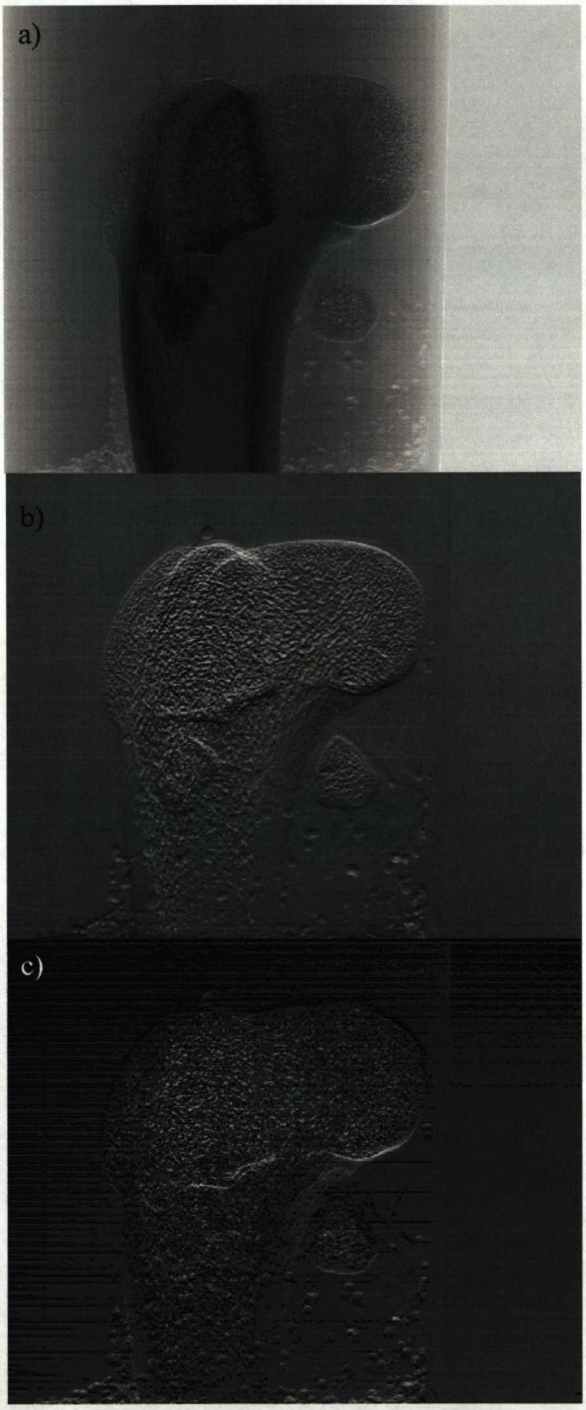

Figure A2-9: The ±15% MIR images of the disarticulated sample in the first orientation. a) The absorption image. b) The refraction image. c) The USAXS image.

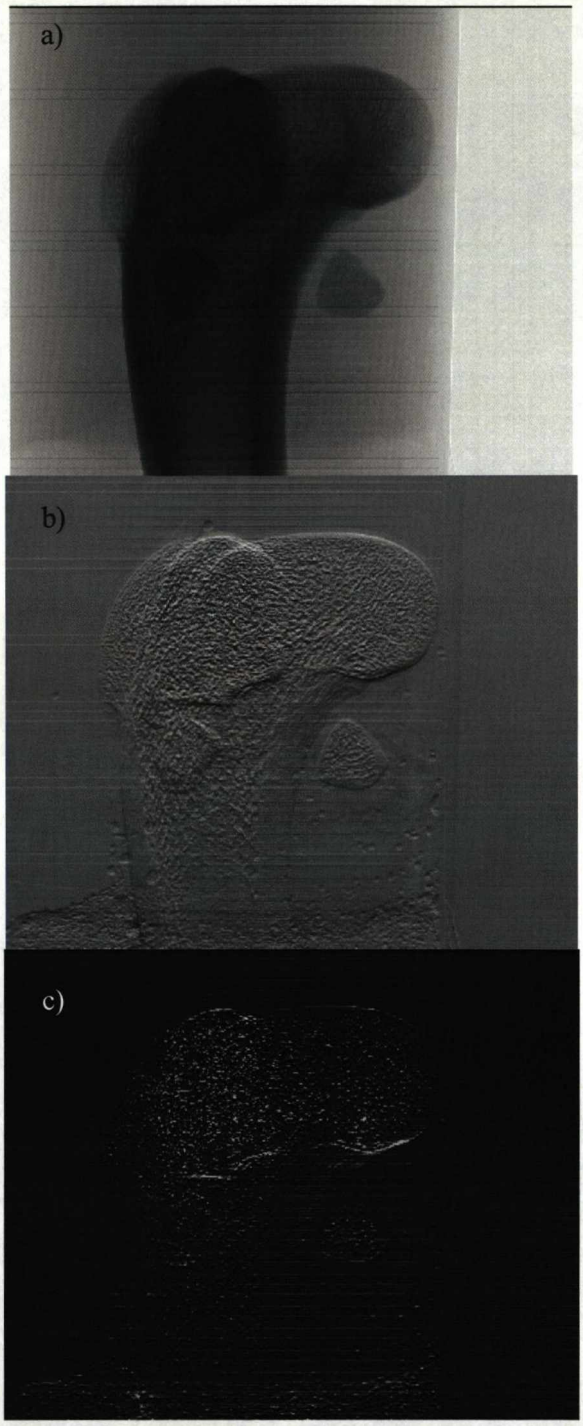

Figure A2-10: The ±50% MIR images of the disarticulated sample in the first orientation. a) The absorption image. b) The refraction image. c) The USAXS image.

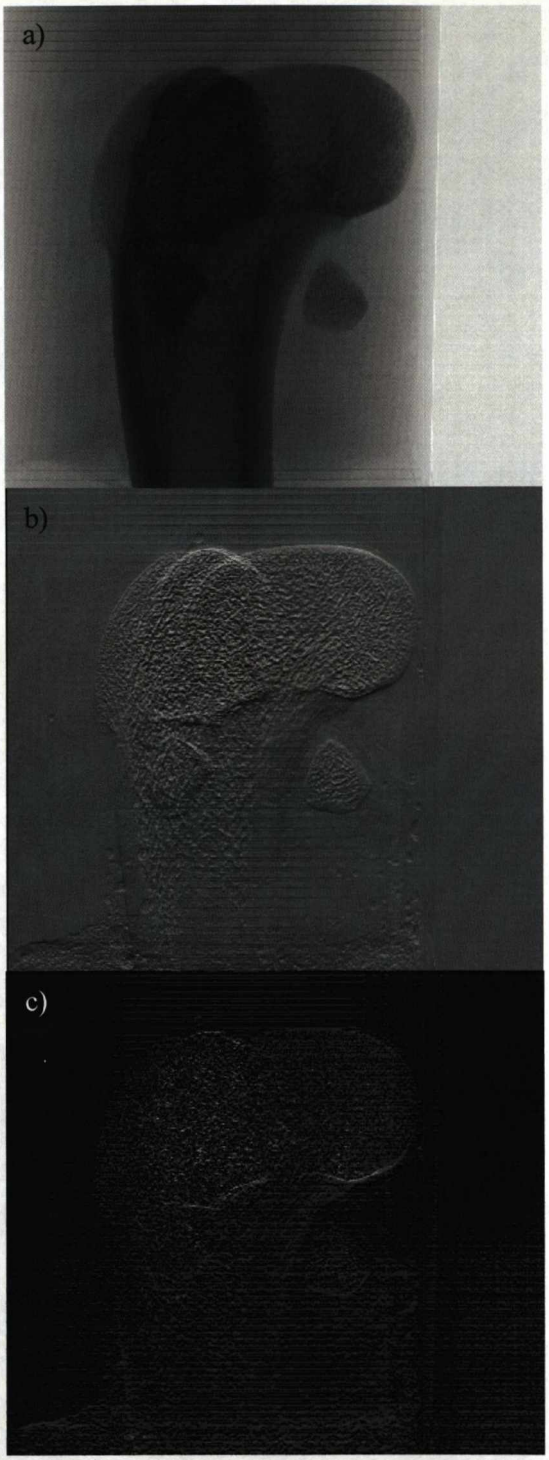

Figure A2-11: The ±80% MIR images of the disarticulated sample in the first orientation. a) The absorption image. b) The refraction image. c) The USAXS image.

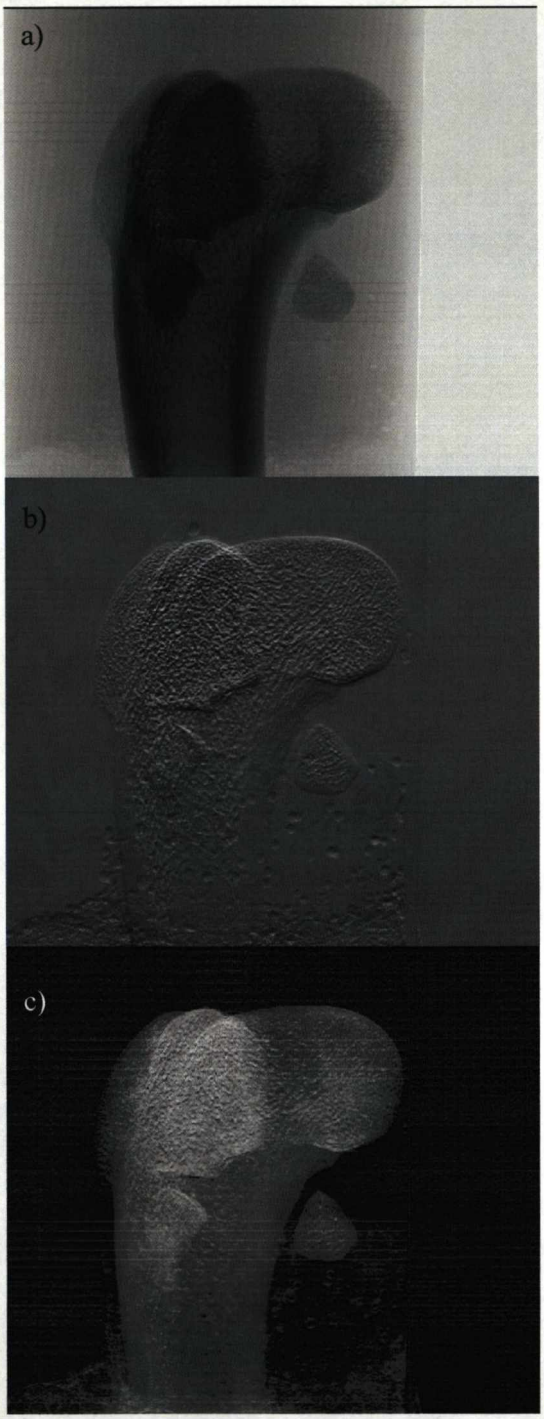

Figure A3-12: The peak ±15% MIR images of the disarticulated sample in the first orientation. a) The absorption image. b) The refraction image. c) The USAXS image.

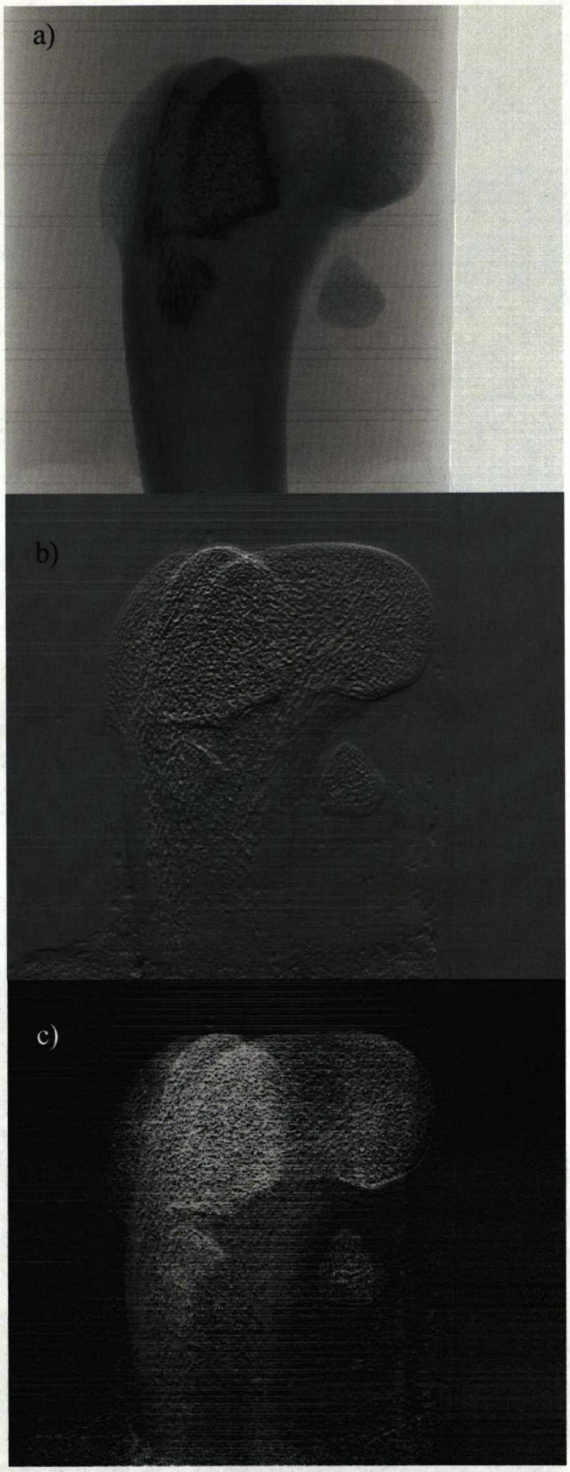

Figure A2-13: The peak ±50% MIR images of the disarticulated sample in the first orientation. a) The absorption image. b) The refraction image. c) The USAXS image.

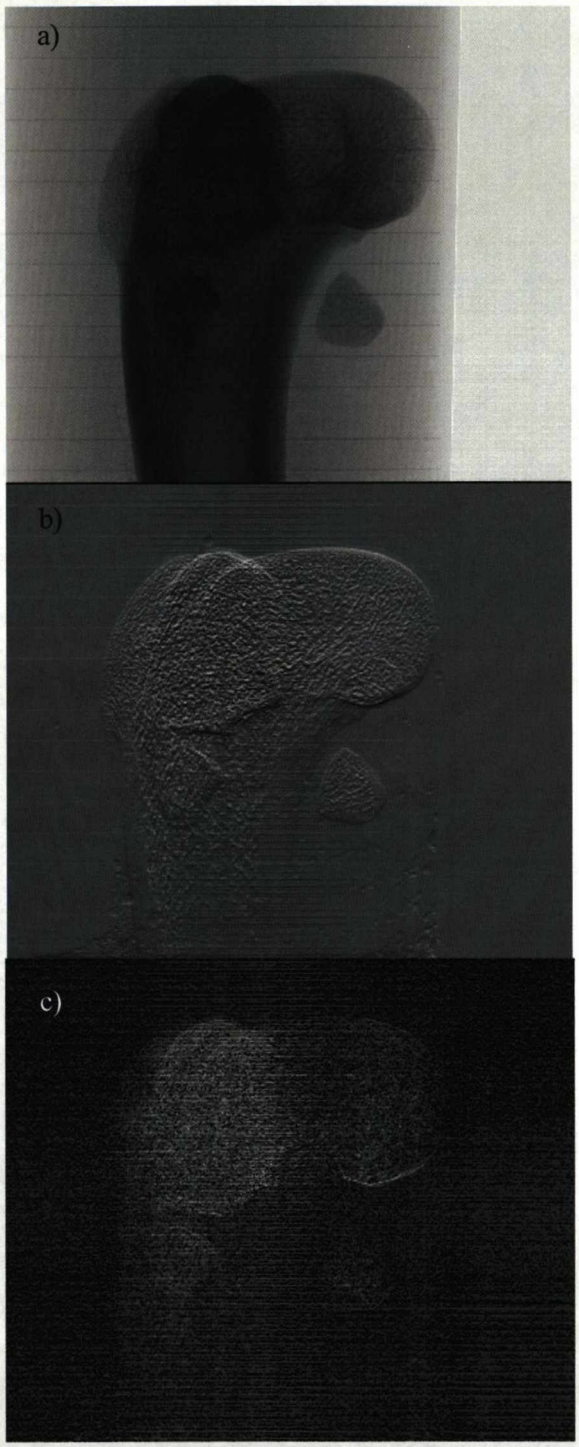

Figure A2-14: The peak ±80% MIR images of the disarticulated sample in the first orientation. a) The absorption image. b) The refraction image. c) The USAXS image.

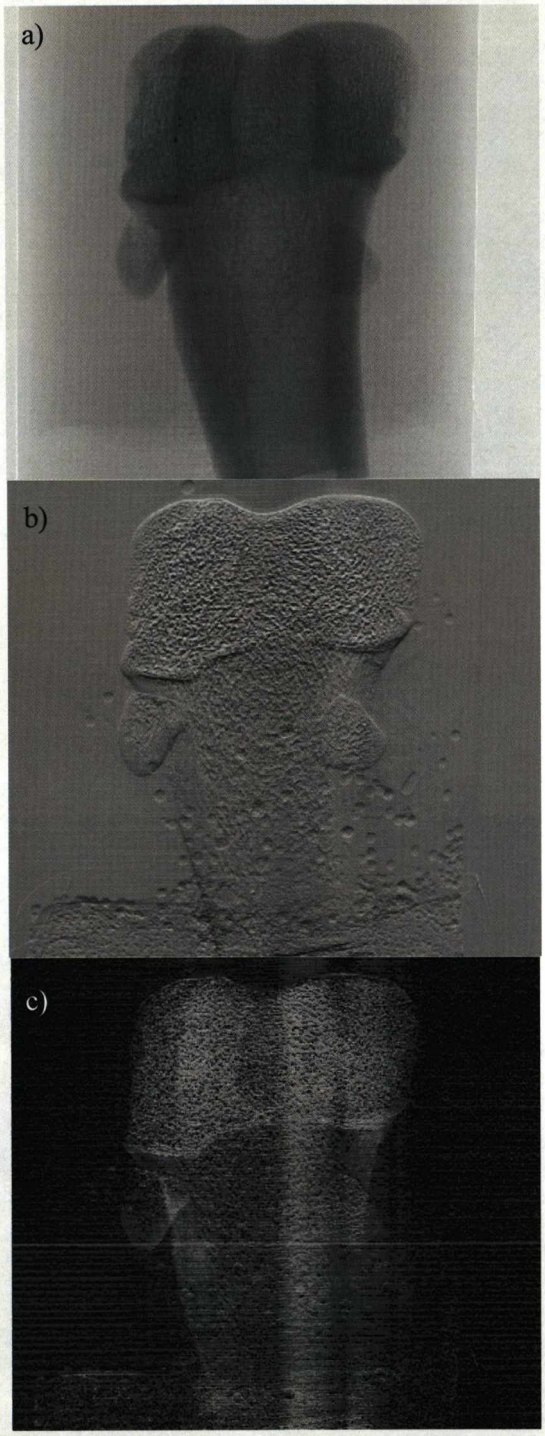

Figure A2-15: The peak ±50% MIR images of the disarticulated sample in the second orientation. a) The absorption image. b) The refraction image. c) The USAXS image.

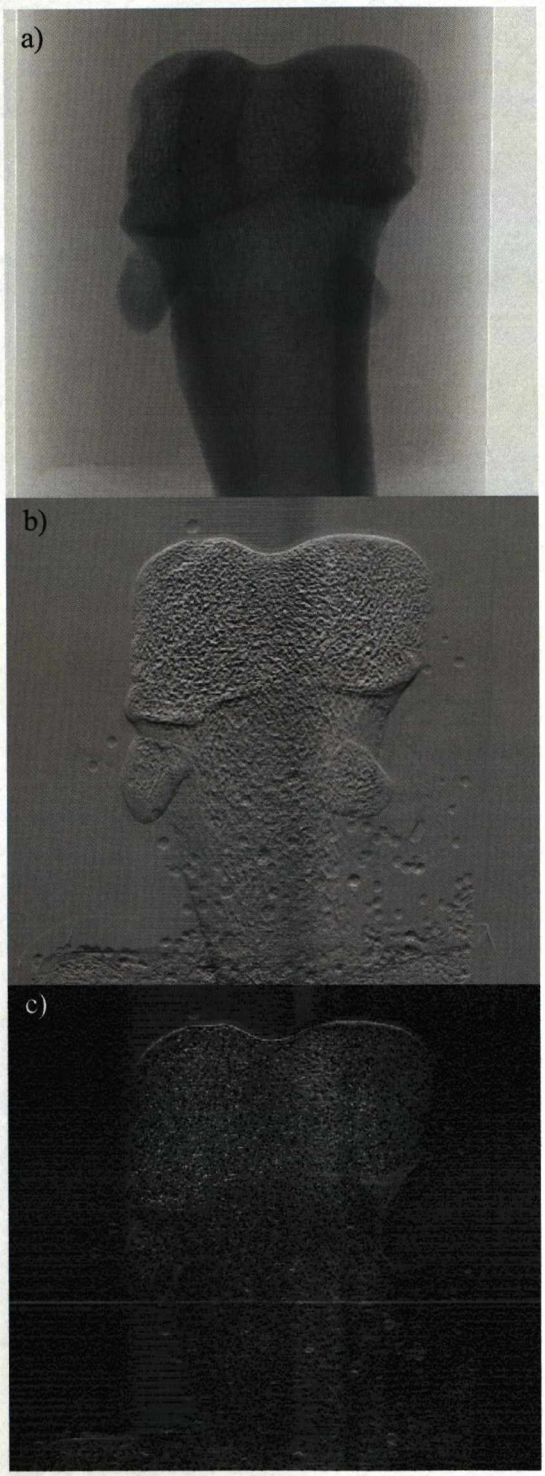

Figure A2-16: The peak ±80% MIR images of the disarticulated sample in the second orientation. a) The absorption image. b) The refraction image. c) The USAXS image.

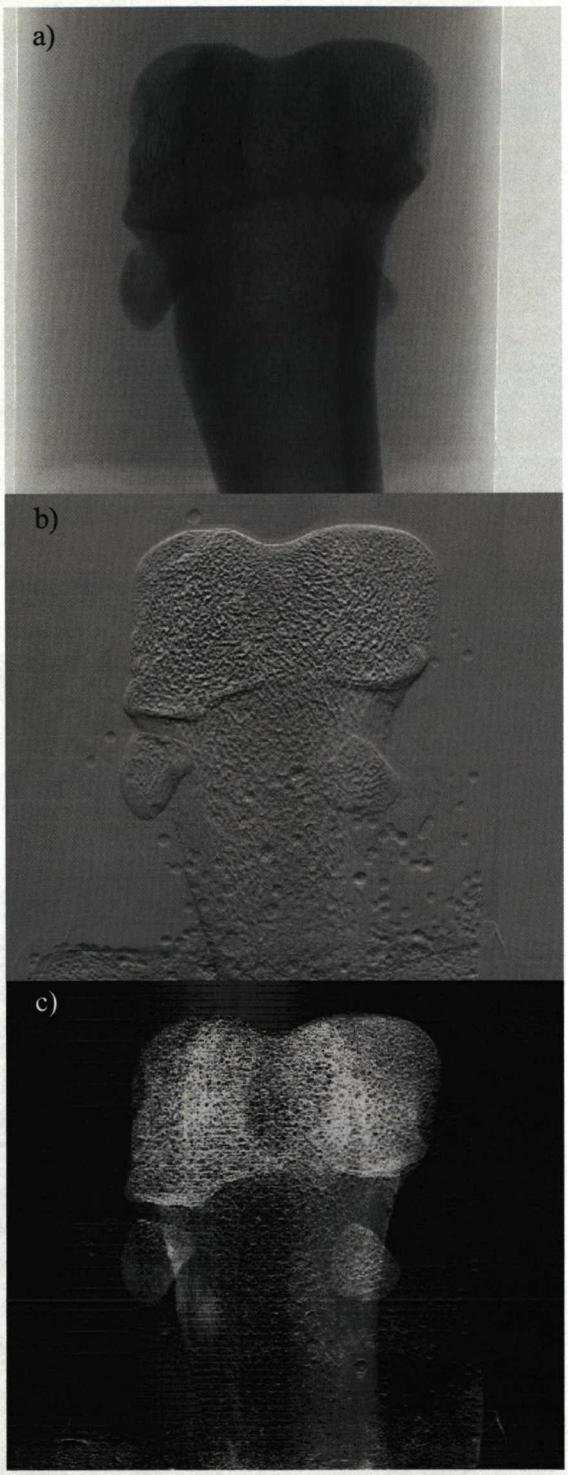

Figure A2-17: The peak ±50% ±80% MIR images of the disarticulated sample in the second orientation. a) The absorption image. b) The refraction image. c) The USAXS image.

3 WHOLE SAMPLE RESULTS

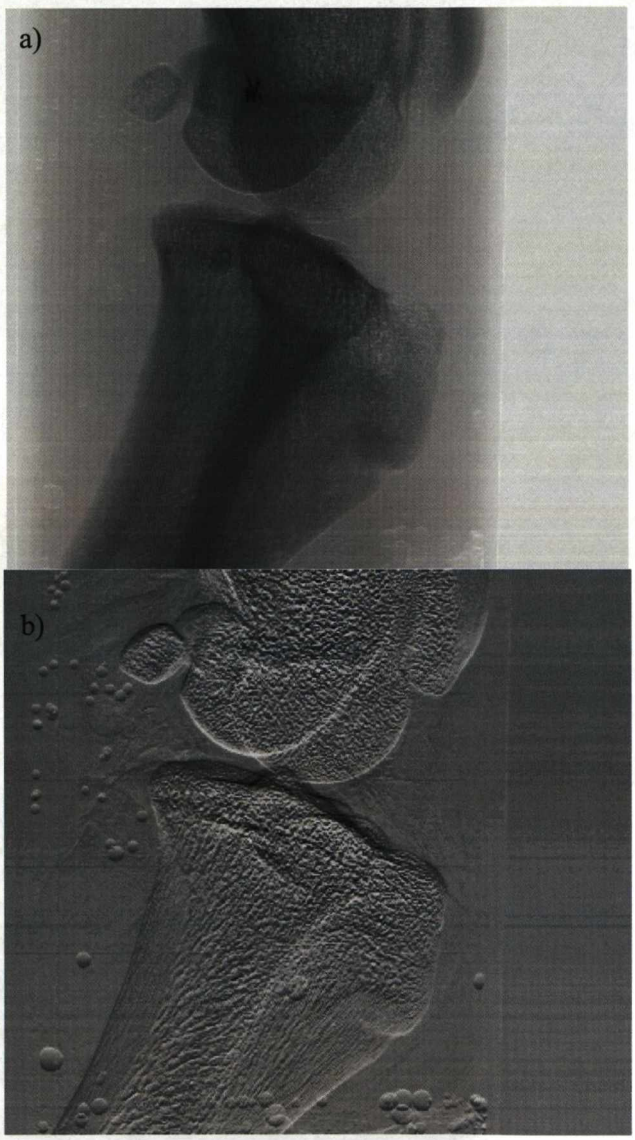

Figure A2-18: The ±15% DEI images of the disarticulated sample in the first orientation. a) The apparent absorption image. b) The refraction image.

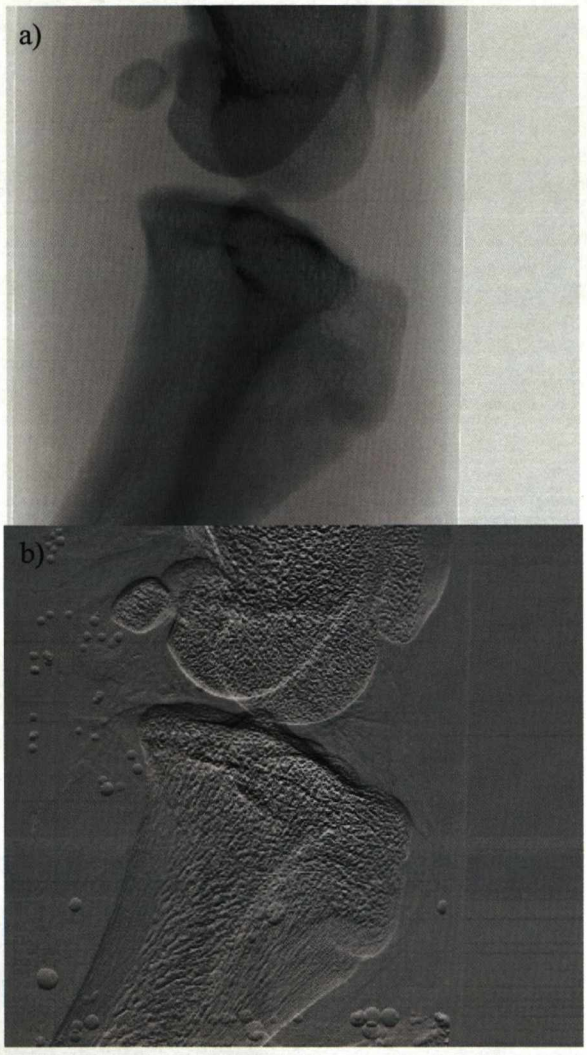

Figure A2-19: The ±30% DEI images of the disarticulated sample in the first orientation. a) The apparent absorption image. b) The refraction image.

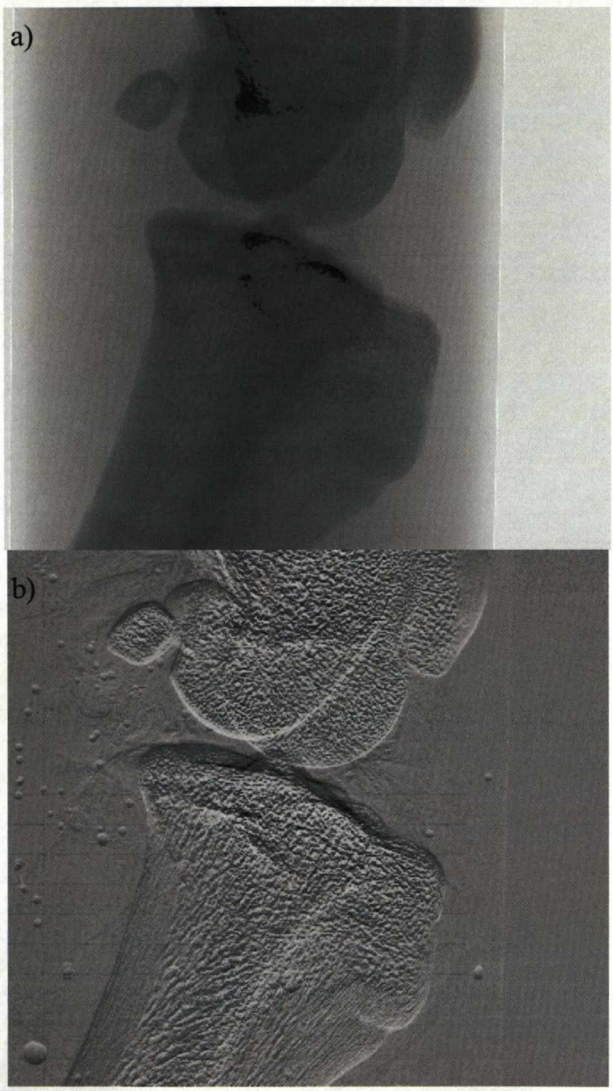

Figure A2-20: The ±80% DEI images of the disarticulated sample in the first orientation. a) The apparent absorption image. b) The refraction image.

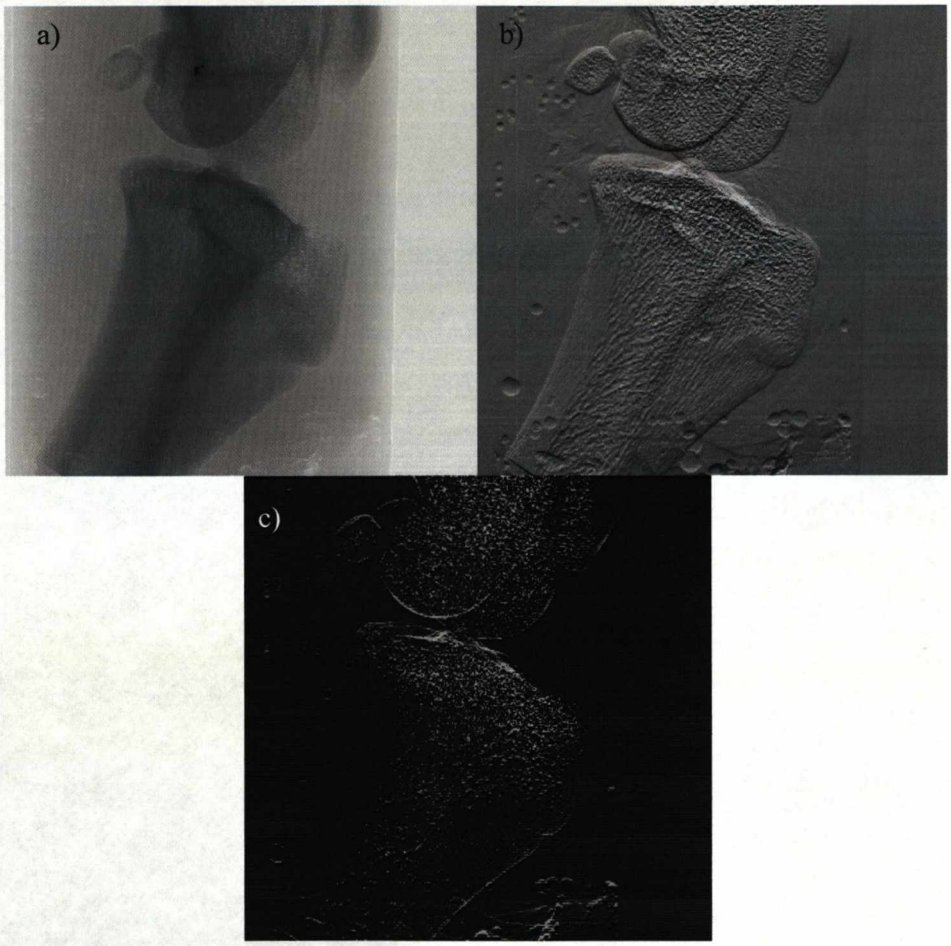

Figure A2-21: The ±15% MIR images of the disarticulated sample in the first orientation. a) The absorption image. b) The refraction image. c) The USAXS image.

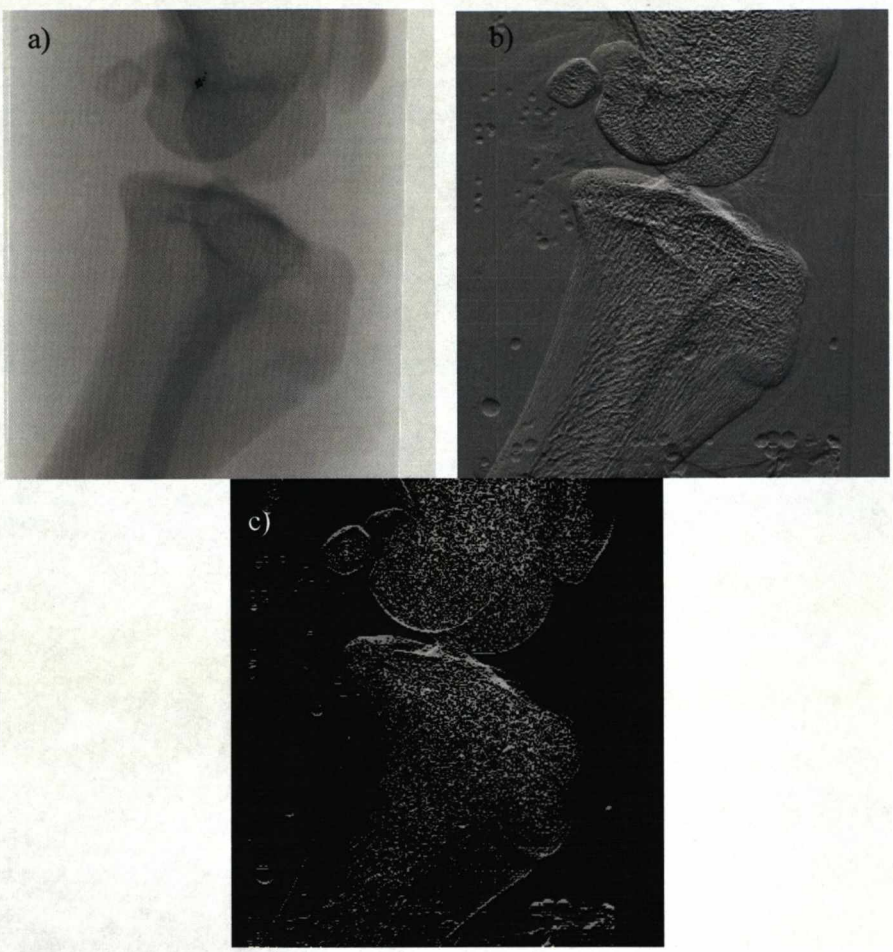

Figure A2-22: The ±30% MIR images of the disarticulated sample in the first orientation. a) The absorption image. b) The refraction image. c) The USAXS image.

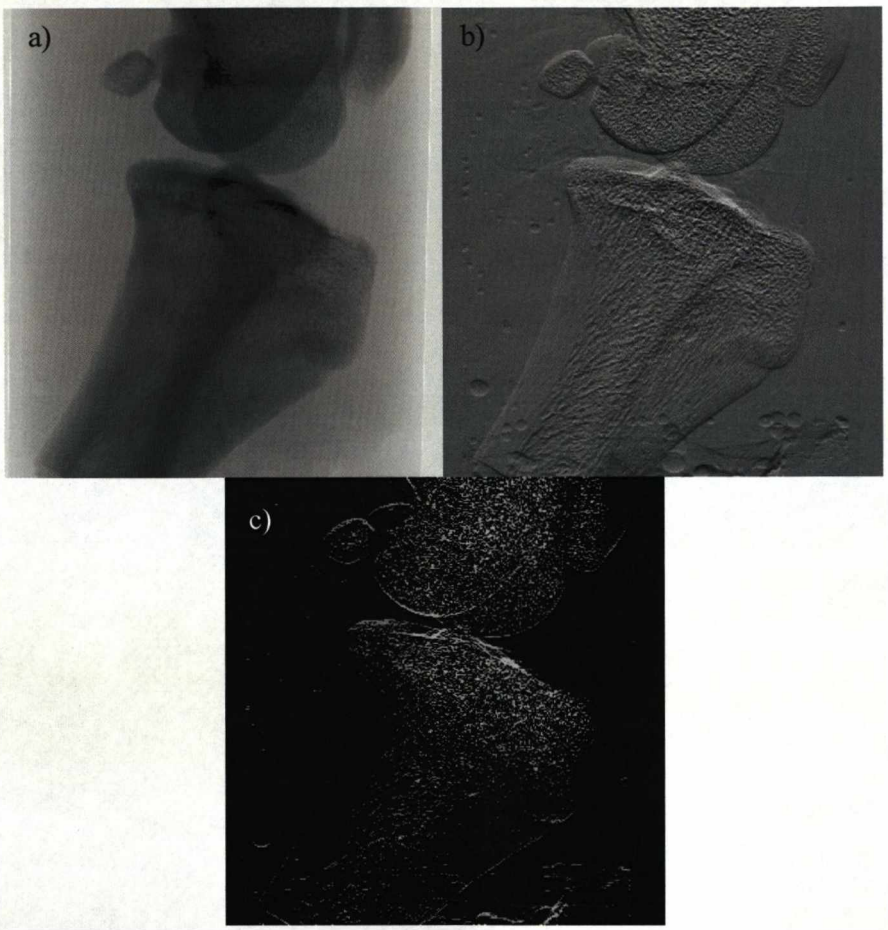

Figure A2-23: The ±80% MIR images of the disarticulated sample in the first orientation. a) The absorption image. b) The refraction image. c) The USAXS image.

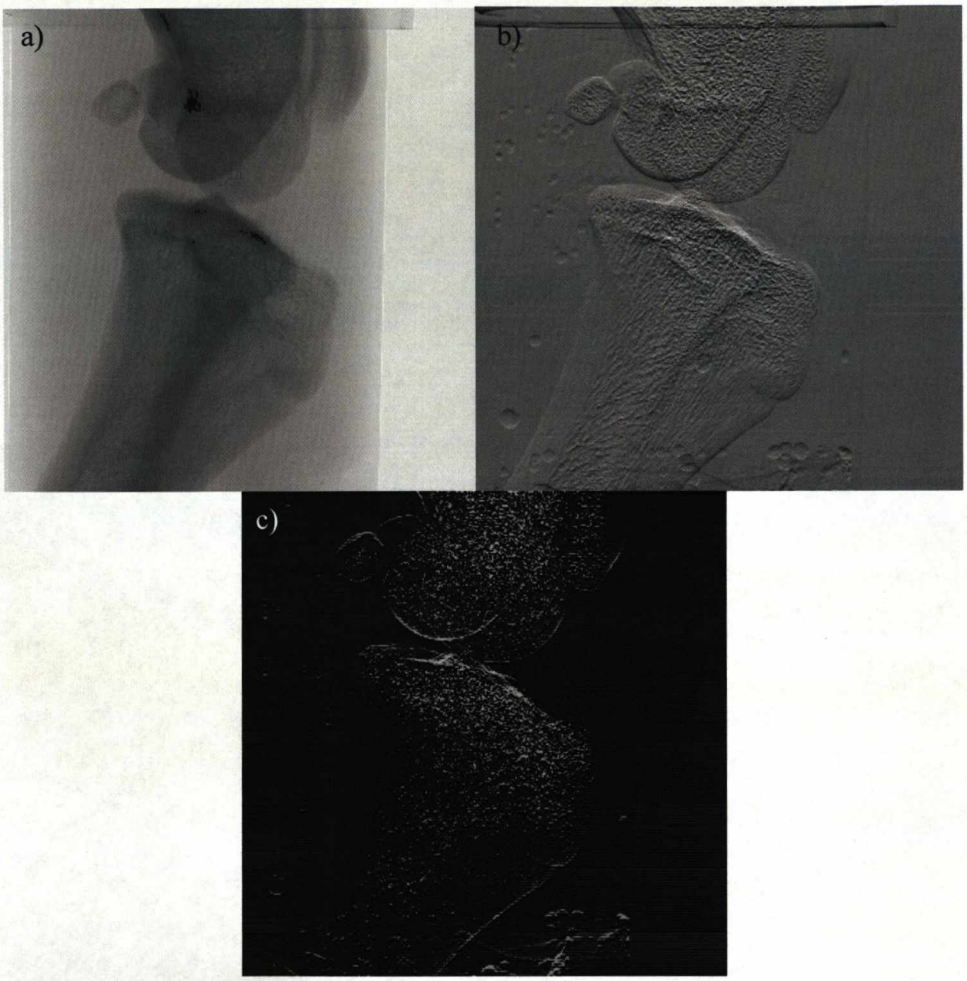

Figure A2-24: The ±15% peak MIR images of the disarticulated sample in the first orientation. a) The absorption image. b) The refraction image. c) The USAXS image.

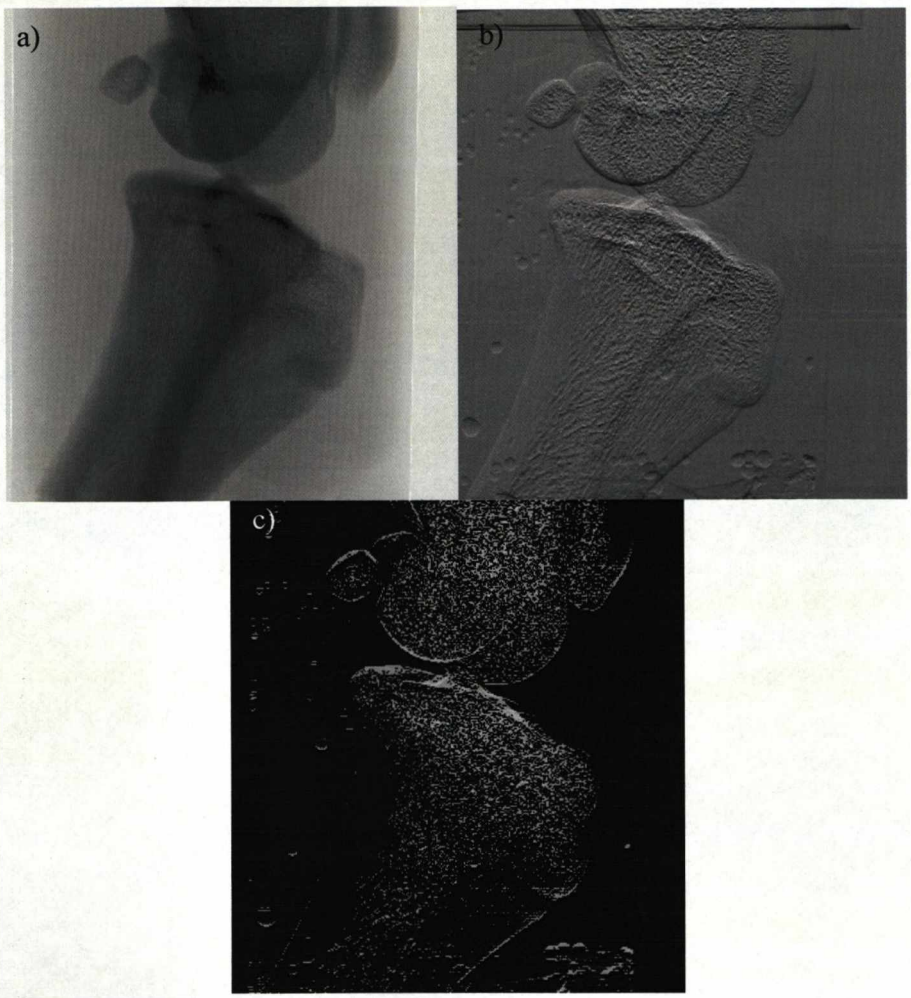

Figure A2-25: The ±30% peak MIR images of the disarticulated sample in the first orientation. a) The absorption image. b) The refraction image. c) The USAXS image.

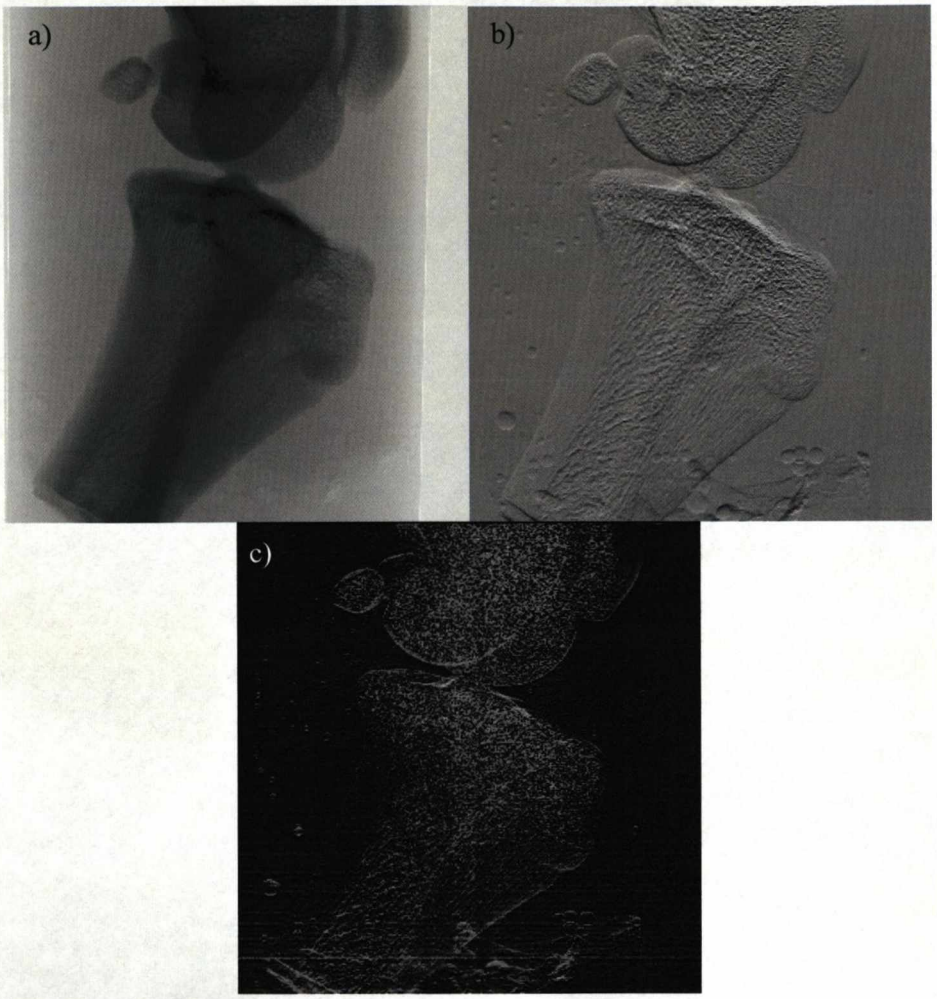

Figure A2-26: The ±80% peak MIR images of the disarticulated sample in the first orientation. a) The absorption image. b) The refraction image. c) The USAXS image.

Figure A2-27: The ±15% ±30% ±50% ±80% peak MIR images of the disarticulated sample in the first orientation. a) The absorption image. b) The refraction image. c) The USAXS image.

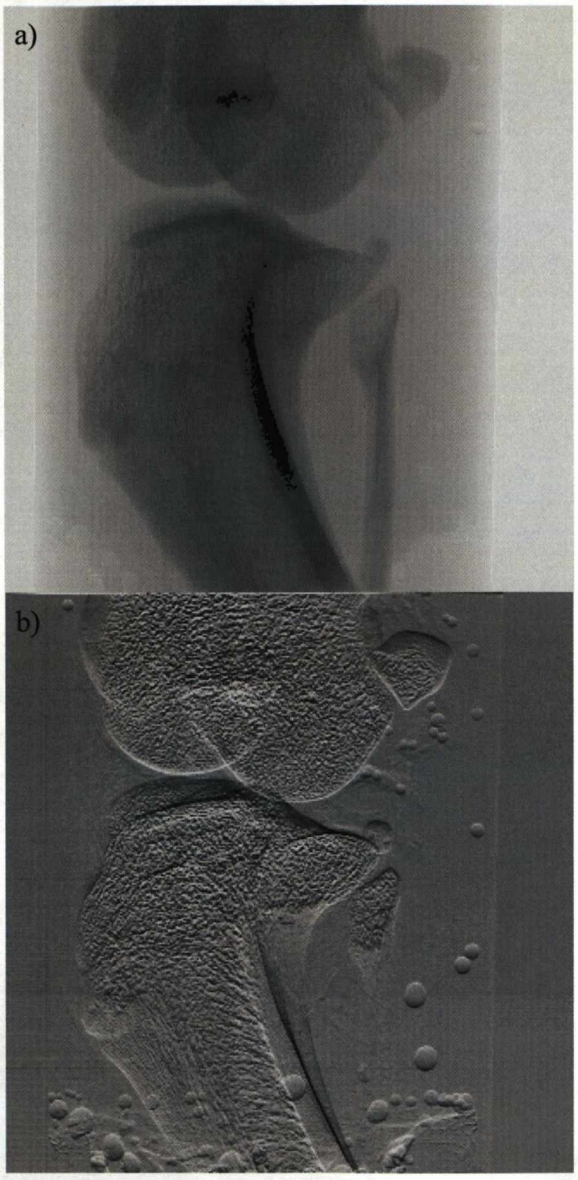

Figure A2-28: The ±30% DEI images of the disarticulated sample in the second orientation. a) The apparent absorption image. b) The refraction image.

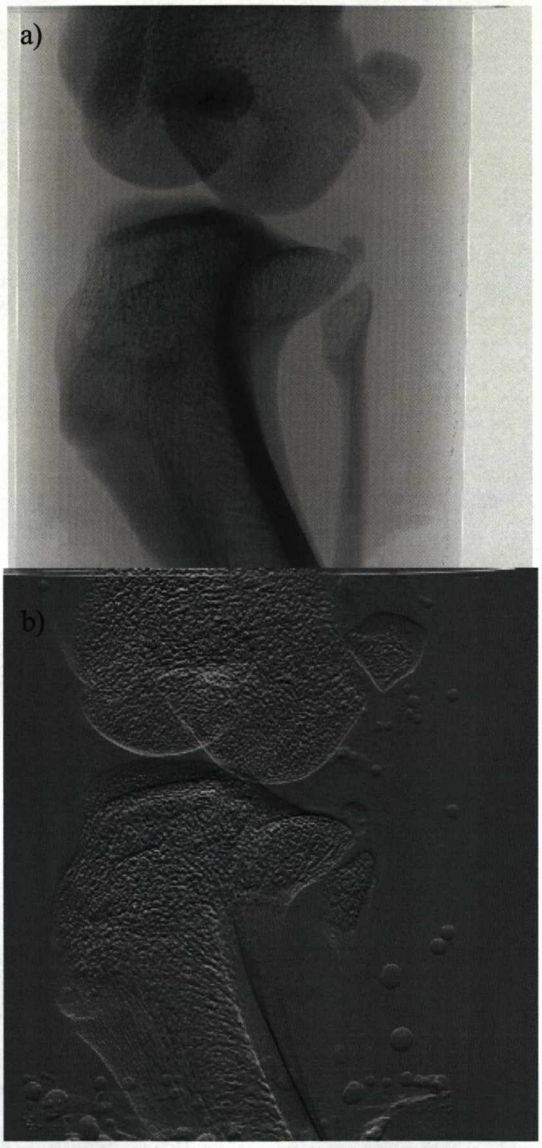

Figure A2-29: The ±80% DEI images of the disarticulated sample in the second orientation. a) The apparent absorption image. b) The refraction image.

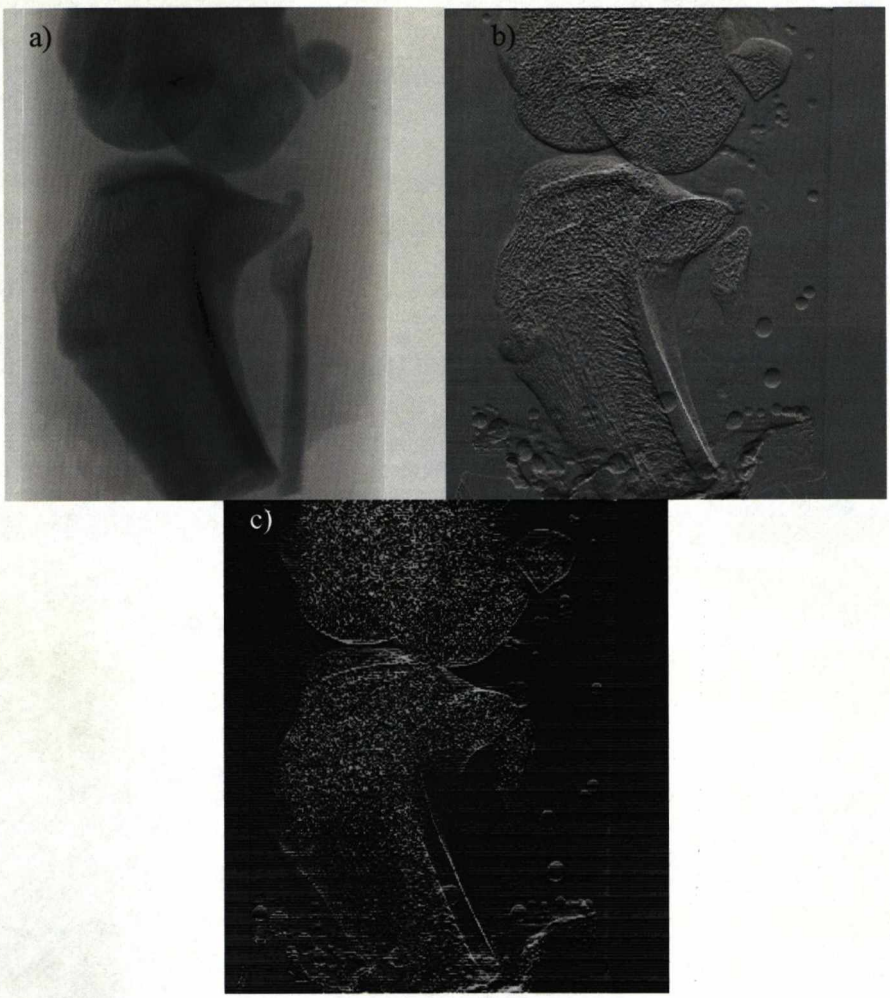

Figure A2-30: The ±30% MIR images of the disarticulated sample in the second orientation. a) The absorption image. b) The refraction image. c) The USAXS image.

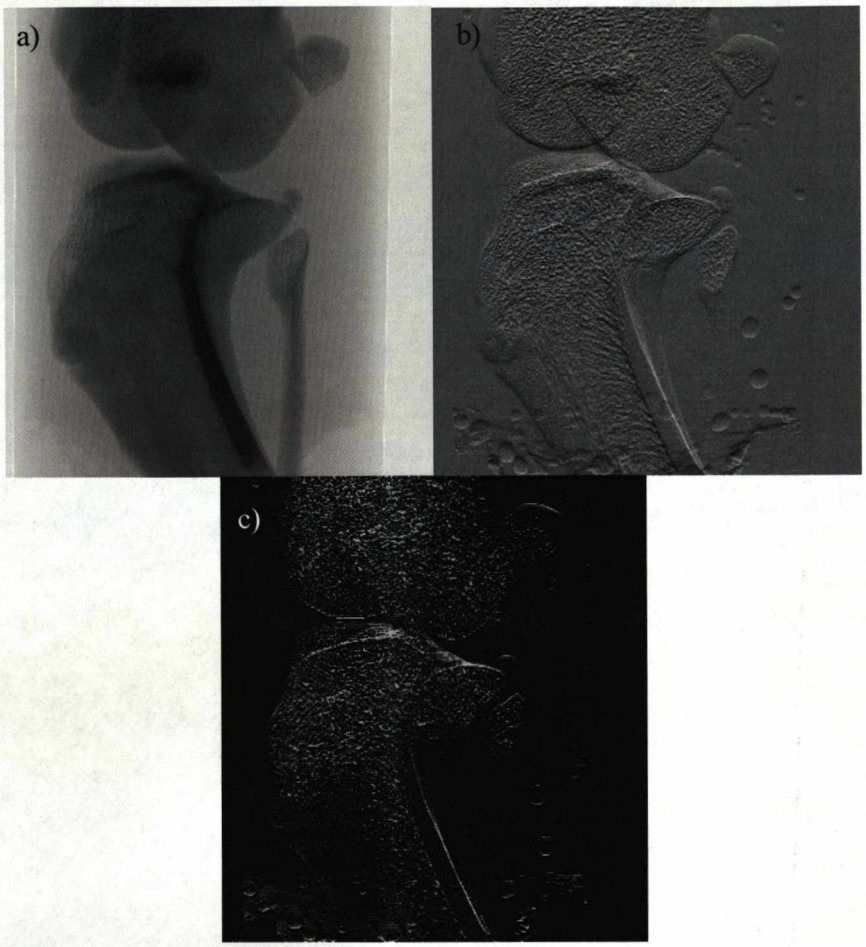

Figure A2-31: The ±80% MIR images of the disarticulated sample in the second orientation. a) The absorption image. b) The refraction image. c) The USAXS image.

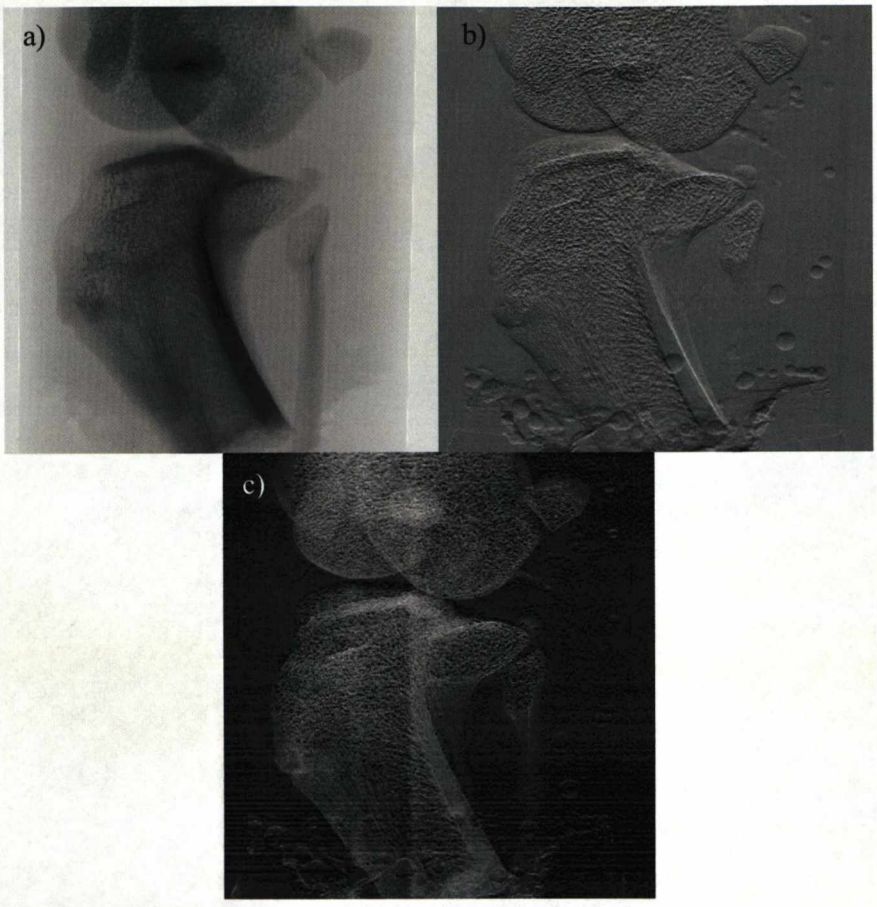

Figure A2-32: The ±30% peak MIR images of the disarticulated sample in the second orientation. a) The absorption image. b) The refraction image. c) The USAXS image.

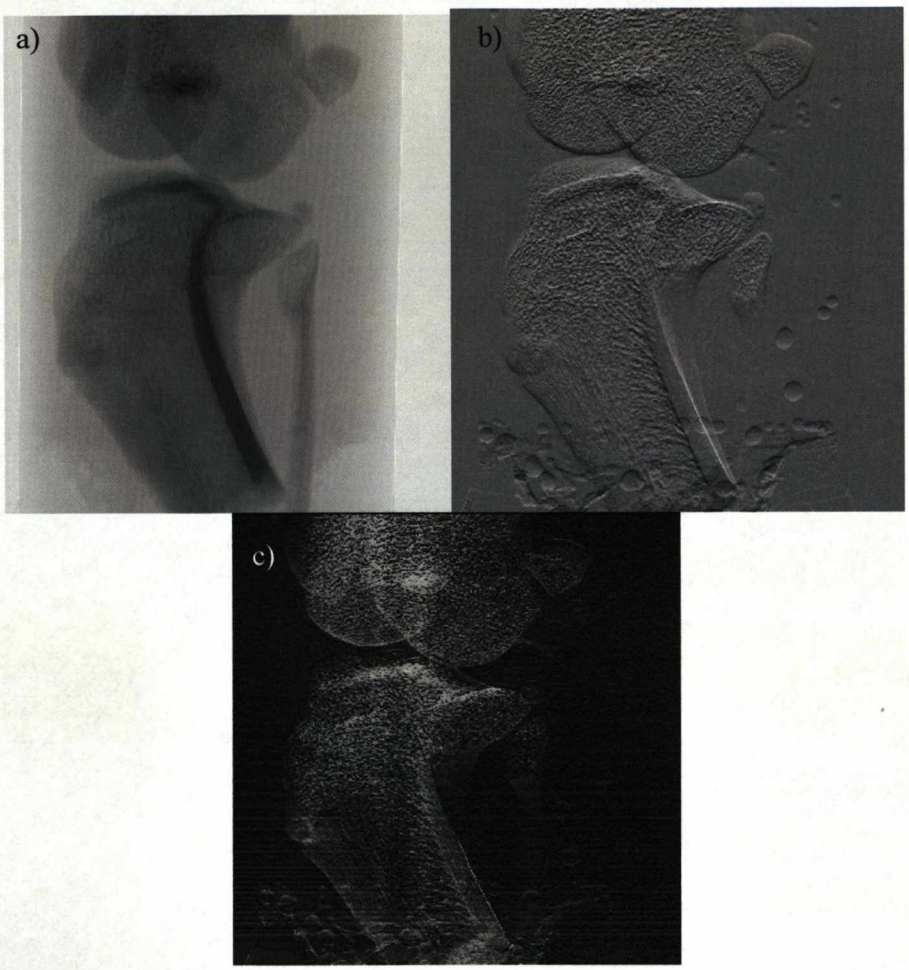

Figure A2-33: The ±50% peak MIR images of the disarticulated sample in the second orientation. a) The absorption image. b) The refraction image. c) The USAXS image.

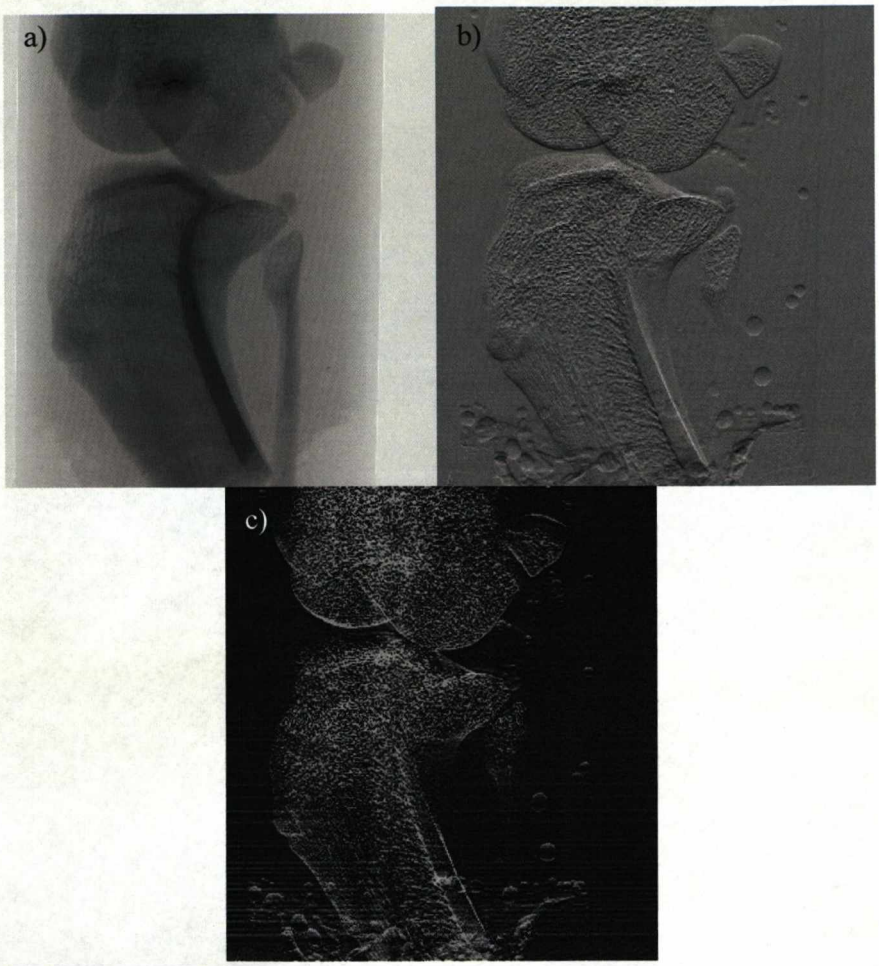

Figure A2-34: The ±80% peak MIR images of the disarticulated sample in the second orientation. a) The absorption image. b) The refraction image. c) The USAXS image.

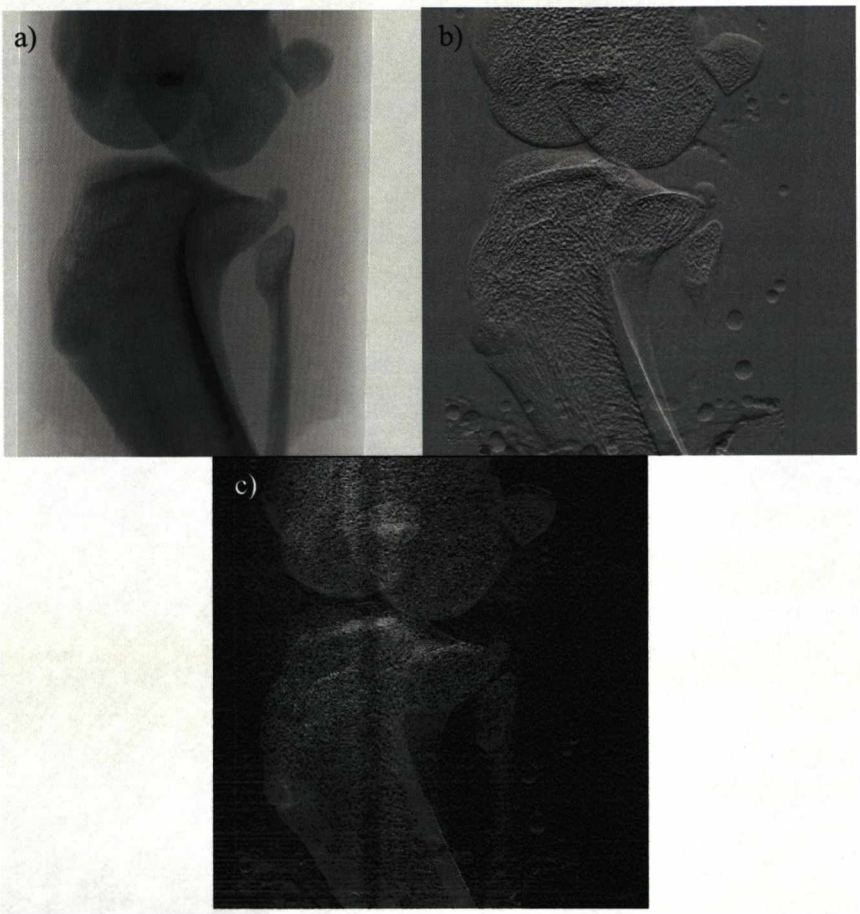

Figure A2-35: The ±30% ±50% ±80% peak MIR images of the disarticulated sample in the second orientation. a) The absorption image. b) The refraction image. c) The USAXS image.

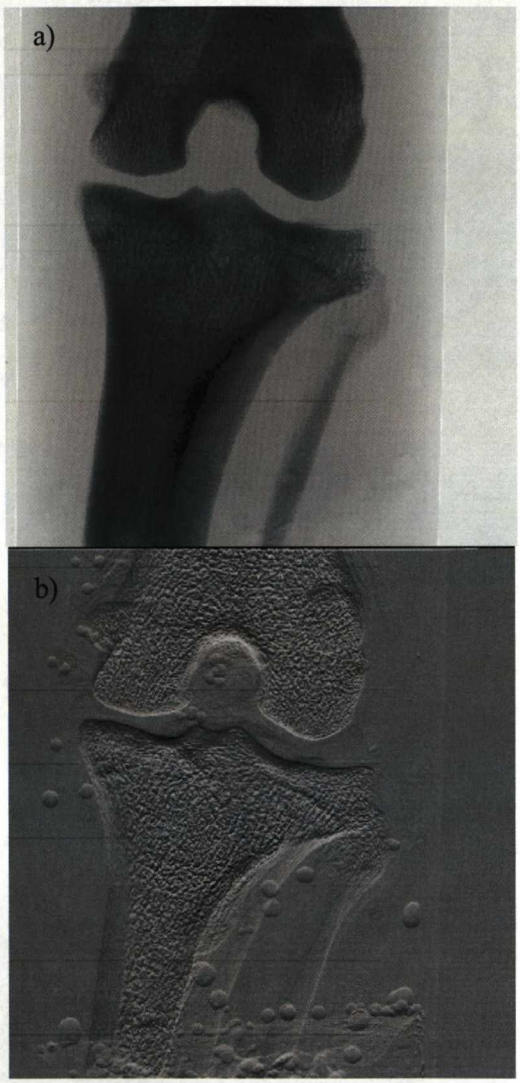

Figure A2-36: The ±80% DEI images of the disarticulated sample in the second orientation. a) The apparent absorption image. b) The refraction image.

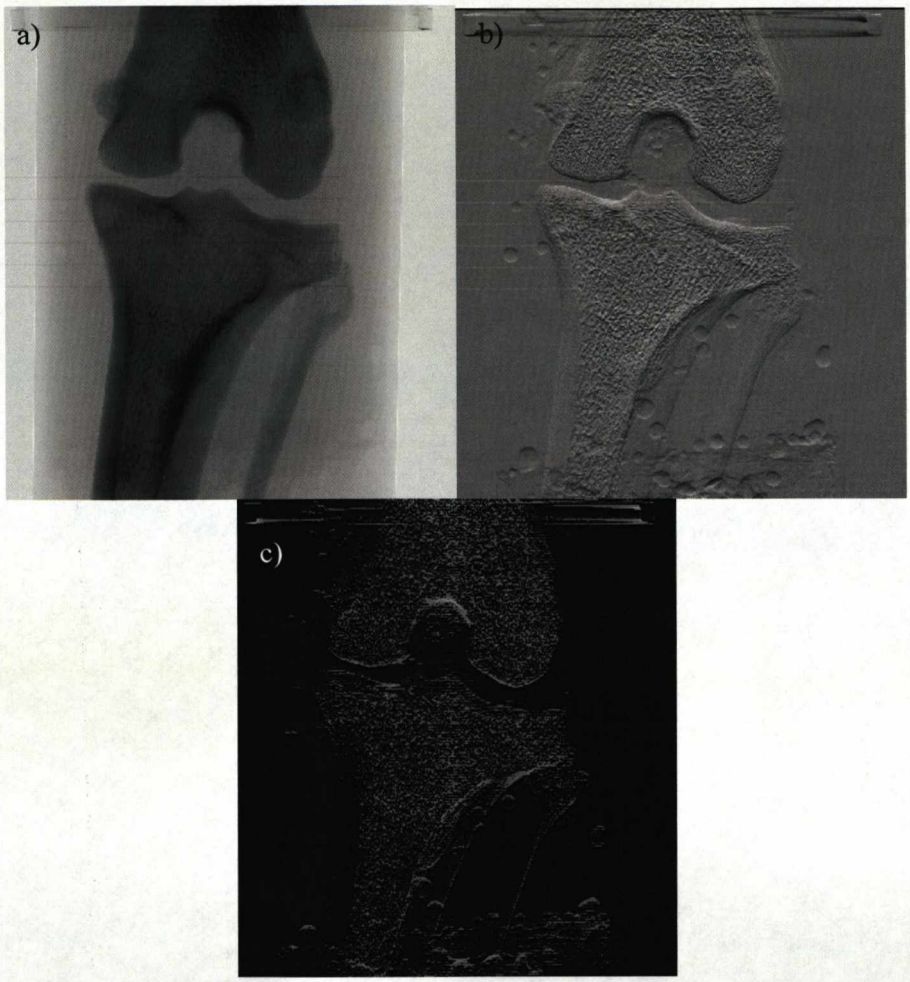

Figure A2-36: The ±80% MIR images of the disarticulated sample in the third orientation. a) The absorption image. b) The refraction image. c) The USAXS image.

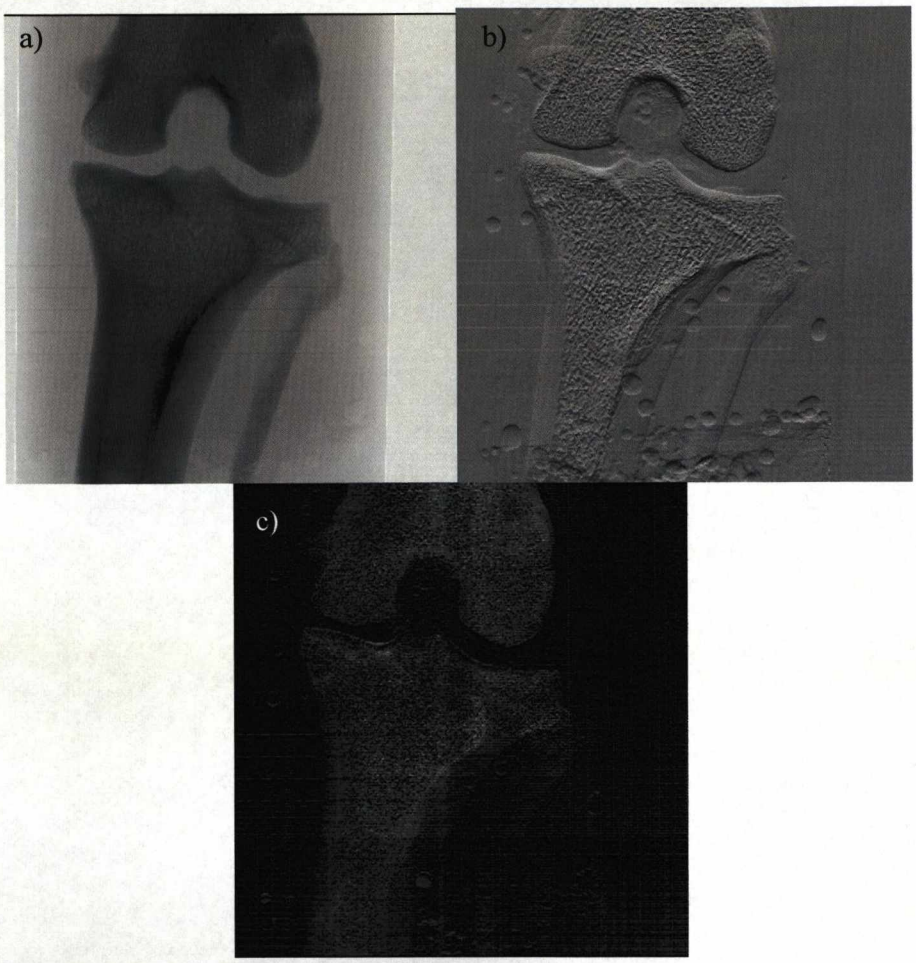

Figure A2-37: The ±50% peak MIR images of the disarticulated sample in the third orientation. a) The absorption image. b) The refraction image. c) The USAXS image.

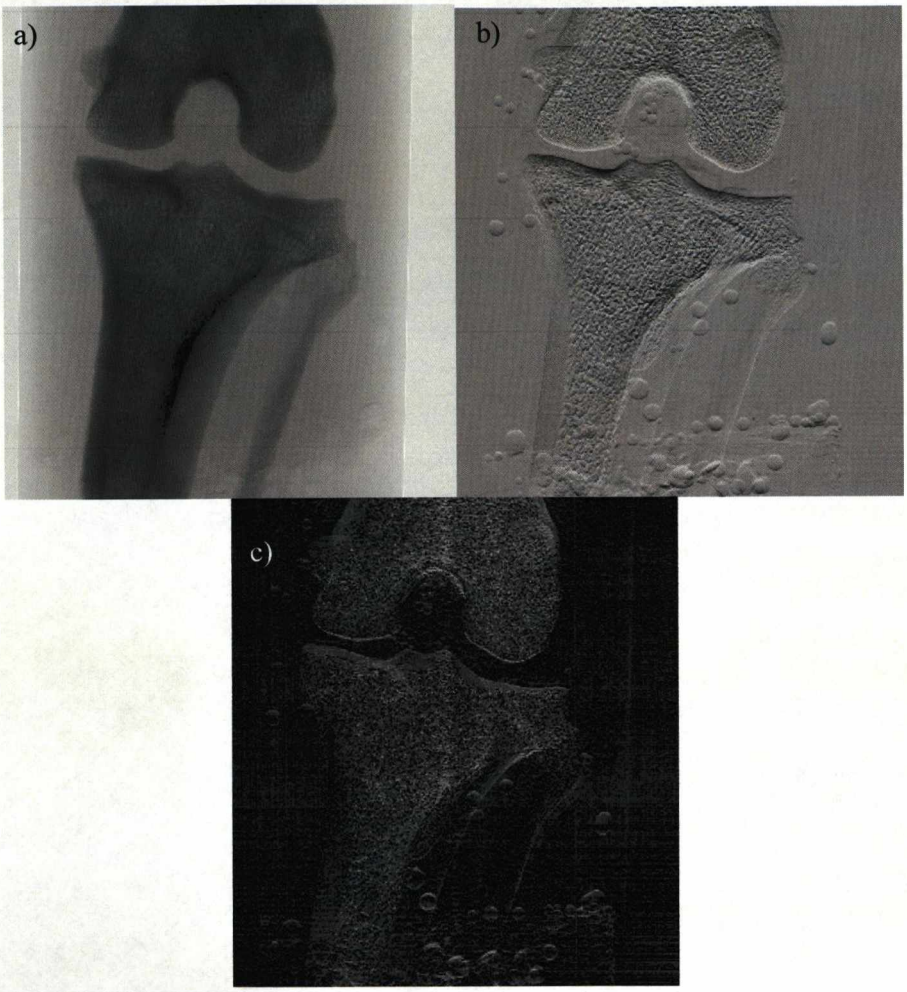

Figure A2-38: The ±80% peak MIR images of the disarticulated sample in the third orientation. a) The absorption image. b) The refraction image. c) The USAXS image.

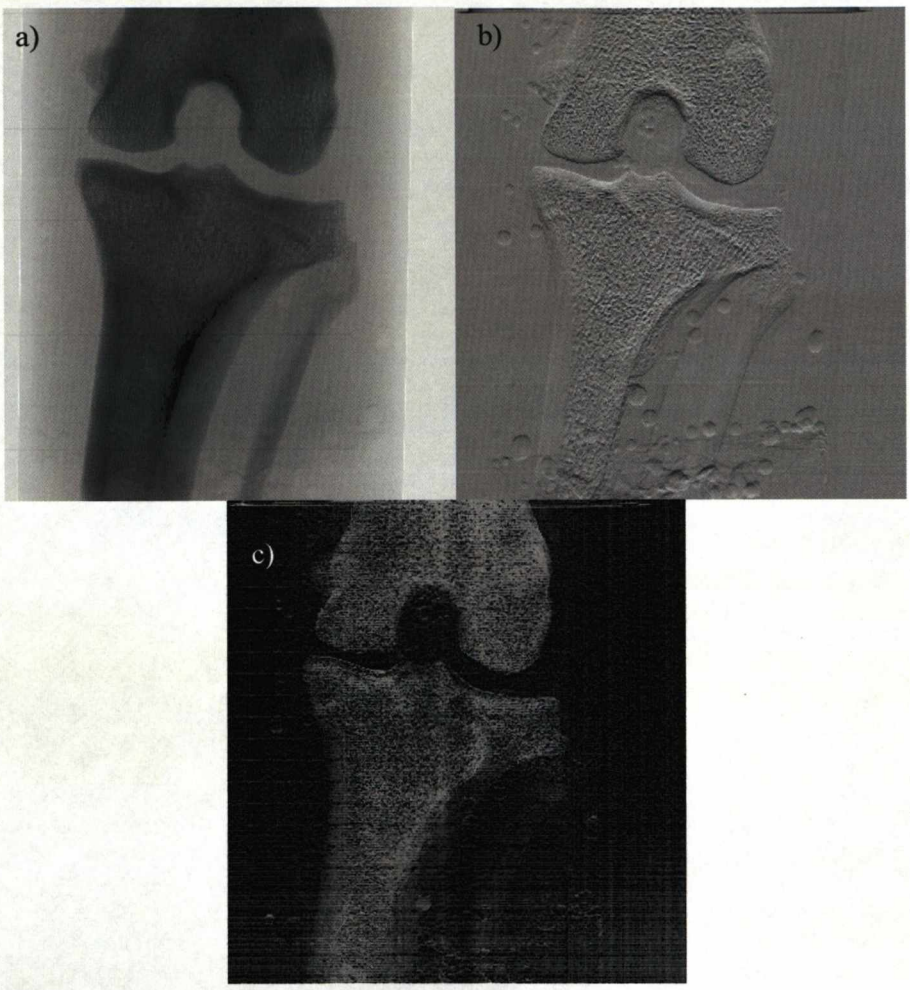

Figure A2-39: The ±50% ±80% peak MIR images of the disarticulated sample in the third orientation. a) The absorption image. b) The refraction image. c) The USAXS image.

APPENDIX 3

1 HUMAN KNEE SAMPLE RESULTS

The ABI images from the knee sample experiment.

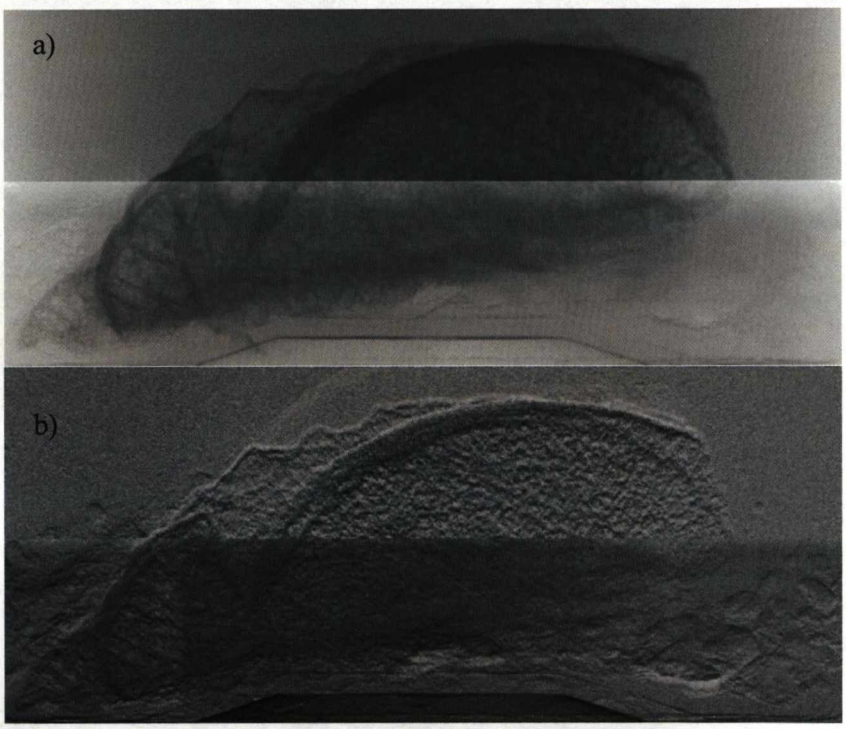

Figure A3-1: The DEI images of Sample 001A. a) The apparent absorption image. b) The refraction image.

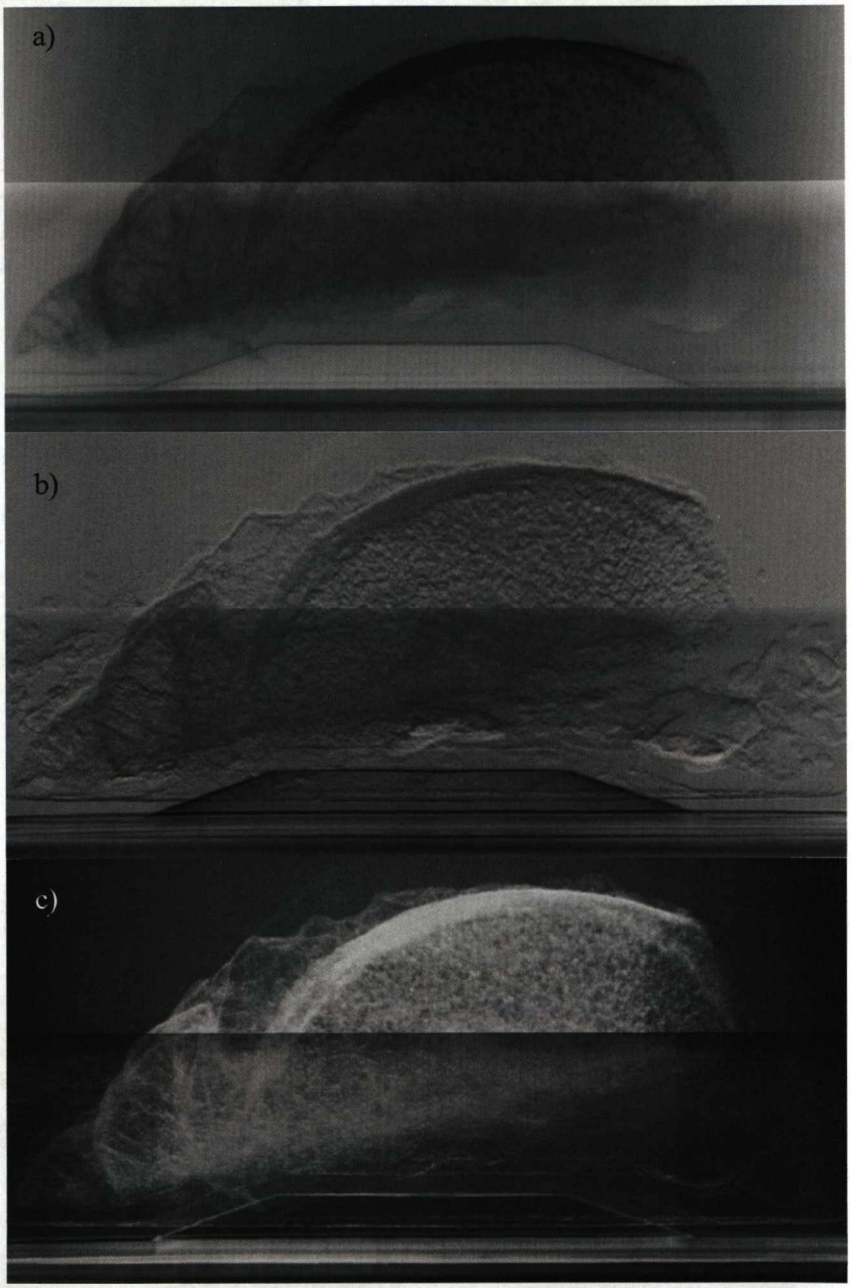

Figure A3-1: The MIR images of Sample 001A. a) The absorption image. b) The refraction image. c) The USAXS image.

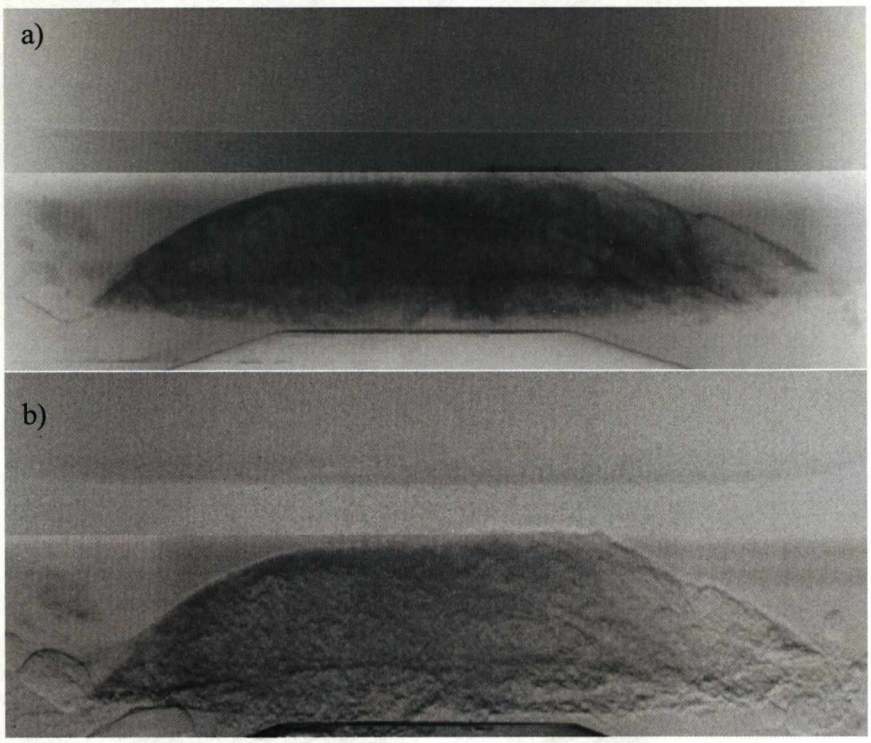

Figure A3-3: The DEI images of Sample 001B. a) The apparent absorption image. b) The refraction image.

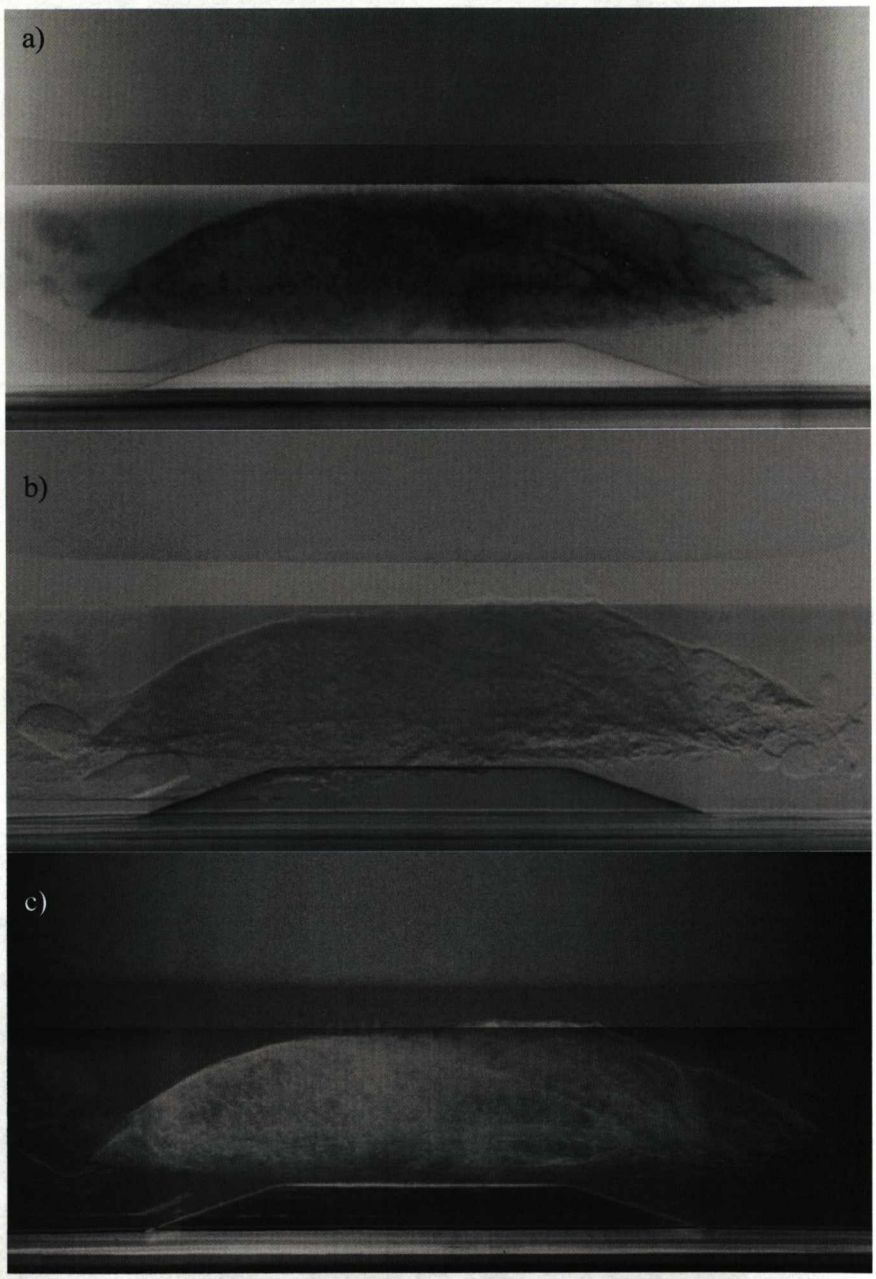

Figure A3-4: The MIR images of Sample 001B. a) The absorption image. b) The refraction image. c) The USAXS image.

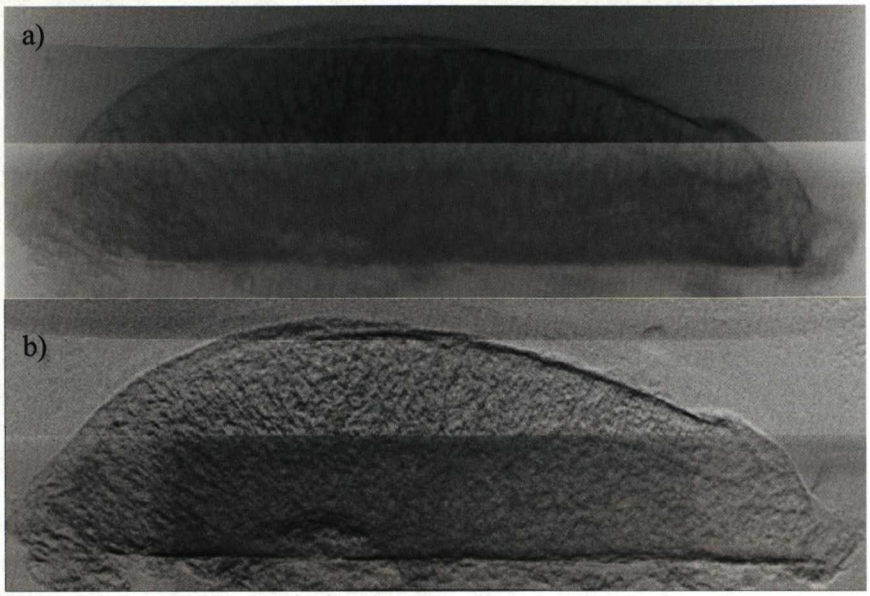

Figure A3-5: The DEI images of Sample 002A. a) The apparent absorption image. b) The refraction image.

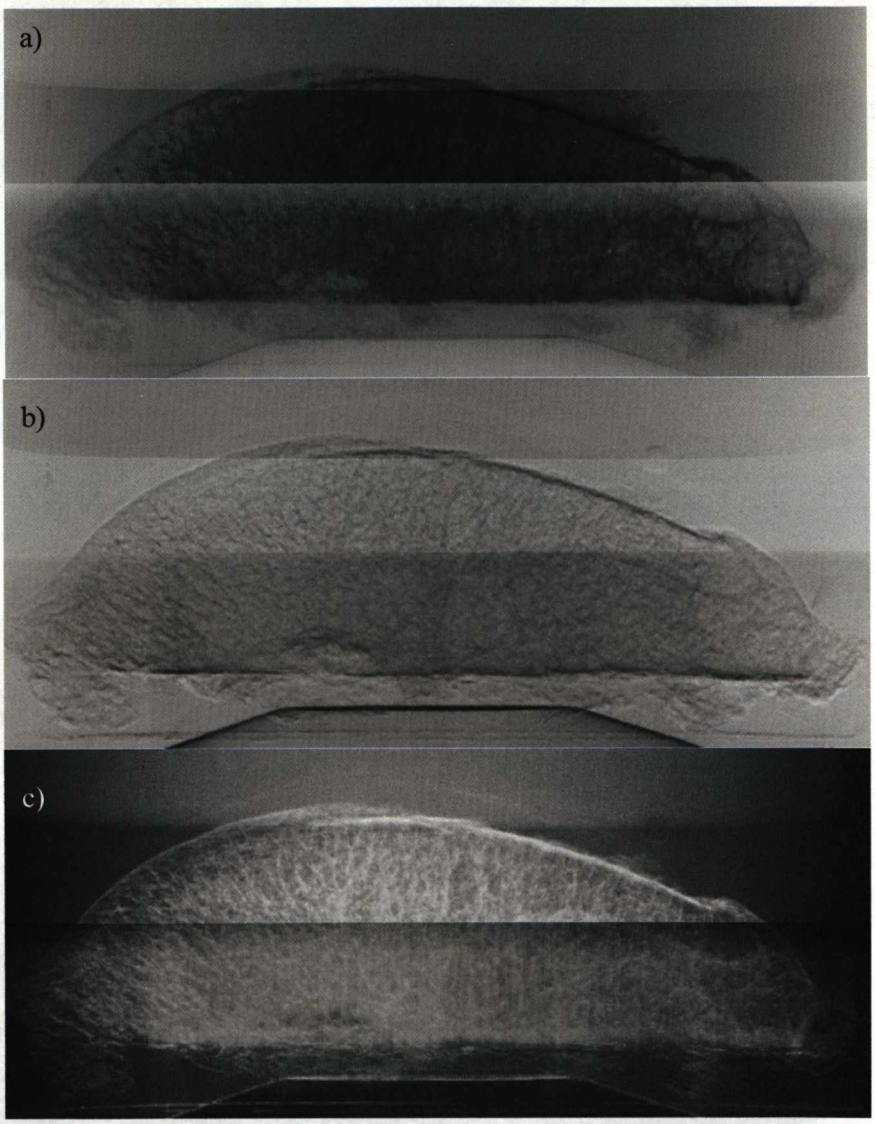

Figure A3-6: The MIR images of Sample 002A. a) The absorption image. b) The refraction image. c) The USAXS image.

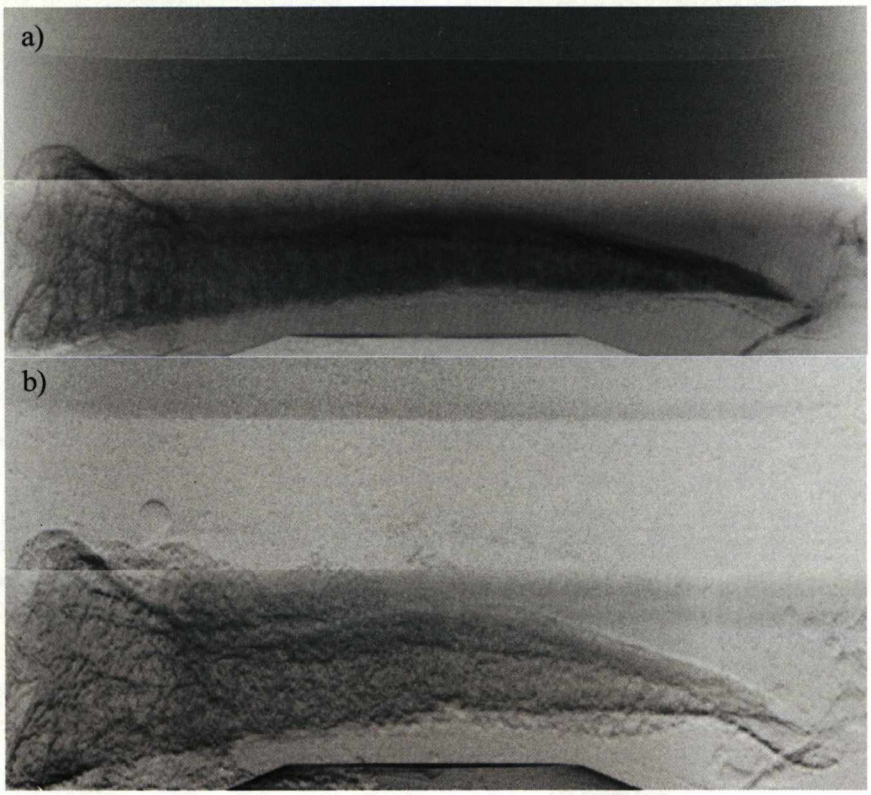

Figure A3-7: The DEI images of Sample 002B. a) The apparent absorption image. b) The refraction image.

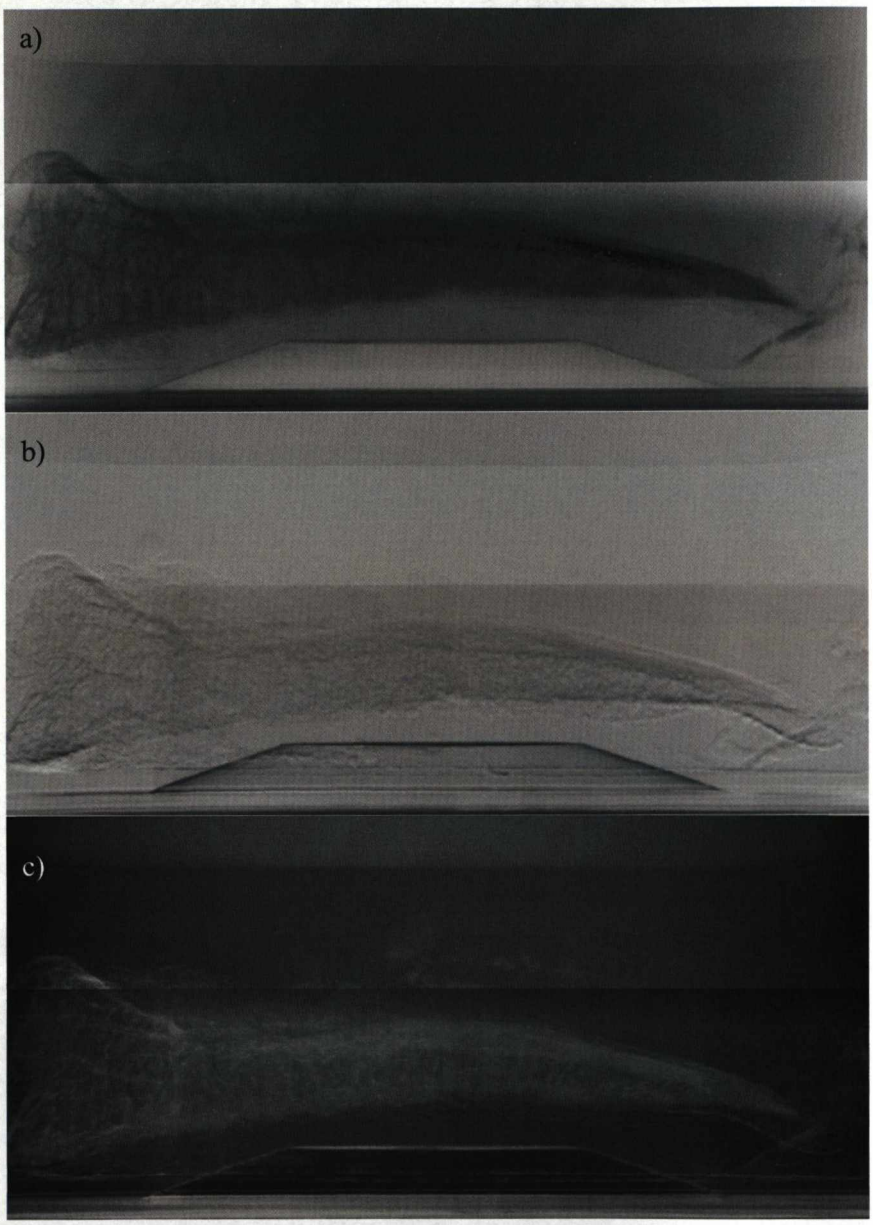

Figure A3-8: The MIR images of Sample 002B. a) The absorption image. b) The refraction image. c) The USAXS image.

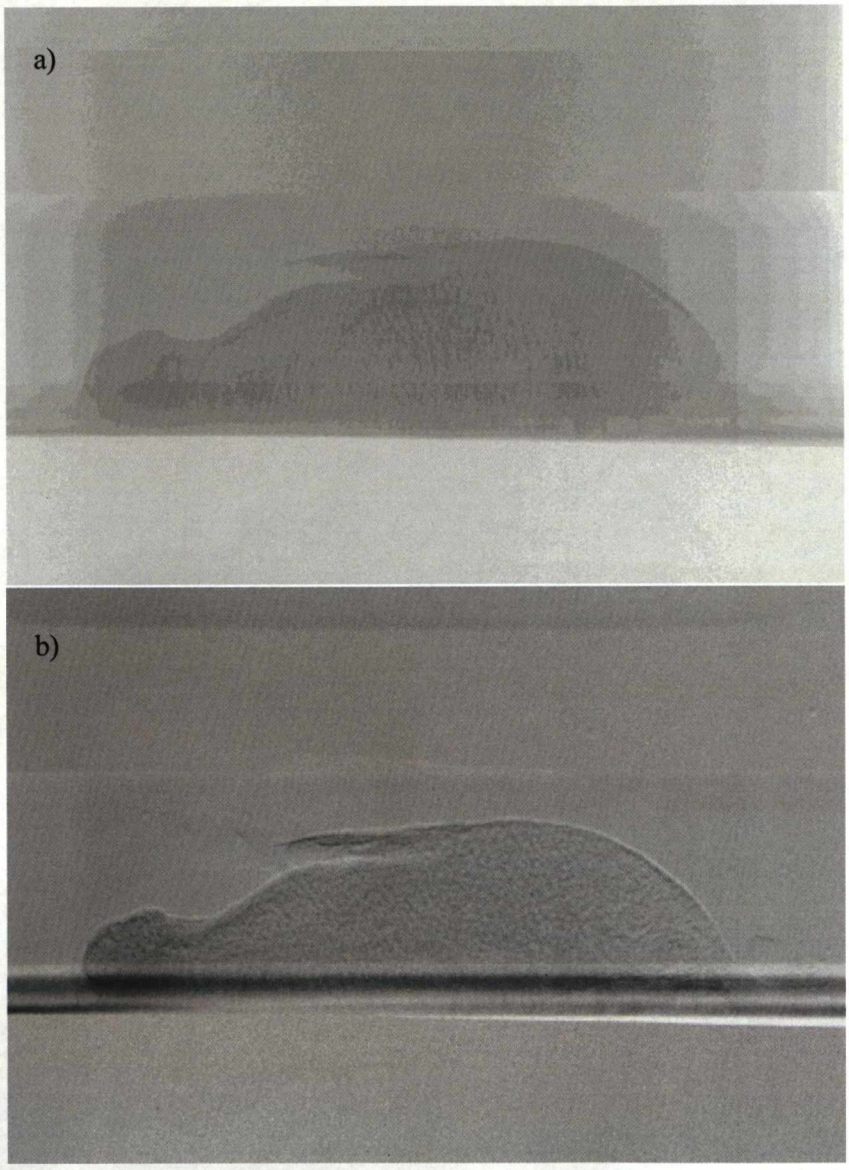

Figure A3-9: The DEI images of Sample 003B. a) The apparent absorption image. b) The refraction image.

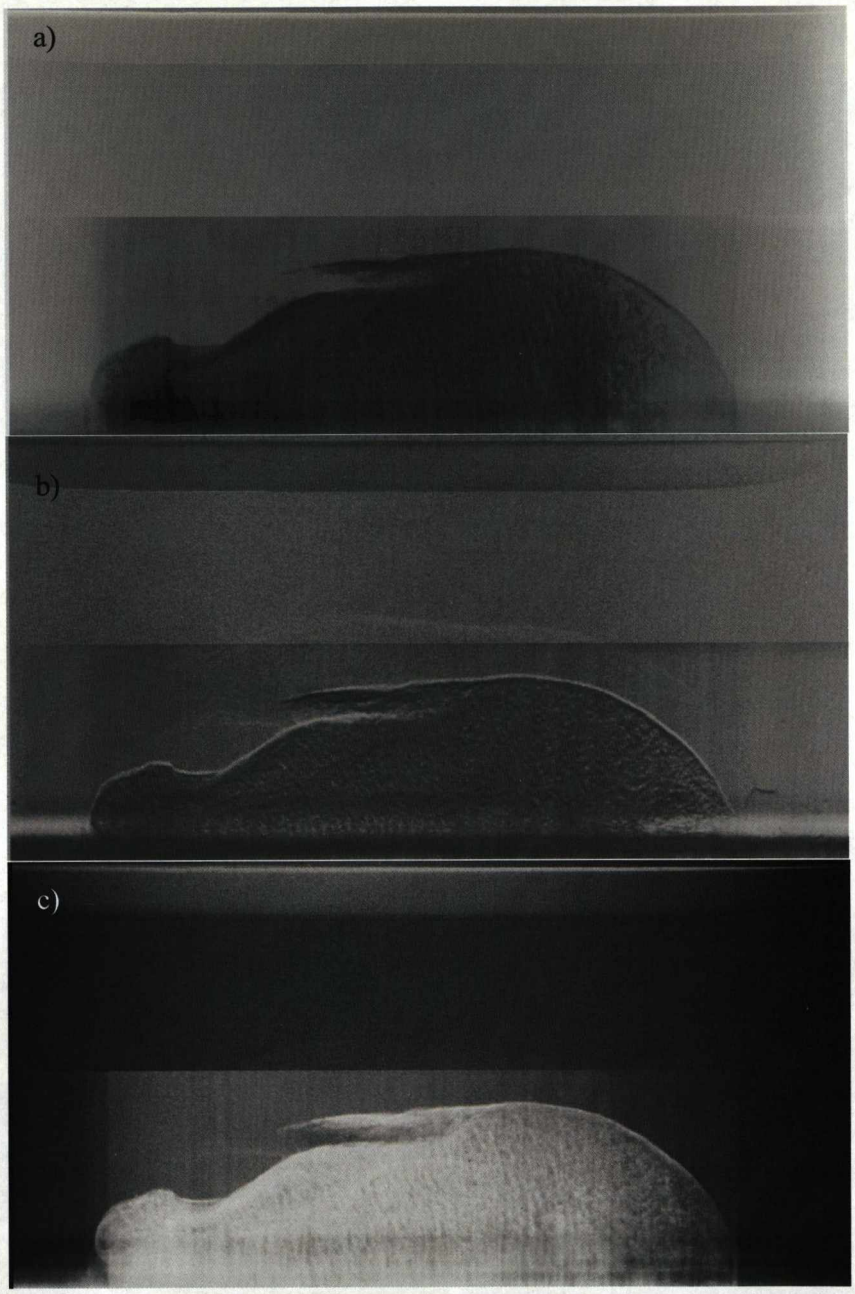

Figure A3-10: The MIR images of Sample 003B. a) The absorption image. b) The refraction image. c) The USAXS image.

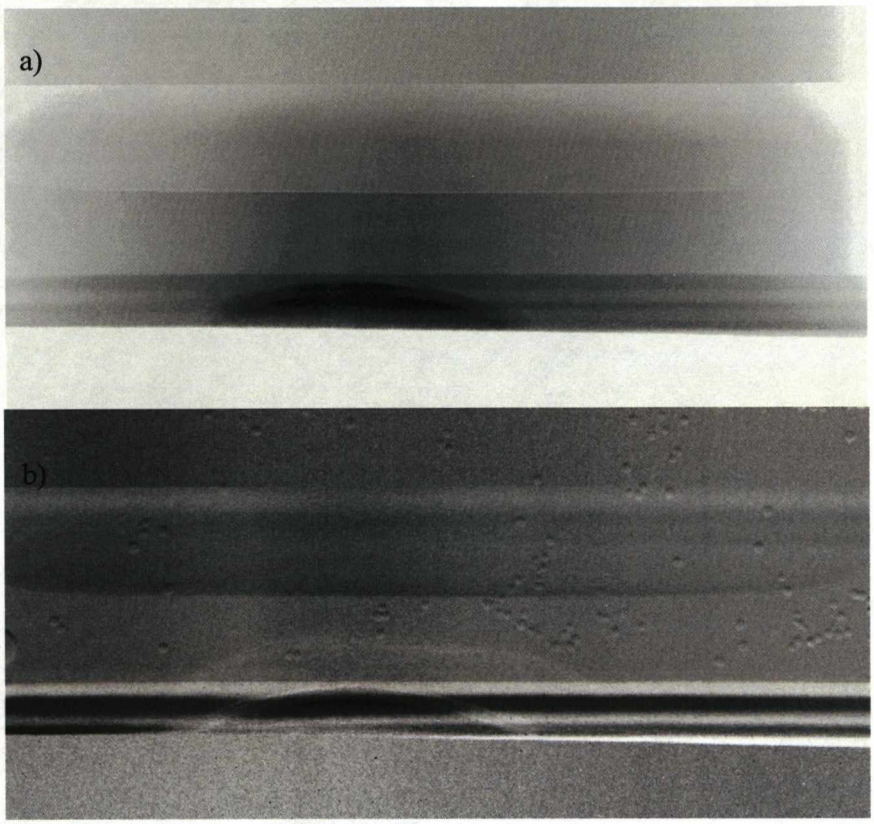

Figure A3-11: The DEI images of Sample 005A. a) The apparent absorption image. b) The refraction image.

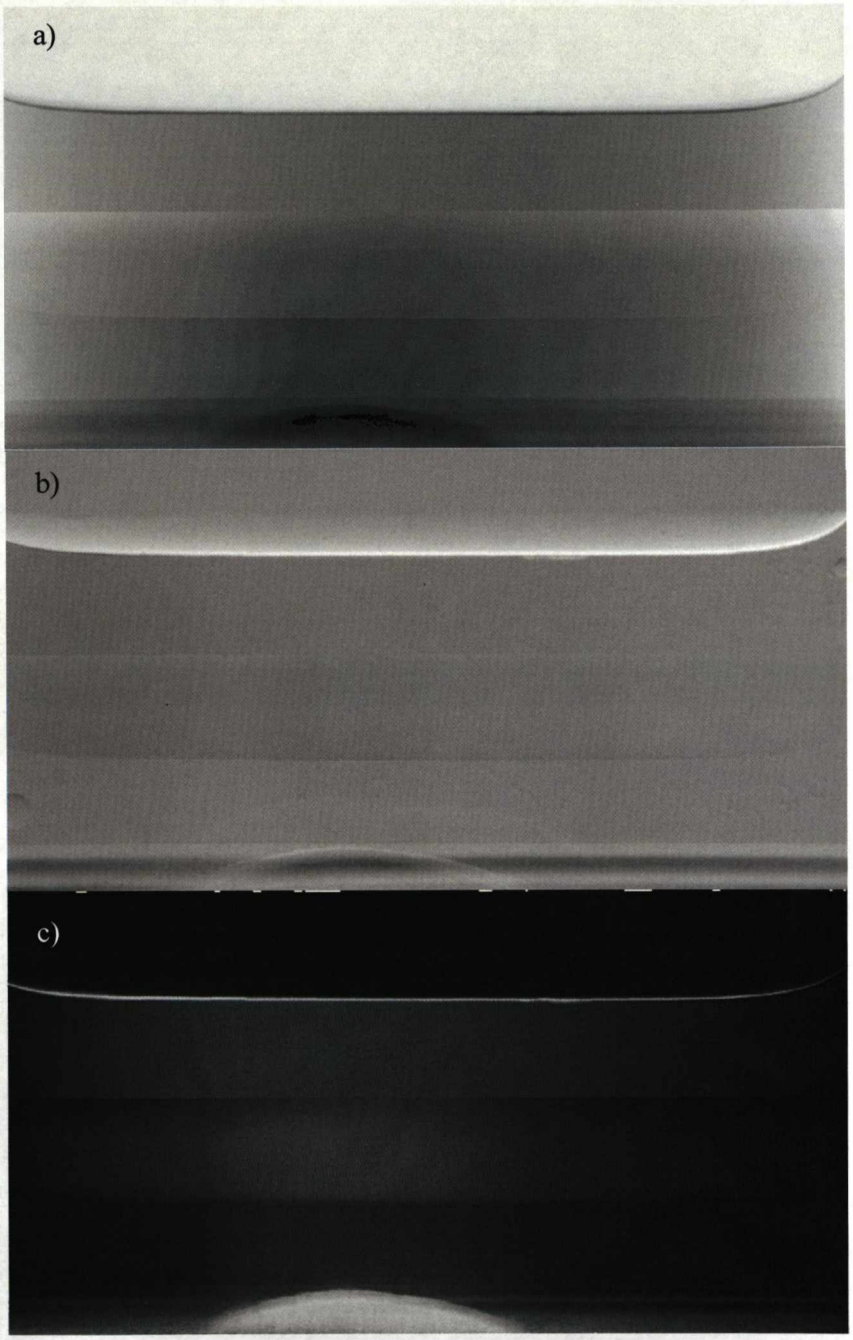

Figure A3-12: The MIR images of Sample 005A. a) The absorption image. b) The refraction image. c) The USAXS image.

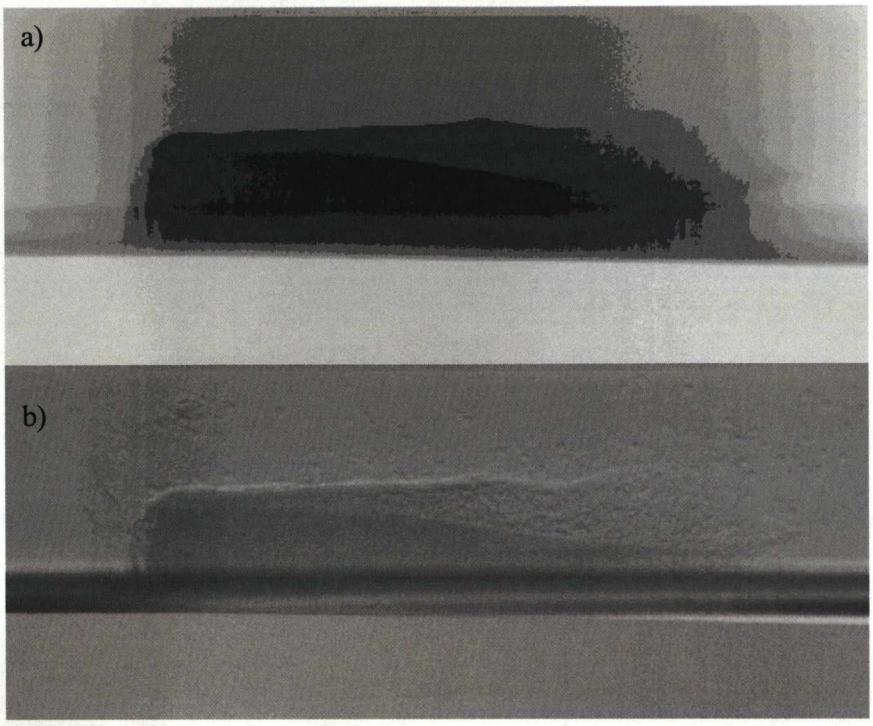

Figure A3-13: The DEI images of Sample 005B. a) The apparent absorption image. b) The refraction image.

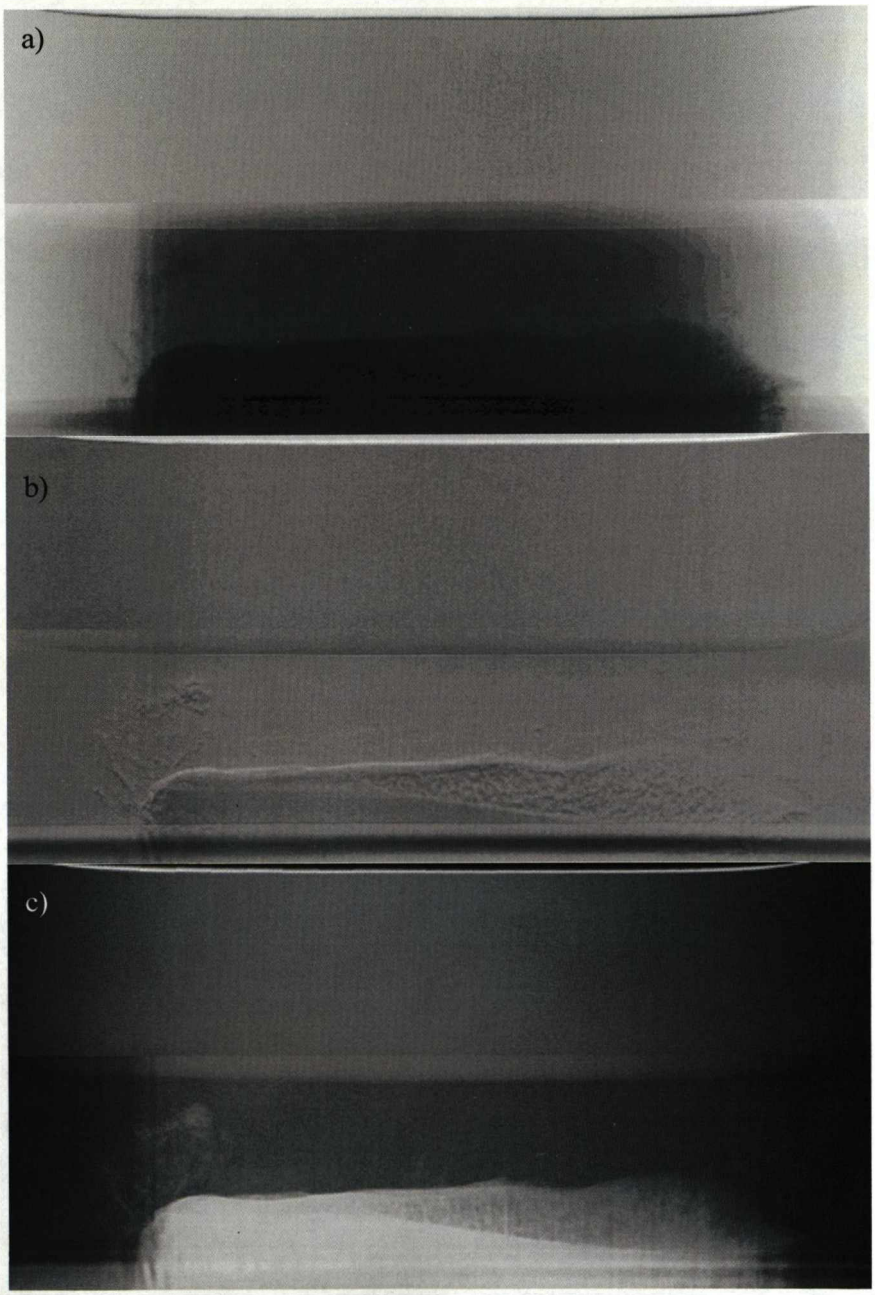

Figure A3-14: The MIR images of Sample 005B. a) The absorption image. b) The refraction image. c) The USAXS image.

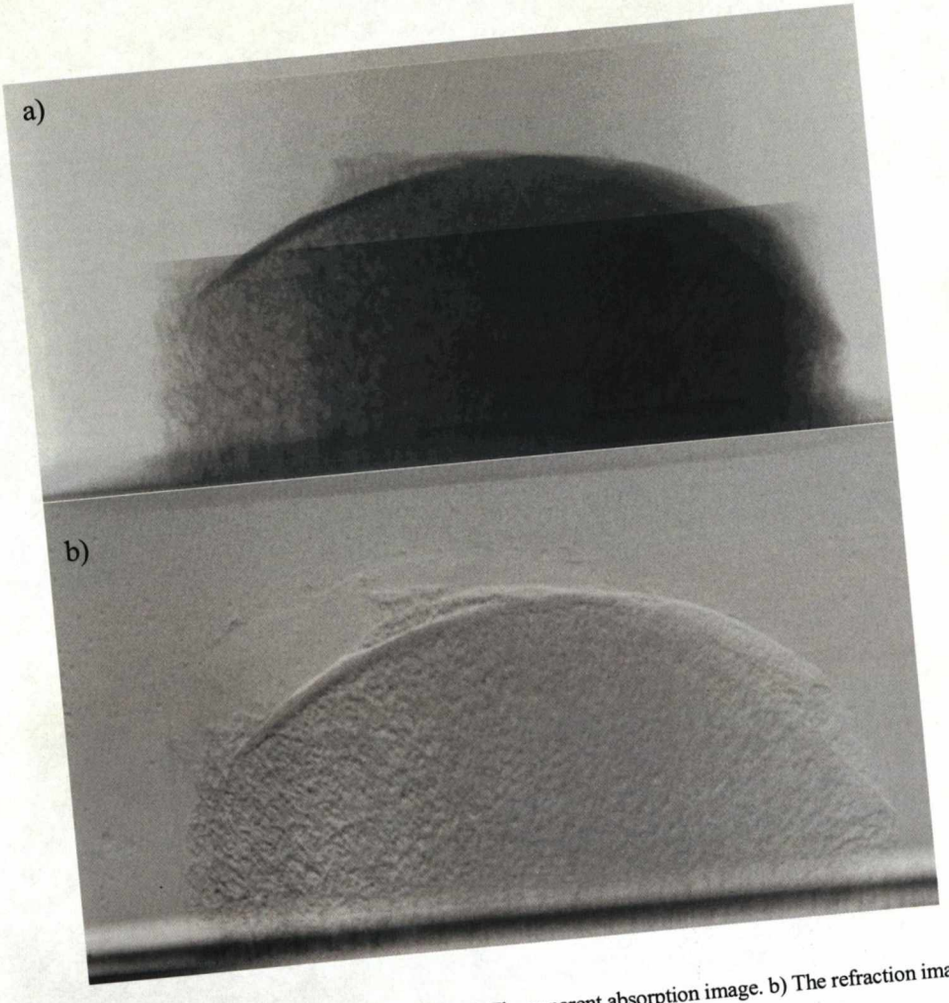

Figure A3-15: The DEI images of Sample 006A. a) The apparent absorption image. b) The refraction image.

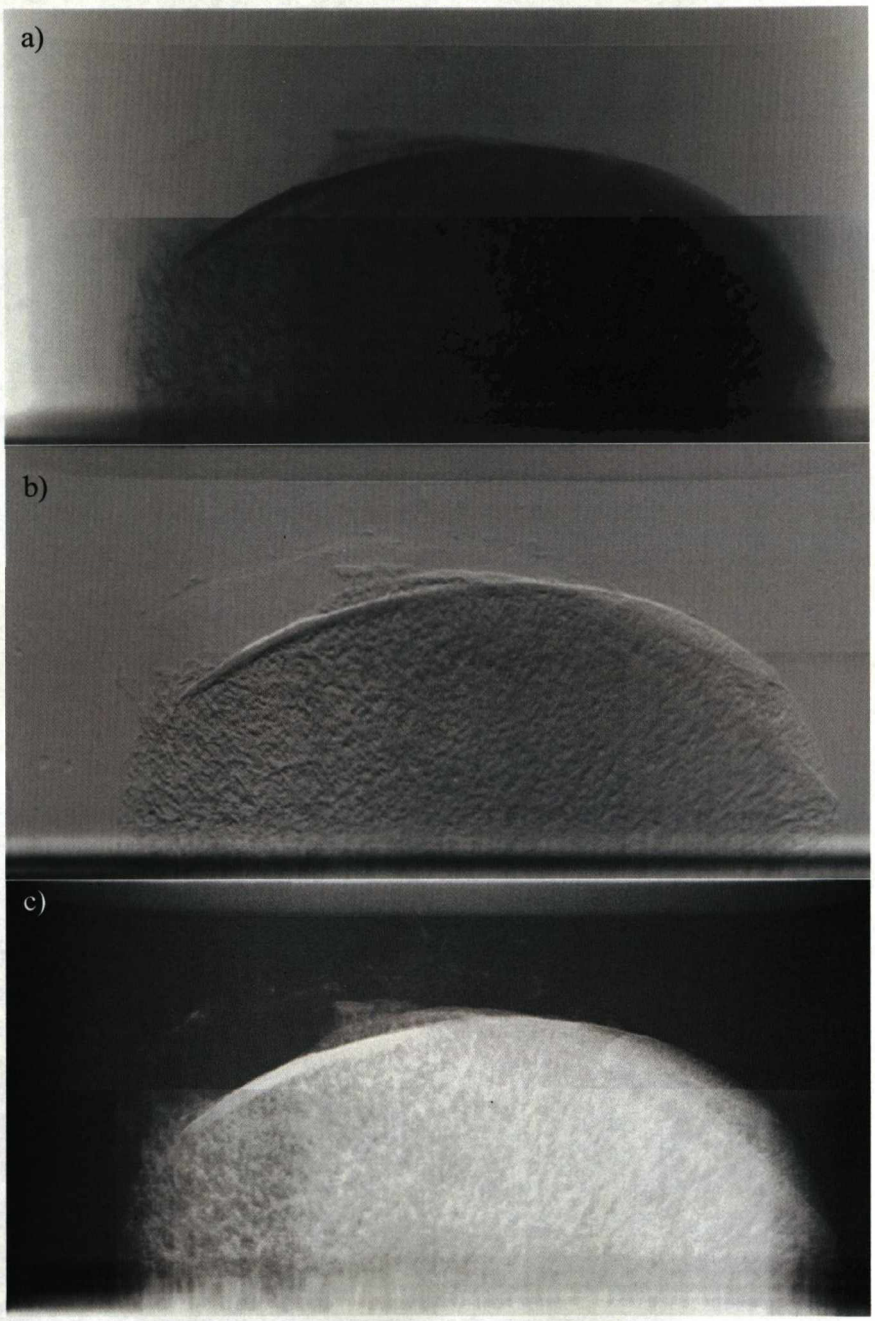

Figure A3-16: The MIR images of Sample 006A. a) The absorption image. b) The refraction image. c) The USAXS image.

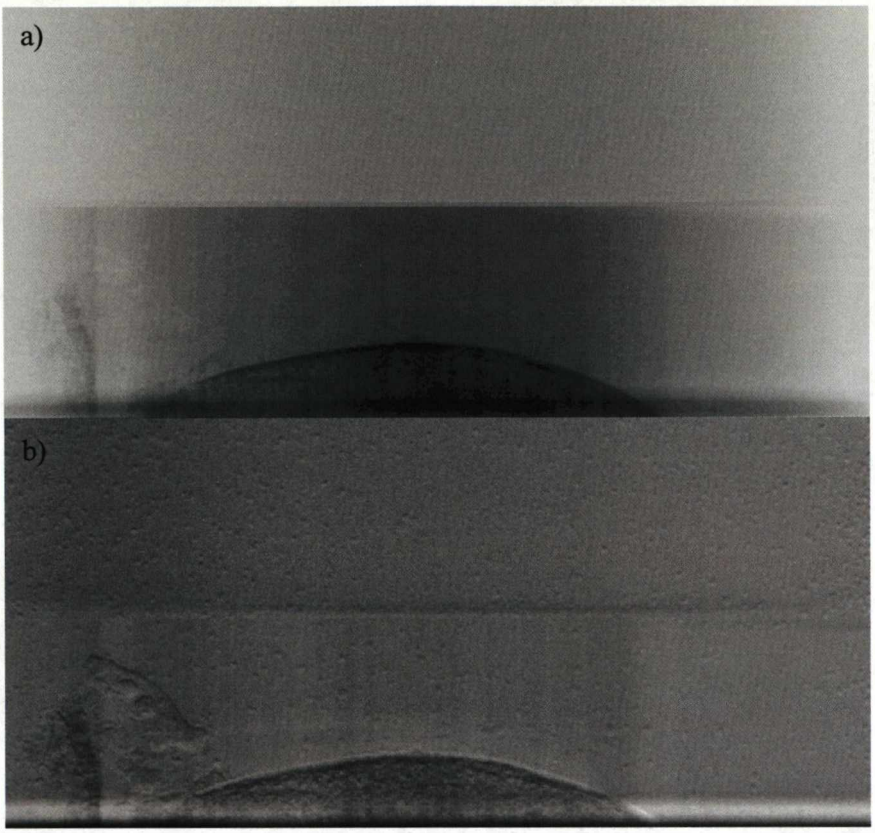

Figure A3-17: The DEI images of Sample 007A. a) The apparent absorption image. b) The refraction image.

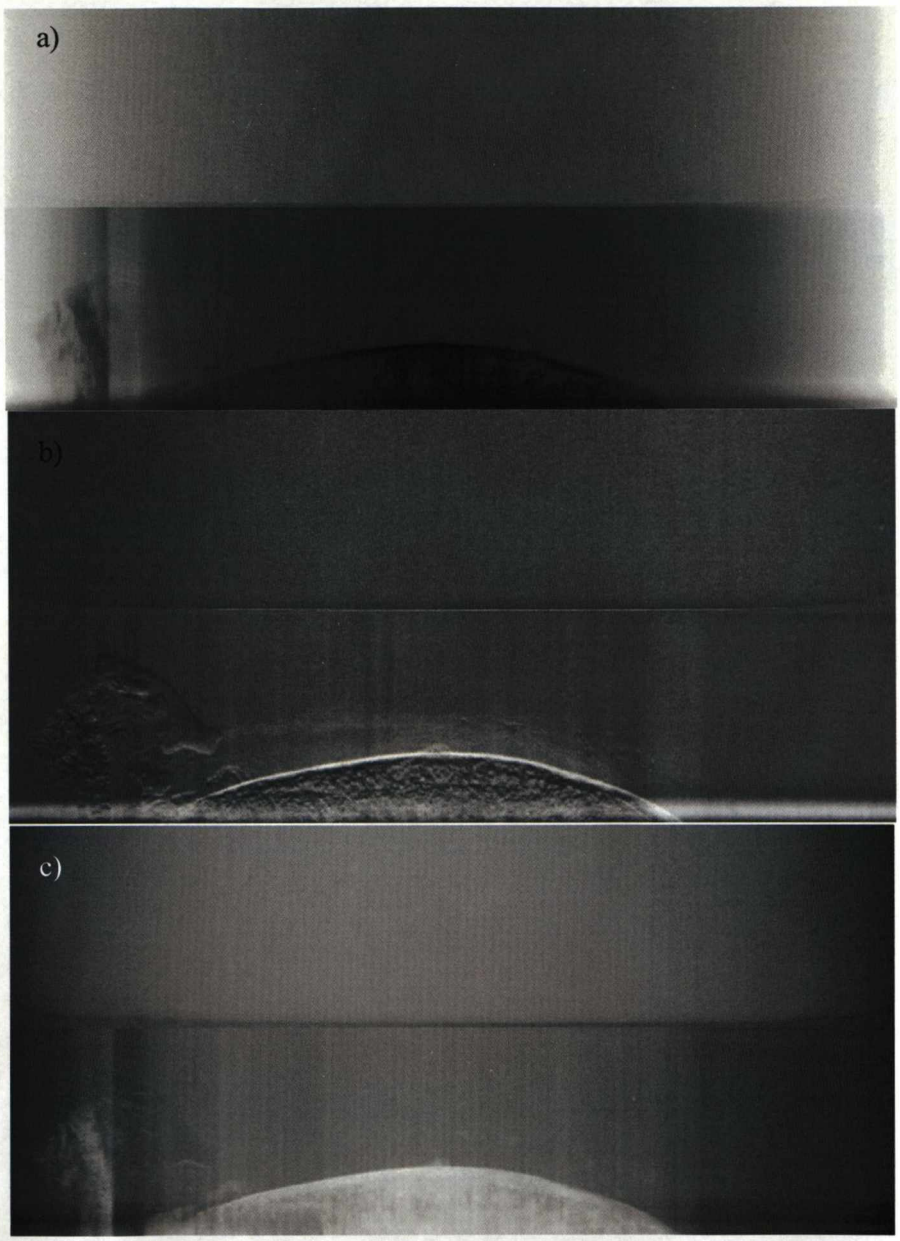

Figure A3-18: The MIR images of Sample 007A. a) The absorption image. b) The refraction image. c) The USAXS image.

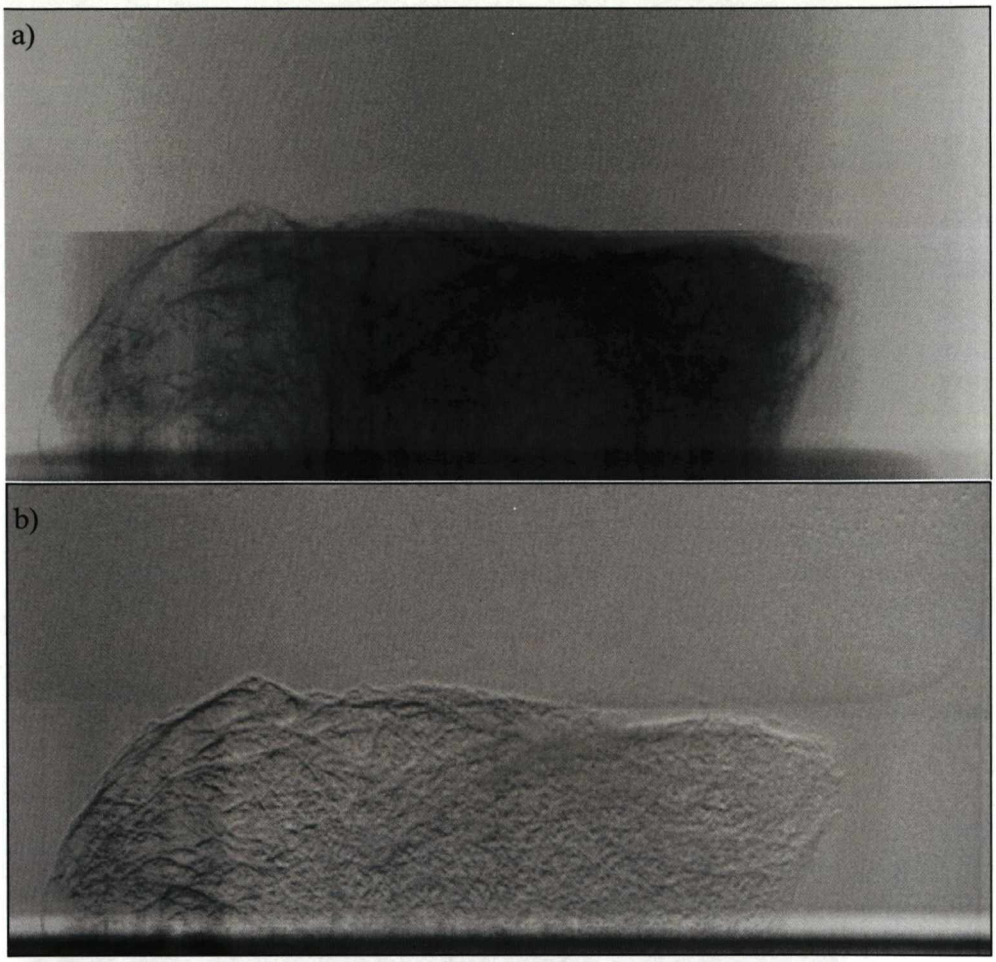

Figure A3-19: The DEI images of Sample 007B. a) The apparent absorption image. b) The refraction image.

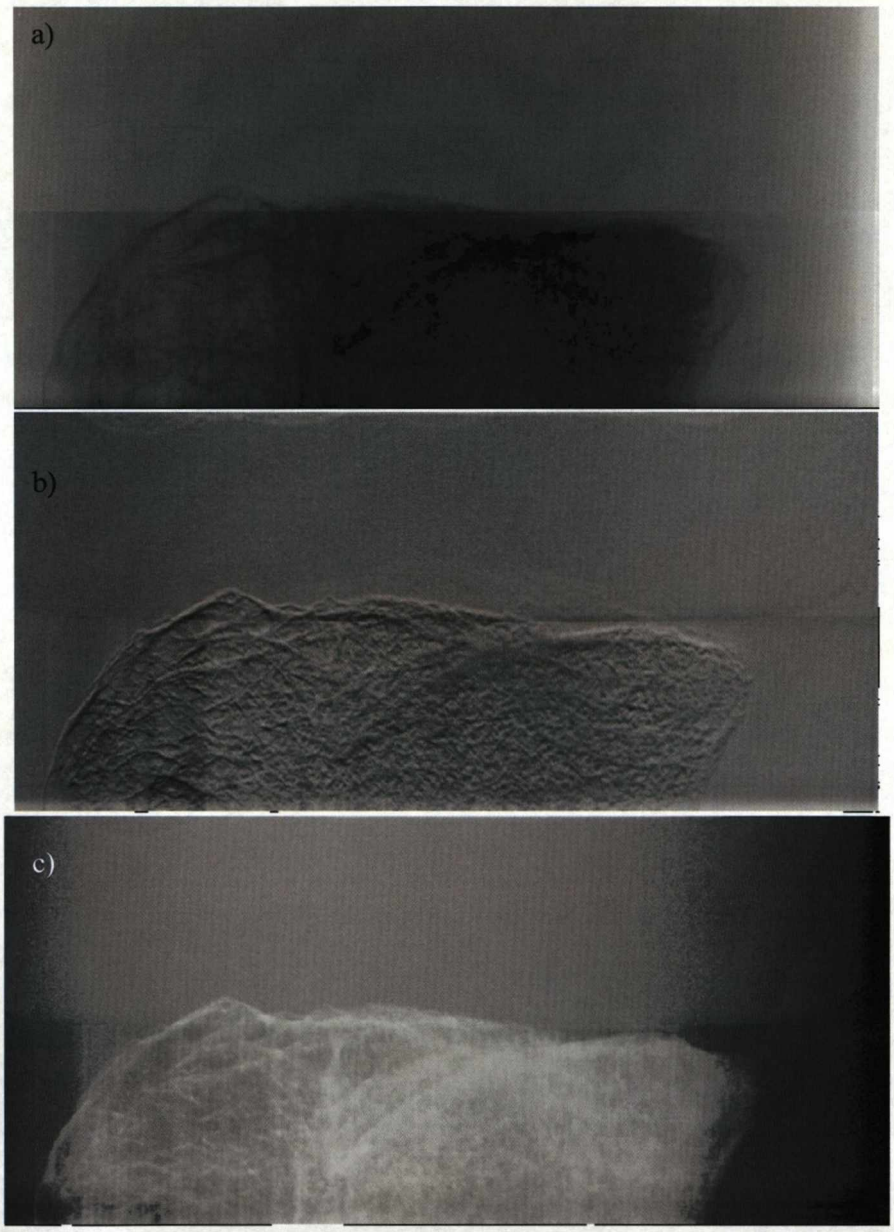

Figure A3-20: The MIR images of Sample 007B. a) The absorption image. b) The refraction image. c) The USAXS image.

APPENDIX 4

1 PUBLICATIONS

Available online at www.sciencedirect.com
ScienceDirect
ELSEVIER
Nuclear Instruments and Methods in Physics Research A 573 (2007) 126–128
NUCLEAR INSTRUMENTS & METHODS IN PHYSICS RESEARCH Section A
www.elsevier.com/locate/nima

Diffraction enhanced imaging of normal and arthritic mice feet

Suzanne Crittell[a,*], K.C. Cheung[b], Chris Hall[b], Mark Ibison[a,b], Paul Nolan[a], Robert Page[a], David Scraggs[a], Steve Wilkinson[b]

[a]Department of Physics, Oliver Lodge Laboratory, Oxford street, Liverpool L69 7ZE, UK
[b]CCLRC Daresbury Laboratory, Daresbury, Warrington, Cheshire WA4 4AD, UK

Available online 8 December 2006

Abstract

The aim of this experiment was to produce X-ray images of mice feet using the diffraction-enhanced imaging (DEI) system at the UK Synchrotron Radiation Source (SRS) at Daresbury. There were two broad types of mice feet samples studied: normal and arthritic. The two types of samples were imaged using several views and compared in order to determine whether it would be possible to detect the early morphological changes linked with this form of arthritis. We found that the DEI images produced were indeed of sufficient quality to show the presence of some osteoarthritic changes.
© 2006 Elsevier B.V. All rights reserved.

PACS: 29.40.G; 87.59.E; 87.64

Keywords: Diffraction enhanced imaging; Osteoarthritis

1. Introduction

The aim of this experiment was to use the X-ray diffraction enhanced imaging (DEI) system at the Daresbury Synchrotron Radiation Source (SRS) to produce DEI images of both healthy and arthritic mice feet. The two types of sample were imaged simultaneously so they could be directly compared. Comparisons were made in order to establish whether the changes in the bone and cartilage linked with this form of arthritis are detectable using this novel X-ray imaging method.

1.1. DEI

In 1997 Chapman et al. published the first paper on what became known as DEI [1]. Since then the technique has been the subject of investigation for use in both industrial and medical applications [1,2].

DEI is a revolutionary imaging modality that is capable of producing two types of radiographic images, one with contrast based on the apparent absorption properties of the sample and the other with its contrast governed by the refraction properties [1,2]. DEI provides more information on tissue morphology than conventional X-ray radiography techniques. Conventional absorption radiology produces a single image with contrast arising from the differing absorption of the sample. DEI however, utilises both the absorption and the refraction properties of the intervening tissue. It is able to do this because a bright, monochromatic, and highly collimated beam is used as a source. This beam is created by positioning a monochromator crystal in a collimated 'white' synchrotron X-ray beam. Once the conditioned beam has traversed the sample it is incident on an analyser crystal which uses the crystal's diffraction properties to reject the highly scattered components of the beam, the remaining components are then incident on a CCD detector to produce an image.

1.2. Osteoarthritis and DEI

The term arthritis indicates a non-specific inflammation of a joint [3]. Osteoarthritis is a degenerative form of arthritis where the cartilage in the joint becomes irritated and inflamed resulting in the degeneration of the cartilage.

*Corresponding author. Tel.: +44 151 794 3379 3388.
E-mail address: stc@ns.ph.liv.ac.uk (S. Crittell).

0168-9002/$ - see front matter © 2006 Elsevier B.V. All rights reserved.
doi:10.1016/j.nima.2006.11.044

In advanced cases there is a total loss of cartilage between the bones that make up the joint [4]. Diagnosis of osteoarthritis is usually made on a clinical basis often with the support of radiographs. These radiographs would be expected to show a narrowing of the joint space and the possible formation of small bony outgrowths [4]. The resolution and contrast on these X-ray radiographs make it very difficult to diagnose the condition early. Magnetic resonance imaging (MRI) allows the cartilage to be made visible but the image resolution is relatively poor.

Several groups in the past have performed experiments to investigate the medical uses of DEI. Some have paid particular attention to its use in cartilage imaging. In 2002 Molenhauer et al. [5] used DEI to image articular cartilage in human knee and ankle joints. They concluded that DEI was capable of detecting cartilage damage when it was at very early stages. Muehleman et al. [6] imaged Rabbit articular cartilage in 2003, agreeing that DEI had the potential for studying cartilage degeneration.

DEI therefore seems to have potential for imaging the progress of osteoarthritis from its early stages.

2. DEI—theory

When monochromatic X-rays are incident on a sample the intensity of the beam is reduced due to the absorption of photons. The X-ray photons that make up the incoming beam interact with the sample in other ways, including being scattered or diffracted both through large angles, of the order of degrees and through small angles in the milli and micro radian range. The analyser optic used in this experiment was identical to the monochromator crystal. It was a silicon crystal cut so that the (1 1 1) plane was parallel to the optical surface. The Bragg diffraction from this crystal has an acceptance range in the region of micro-radians. This means only the components of the beam which deviate less than a few microradians as they traverse the sample are transmitted.

The angular acceptance or reflectivity of the analyser crystal is characterized by its so called 'rocking curve', a plot of relative intensity against angle of incidence (θ), shown in Fig. 1.

Two images are taken in DEI, at 50% relative intensity on either side of the rocking curve. At these positions the rocking curve acts as an amplifier turning small angular deviations into large intensity differences. So when traversing the sample, if the X-ray beam at a certain point was refracted by an angle $\pm\Delta\theta_z$ this point in the 50% image would be at slightly higher or lower intensity.

3. Experimental procedure

The experimental procedure can be separated into three distinct areas: beam alignment, sample preparation, and imaging. These are explained in the following sections.

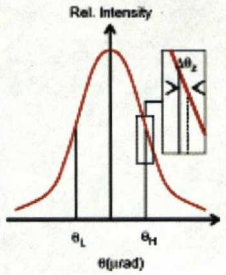

Fig. 1. A schematic of a rocking curve showing the positions of interest for the experiment, where θ_L and θ_H are the angles corresponding to the 50% relative intensities and the low-angle and high-angle sides of the rocking curve, respectively.

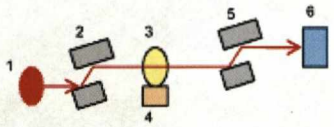

Fig. 2. The DEI system where 1 is the synchrotron source; 2 is the monochromator crystal; 3 is the sample; 4 is the sample stage; 5 is the analyser crystal and 6 is the CCD detector.

3.1. Beam alignment

The experimental set-up is show below in Fig. 2.

The first stage of the experiment was to align the monochromator crystal with the beam using lasers and X-ray sensitive paper. The monochromator was rotated so the incoming X-ray beam was incident on it at the correct angle so as to produce a 15 keV beam. This energy was checked by using a calibrated silicon PIN diode detector. The analyser crystal was then aligned with the monochromatic beam in a similar fashion.

The rocking curve of the analyser crystal could then be plotted and the peak and $\pm 50\%$ intensity angular positions were found by performing a fine angle scan.

3.2. Sample preparation

Prior to imaging, all the samples were stored in 10% neutral buffered formalin. The sample set contained one healthy and one arthritic foot. The samples were clamped between two elastomer membranes in a small sample box. The membranes and the box structure were thin polymers making them virtually transparent to X-rays at this energy.

3.3. Imaging procedure

In order to capture an image the sample and the detector were scanned through the monochromatic X-ray beam

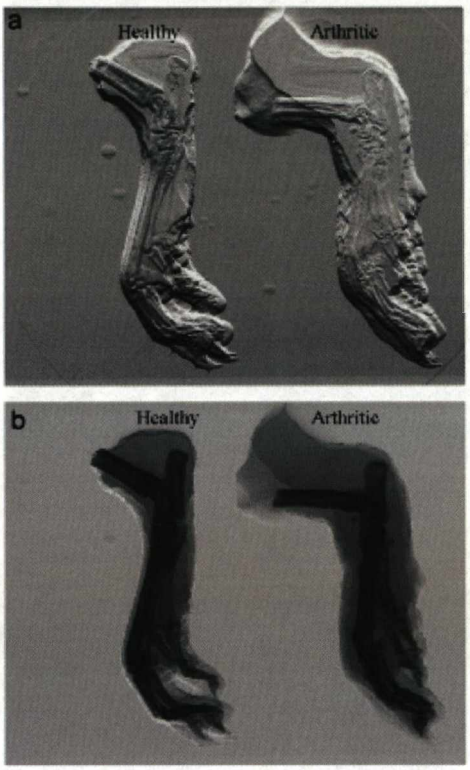

Fig. 3. (a) The refraction image produced and (b) the apparent absorption image produced.

simultaneously. Initially the analyser was positioned on the peak of its rocking curve with no sample in place. Flat field and dark field images were taken. The samples were then positioned on the sample stage imaged. The analyser was then moved to the 50% intensity on one side of the rocking curve and the whole image capture procedure was repeated. This was repeated for the opposite side of the rocking curve.

4. Results and discussion

The raw data were processed using the flat and dark fields to carry out a noise correction. The clean images were used to produce the refraction and apparent absorption images using the algorithm of Chapman et al. [1]. All of these image manipulations were made using the group software PCDetpak. The refraction and apparent absorption images produced are shown in Fig. 3.

The DEI images are of a good quality and the apparent absorption image shows good spatial resolution.

However the orientation of the samples means that the bones in the toes are not as clearly visible as they could be.

When looking at the refraction image it is apparent that it is capable of showing more information than the apparent absorption image, for instance soft tissue structures can be clearly seen around the ankle and the heel.

Despite this there is a shadowing effect present in the refraction image, which has caused the top edges of the sample to be brighter than those on the bottom, this is caused by a slight misalignment in selecting the 50% intensities and highlights a need for further refinement of our method before carrying out further experiments.

These DEI images, particularly the refraction image, show the arthritic foot being more swollen than the healthy foot. The refraction image also shows the spaces between the bones in the ankle joint of the arthritic foot to be less well defined than those in the healthy foot. This is not distinguishable in the apparent absorption image.

We have not as yet been able to perform a direct comparison to determine whether these images can provide more information than conventional radiographs. Despite this DEI's ability to simultaneously produce an absorption image free from large angle scattering and a refraction image which is, as shown above, capable of imaging soft tissue means the DEI images are capable of providing more information than conventional radiographs.

In the future the DEI system at Daresbury will be moving to a new beam line which will enable imaging with a higher energy, more penetrating X-ray beam, allowing images of larger (thicker) samples to be produced.

5. Conclusion

In conclusion, the experiment was successful in taking clear DEI images of a sample set composed of normal and arthritic mice feet. The images were able to show differences between the healthy and arthritic foot that are consistent with osteoarthritis.

Acknowledgments

I would like to acknowledge everyone involved in this project at both the University of Liverpool and CCLRC Daresbury. I would also like to acknowledge EPSRC and MRC.

References

[1] D. Chapman, et al., Phys. Med. Biol. 42 (1997) 2015.
[2] Z. Zhong, et al., Nucl. Instr. and Meth. (2000) 556.
[3] Concise English Dictionary, third ed, Harper Collins, New York, 1991.
[4] R. Hinton, et al., Am. Fam. Physician 65 (5) (2002).
[5] J. Mollenhauer, et al., Osteoarthritis Cartilage 10 (2002) 163.
[6] C. Muehleman, et al., The Anat. Rec. A 272A (2003) 392.

Available online at www.sciencedirect.com
ScienceDirect
Nuclear Instruments and Methods in Physics Research A 580 (2007) 1131–1133
NUCLEAR INSTRUMENTS & METHODS IN PHYSICS RESEARCH Section A
www.elsevier.com/locate/nima

Quantitative analysis of diffraction enhanced images

S. Crittell[a,*], M. Ibison[a,b], K.C. Cheung[b], R. Hodgson[a], D. Gould[a], C. Hall[b], P.J. Nolan[a], R.D. Page[a]

[a]*The University of Liverpool, Liverpool, L69 3BX, UK*
[b]*CCLRC Daresbury Laboratory, Daresbury, Warrington, Cheshire, WA4 4AD, UK*

Available online 23 July 2007

Abstract

In a recent preliminary experiment, a test phantom was imaged using Diffraction Enhanced Imaging (DEI). DEI is a synchrotron-based radiographic imaging technique which uses a single energy of X-rays and the fine angular acceptance of Bragg diffraction to separate out the components of the X-ray beam that have undergone different interactions within the sample. The test phantom was imaged using a beam with energy of 14 keV. The techniques used in this experiment meant that two sets of images were produced of the phantom. The first set is composed of refraction and apparent absorption images. The second technique produced an additional ultrasmall angle scattering image. The use of this second method gave more information than the first technique by showing the scattering properties of the phantom components, we intend to study this feature further in future experiments.
© 2007 Elsevier B.V. All rights reserved.

PACS: 87.59.−e

Keywords: Diffraction enhanced imaging; X-ray imaging; Phase contrast imaging

1. Introduction

Diffraction Enhanced Imaging (DEI) is carried out at a synchrotron and is a form of analyzer-based phase contrast imaging [1,2]. As a method DEI was first reported in 1997 by Chapman [3]. It utilises the fine angular acceptance of a diffracting analyser crystal in such a way that it is possible to create several physically unique images. Depending on the algorithms used it is possible to create Apparent Absorption, Refraction and UltraSmall Angle Scattering (USAS) images [3,4]. In work carried out by other groups these images have been shown to offer great advantages over standard X-ray absorption imaging techniques when imaging soft tissue [5–7].

The analyser crystal's angular acceptance is described by its rocking curve which is a plot of reflectivity against the angle of incidence of the X-ray beam on the crystal. The analyser's rocking curve is key to the separation of Diffraction Enhanced images (DE-images) [3].

There are two analysis methods used to create the DE-images. In the first method sample and flat-field images are taken at three different positions on the rocking curve, one at the peak, and then two at the $\pm 50\%$ relative intensity positions. In this technique refraction images and apparent absorption images are obtained [3].

In the second method sample and flat-field images are taken with the analyser tuned to several different values of relative intensity each with known values of angular position. This makes it possible to create a flat-field rocking curve and a sample rocking curve for each part of the image. Calculating the differences between the two rocking curves means that Refraction, Apparent Absorption and USAS images can be extracted [4].

In order to effectively compare the two DEI analysis methods it is necessary to quantify image quality. In the case of the apparent absorption images the image quality is

*Corresponding author. Oliver Lodge Laboratory, The University of Liverpool, Oxford Street, Liverpool, L69 7ZE, UK.
Fax: +44 151 794 3379.
E-mail address: stc@ns.ph.liv.ac.uk (S. Crittell).

0168-9002/$ - see front matter © 2007 Elsevier B.V. All rights reserved.
doi:10.1016/j.nima.2007.06.110

measured by calculating the contrast, which is found using the following equation:

$$\text{Contrast} = \frac{I_{ave} - I_{min}}{I_{ave}}, \quad (1)$$

where, I_{ave} is the average intensity value over a region in the background in which the beam has not traversed the sample and I_{min} is the minimum value in the image. This will correspond to the component of the beam that has seen the maximum attenuation by the sample [8].

For both the refraction and USAS images, however, any components of the beam that do not go through the sample will not be refracted or scattered and will therefore have an average intensity value of zero. Consequently, it is not possible to use contrast as a measure of image quality. Instead the Signal-to-Noise Ratio (SNR) is calculated as follows:

$$\text{SNR}_{ref} = \frac{\theta_{max} - \theta_{min}}{\sigma_{ref}}, \quad (2)$$

where θ_{max} is the maximum refraction value, θ_{min} is the minimum refraction value and θ_{ref} is the standard deviation of the noise in a region of the background of the image [8], and

$$\text{SNR}_{scat} = \frac{S_{max}}{\sigma_{scat}}, \quad (3)$$

where S_{max} is the maximum scatter value and σ_{scat} is the standard deviation of the noise from a region in the background of the image.

2. Method

The DEI system on station 7.6 at the Synchrotron Radiation Source (SRS) at Daresbury Laboratory uses two channel cut silicon crystals, cut in the (1 1 1) plane, the first as the monochromator crystal and the second, positioned after the sample, as the analyser crystal.

The test phantom, shown in Fig. 1, was composed of three layers of paper, three layers of aluminium, three different diameters of nylon thread (ranging from 0.12 to 0.5 mm) and a piece of rubber ~1 mm thick. These materials were chosen in order to emphasise on the differences between the three sources of contrast.

An X-ray beam energy of 14 keV was used and the phantom was imaged at five different positions on the rocking curve, one at the peak, two at the ±50% intensities and two at the ±70% intensities. At each position a sample image, a flat image and a dark image were taken.

3. Results and discussion

The images that were produced of the test phantom are shown below in Fig. 1.

The differences between the different sources of contrast are apparent when looking at the DE-images (Fig. 1). The aluminium layers in all the images are clearly visible, but

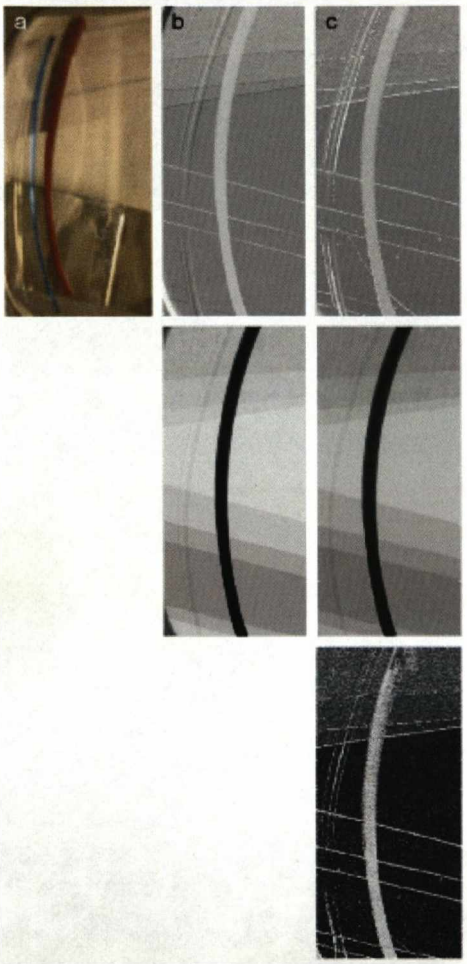

Fig. 1.

for different reasons. In the absorption images the contrast is due to the increasing attenuation with each layer, but in the refraction and USAS images it is due to the refraction and scattering of the X-rays occurring at the edge of each piece of aluminium. It is because of this effect that when looking at the thinnest of the nylon threads (on the left-hand side of the DE-images) it is much more visible in the refraction images than in the apparent absorption image. This demonstrates the advantages of the additional refraction image. Turning attention to the layers of paper,

in the apparent absorption image, as with the aluminium, their contrast is due to the increasing attenuation of the beam with each layer; a similar effect is also seen in the USAS image. With each additional layer of paper there is more scattering of the X-rays. In both the USAS and refraction images the edges are enhanced due to increased scattering and refraction at these points.

Comparing the two DEI analysis methods, it is clear that the second set of images (c) are not as clear as the first (b). However, this is attributed to the increased uncertainties in the angular position of the analyser crystal during the experiment and is echoed in the image quality results. The values of contrast found were 0.9992 for the first method and 0.9975 for the second. The values of SNR for the refraction images were 2.29×10^6 for the first method and 1.61×10^5 for the second with a SNR for the USAS image of 1.68×10^4. However, all the values calculated in assessing the image quality are good with the values of contrast for both apparent absorption images tending to one and high SNR values for the refraction images and the scatter images.

4. Conclusions and future work

We have presented the findings of a preliminary experiment in which a test phantom was successfully imaged using two different DEI analysis methods. We produced two sets of DE-images from the raw images. These images highlighted the differences in the contrast mechanisms and emphasized the properties that would be useful for the purpose built DEI phantoms that are currently under construction at Liverpool and will be used in the future to characterize and compare different DEI systems. We have also implemented image quality measures which reflect the quality of images that can be produced using DEI. The results show a reduction in quality of the images produced using our second set of data. We anticipate that the image quality for this method will be greatly improved once the problems with the stability of the angular position of the analyser crystal have been resolved.

References

[1] K. Goetz, M.P. Kalashnikov, Yu.A. Mikhailov, et al., Sov. J. Quantum Electron 9 (1979) 807.
[2] V.N. Ingal, E.A. Beliaevskaya, J. Phys. D 28 (1995) 2314.
[3] D. Chapman, W. Thomlinson, R.E. Johnston, et al., Phys. Med. Biol. 42 (1997) 2015.
[4] E. Pagot, P. Cloetens, S. Fiedler, et al., Appl Phys Lett 82 (2003) 3421.
[5] J. Li, Z. Zhong, R. Lüdtke, et al., J. Anat. 202 (2003) 463.
[6] J. Mollenhauer, M.E. Aurich, Z. Zhong, et al., Osteoarthritis Cartilage 10 (2002) 163.
[7] E.D. Pisano, R.E. Johnston, D. Chapman, et al., Radiology 214 (2000) 895.
[8] M.Z. Kiss, D.E. Sayers, Z. Zhong, Phys. Med. Biol 48 (2003) 325.

REFERENCES

[1] "Diffraction enhanced x-ray imaging" D. Chapman, W. Thomlinson, R. E. Johnston, D. Washburn, E. Pisano, N. Gmür, Z. Zhong, R. Menk, F. Arfelli, D. Sayer. Phys. Med. Biol. **42** (1997) 2015-2025

[2] "X-rays and their Applications" J. G. Brown, London Iliffe Books Ltd (1966)

[3] "Medical Applications of Nuclear Physics" K. Bethge, G. Kraft, P.Kreisler, G. Walter, Springer (2004)

[4] "Physics for Medical Imaging" R. F. Farr, P. J. Allisy-Roberts, Saunder (2003)

[5] "Radiation Exposure and Image Quality in X-ray Diagnostic Radiology" Horst Aichinger, Joachim Dierker, Sigrid Joite-Barfuβ, Manfred Säbel, Springer (2004)

[6] "Elements of Modern X-ray Physics" Jens Als-Nielsen Des McMorrow, Wiley (2001)

[7] "Elements of Synchrotron Light for Biology, Chemistry, & Medical Research" Giorgio Margaritondo, Oxford University Press (2002)

[8] "Radiation Detection and Measurement" G. Knoll,Wiley (1999)

[9] "Introduction to Solid State Physics" Charles Kittel, Wiley (1996)

[10] "Comparison between a position sensitive germanium detector and a taper optics CCD "FRELON" camera for diffraction enhanced imaging" A. Bravin,

S. Fiedler, P. Coan, J. –C. Labiche, C. Ponchut, A. Peterzol, W. Thomlinson. Nuclear Instruments and Methods in Physics Research A 510 (2003) 35-40

[11] hhtp://www.xray.hmc.psu.edu/rci/ss1/ss1_2.html

[12] "Exploiting the x-ray refraction contrast with an analyser: the state of the art" A. Bravin. J.Phys. D: Appl. Phys. **36** (2003) A24-A29

[13] "X-ray refraction effects: application to the imaging of biological tissues" R. A. Lewis, C. J. Hall, A. P. Hufton, S. Evans, R. H. Menk, F. Arfelli, L. Rigon, G. Tromba, D. R. Dance, I. O. Ellis, A. Evans, E. Jacobs, S. E. Pinder, K. D. Rogers. The British Journal of Radiology, **76** (2003)

[14] Forster E, Goetz K, Zaumseil P 1980 Krist.Tech.**15** 937-45

[15] Ingal V Beliaevskaya E1997 Surf Invest. **12** 441-50

[16] "A new DEI algorithm capable of investigating sub-pixel structures" L. Rigon, H-J. Besch, F. Arfelli, R. Menk, G. Heitner, H. Plothow-Besch. J. Phys. D: Appl. Phys **36** (2003) A107-A112

[17] "Preliminary investigation of a Multiple-Image Radiography method" M. Wernick, O. Wirjadi, D. Chapman, O. Ortulu, Z. Zhong, Y. Yang. IEEE (2003)

[18] "A method to extract quantitative information in analyzer-based x-ray phase contrast imaging" E. Pagot, P. Cleotens, S. Fiedler, A. Bravin, P. Coan, J. Barachel, J. Härtwig, W. Thomlinson. Applied Physics Letters, Volume 83, Number 20.

[19] "Implementation of diffraction-enhanced imaging experiments: at the NSLS and APS" Z. Zhong, W. Thomlinson, D. Chapman, D. Sayers. Nuclear Instruments and Methods in Physics Research A 450 (2000) 556-567

[20] "Diffraction-Enhanced x-ray imaging of in vitro breast tumours" J. Keyriläinen, Academin Dissertation, Helsinki 2004

[21] "Diffraction Enhanced x-ray Imaging of Biological Tissues" C. Hall, A. Hufton, S. Evans, D. Dance, F. Arfelli, A. Olivo, L. rigon, C. Boggis, I. Ellis, A. Evans, S. Pinder, L. Jacobs, P. McArthur, R. Menk, G. Tromba, K. Rogers. Research Highlights 12, Biomedical Sciences.

[22] "Extraction of extinction, refraction and absorption properties in diffraction enhanced imaging" O. Ortulu, Z. Zhong, M. Hasnah, M. Wernick, D. Chapman. J. Phys. D: Appl. Phys. **36** (2003) 2152-2156

[23] "Multiple-image radiography" M. Wernick, O. Wirjadi, D. Chapman, Z. Zhong, N. P. Galatsanos, Y. Yang, J. Brankov, O. Ortulu, M. Anastasio, C. Muehleman, Phys. Med. Bio. **48** (2003) 3875-3895

[24] "Noise and sampling analysis for multiple-image radiography" B. Marquet, J. Brankov, M. Wernick, IEEE 2006.

[25] "Principles of Computed Tomographic Imaging" A. C. Kak, M. Slaney. Siam (2001)

[26] "Computed tomography of x-ray index of refraction using the diffraction enhanced imaging method" F. Dilmanian, Z. Zhong, B. Rent, X. Wu, L. Chapman, I. Orion, W. Thomlinson. Phys. Med. Biol. **45** (2000) 933-946

[27] "Wave propagation and scattering in Random media" A. Ishimaru, Piscataway, New Jersey (1997)

[28] "Multiple-Image computed tomography" J. Brankov, M. Wernick, D. Chapman, Z. Zhong, C. Muehleman, J. Li, M. Anastasio, IEEE (2004)

[29] "Medical applications of synchrotron radiation at the SYREMO beamline of ELETTRA" A. Abrami, F. Arfelli, R. Barroso, F. Billè, P. Bregant et. al. Nuclear Instruments and Methods in Physics Research A 548 (2005) 221-227

[30] "Human Breast Cancer Specimens: Diffraction-enhanced Imaging with Histologic Correlation- Improved Conspicuity of Lesion Detail Compared with Radiography" E. Pisano, R. Johnston, D. Chapman, J. Geradts, M. Iacocca et. al. Radiology (2000) 214: 895-901

[31] "Improved image contrast of calcifications in breast tissue specimens using diffraction enhanced imaging" M. Kiss, D. Sayers, Z. Zhong, C. Parham, E. Pisano Phys. Med. Biol. **49** (2004) 3427-3429

[32] "Imaging lobular breast carcinoma: comparison of synchrotron radiation DEI-CT technique with clinical CT, mammography and histology" S. Fiedler, A. Bravin, J. Keyriläinen, M. Fernández, P. Suortti, W. Thomlinson, M. Tenhunen, P. Virkkunen, M-L. Karjalinen-Lindsberg. Phys. Med. Biol. **49** (2004) 175-188

[33] "X-ray detection of structural orientation in human articular cartilage" C. Muehleman, S. Majumdar, A. Issever, F. Arfelli, R. Menk et. al. Osteoarthritis and Cartilage (2004) **12** 97-105

[34] "Options and Limitations of joint cartilage imaging: DEI in comparison to MRI and sonography" A. Wagner, M. Aurich, N. Sieber, M. Stoessel, W.-D. Wetzel. Nuclear Instruments and Methods in Physics Research A 548 (2005) 47-53

[35] "Diffraction-enhanced X-ray imaging of articular cartilage" J. Mollenhauer, M. Aurich, Z. Zhong, C. Muehleman, A. Cole et al. Osteoarthritis and Cartilage (2002) **10** 163-171

[36] "Radiography of Rabbit Articiular Cartilage With Diffraction-Enhnaced Imaging" C. Muehleman, L. Chapman, K. Kuettner, J. Rieff et. al. The Anatomical Record Part A 272A:392-397 (2003)

[37] "Diffraction enhanced imaging of articular cartilage and comparison with micro-computed tomography of the underlying bone structure" Eur Radiol (2004) 14: 1440-1448

[38] "Synchrotron supported DEI/ KES of a brain tumor in an animal model: The search for a miroimaging modality" K. Mannan, E. Schültke, R. Menk, K. Siu, K. Pavlov et. al. Nuclear Instruments and Methods in Physics Research A 548 (2005) 106-110

[39] "Image quality dependence on the thickness of sliced rat kidney taken by a simplest DEI construction" L. Gang, C. Zhihua, W. Ziyu, M. Ando, P. Lin, J. Wang, X. Jiang Nuclear Instruments and Methods A 548 (2005) 200-206

[40] "Diffraction enhanced imaging of controlled defects within bone, including bone-metal gaps" D. Conner, D. Sayers, D. Sumner, Z. Zhong. Phys. Med. Biol. **51** (2006) 3283-3300

[41] "Combined Diffraction and Refraction Imaging study of a Roman Knife" W. Paszkowicz, T. Wronleski, W. Weker. KSUPS 2005: Extended abstracts/ Synchrotron Radiation in Natural Science Vol. 4, No 1-2 (2005)

[42] "Measurement of image contrast using diffraction enhanced imaging" M. Kiss, D, Sayers, Z. Zhong. Phys. Med. Biol. **48** (2003) 325-340

[43] "Application of absorption and refraction matching techniques for diffraction enhanced imaging" M. Hasnah, O. Oltulu, Z. Zhong, D. Chapman Review of Scientific Instruments Volume 73, Number 3 (2002)

[44] "Mass density images from the diffraction enhanced imaging technique" M. hasnah, C. Parham, E. Pisano, Z. Zhong, O. Oltulu, D. Chapman. Med. Phys. **32** (2) (2005)

[45] "Single-exposure simultaneous diffraction-enhanced imaging" M. Hasnah, O. Oltulu, Z. zhong, D. Chapman. Nuclear Instruments and Methods in Physics Research A 492 (2002) 236-240

[46] "Contrast Improvement with Diffraction Enhanced Imaging for Scattering Materials" F. Arfelli, R. Menk, H. Besch, L. Rigon, H. Plothow-Besch. IEEE (2002)

[47] "Analyser-based mammography using single-image reconstruction" D. Briedis, K. Siu, D. Paganin, K. Pavlov, R. Lewis. Phys. Med, Biol. **50** (2005) 3599-3611

[48] "Crystal tilt error and its correction in diffraction enhanced imaging system" H. Zhang, D. Chapman, Z. Zhong, C. Parham, M.Gupta. Nuclear Instruments in Physics Research A 572 (2007) 961-970

[49] "First test pictures from X-ray diffraction enhanced imaging camera for high contrast medical imaging at SRS" Kan-Cheung Cheung, Khalid Fayz, David Laundy, Rob Lewis, Barry Dobson, Chris Hall. Nuclear Instruments and Methods in Physics Research A 513 (2003) 32-33